THE PIVOTAL ROLE OF THE AXL/GAS6 SIGNALING NODE IN THE MESENCHYMAL SUBTYPE OF OVARIAN CANCER, AND ITS MODULATION BY THE TUMOR SUPPRESSOR OPCML

JANE ANTONY

B.Eng (Hons), NUS

A THESIS SUBMITTED

FOR THE DEGREE OF DOCTOR OF PHILOSOPHY

NUS GRADUATE SCHOOL FOR INTEGRATIVE SCIENCES AND ENGINEERING

NATIONAL UNIVERSITY OF SINGAPORE

2016

DECLARATION OF ORIGINALITY

I hereby declare that this thesis is my original work and it has been written by me in its entirety.

I have duly acknowledged all the sources of information which have been used in the thesis.

This thesis has also not been submitted for any degree in any university previously.



JANE ANTONY

8 August 2016

COPYRIGHT DECLARATION

The copyright of this thesis rests with the author and is made available under a Creative Commons Attribution Non-Commercial No Derivatives licence. Researchers are free to copy, distribute or transmit the thesis on the condition that they attribute it, that they do not use it for commercial purposes and that they do not alter, transform or build upon it. For any reuse or redistribution, researchers must make clear to others the licence terms of this work.

ACKNOWLEDGEMENTS

This journey has been a beautiful experience, and my heart is full of gratitude to everyone who has made this Ph.D. truly memorable. I would like to thank:

Professor Jean Paul Thiery for his guidance and support, it has been an honor to work under his mentorship. His passion and energy for the sciences were absolutely infectious, and I am truly grateful to him for introducing me to the mesmerizing world of RTK signaling, EMT and cell biology.

Dr. Ruby Huang, my co-supervisor for being a pillar of strength and direction, patiently correcting my thesis, and giving me the freedom and confidence to develop my projects. I am indebted to her for all the time, energy and kindness she has poured into me, that propelled me to finish this Ph.D.

Professor Hani Gabra, my co-supervisor for welcoming me to the lab at Imperial College London, and helping me develop a second project while teaching me the delicate art of balancing multiple commitments. His unrelenting confidence in me helped me grow out of my comfort zone and push my boundaries.

Dr. Chiara Recchi my co-supervisor for being so kind and patient, and making me fall in love with membrane biology. Even on days when I was tired or exhausted, she gave me the impetus to turn it around, usually with chocolate, or even stepping in to help me with the lab work. I am indebted for all that she has done, and also for extensively proofreading my thesis.

NUS Graduate School for Integrative Sciences and Engineering, and all the wonderful admin and staff, who made it possible for me embark on this NUS-ICL Joint Program, and for funding my research and giving me so many unique opportunities.

My lab mates at Jean Paul and Ruby's lab – Dr. Tuan Zea Tan for all his help with bioinformatics and statistics, Dr. Vin Yee Chung for teaching me western

blotting, helping me grow numerous cell lines, and helpful conversations about my work and projects, Jieru for keeping the lab absolutely impeccable, ordering reagents and teaching me infection protocols, Asad for teaching me immunostaining, Tan Ming for helping me with qPCRs and for sharing a lot of other things during our Ph.D., Angele for helping me set up the CAM model and cheering me up on days I have been stressed, and also Eddy, Katty and Valerie for being helpful and friendly lab mates.

All my friends from the CSI floor, for all our lunches and coffees and dancing, for bailing me out with reagents when I desperately needed them, and also for their smiling faces and support through this journey – Rohit, Shikha, Eve, Shreya, Madhu, Wan Pei, Mohit, Li Ren, Patrick, Pras, Richard, Lavina, Azhar, Serena.

My wonderful UTown housemates and friends who made this place a second home – Niveditha, Achala, Divya, Maha, Patro, and Mihow.

My lab mates at Hani and Chiara's lab – Dr. Elena Sokolskaja for generating the OPCML transduced cell lines, Dr. Andrew Patterson for teaching me migration assays and tracking cell motility on the confocal, Dr. Zoe Kelly for teaching me the CAM assay, Dr. Evi Karali for helping me trouble shoot various assays, and helping me with bits and pieces of cloning, Young Rock for helping me with the cholesterol depletion protocols and a lot of other things, Haonan for helping me with bioinformatics and giving me the FTE190 cell line. A special thanks with lots of love to Dr. Elisa Zanini for being a calm, composed and absolutely wonderful friend during my Ph.D. (and in my life), teaching me the ropes around the lab, helping me extensively with my project, collaborating with me on her work, unwinding the workday with zumba step, and feeding me pimms and pizzas through my stay in ICL. Eli, you have made this Ph.D. so lovely in so many ways.

Also the other members of the OPCML lab and IRDB floor, Dr. Manuela Mura, Dr. Elaina Maginn, Aline, Eloise, Mohammad, Tommy, Stefan, Phil, Joel for being absolutely wonderful people to work with.

All my close friends for their unwavering support and belief in me, I am truly blessed to have such wonderful people in my life – Akhi, Zac, Himmy, Maanu, Mits, you guys made Singapore a second home for me. Nayani, and Karen, you guys made London feel so magical and helped me so much during the course of my Ph.D., I am truly grateful for all the talks, love and support. Musky, Ganesh, Bharath, Ashta, Venkat, Sudha, Gauthu, Dheeraj and Veej for their unshakable kindness and affection – you guys mean the world to me. Aksh, Vani, Shru, Aarti, and Sow, for letting me climb into their beds and giving me the strength to face just about anything – you girls have shown me that while blood might be thicker than water, some friendships are thicker than both.

And finally, my family. My parents Latha and Antony for all their generosity and kindness, and the ever-gentle reminder to strive to be the best possible version of myself. My darling brother Adi, for being my absolute rock. My uncle Ravi and my cousins for all their laughter and love through my life and Ph.D. My aunt Anu for welcoming me into her home and being a wonderful friend during my stay in Singapore. My Chithamma, uncle Jeff, and baby brother Jothi, for lighting up my world and being my happy bubble. My wonderful family, I am so fortunate to have you all in my life. All your love and kindness is a true blessing and honor. This Ph.D. is dedicated to all of you.

TABLE OF CONTENTS

DECLARATION OF ORIGINALITY III

COPYRIGHT DECLARATION IV

ACKNOWLEDGEMENTS V

TABLE OF CONTENTS VIII

SUMMARY XI

LIST OF TABLES 1

LIST OF ILLUSTRATIONS 2

LIST OF FIGURES 3

LIST OF PUBLICATIONS 6

LIST OF ABBREVIATIONS 7

CHAPTER I: INTRODUCTION 11

1.1 OVARIAN CANCER 12
1.1.1 DISEASE BIOLOGY 12
1.1.2 DIAGNOSIS AND TREATMENT 17
1.1.3 MOLECULAR SUBTYPES OF EOC 19
1.2 EPITHELIAL MESENCHYMAL TRANSITION 20
1.2.1 EMT INDUCERS AND TRANSCRIPTION FACTORS. 22
1.2.2 EMT IN CANCER 24
1.2.3 EMT IN EOC DISEASE BURDEN 26
1.3 THE RECEPTOR TYROSINE KINASE AXL 28
1.3.1 AXL SIGNALING 30
1.3.2 AXL IN EMT AND CANCER 32
1.3.3 TARGETING AXL 33
1.4 THE TUMOR SUPPRESSOR OPCML 35
1.4.1 OPCML AND MEMBRANE ORGANIZED MICRO DOMAINS 36
1.4.2 OPCML AND RTK MODULATION 36
1.4.3 OPCML AND EMT 37
1.5 AIMS AND HYPOTHESIS 38

CHAPTER II: MATERIALS AND METHODS 39

2.1 EOC CELL LINES AND CULTURE 40
2.2 EOC PATIENT TUMOR SAMPLES 42
2.3 SHRNA MEDIATED AXL-KNOCKDOWN 42
2.4 OPCML OVEREXPRESSION 43
2.5 SIRNA MEDIATED GENE SILENCING 44
2.6 ANTIBODIES 45
2.7 WESTERN BLOTTING 46
2.8 IMMUNOFLUORESCENCE STAINING 47
2.9 DUOLINK PROXIMITY LIGATION AMPLIFICATION (PLA) ASSAY 48
2.10 COLORIMETRIC ASSAYS 49
2.11 SINGLE CELL MOTILITY TRACKING 50

2.12 GAP CLOSURE ASSAYS 51
2.13 SOFT AGAR ASSAY 52
2.14 SPHEROID INVASION ASSAY 52
2.15 SKOV3 ORTHOTOPIC XENOGRAFT MOUSE MODEL 54
2.16 CHICK CHORION AALLANTOIC MEMEBRANE (CAM) MODEL 54
2.17 REVERSE PHASE PROTEIN ARRAY 55
2.18 GENE EXPRESSION ANALYSIS AND *AXL* SIGNATURE 56
2.19 STATISTICAL ANALYSIS 56
2.20 GST-PULL DOWN ASSAY 57
2.21 CO-IMMUNOPRECIPITATION ASSAY 58
2.22 MEMBRANE FRACTIONATION PROTOCOL FOR LIPID RAFT GENERATION 58
2.23 CHOLESTEROL DEPLETION PROTOCOL 59

CHAPTER III: GAS6/AXL SIGNALING NETWORK AS A MES MOLECULAR SUBTYPE SPECIFIC THERAPEUTIC TARGET FOR EPITHELIAL OVARIAN CANCER 61

3.1 INTRODUCTION 62
3.2 RESULTS 64
3.2.1 KINOME PROFILING IDENTIFIES *AXL* AS BEING HIGHLY EXPRESSED IN MES, AND *AXL* OVER EXPRESSION IS ASSOCIATED WITH WORSE PATIENT SURVIVAL. 64
3.2.2 AXL EXPRESSION IS PREFERENTIALLY ENRICHED IN THE EMT-ED MES SUBTYPE, AND MODERATELY PRESENT IN THE EPITHELIAL EPI-A SUBTYPE. 69
3.2.3 EXCLUSIVE TO MES, AXL ACTIVATION AMPLIFIES PHOSPHO-ERK SIGNALING. 71
3.2.4 GEMS-SPECIFIC AXL SIGNALING SCHEMA HAS DIVERGENT CONSEQUENCES IN CELL PROLIFERATION AND MOTILITY. 76
3.2.5 GEMS-SPECIFIC AXL ACTIVATION REVEALS AN EXTENSIVE RTK CROSSTALK NETWORK IN MES. 80
3.2.6 THE MES SUBTYPE IS MORE SENSITIVE TO THE AXL INHIBITOR R428. 85
3.2.7 AXL INHIBITION ATTENUATES MOTILITY AND *IN OVO* TUMOR GROWTH IN MES. 88
3.2.8 AXL GOVERNS THE SEQUENTIAL PHENOTYPIC AND FUNCTIONAL TRANSITIONS OF EMT. 91
3.2.9 AXL KNOCKDOWN REDUCES ANCHORAGE INDEPENDENT GROWTH, INVASION, AND TUMOR FORMATION. 94
3.2.10 *AXL* SIGNATURE POSITIVELY CORRELATES WITH EMT AND CONFERS WORSE PROGNOSIS. 97
3.3 DISCUSSION 101

CHAPTER IV: THE TUMOR SUPPRESSOR OPCML BINDS TO, COMPARTMENTALIZES AND INHIBITS THE ONCOGENIC SIGNALING OF AXL 105

4.1 INTRODUCTION 106
4.2 RESULTS 107
4.2.1 OPCML EXPRESSION MODERATES AXL SURVIVAL DETRIMENT. 107
4.2.2 AXL AND OPCML FUNCTION IN THE SAME PATHWAY. 109
4.2.3 OPCML INTERACTS WITH AXL. 111
4.2.4 OPCML HAS INCREASED AFFINITY FOR ACTIVATED AXL. 114
4.2.5 OPCML CURTAILS THE SUSTAINED GAS6/AXL SIGNALING IN MES. 118
4.2.6 OPCML ABROGATES GAS6/AXL MEDIATED CELL MOTILITY AND INVASION. 123
4.2.7 INTEGRITY OF LIPID RAFTS IS CRUCIAL FOR OPCML MODULATION OF AXL SIGNALING. 127
4.2.8 OPCML MODULATION OF OTHER RTK SIGNALING NODES. 132
4.2.9 SILENCING OPCML INCREASES TEMPORAL DURATION OF GAS6/AXL SIGNALING. 135
4.2.10 OPCML POTENTIATES THE EFFECTS OF THE AXL INHIBITOR R428. 138
4.3 DISCUSSION 141

CHAPTER V: CONCLUSIONS AND FUTURE DIRECTIONS 143

5.1 SUMMARY OF RESULTS 144
5.2 CONSIDERATIONS 145
5.3 LIMITATIONS 149
5.3.1 PHENOTYPIC ASSAYS WITH SMALL MOLECULE INHIBITOR R428. 149
5.3.2 GENE MANIPULATION USING RNAI AND OVEREXPRESSION SYSTEMS. 150
5.3.3 COMPARISON BETWEEN R428 INHIBITION ASSAYS AND SHAXL STUDIES. 150
5.3.4 HISTOLOGY OF CELL LINES USED IN THE STUDY. 151
5.4 ON-GOING AND FUTURE WORK 152
5.4.1 PULL DOWN SILAC MASS-SPECTROMETRY OF AXL TO DISCERN BINDING PARTNERS IN EPITHELIAL AND MESENCHYMAL SYSTEMS. 152
5.4.2 FCCS OF AXL-OPCML TO ESTABLISH MEMBRANE DYNAMICS 153
5.4.3 PHOSPHATASE SCREEN 153
5.5 CONCLUDING REMARKS 154

REFERENCES 155

APPENDICES 174

APPENDIX I 175
APPENDIX II 176
APPENDIX III 177
APPENDIX IV 178
APPENDIX V 179

SUMMARY

Epithelial Ovarian Cancer (EOC) is a complex and lethal gynecological malignancy as demonstrated by the heterogeneity in gene expression molecular subtypes (GEMS). To address the GEMS-specific lethality in ovarian cancer, we highlight the relevance of how a receptor tyrosine kinase (RTK) differs in the signaling pattern, functional consequences, and therapeutic implications in the context of GEMS.

An enrichment analysis of the human kinome among the ovarian cancer GEMS shows that AXL is the top-ranking RTK for the EMT-driven, poor prognosis Mes subtype. Interestingly, AXL is also expressed, at a lower rank, in the epithelial, better prognosis Epi-A subtype. Upon ligand stimulation with Gas6, specific to Mes, there is recurrent temporal activation of the extracellular regulated kinase (ERK) signaling downstream of AXL. Reverse Phase Protein Analysis (RPPA) and proximity ligation assays further show that Gas6/AXL signaling transactivates other RTKs such as cMET, EGFR, and HER2 in Mes, exclusively. This RTK crosstalk in concert with the sustained activation of FRA1 downstream to ERK, coincides with the induction of the EMT driver Slug in Mes but not Epi-A. This suggests that the intrinsic property of GEMS influences the complexity and duration of signal propagation. This signal amplification downstream to the Gas6/AXL axis alludes to pathway addiction in Mes. Functionally, the recurrent ERK activation results in a motile and invasive phenotype synonymous to Mes and EMT. This further sensitizes Mes to a selective AXL inhibitor, R428, by attenuating the RTK-ERK activation, reducing the in vitro motility and invasion, and inhibiting the in ovo tumor growth in the chick chorion-allantoic membrane (CAM) assay at a lower GI50 dose compared to Epi-A. Furthermore, silencing AXL in Mes reverses the mesenchymal phenotype and abolishes tumor formation in SCID mice. Our results imply that the mesenchymal state is more sensitive to AXL inhibition, and the RTK crosstalk along the EMT gradient rewires the

system, thereby drastically sensitizing it to RTK node inhibition. The epithelial state might retain a linear signaling axis and shows less therapeutic advantage to targeting AXL. Stratifying ovarian cancer patients based on the GEMS and EMT states followed by targeting AXL is promising in a prospective clinical setting.

The second part of this project is modulation of AXL by the GPI-anchored tumor suppressor OPCML (Opioid-binding Protein/Cell-adhesion Molecule Like). OPCML is abrogated in 83% of sporadic EOCs and 44% of all human cancer by somatic methylation. OPCML is a potent tumor suppressor that severely attenuates tumorigenesis by down modulating a spectrum of RTKs, including, but not limited to FGFR1, FGFR3, HER2, HER4 and EPHA2. Here we show that OPCML interacts with and represses AXL. OPCML preferentially binds to the activated form of AXL and alters its membrane distribution, thereby preventing downstream oncogenic signaling and Gas6/AXL-mediated increase in migration and invasion. OPCML potentiated the effect of AXL inhibitor R428, increasing signaling inhibition and cell death. This completely novel mechanism of regulation of RTKs may be a general mechanism for coordinated regulation of signaling, and may contribute to pro-oncogenic cancer signaling through epigenetic inactivation of OPCML.

LIST OF TABLES

TABLE A: THE FIGO STAGING OF EOC. 13

TABLE B: TYPE I AND TYPE II EOC TUMORS. 17

TABLE C: EMT-INDUCING SIGNALS, TRANSCRIPTION FACTORS AND MARKERS/EFFECTORS. 22

TABLE D: SUMMARY OF AXL INHIBITORS. 33

TABLE I: EOC CELL LINES WITH THEIR RESPECTIVE EMT SUBTYPE AND EMT PHENOTYPE AND CULTURE MEDIA. 41

TABLE II: EOC PATIENT TUMOR SAMPLES WITH THEIR RESPECTIVE EMT MOLECULAR SUBTYPE. 42

TABLE 1: MULTIVARIATE ANALYSIS IDENTIFIES AXL AS AN INDEPENDENT PROGNOSTIC FACTOR FOR WORSE PROGNOSIS IN EOC. 66

TABLE 2: MULTIVARIATE ANALYSIS ACCOUNTING FOR THE EMT MOLECULAR SUBTYPES IDENTIFIES AXL AS AN INDEPENDENT PROGNOSTIC FACTOR IN EOC. 69

TABLE 3: PANEL OF 10 CELL LINES CHOSEN TO REPRESENT THE EOC GEMS AND THE EMT PHENOTYPES TO STUDY AXL SIGNALING KINETICS. 71

TABLE 4: HISTOPATHOLOGY OF 38 OVARIAN CANCER CELL LINES. 179

LIST OF ILLUSTRATIONS

FIGURE A: OVARIAN CANCER IS A HETEROGENEOUS DISEASE ARISING FROM DIFFERENT TISSUES. 16

FIGURE B: JUNCTION INTEGRITY IS COMPROMISED DURING EMT. 21

FIGURE C: DIVERSE REPERTOIRES OF SIGNALING PATHWAYS CONVERGE ONTO THE EMT PROGRAM. 23

FIGURE D: ILLUSTRATION OF EMT FACILITATED METASTASIS BY COLLECTIVE OR SINGLE CELL MIGRATION. 25

FIGURE E: EOC DISEASE BURDEN. 27

FIGURE F: AXL BELONGS TO THE TAM FAMILY OF RTKS. 29

FIGURE G: GAS6/AXL SIGNALING SCHEMA. 31

FIGURE H: SCHEMATIC REPRESENTATION OF OPCML STRUCTURE. 36

FIGURE I: MAMMALIAN-2-HYBRID ASSAY SHOWS A CLEAR SIGNAL FOR INTERACTION BETWEEN OPCML AND AXL. 37

FIGURE J: SPHEROID INVASION ASSAY. 53

FIGURE K: OVERVIEW OF AXL SIGNALING IN EPITHELIAL AND MESENCHYMAL STATES, AND MODULATORY MECHANISMS. 147

FIGURE L: AXL KINASE DOMAIN IS CRUCIAL TO INITIATE PHOSPHORYLATION OF RTKS IN GAS6/AXL-RTK CROSSTALK NETWORKS IN MES. 148

LIST OF FIGURES

FIGURE 1: KINOME PROFILE OF EMT SUBTYPED EOC TUMORS AND CELL LINES. 64

FIGURE 2: *AXL* EXPRESSION IS ENRICHED IN THE MES SUBTYPE OF OVARIAN CANCER. 65

FIGURE 3: *AXL* OVER EXPRESSION CONFERS WORSE PROGNOSIS IN OVARIAN CANCER. 66

FIGURE 4: *AXL* EXPRESSION IS ENRICHED IN THE MES SUBTYPE OF OVARIAN CANCER. 70

FIGURE 5: AXL ACTIVATION HAS DIVERGENT CONSEQUENCES IN DOWNSTREAM PERK AND PAKT SIGNALING IN THE CONTEXT OF GEMS AND EMT PHENOTYPES. 73

FIGURE 6: MES GEMS DELINEATES RECURRENT PERK RESPONSE, WHILE EMT PHENOTYPE MODULATES PAKT RESPONSE. 74

FIGURE 7: SILENCING AXL PREVENTS GAS6/AXL MEDIATED PHOSPHORYLATION ERK 75

FIGURE 8: GAS6/AXL ACTIVATION MARGINALLY INCREASES CELL PROLIFERATION IN ALL EOC CELL LINES IRRESPECTIVE OF GEMS STATUS OR EMT PHENOTYPE. 76

FIGURE 9: GAS6/AXL ACTIVATION INCREASES SINGLE CELL MOTILITY EXCLUSIVELY IN MES. 78

FIGURE 10: GAS6/AXL ACTIVATION ACCELERATES GAP CLOSURE IN MES SUBTYPE. 79

FIGURE 11: AXL IN ENMESHED IN AN RTK NETWORK IN THE MES SUBTYPE. 81

FIGURE 12: IN THE MES SUBTYPE, AXL ACTIVATED BY GAS6, CO-CLUSTERS WITH, AND PHOSPHORYLATES MET, EGFR AND HER2. 82

FIGURE 13: MEK INHIBITION PREVENTS SIGNALING DOWNSTREAM OF THE GAS6/AXL AXIS. 83

FIGURE 14: INHIBITION OF MEK PREVENTS GAS6/AXL INDUCED CELL MOTILITY. 84

FIGURE 15: MES SUBTYPE IS MORE SENSITIVE TO AXL INHIBITIOR R428. 85

FIGURE 16: AXL INHIBITION CURTAILS SIGNALING AT LOWER DOSES IN MES. 86

FIGURE 17: EOC CELL LINES ARE SENSITIZED ALONG AN EMT GRADIENT TO AXL INHIBITION. 87

FIGURE 18: AXL INHIBITIOR R428 REDUCES CELL MOTILITY AT LOWER DOSES IN MES. 89

FIGURE 19: AXL INHIBITION PREFERENTIALLY SENSITIZES *IN OVO* TUMOR GROWTH IN MES. 90

FIGURE 20: AXL GOVERNS THE SEQUENTIAL PHENOTYPIC TRANSITIONS OF EMT. 92

FIGURE 21: SILENCING AXL REDUCES CELL MOTILITY. 93

FIGURE 22: AXL KNOCKDOWN SLOWS CELL PROLIFERATION. 94

FIGURE 23: AXL KNOCKDOWN REDUCES ANCHORAGE INDEPENDENT GROWTH AND INVASION. 95

FIGURE 24: SILENCING AXL ABROGATES TUMOR FORMATION AND GROWTH. 96

FIGURE 25: *AXL* SIGNATURE IN OVARIAN TUMORS. 97

FIGURE 26: HIGH *AXL* SIGNATURE CONFERS WORSE PROGNOSIS IN SPECIFIC CANCERS. 98

FIGURE 27: *AXL* SIGNATURE EXPRESSION LEVELS IN OMENTAL METASTASIS AND RELAPSED TUMORS. 99

FIGURE 28: PHOSPHO-MAPK LEVELS ACROSS EOC GEMS 100

FIGURE 29: OPCML EXPRESSION ALTERS THE ASSOCIATION BETWEEN AXL AND PATIENT SURVIVAL. 107

FIGURE 30: OPCML METHYLATION ALTERS THE ASSOCIATION BETWEEN AXL AND PATIENT SURVIVAL. 108

FIGURE 31: GENERATION OF OPCML EXPRESSING SKOV3 AND PEA1 CLONES. 109

FIGURE 32: MODULATION OF CELL MOTILITY BY AXL AND OPCML. 110

FIGURE 33: PULL DOWN AND CO-IMMUNOPRECIPITATION ASSAYS TO DETECT AXL-OPCML INTERACTION. 111

FIGURE 34: IMMUNOSTAINING AND PROXIMITY LIGATION ASSAY TO VISUALIZE AXL-OPCML ASSOCIATION. 112

FIGURE 35: OPCML EXPRESSION ALTERS MEMBRANE DISTRIBUTION OF AXL. 113

FIGURE 36: IMMUNOSTAINING REVEALS INCREASE IN AXL-OPCML INTERACTION UPON GAS6 STIMULATION. 114

FIGURE 37: PLA REVEALS INCREASE IN AXL-OPCML INTERACTION UPON GAS6 STIMULATION. 115

FIGURE 38: OPCML BINDS TO, AND HAS A HIGHER AFFINITY FOR ACTIVATED AXL. 116

FIGURE 39: OPCML CHANGES COMPARTMENTALIZATION OF ACTIVATED AXL TO MODULATE SIGNALING. 117

FIGURE 40: OPCML EXPRESSION REDUCED TEMPORAL DURATION OF PAXL AND PERK SIGNALING. 118

FIGURE 41: OPCML EXPRESSION REDUCED PERK RESPONSE TO GAS6 STIMULATION. 119

FIGURE 42: FUNCTIONAL PROTEOMICS REVEALS SUPPRESSION OF ONCOGENIC SIGNALING BY OPCML AT A SYSTEMS LEVEL. 121

FIGURE 43: OPCML OVEREXPRESSION DOES NOT ALTER SIGNALING DYNAMICS IN EPITHELIAL PEO1 CELLS. 122

FIGURE 44: OPCML EXPRESSION ABROGATES GAS6/AXL INDUCED CELL MOTILITY. 123

FIGURE 45: OPCML EXPRESSION REDUCES GAP CLOSURE RATES. 124

FIGURE 46: IMMUNOSTAINING OF GAP CLOSURE REVEALS ABROGATION OF PERK UPON OPCML EXPRESSION. 125

FIGURE 47: OPCML NEGATES GAS6/AXL MEDIATED SPHEROID INVASION. 126

FIGURE 48: MBCD TREATMENT DEPLETES CELLS OF CHOLESTEROL. 127

FIGURE 49: DISRUPTION OF LIPID RAFTS PREVENTS OPCML MEDIATED SEQUESTERING OF AXL IN THE RAFTS, AND CONSEQUENTLY FAILS TO CURTAIL SIGNALING. 129

FIGURE 50: LIPID RAFT PERTURBATION PREVENTS OPCML FROM RESTRAINING GAS6/AXL SIGNALING. 130

FIGURE 51: PLA ASSAY REVEALS AXL-OPCML INTERACTION IRRESPECTIVE OF LIPID RAFT INTEGRITY. 131

FIGURE 52: IN ADDITION TO GAS6, OPCML SUPPRESSES HGF MEDIATED SIGNALING, BUT NOT EGF. 132

FIGURE 53: GST-OPCML PULL DOWN ASSAY REVEALS OPCML INTERACTION WITH HER2 AND CMET, BUT NOT EGFR. 133

FIGURE 54: OPCML EXPRESSION CURTAILS HGF MEDIATED SIGNALING. 134

FIGURE 55: SIRNA MEDIATED OPCML SILENCING IN FTE190. 135

FIGURE 56: SIOPCML FTE190 SHOW INCREASED RESPONSE TO GAS6 STIMULATION. 136

FIGURE 57: SILENCING OPCML IN FTE190 INCREASES PROLIFERATION BUT NOT MOTILITY UPON GAS6 STIMULATION. 137

FIGURE 58: OPCML EXPRESSION SENSITIZES SKOV3 CELL LINES TO AXL INHIBITOR R428. 138

FIGURE 59: OPCML EXPRESSION SYNERGIZES SIGNALING INHIBITION BY AXL INHIBITOR R428. 139

FIGURE 60: OPCML EXPRESSION SENSITIZES SKOV3 TO AXL INHIBITOR MEDIATED IN OVO TUMOR REDUCTION. 140

FIGURE I: EMT STATUS INFLUENCES GAS6/AXL SIGNALING. 175

FIGURE II: MEMBRANE RAFTS AND CELLULAR PHOSPHATASES REGULATE AXL SIGNALING IN EPITHELIAL SYSTEMS. 176

FIGURE III: AXL KINASE DOMAIN IS CRUCIAL FOR PHOSPHORYLATION OF OTHER RTKS 177

FIGURE IV: OPCML-AXL INTERACTION UPON GAS6 STIMULATION AFFECTS DIFFUSION OF AXL. 178

LIST OF PUBLICATIONS

The GAS6-AXL signaling network is a mesenchymal (Mes) molecular subtype–specific therapeutic target for ovarian cancer.

Antony J, Tan TZ, Kelly Z, Low J, Choolani M, Recchi C, Gabra H, Thiery JP, Huang RJY.
Sci. Signal. 9, ra97 (2016).

Targeting the AXL signaling pathway in ovarian cancer
Huang RJY, **Antony J**, Tan TZ, Tan DSP
Molecular and Cellular Oncology (2016)

The tumor suppressor OPCML sequesters AXL in plasma membrane lipid domains, mediating its inactivation by the phosphatase PTPRG in ovarian cancer.

Antony J, Zanini E, Tan TZ, Kelly Z, Jung Y, Nawathe SR, Huang RYJ, Thiery JP, Recchi C, Gabra H.
(Manuscript in preparation)

OPCML negatively regulates the FGF10-FGFR1 pathway in breast cancer.

Zanini E, **Antony J**, Birtley JR, Carter EP, Cheung A, Grose RP, Recchi C, Gabra H.
(Manuscript in preparation)

OPCML potentiates anti-EGFR and anti-HER2 targeted therapy in HER2-positive Ovarian and Breast Cancers.

Zanini E, Louis LS, **Antony J**, Okon I, McKie AB, El-Bahrawy M, Stebbing J, Recchi C, Gabra H.
(Manuscript in preparation)

LIST OF ABBREVIATIONS

Gene / Protein Names

α-SMA	Alpha Smooth Muscle Actin
AEBP1	Adipocyte Enhancer Binding Protein 1
AKT	Protein Kinase B
ARID1A	AT-Rich Interactive Domain-Containing Protein 1A
AXL	Anexeleto
Bcl-2	B-Cell Lymphoma 2
Bcl-xl	B-Cell Lymphoma Extra Large
BMP	Bone Morphogenetic Protein
BRAF	B-Raf Proto-Oncogene Serine/Threonine-Protein Kinase
BRCA1	Breast Cancer Type 1 Susceptibility Protein
BRCA2	Breast Cancer Type 2 Susceptibility Protein
C1-TEN	C1 Domain-Containing Phosphatase And Tensin Homologue
CA125	Cancer Antigen 125
Cbl-b	Casitas B-Lineage Lymphoma-B
CDH11	Cadherin 11
CDK12	Cyclin-Dependent Kinase 12
CDKN2A	Cyclin-Dependent Kinase Inhibitor 2A
cMET	Hepatocyte Growth Factor Receptor
COL10A1	Collagen Type X Alpha 1
COL1A1	Collagen Type I Alpha 1
COL3A1	Collagen Type III Alpha 1
COL5A1	Collagen Type V Alpha 1
COL5A2	Collagen Type V Alpha 2
CRB3	Crumbs 3, Cell Polarity Complex Component
CRISPLD2	Cysteine Rich Secretory Protein LCCL Domain Containing 2
CTNNB1	Catenin Beta 1
CTSK	Cathepsin K
CXCL12	C-X-C Motif Chemokine 12
DAPI	4',6-Diamidino-2-Phenylindole
DCN	Decorin
DUSP4	Dual Specificity Phosphatase 4
EFEMP1	Egf Containing Fibulin-Like Extracellular Matrix Protein 1
EGF	Epidermal Growth Factor
EGFR	Epidermal Growth Factor Receptor
ELK1	ETS Domain-Containing Protein
EPHA2	Eph Receptor A2
ERK	Extracellular Signal-Regulated Kinase
FAP	Fibroblast Activation Protein Alpha
FBN1	Fibrillin 1
FGFR1	Fibroblast Growth Factor Receptor 1
FGFR3	Fibroblast Growth Factor Receptor 3
FN1	Fibronectin 1
FNIII	Fibronectin Type III
FRA1	Fos-Related Antigen 1
GAPDH	Glyceraldehyde 3-Phosphate Dehydrogenase

Gas6	Growth Arrest-Specific 6
GPI	Glycosylphosphatidylinositol
Grb2	Growth Factor Receptor-Bound Protein 2
GRHL2	Grainyhead Like Transcription Factor 2
GSK3	Glycogen Synthase Kinase 3
GST	Glutathione S-Transferase
HER2	Human Epidermal Growth Factor Receptor 2
HER4	Human Epidermal Growth Factor Receptor 4
HGF	Hepatocyte Growth Factor
HNT	Neurotrimin
Ig-like	Immunoglobulin-Like
IGF	Insulin-Like Growth Factor 1
IL6	Interleukin 6
ILK	Integrin-Linked Kinase
INHBA	Inhibin Beta A
JAK	Janus Kinase
JNK	c-Jun N-terminal Kinase
K-Ras	V-Ki-Ras2 Kirsten Rat Sarcoma Viral Oncogene Homolog
LSAMP	Limbic System-Associated Membrane Protein
LUM	Lumican
MAPK	Mitogen-Activated Protein Kinase
MDM2	Mouse Double Minute 2 Homolog
MEK1	MAPK/ERK Kinase 1
MMP2	Matrix Metalloproteinase-2
MMP3	Matrix Metalloproteinase-3
mTOR	Mechanistic Target Of Rapamycin
MUC16	Mucin 16
Nck2	Non-Catalytic region of Tyrosine Kinase, Beta
NEGR1	Neuronal Growth Regulator 1
NF1	Neurofibromatosis Type I
NFkB	Nuclear Factor Kappa-Light-Chain-Enhancer Of Activated B Cells
OLFML3	Olfactomedin Like 3
OPCML	Opioid Binding Protein/Cell Adhesion Molecule-Like
p53	Tumor Protein P53
p90RSK	p90 Ribosomal S6 Kinase
pAKT	phosphorylated-AKT
Par-3/6	Partitioning Defective Protein-3/6
PARP	Poly (ADP-Ribose) Polymerase
pAXL	phosphorylated-AXL
PDGF	Platelet-Derived Growth Factor
pEGFR	phosphorylated-EGFR
pERK	phosphorylated-ERK
pHER2	phosphorylated-HER2
PI3KCA	Phosphoinositide-3-Kinase, Catalytic, Alpha Polypeptide
PKC-β	Protein kinase C Beta
PLCγ	Phosphoinositide Phospholipase C
pMET	phosphorylated-cMET
PPP2R1A	Protein Phosphatase 2 Regulatory Subunit A, Alpha
PTEN	Phosphatase and Tensin Homolog

PTGIS	Prostaglandin I2 (Prostacyclin) Synthase
RON	Recepteur d'Origine Nantais Kinase
RTK	Receptor Tyrosine Kinase
S6	Ribosomal Protein S6
S6K	Ribosomal Protein S6 Kinase
SERPINF1	Serine Proteinase Inhibitor, Clade F, Member 1
SFRP4	Secreted Frizzled-Related Protein 4
SH1	Src Homology 1 Domain
SH3	Src Homology 3 Domain
SHC	SHC (Src Homology 2 Domain Containing) Transforming Protein
SHP2	Protein Tyrosine Phosphatase, Non-Receptor Type 11
SMAD	Mothers Against DPP Homolog
SNAI1	Snail Family Zinc Finger 1
SNAI2	Snail Family Zinc Finger 2
SOCS-1	Suppressor Of Cytokine Signaling 1
SPARC	Secreted Protein Acidic and Cysteine Rich
SRC	V-Src Avian Sarcoma (Schmidt-Ruppin A-2) Viral Oncogene Homolog
STAT	Signal Transducer And Activator Of Transcription
TAM	Tyro3-AXL-Mer
TGF-β	Transforming growth factor beta
TGFβRI	Transforming growth factor, beta receptor I
TGFβRII	Transforming growth factor, beta receptor II
THBS1	Thrombospondin 1
THBS2	Thrombospondin 2
TIMP3	Tissue Inhibitor Of Metalloproteinases-3
TWIST1	Twist Family BHLH Transcription Factor 1
VCAM1	Vascular Cell Adhesion Molecule 1
VCAN	Versican Proteoglycan
VEGF	Vascular Endothelial Growth Factor
WFDC2	WAP Four-Disulfide Core Domain 2
ZEB1	Zinc Finger E-Box Binding Homeobox 1
ZEB2	Zinc Finger E-Box Binding Homeobox 2
ZO-1	Zona Occludens 1

Cells / Tissues / Cellular processes / Clinical terms

AOCS	Australian Ovarian Cancer Study
CML	Chronic Myeloid Leukemia
CTC	Circulating Tumor Cells
DNA	Deoxyribonucleic Acid
DRM	Detergent Resistant Membrane
DSM	Detergent Soluble Membrane
E	Epithelial
EMT	Epithelial-Mesenchymal Transition
EOC	Epithelial Ovarian Cancer
Epi-A	Epithelial-A
Epi-B	Epithelial-B
FTE190	Fallopian Tube Epithelial Cell Line 190
GEMS	Gene Expression Molecular Subtype

GSEA	Gene Set Enrichment Analysis
HGSC	High-Grade Serous Carcinoma
IE	Intermediate Epithelial
IM	Intermediate Mesenchymal
LGSC	Low-Grade Serous Carcinoma
LOH	Loss Of Heterozygosity
M	Mesenchymal
Mes	Mesenchymal
MET	Mesenchymal–Epithelial Transition
MMR	DNA Mismatch Repair
NSCLC	Non-Small Cell Lung Cancer
OS	Overall Survival
OSE	Ovarian Surface Epithelium
PFS	Progression Free Survival
ROMA	Risk Ovarian Malignancy Algorithm
Stem-A	Stem-like-A
Stem-B	Stem-like-B

Others

CAM	Chick Chorioallantoic Membrane
DMSO	Dimethyl Sulfoxide
FCS	Fluorescence Correlation Spectroscopy
FFPE	Formalin-Fixed, Paraffin-Embedded
GI50	Growth Inhibition Of 50%
HR	Hazard Ratio
MBCD	Methyl-Beta-Cyclodextrin
PLA	Proximity Ligation Assay
RPPA	Reverse Phase Protein Array
SCID	Severe Combined Immunodeficiency
SILAC	Stable Isotope Labeling With Amino Acids In Cell Culture
TCGA	The Cancer Genome Atlas
WB	Western Blot

CHAPTER I: INTRODUCTION

1.1 OVARIAN CANCER

Ovarian cancer is one of the top five leading causes of cancer related deaths in woman and the deadliest gynecological malignancy[1]. Most cases are of a sporadic nature with no clear elucidation for the etiology of the disease. The malignancy is characterized by non-specific symptoms and dissemination in the pelvic region in the early stages (International Federation of Gynecology and Obstetrics, Stages I and II, Table A), and further metastasis involving the peritoneal cavity and beyond in advanced stages (Stages III and IV, Table A)[2]. As ovarian cancer shows no specific symptoms, it is diagnosed at advanced stages and is therefore characterized by high morbidity and mortality. When caught early, the five-year survival rate for woman affected by ovarian cancer is greater than 90%, however only about 15% of cases are diagnosed at this localized stage. Unfortunately, most cases are diagnosed at an advanced stage and this causes the survival to dip lower than 30%. Like other cancers, both environmental and genetic factors contribute to the etiology of ovarian cancer. Only 6-25% of ovarian cancers have a strong family history[3] and are characterized by inherited defects; germ line mutations in BRCA1 and BRCA2 genes[4,5] and in the mismatch repair genes[6] represent inherited defects. In the remaining cases ovarian cancers occur sporadically with amplification, over expression and mutations in oncogenes and silencing of tumor suppressor genes[7].

1.1.1 Disease Biology

Ovarian cancer is classified into three main subgroups comprising of epithelial ovarian cancer (EOC), which accounts for 90% and gonadal-stromal and germ cell tumors that account for the remaining 10%. The EOC subgroup can be further classified into 4 main subtypes based on histopathology

STAGE I	**Tumor confined to ovaries**		
	IA	Tumor limited to 1 ovary, capsule intact, no tumor on surface, negative washings.	
	IB	Tumor involves both ovaries otherwise like IA.	
	IC	Tumor limited to 1 or both ovaries	
		IC1	Surgical spill
		IC2	Capsule rupture before surgery or tumor on ovarian surface.
		IC3	Malignant cells in the ascites or peritoneal washings.
STAGE II	**Tumor involves 1 or both ovaries with pelvic extension (below the pelvic brim) or primary peritoneal cancer**		
	IIA	Extension and/or implant on uterus and/or Fallopian tubes	
	IIB	Extension to other pelvic intraperitoneal tissues	
STAGE III	**Tumor involves 1 or both ovaries with cytologically or histologically confirmed spread to the peritoneum outside the pelvis and/or metastasis to the retroperitoneal lymph nodes**		
	IIIA	Positive retroperitoneal lymph nodes and /or microscopic metastasis beyond the pelvis	
		IIIA1	Positive retroperitoneal lymph nodes only
			IIIA1(i) Metastasis ≤ 10 mm
			IIIA1(ii) Metastasis > 10 mm
		IIIA2	Microscopic, extrapelvic (above the brim) peritoneal involvement ± positive retroperitoneal lymph nodes
	IIIB	Macroscopic, extrapelvic, peritoneal metastasis ≤ 2 cm ± positive retroperitoneal lymph nodes. Includes extension to capsule of liver/spleen	
	IIIC	Macroscopic, extrapelvic, peritoneal metastasis > 2 cm ± positive retroperitoneal lymph nodes. Includes extension to capsule of liver/spleen.	
STAGE IV	**Distant metastasis excluding peritoneal metastasis**		
	IVA	Pleural effusion with positive cytology	
	IVB	Hepatic and/or splenic parenchymal metastasis, metastasis to extra-abdominal organs (including inguinal lymph nodes and lymph nodes outside of the abdominal cavity)	

Table A: The FIGO staging of EOC.
EOC tumors are categorized into four distinct stages on the basis of tumor size, extension into other tissues, lymph nodes, loco-regional dissemination as well as metastases. (Adapted from FIGO Committee on Gynecologic Oncology, 2014).

1. **Serous carcinomas** are the most common subtype of ovarian cancer and form 36% of Stage I/II and 88% of Stage III/IV cases[8]. The serous carcinomas can be classified into low-grade serous carcinomas (LGSC) and high-grade serous carcinomas (HGSC) on the basis of their molecular signature, morphology and prognosis. p53 and BRCA mutations are defining characteristics of HGSC[9], which are highly aggressive tumors. They respond to platinum-based chemotherapy initially; however upon recurrence they tend to become chemo-resistant and the prognosis is poor[8]. K-Ras, BRAF and HER2 mutations are typical of LGSCs[9], which are less aggressive when compared to the HGSC. They show more indolent behavior and retrospective studies describe low response rates to cytotoxic and hormonal agents. Although MEK inhibitors seem promising, these mutations are often absent in responders. As a result, no predictive biomarkers exist to guide treatment[1].

2. **Endometrioid carcinoma** is the next most common subtype of ovarian cancer. It is characterized by ARID1A[10], β-catenin, PTEN, and K-Ras mutations and microsatellite instability[8,11]. Due to early detection and platinum sensitivity of the tumor, endometrioid carcinomas have better prognosis.

3. **Mucinous carcinomas** are relatively rare and constitute only around 5% of total ovarian cancers. Based on their histology, they are often referred to as an intestinal type. They are diagnosed at early stages usually as a benign cystadenoma, and prognosis after treatment is quite good, although they tend to respond less compared to the HGSC to platinum based therapy. However, recurrence is linked to poor prognosis[8,11]. HER2 amplification is common, and K-Ras mutations are present right from the early stages of carcinogenesis[12,13].

4. **Clear cell carcinomas** have a distinct gene expression pattern that distinguishes them from the other subtypes[14]. It is highly heterogeneous with ARID1A[10] and PIK3CA mutations, glutathione-peroxide-3 overexpression, FXYD-domain-containing-ion-transport-regulator-2 amplification, and retinol-binding-protein-4 overexpression[11,14]. Early stage diagnosis can lead to favorable prognosis, but advanced stage disease presents with poor prognosis and chemo-resistance[8].

The ovarian surface epithelium (OSE) is involved in the rupture and repair processes that occur with ovulation. The fimbriated ends of the fallopian tubes are located in the peritoneal cavity and often scrape against the ovaries. As a result of inflammation they adhere to the ovarian surface. There are two disparate theories to elucidate the process of carcinogenesis – the incessant ovulation theory[15-17] and the gonadotrophin theory[18,19]. In the former, it is proposed that monthly ovulation results in chronic inflammation due to repeated rupture and repair of the OSE and this elevates the risk for carcinogenesis. The second theory states that the high gonadotropin and estrogen levels result in stimulation and proliferation of the OSE, eventually resulting in neoplastic transformation and DNA damage. Both theories are supported by the observation that contraceptive use and multiple pregnancies reduce the risk for ovarian cancer[20]; however they don't clarify why there is a resemblance between the different EOC subtypes and tissues originating from the Müllerian duct during embryological development. The Müllerian duct is unrelated to the tissue of origin of the ovaries, which happens to be the coelomic epithelium[21]. However, unlike the ovaries, the fallopian tubes are of Müllerian origin, and in situ lesions of the fallopian tube epithelium are characterized by BRAC1/2 mutations, DNA damage and p53 mutations, very similar to HGSCs[22]. The serous, endometrioid and clear cell

carcinomas are of Müllerian origin, while only the gonadal-stromal and germ cell tumors are true ovarian neoplasms[23].

In summary, HGSC arises from the distal fallopian epithelium undergoing transformation and migrating to the ovarian surface epithelium, while LGSC originates from precursor inclusion cysts at the OSE undergoing transformation. Endometriosis and associated retrograde menstruation from the endometrium give rise to endometrioid and clear cell ovarian cancer. Invasive mucinous ovarian carcinomas arise from gastrointestinal tract metastases[24,25] (Figure A).

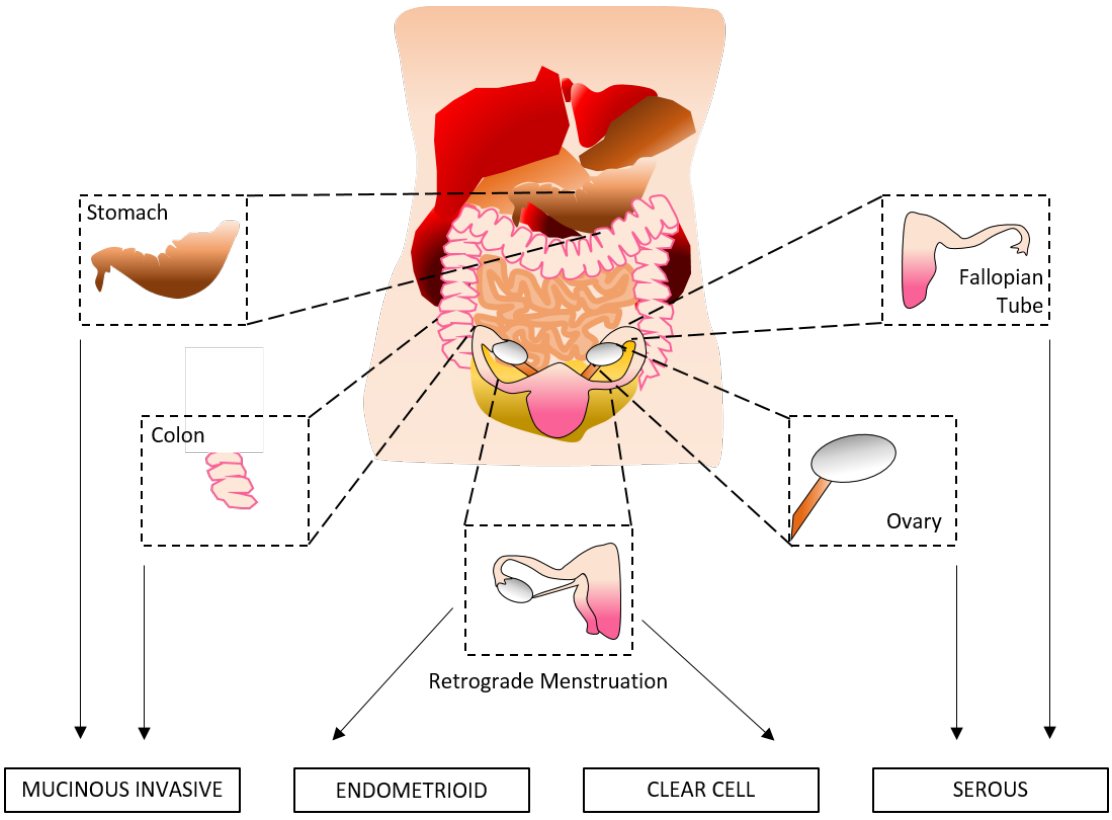


Figure A: Ovarian cancer is a heterogeneous disease arising from different tissues.
High-grade serous ovarian cancers arise from the distal fallopian tubes and the ovarian surface. Retrograde menstruation from the endometrium can cause endometrioid and clear cell carcinomas. Metastases from the gastrointestinal tract are responsible for more invasive mucinous ovarian cancers (Adapted from Vaughan, S. et al., 2011[25]).

The major histologic subtypes of ovarian cancer fall into two sub classifications (Table B). Type I tumors are low-grade, slow growing carcinomas that typically arise from well recognized precursors lesions (borderline tumors) that themselves develop from the ovarian surface epithelium, inclusion cysts, or endometriosis. In contrast, Type II tumors are high-grade and rapidly growing carcinomas. Typically, they have spread well beyond the ovary at the time of diagnosis[26].

Classes	Histotype (Percentage)	Genetic abnormalities
Type I	Low-grade serous carcinomas (<5%)	BRAF, KRAS, NRAS, ERB2 mutations
	Mucinous carcinomas (3%)	KRAS mutations ERBB2 amplification
	Endometrioid carcinomas (10%)	PTEN mutations/LOH CTNNB1, KRAS, PIK3CA, PPP2R1A, ARID1A mutations Microsatellite instability MMR deficiency
	Clear cell carcinomas (10%)	KRAS, HNF1, ARID1A, CTNNB1, TGF-b RII, PIK3CA, PPP2R1A mutations PTEN mutations/LOH Microsatellite instability
	Malignant Brenner tumours	Not yet identified
Type II	High-grade serous carcinomas (70%)	TP53, BRCA1/2 mutations, ERBB2 amplification AKT2 amplification CDKN2A inactivation NF1, CDK12 mutations Homologous recombinant repair genes mutations PI3/Ras/Notch/FoxM1 signaling alterations
	Malignant mixed mesodermal tumours (carcinosarcomas)	TP53 mutations
	Undifferentiated carcinoma	Not yet identified

Table B: Type I and Type II EOC tumors.
EOC tumors categorized into Type I and Type II classes based on their histotypes and genetic abnormalities. (Adapted from Hennessy et al, 2009[27]; Jayson et al, 2014[1]; Prat, 2012[28]; Shih and Kurman, 2004[29])

1.1.2 Diagnosis and Treatment

Coupled with the asymptomatic nature of the disease in the early stages, and lack of screening strategies, early diagnosis is rare. The non-cancerous OSE express very low levels of the mucin MUC16, more commonly known as the cancer antigen 125

(CA125), however during carcinogenesis increasing levels of this protein can be detected. It is primarily used to assess disease progression and to detect recurrence post treatment[30]. In order to improve sensitivity and facilitate early detection, CA125, mesothelin, and human epididymis protein-4 are measured simultaneously[31]. Apart from CA125, WFDC2 (WAP Four-Disulfide Core Domain 2), in combination with ROMA (risk of ovarian malignancy algorithm) is also used to diagnose EOC[32]. With respect to screening and early diagnosis of EOC, there is more benefit accorded to patients with sporadic disease as they show slow stepwise progression with preclinical increment in CA125; hereditary cases with mutated BRCA1/2 or p53 are far too aggressive to be caught in the pre-cancerous window[24].

Initial detection of ovarian cancer is via suprapubic or transvaginal ultrasonography and this is evaluated by surgical exploration and histopathological examination to ensure accurate staging and grading of the disease[33]. The gold standard for early stage disease is platinum based chemotherapy in combination with surgery. In more advanced cases, optimal surgical debulking is followed by the mitotic inhibitor paclitaxel and platinum[2]. In cases where primary debulking is not possible, the practice is to first administer chemotherapy (neoadjuvant therapy) and this is followed by cytoreduction[1]. The standard of care is six cycles of carboplatin combined with paclitaxel or docetaxel, administered once every 3 weeks[1]. Development of platinum resistance is a major bottleneck in treatment of the disease with most advanced cases relapsing and ultimately dying from their cancer. Hence there is a need to improve early detection and also develop better treatment options for advanced cases. Aside from chemotherapy, angiogenesis inhibitors such as bevacizumab[34] and pazopanib[35] have also recently been used in the treatment of EOC. Bevacizumab in combination with chemotherapy improves progression free survival (PFS)[34,36,37]. Also, olaparib, a poly ADP-ribose polymerase (PARP) inhibitor improves

PFS in patients with platinum sensitive relapse, providing support for an emerging group of therapeutics[38].

1.1.3 Molecular subtypes of EOC

Given the diverse histopathological subtypes, each with their characteristic genetic aberrations, EOC is largely a complex, diffuse and genetically heterogeneous disease. In order for effective treatment, there is a need to stratify patients by dissecting the heterogeneity of genetic aberrations and developing therapeutics targeting key drivers within each subtype. Besides focusing on genetic alterations for delineating EOC subtypes, research studies are developing large scale gene expression profiling. The pioneer study by Tothill et al., reported six gene expression molecular subtypes (GEMS) of EOC (C1 to C6), based on the analysis of 285 serous and endometrioid tumors[39]. Four of these GEMS are prevalent in HGSCs; C1 (reactive stroma), C2 (immune-related), C4 (low stromal response), and C5 (mesenchymal). Subsequently, the Cancer Genome Atlas Research Network (TCGA) also performed integrated genomic analyses on 489 high-grade serous EOC and generated three miRNA, four promoter methylation, and four transcriptional subtypes[40]. In an independent meta-analysis of a large repertoire of 1538 EOC samples, our group identified five Epithelial Mesenchymal Transition (EMT) based molecular subtypes, Epi-A, Epi-B, Mes, Stem-A and Stem-B, each with distinct expression signatures and clinical prognosis[41]. Remarkably, all three studies identified a mesenchymal subtype enriched in genes pertaining to the evolutionarily conserved EMT pathway.

1.2 EPITHELIAL MESENCHYMAL TRANSITION

Epithelial Mesenchymal Transition is the sequential mechanism by which polarized epithelial cells lose their apical-basal polarity, junctional integrity and acquire the hallmarks of a mesenchymal phenotype, including fibroblastic morphology and motility. In the developmental biology of most metazoans, during gastrulation, EMT is crucial for the morphological and biochemical processes that guide body plan formation. The plasticity of epithelial cells is mandatory for the EMT process where there is reorganization of the primitive ectoderm to form the three body layers in triploblasts (two layers in diploblast). EMT is also involved in several fundamental processes such as the delamination of the neural crest in the vertebrate embryo, wherein there is migration and differentiation of the progenitor cells form the peripheral nervous system and craniofacial features, heart morphogenesis, and somite morphogenesis to form the striated muscles and vertebrae[42-44].

The defining feature of epithelial cells is their morphological arrangement, giving rise to apical-basal polarity and the formation of junctional complexes (Tight junctions at the apex, followed by the Adherens junction, and the Demosomes towards the basal end), (Figure B). The basement membrane partitions the epithelium from the mesenchyme and serves as a lining. Mesenchymal cells lack junctional integrity and are dispersed loosely in the extracellular matrix. They are characterized by their front-rear polarity, a morphology that facilitates motility and invasion. During their transition to mesenchymal cells, epithelial cells lose the components from their junctional complexes. Proteins that are integral to the tight junction architecture such as zonula occludens-1 (ZO-1), occludins, claudins, as well as E-cadherin from the adherens junction, are among the earliest proteins to be targeted. Subsequently there is deregulation of chief polarity complex components, such as partitioning defective protein-3/6 (Par-3/6) and Crumbs protein homolog 3 CRB3[45]. Eventually the

cytokeratin intermediate filaments that maintain the stability of desmosomes are disrupted and replaced by vimentin intermediate filaments, and the actin cytoskeleton is reorganized to enable actin-myosin contractility for migration.

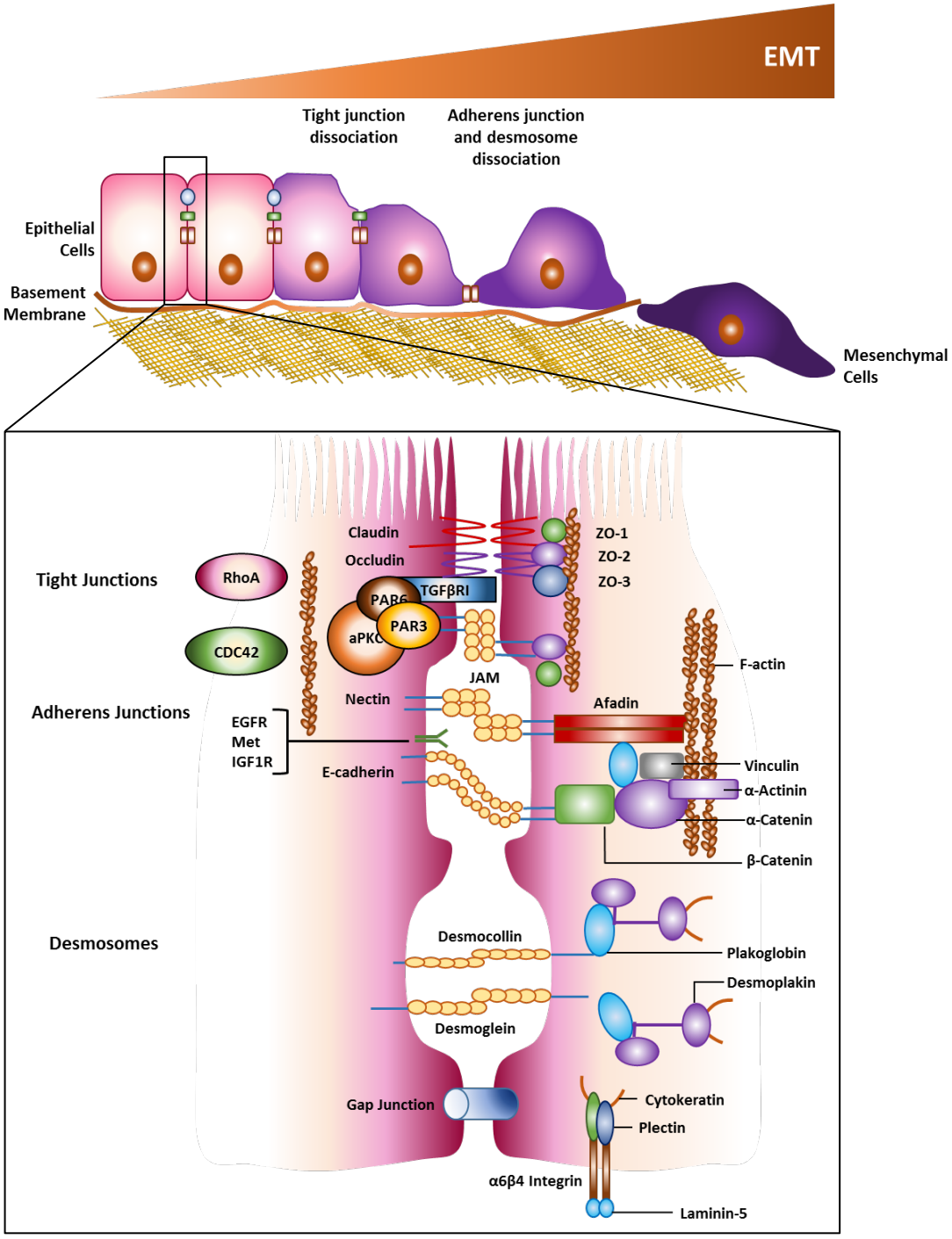


Figure B: Junction Integrity is compromised during EMT.
A schematic overview of the EMT process depicting the disruption of the Tight Junction, Adherens Junction, and Desmosomes. The components of the junctions are also depicted (Adapted from Thiery and Sleeman, 2006[46]).

1.2.1 EMT inducers and transcription factors.

Growth factors and cytokines are principal inducers of EMT, during development as well as carcinoma progression. They activate a diverse repertoire of signaling pathways that modulate EMT effectors including transcriptional repressors belonging to the Twist basic helix-loop-helix transcription factor (Twist), and the Snail and Zinc finger E-box binding homolog (Zeb) families. These transcriptional regulators bind proximal to E-cadherin promoter at the E-box elements, thereby repressing E-cadherin. The transforming growth factor-β (TGF-β) superfamily, comprising of the cytokine TGF-β and bone morphogenic proteins (BMPs) are one of the principal effectors of EMT[47]. They activate the TGF-β receptors TGFβRI and TGFβRII, which in turn activate polarity proteins such as occludin and Par6 to remodel the cytoskeleton and disrupt the epithelial polarity. The SMAD factors are also activated to induce EMT drivers SNAI1/2 and ZEB1/2. Other inducers of EMT include Wnt[48], Notch[49], and the ligands for receptor tyrosine kinases (RTKs) - epidermal growth factor[50,51] (EGF), hepatocyte growth factor[52-54] (HGF), insulin-like growth factor[55-58] (IGF), platelet-derived growth factor (PDGF)[59,60], and vascular endothelial growth factor[61-63] (VEGF).

EMT-inducing signals		EMT-inducing transcription factors	EMT effectors/markers	
TGF-β	Wnt	SNAI1	Epithelial	Mesenchymal
BMP	Shh	SNAI2	E-cadherin	Vimentin
EGF	ILEI, IL-6	ZEB1	Claudins	Fibronectin
FGF	PGE(2)/COX2	ZEB2	Occludins	Vitronectin
SCF	Hypoxia	TWIST1	Desmoplakin	FSP1
HGF	Bile acids	FOXC2	Cytokeratin	α-SMA
PDGF	Nicotine, UV	GOOSECOID	Mucin-1	N-cadherin
IGF	Integrins	TCF3/E47	ZO-1	MMPs
VEGF	MMP3	TCF4/E2-2		
Notch		KLF8		

Table C: EMT-inducing signals, transcription factors and markers/effectors. (Thiery et al, 2009[58]; Yang and Weinberg, 2008[64]; Kalluri and Weinberg, 2009[65])

The growth factors bind to their respective cell surface receptors, usually resulting in dimerization of the RTK and trans-phosphorylation of the kinase domains and subsequent activation of their substrates via transfer of phosphate moieties to tyrosine amino acid residues. This enables activation of biochemical signaling cascades such as the PI3K/Akt, Ras/MAPK, Rac/Cdc42 pathways. These networks modulate cell survival and proliferation, and also activate the EMT transcription factors, subsequently down modulating the epithelial markers and inducing the mesenchymal factors[64]. IGF utilizes the RTK signal transduction cascade, as well as the Nuclear Factor kappa-light-chain-enhancer of activated B cells (NFkB)-SNAI2 to induce EMT. Of note, there is potential crosstalk between TGF-β/SMAD, Wnt/β-catenin, Notch, and RTK/Ras cascades[58,64]. Apart from ligand or cytokine induced EMT, inflammation and hypoxia can also activate EMT transcription factors such as SNAI1 and TWIST1 through NFkB and JAK/STAT pathways[66].

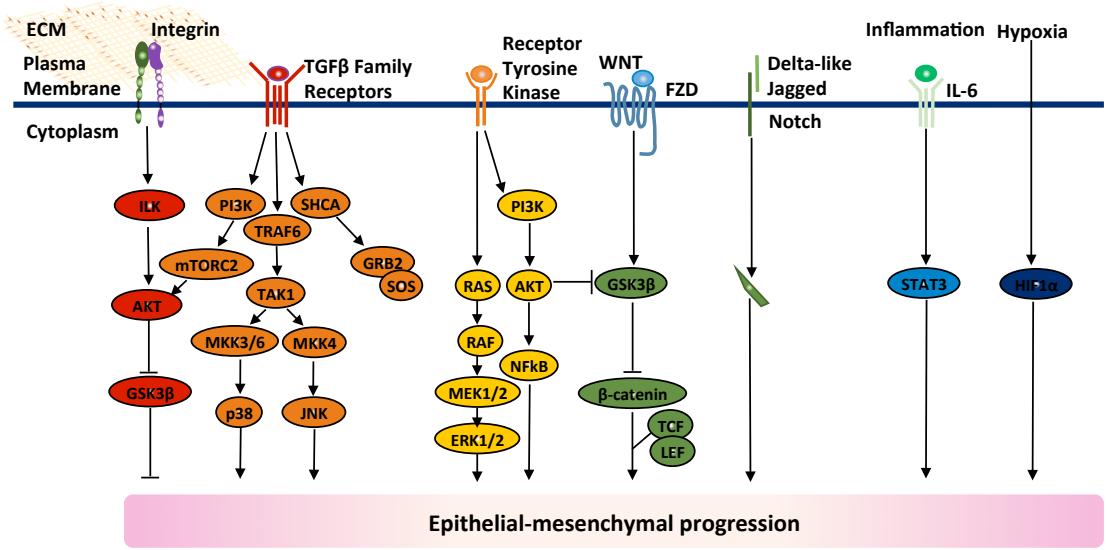


Figure C: Diverse repertoires of signaling pathways converge onto the EMT program.
Several cellular signaling pathways converge on the EMT program. A simplified version is represented here, depicting signaling through Integrins, TGFβR, RTKs, Wnt, notch, Inflammation, and hypoxia pathways.
(Adapted from Lamouille, Xu et al., 2014[67])

1.2.2 EMT in cancer

Tumor progression eventually results in metastasis, and at this stage the tumor cells intravasate into lymph or blood vessels, either collectively or as individual cells. There is increasing evidence to suggest that cancer cells utilize EMT to facilitate transition of carcinoma in situ to invasive tumor, and metastasize. Circulating tumour cells (CTCs) show the presence of both single cells and cell clusters called microemboli[58,68-70]. It is hypothesized that microemboli and single cells intravasate through distinct mechanisms, although it is possible that carcinoma cells at the leading edge of the invasion zone undergo partial EMT to guide invasion of the cell cluster. Single cell invasion, on the contrary, requires carcinoma cells to harness the EMT program, delaminate from the periphery of primary tumor, and intravasate into blood and lymph vessels[58]. The plasticity accorded to cancer cells enables them to alternate between epithelial and mesenchymal states by harnessing both EMT as well as its reverse process mesenchymal to epithelial transition (MET), and this facilitates tumor spread along the walls of the peritoneal cavity and pelvic-abdominal organs such as colon and stomach. The EMT state also confers the cancer cells with chemoresistance properties that result in failure of chemotherapeutic regimes[71]. miRNAs that negatively modulate EMT effectors are suppressed in chemoresistant cancer cells and result in poor survival in patient populations[72-74]. Forced re-expression of the repressed miRNA restores sensitivity to chemotherapeutics[75]. Hence, therapies that prevent the onset of EMT, or reverse the EMT process would have clinical relevance in improving chemo response and patient outcome.

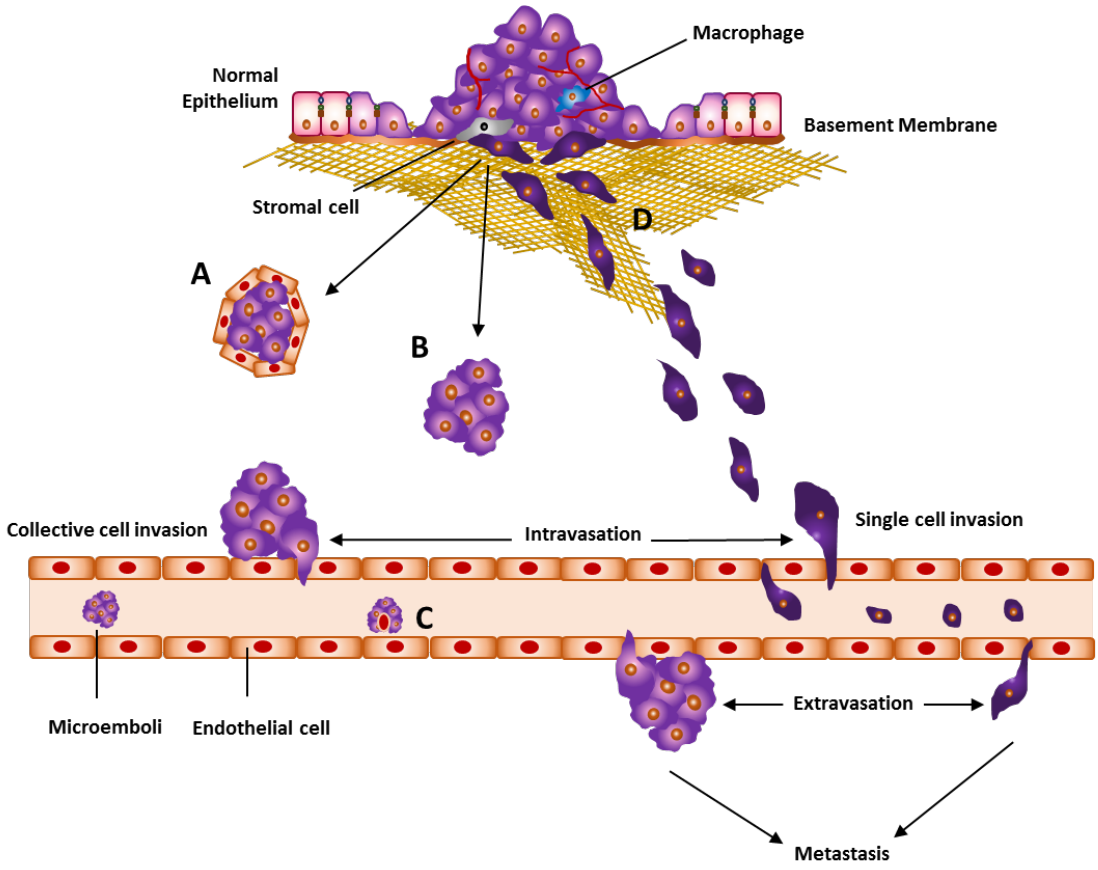


Figure D: Illustration of EMT facilitated metastasis by collective or single cell migration.
In collective cell migration a cell cluster or 'microemboli' can be formed by A) entrapment of carcinoma cells by endothelial cells; B) direct detachment of a collection of cells from the primary tumor; C) proliferation in the vasculature or platelet mediated proliferation. Single cell migration is mediated by D) EMT, wherein cells assume a mesenchymal phenotype, disengage from the primary tumor, and intravasate into the blood or lymph vessels. Upon extravasation from vasculature, these microemboli and single cells form micrometastases at metastatic niches.
(Adapted from Bacac and Stamenkovic, 2008[76])

1.2.3 EMT in EOC disease burden

Regional dissemination of the tumor and metastases are hallmarks of ovarian carcinoma progression[77]. At the earliest stage, the ovarian capsule is unimpaired and there is no spread of the tumor beyond the OSE into the peritoneal fluid. Carcinoma progression necessitates the disruption of the capsule and subsequent dissemination of the tumor beyond the OSE. The carcinoma cells can directly extend and invade to adjacent tissues such as the uterus, fallopian tubes and the peritoneum. Tumor cells that are shed into the peritoneal fluid are transported to distant locations on the peritoneum and mesothelial linings of pelvic and abdominal organs, where they seed and form metastases. Metastases can also occur through lymph nodes that drain the ovaries. Unlike other carcinomas, metastases via blood vessels is rare; however, when it occurs, it can involve many organs[77]. There is a need for better understanding of mechanisms involved in spread of ovarian carcinoma. EMT is an important phenomenon that provides clarity in understanding tumor progression, regional dissemination of tumor and peritoneal metastasis in ovarian cancer. For example, E-cadherin is highly expressed in primary ovarian carcinomas, but this is lost in the advanced stages, and given how loss of E-cadherin expression is a hallmark of EMT, this alludes to EMT facilitating the invasive phenotype in ovarian cancer[78]. However, it is to be noted that other studies show upregulation of E-cadherin in peritoneal and metastatic EOC lesions, possibly to mediate cell survival by repressing anoikis or to enable MET[79]. In some cases, loss of E-cadherin by upregulation of transcriptional repressors like Snail, Slug, Twist[80] is paralleled by increased N-cadherin expression[81]. It is likely that EMT is not complete in EOC and tumors retain both the epithelial as well as the mesenchymal phenotypes[81].

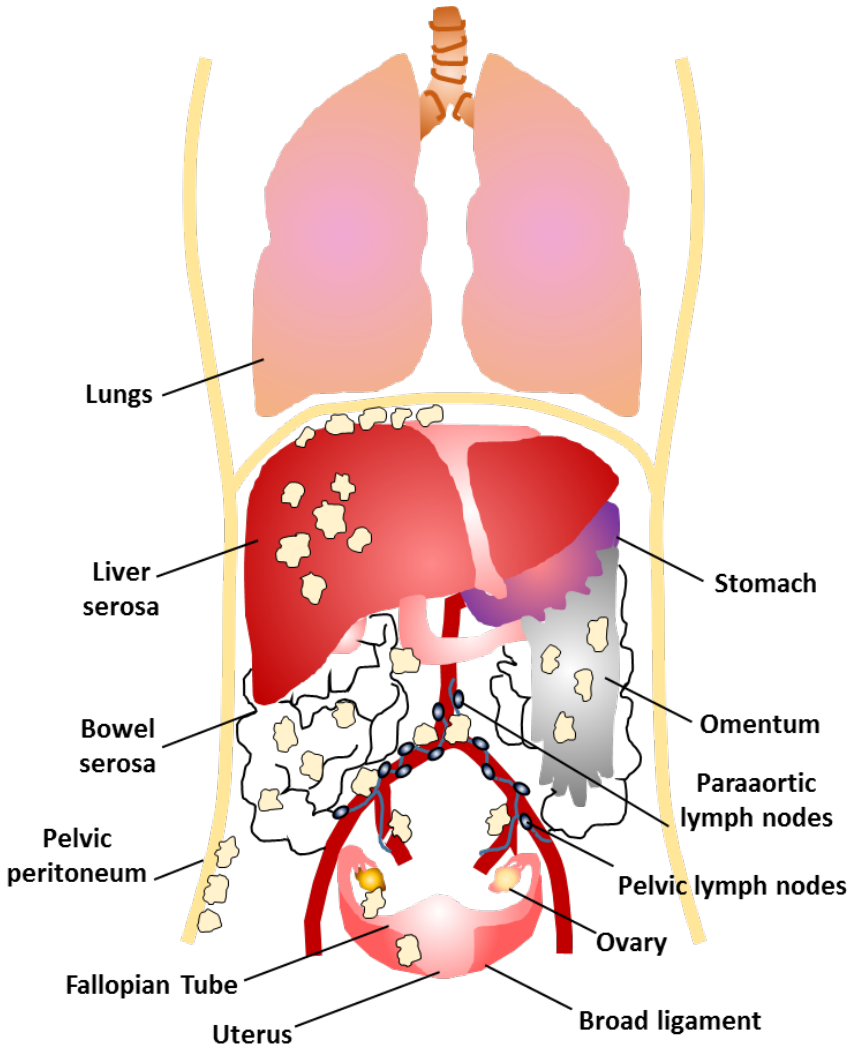


Figure E: EOC disease burden.
In patients suffering from ovarian cancer, there is extensive build up of ascites, and loco-regional dissemination of the primary tumor into the peritoneal fluid, and mesothelial linings of pelvic and abdominal organs.
(Adapted from Naora and Montell, 2005[77])

1.3 THE RECEPTOR TYROSINE KINASE AXL

AXL, which stems from the Greek word for uncontrolled, 'anexelekto', is an RTK belonging to the TAM family (comprising of TYRO-3, AXL and MER). Structurally, the TAM receptors comprise two Immunoglobulin-like (Ig) domains, and two fibronectin type III (FNIII) moieties in their extracellular domain, and the conserved amino acid sequence KW(I/L)A(I/L)ES in their kinase domain[82]. Among the RTK family, TIE and TEK are also known to contain both Ig and FNIII motifs on their ectodomains. The Ig domains are common to the FGF, VEGF and PDGF growth factor receptor families, while the FNIII is prevalent in the Ephrin and Insulin families. The MET RTK family, comprising of cMET and RON, share high degree of sequence similarity in the kinase domain[83].

The human AXL gene resides on chromosome 19q13.2 and is encoded by 20 exons to form the full length protein comprising of 894 amino acids. Though the expected molecular weight is 98 kDa, it is post-translationally glycosylated to form either a 120 kDa (partially glycosylated form), or 140 kDa protein[84]. It is activated by its ligand Growth Arrest Specific 6 (Gas6)[85], which becomes biologically active upon Vitamin K-dependent post translational modifications[86].

AXL was originally identified in 1991 as a transforming gene in Chronic Myeloid Leukemia (CML)[84]. Under normal physiological conditions it is ubiquitously expressed in several tissues and organs, including but not limited to the hippocampus, cerebellum, macrophages, platelets, endothelial cells, heart, liver, kidney, and skeletal muscle. It was found to be overexpressed in several other cancers such as breast, lung, liver, colon, gastric, ovarian, pancreatic, and glioblastoma[87].

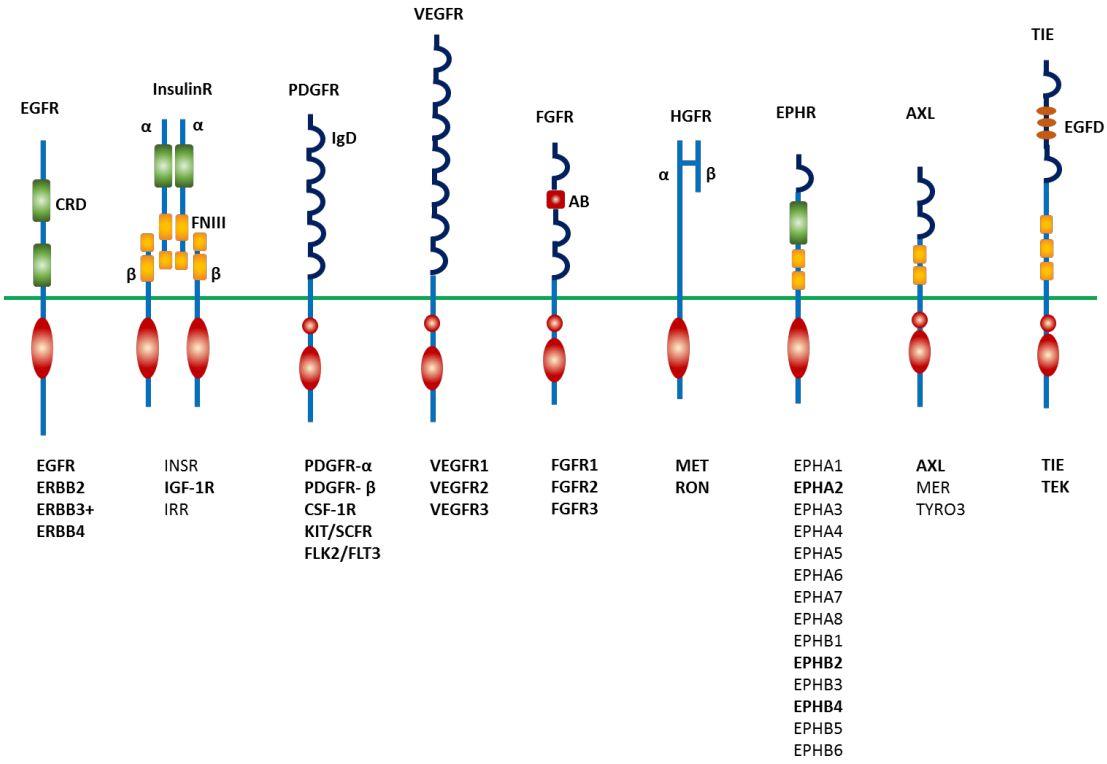


Figure F: AXL belongs to the TAM family of RTKS.

Legend for RTK subfamilies

EGFR: epidermal growth factor receptor, InsulinR: insulin receptor; PDGFR: platelet-derived growth factor receptor, VEGFR: vascular endothelial growth factor receptor, FGFR: fibroblast growth factor receptor, HGFR: hepatocyte growth factor receptor, EPHR, ephrin receptor, TIE: tyrosine kinase receptor in endothelial cells

Abbreviations

CRD: Cysteine-rich domain, FNIII: Fibronectin Type III domain, IgD: Immunoglobulin-like domain, AB: acidic box, EGFD: Epidermal Growth Factor-like Domain. α and β denote distinct RTK subunits.

Note

RTKs in bold font are implicated in human cancers. The '+' on ERBB3 signifies it is devoid of intrinsic kinase activity.

(Adapted from Jensen and Hunter, 2001[88])

1.3.1 AXL Signaling

Gas6 binds to the ectodomain of AXL, causing receptor dimerization with a 2:2 stoichiometry of Gas6 and AXL[89]. The proximity of the kinase domains of two AXL moieties in the RTK-ligand complex enables trans-autophosphorylation of the residues on the cytoplasmic tails, where signaling molecules like PLCγ, PI3K and Grb2 can dock[90,91]. The tyrosine residues 698, 702, and 703 in the human sequence of AXL, are conserved among the TAM receptors and are involved in the functional activity of the kinase. The tyrosine residues 779, 821, and 866 are also potential autophosphorylation sites in the C-terminal AXL domain[91]. Gas6 independent AXL phosphorylation can also occur when the RTK is overexpressed, resulting in RTK dimerization[92,93].

In a cell type dependent context, Gas6/AXL signaling can mediate growth, survival, proliferation, motility, and invasion by harnessing a diverse repertoire of signaling networks such as the Ras/Raf/MEK/ERK cascade, PI3K/Akt signaling pathways. The MAPK/ERK cascade is usually involved in proliferation, while PI3K activation signaling converges on cell survival through the Akt/S6K axis[94]. Gas6/AXL signaling also causes increased expression of anti-apoptotic proteins such as Bcl-2 and Bcl-xl, phosphorylation and activation of NFkB, phosphorylation and stabilization of Bad, and inhibition of proapoptotic proteins such as caspase 3, to induce pro survival signaling[95,96]. Signaling through the PI3K/Ras/Rac axis causes actin reorganization and enables migration[97,98]. The adapter protein Nck2, which comprises of three tandem SH3 and one SH1 domains, is involved in linking AXL with other signaling complexes. In particular, the AXL-Nck2 interaction facilitates AXL mediated modulation of the Integrin Linked Kinase (ILK), a major component of signaling platforms at focal adhesions, thereby enabling AXL to regulate cytoskeleton dynamics[87].

The modulation of AXL required to regulate signaling has not been extensively documented. The phosphatase C1-TEN which is known to prevent signaling downstream of Akt,[99] can interact with AXL[100]. There is evidence to suggest that the Suppressor of cytokine signaling (SOCS-1), could serve to negatively modulate AXL signaling[101,102]. The E3-ubiquitin ligase Cbl-b has also been reported to counteract AXL signaling by ubiquitination and subsequent degradation of AXL[103,104].

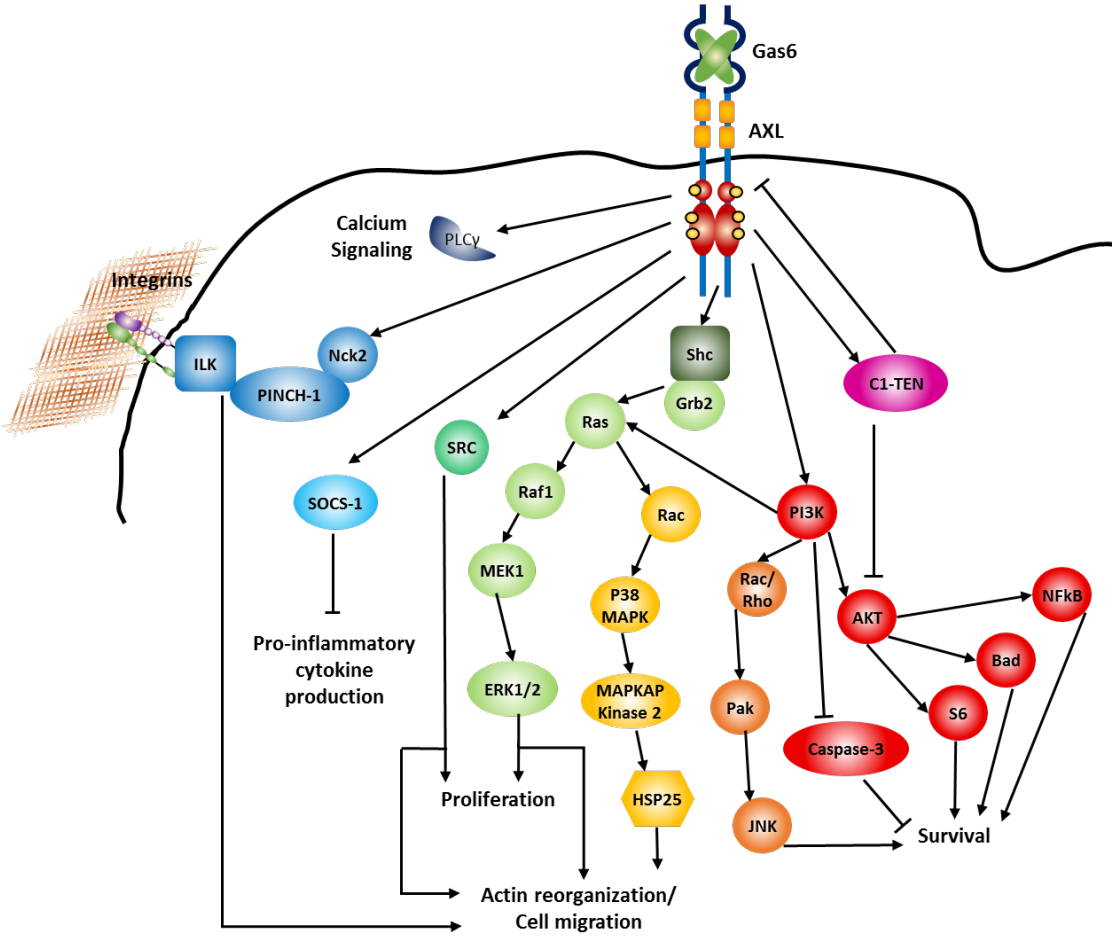


Figure G: Gas6/AXL signaling schema.
AXL signaling is mediated by receptor dimerization, either by Gas6 or due to ligand independent dimerization. Downstream of the RTK signaling cascade, several cellular functions such as proliferation, actin reorganization, cell migration and survival are stimulated.
(Adapted from Linger et al., 2008[82])

1.3.2 AXL in EMT and Cancer

The role of AXL in EMT has been documented in literature for breast, non-small cell lung, pancreatic, ovarian cancer, and glioblastoma amongst others. In breast cancer, AXL overexpression confers worse prognosis in patients, with AXL expression being elevated in metastases. AXL was also identified as a downstream effector of EMT, which facilitated tumor formation and invasiveness. Furthermore, AXL knock down prevented the dissemination of highly metastatic breast cancer cell lines from mammary glands to the lymph nodes, and other organs, thereby increasing survival. This study provided the first in vivo evidence that directly links Axl to metastasis[105]. It has been demonstrated that AXL acts in a positive feedback loop to induce EMT in normal and immortalized human mammary epithelial cells, and regulates self-renewal and chemoresistance in breast cancer stem cells[106]. In non-small cell lung cancer, AXL is shown to confer mesenchymal cells with increased resistance to EGFR targeted therapy, with inhibition of AXL re-sensitizing the cells[107]. Also, in EGFR-mutant lung cancer models, AXL over expression conferred erlotinib resistance even in the absence of EGFR T790M mutation or cMET activation. Genetic or pharmacologic inhibition of AXL restored sensitivity to erlotinib in these tumor models[108]. In pancreatic cancer, AXL knock down resulted in significant reduction in EMT transcription factors SNAI1, SNAI2 and TWIST, and thereby attenuated EMT mediated invasiveness, migration and metastases[109]. In ovarian cancer, AXL inhibition drastically abrogated invasion and matrix metallo-proteinase activity. Furthermore, inhibiting AXL prevented initiation of metastatic dissemination, and also prevented progression of established metastatic lesions[110]. In malignant gliomas, inhibition of AXL using a dominant negative mutant, suppresses brain tumor growth and invasion, thereby prolonging survival[111].

1.3.3 Targeting AXL

Several small molecule inhibitors have been developed to target AXL, and R428[112], which is an AXL specific inhibitor, was shown to block tumor dissemination and prolong survival in metastatic breast cancer mouse models. It is based on a trisubstituted triazole core with nanomolar range potency against AXL in biochemical assays. R428 prevented Gas6 mediated AXL and subsequently Akt phosphorylation, and also suppressed invasion of cancer cells, in a dose dependent manner. In mouse models, R428 suppressed angiogenesis and abrogated breast cancer metastasis, correlating with attenuation of Akt and ERK phosphorylation. Pharmacokinetic profiles in mice showed good plasma stability with a half-life of 13 hours. R428 has also shown to reverse AXL mediated resistance to ALK inhibitors in neuroblastoma[113]. A summary of R428, and other AXL small molecule inhibitors is given in Table D.

Drug	Target	AXL inhibition	Developer	Phase of Development
Foretinib (XL880, GSK1363089)	MET, VEGFR2, AXL, RON	IC50 (in vitro) = 11 nM	GSK	Phase II, active, not recruiting
Merestinib (LY2801653)	MET, MST1R, DDR1, TIE1, MER, TYRO3, AXL	IC50 (in vitro) = 11 nM	Eli Lilly and Co.	Phase I, active, recruiting
NPS-1034	AXL, DDR1, FLT3, KIT, MEK, MET, ROS1, and TIE1	IC50 (in vitro) = 10 nM	NeoPharm	Preclinical
LDC1267	MET, AXL, TYRO3	IC50 (in cells) = 19 nM	Lead Discovery Centre	Preclinical
Bosutinib (SKI-606, marketed as Bosulif)	BCR-ABL, ABL, SRC, YES, MEK, AXL, BMX	IC50 (in vitro) = 0.56 µM	Pfizer	Approved for CML with resistance to treatment
S49076	MET and mutants, AXL, MER, FGFRs	IC50 (in vitro) = 7 nM	Institut de Recherches Internationales Servier	Phase I, active, recruiting
BGB324 (R428)	AXL (selective)	IC50 (in vitro) = 14 nM	Rigel Pharmaceuticals/BerGen BIO	Phase I/II, active, recruiting

Table D: Summary of AXL inhibitors.
(Adapted from Myers et al., 2015[114])

Another small molecule inhibitor n-butylidenephthalide, loaded and delivered through an intra-cerebral gliadel wafer, has shown remarkable efficacy in down modulating AXL expression and tumor invasion in glioblastoma multiforme[115].

Aside from small molecule inhibitors, biologics to target AXL are in preclinical development. The YW327.6S2 antibody inhibits AXL activation by abrogating its binding with Gas6 as well as down regulating the receptor[116]. Also, Axl inhibition with YW327.6S2 enhanced the efficacy of ERGR inhibitors in tumors resistant to EGFR targeted therapy. YW327.6S2 also showed synergy with carboplatin/paclitaxel in lung cancer xenograft model[116]. A potential drawback of this therapeutic approach would be binding of the antibody to soluble AXL (sAXL) in the blood stream; this might severely reduce efficacy of the treatment.

Other biological approaches would include engineering sAXL to sequester Gas6 to prevent Gas6 mediated AXL activation[117]. While this novel approach would ensure high specificity and limited toxicity, Gas6 independent AXL dimerization due to receptor overexpression could still promote tumorigenesis.

1.4 THE TUMOR SUPPRESSOR OPCML

The opioid-binding protein/cell adhesion molecule-like (OPCML) is part of the IgLON family of cell adhesion molecules and is a subset of the Ig superfamily[118]. The four other proteins that complete the IgLON family are LSAMP (limbic system-associated membrane protein), Neurotrimin, NEGR1 (neuronal growth receptor), and IgLON5. The IgLONs consist of three C2-like Ig domains and are bound to the outer phospholipid layer of the plasma membrane by a glycosylphosphatidylinositol (GPI) anchor and are post-translationally glycosylated[119]. Post glycosylation, OPCML forms a 55-kDa protein. The presence of Ig domains enables the IgLONS to engage in homo- and heterophilic interactions and facilitate adhesion between cells or between cell and matrix. The Ig domains are also known to facilitate binding to cadherins, integrins,[120] and RTKs[121,122].

OPCML is ubiquitously expressed in adult and fetal tissues, with highest expression levels detected in the brain. In 1996 Gabra et al., discovered an area of loss-of-heterozygosity (LOH) on 11q23.3-q24.3 in ovarian tumors. This deletion was apparent in 69% of EOC samples and was associated with poor prognosis and survival[123]. Subsequently, Sellar et al., performed LOH analysis and identified OPCML as the target gene whose expression was lost in over 80% of sporadic EOC cases examined. It was also shown that chromosomal deletion at 11q25 in tumors was associated with somatic hypermethylation of the remaining allele[124]. OPCML methylation has been shown to be prognostically relevant[125] and there is evidence to suggest that detection of circulating methylated OPCML could serve as a biomarker for EOC[126]. OPCML is hypermethylated in other cancers like lung, brain, breast, cervical, upper GI and lymphomas as well, suggesting a conserved mechanism of tumor suppression across several tissue types[127-131].

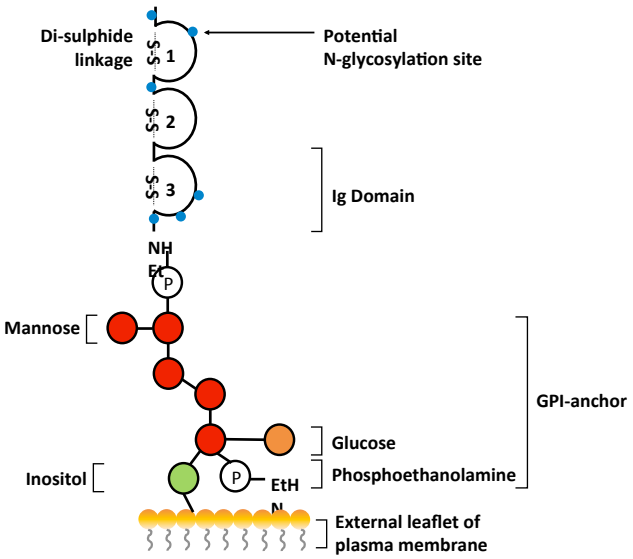


Figure H: Schematic representation of OPCML structure.

1.4.1 OPCML and membrane organized micro domains

OPCML being a GPI-anchored protein is enriched in the cholesterol rich, liquid 'ordered' phase, of the plasma membrane, more commonly referred to as the lipid rafts[132,133]. Lipid rafts are functional membrane micro domains that are enriched in sterols, sphingolipids and phospholipids conjugated with saturated fatty acids. This lends it a highly ordered and packed structure within the fluid, liquid 'disordered' phase of the plasma membrane[134]. The rafts are also known to modulate protein organization on the plasma membrane, and thereby regulate protein signaling by partitioning repertoires of signaling and scaffolding moieties into distinct membrane micro domains[135,136].

1.4.2 OPCML and RTK modulation

OPCML functions as a potent tumor suppressor and inhibits proliferation *in vitro* and *in vivo*[124]. The mechanism of action of OPCML was subsequently elucidated and it was shown to negatively regulate a spectrum of RTKs and thereby attenuate oncogenic signaling[137]. Using HER2 as a paradigm, OPCML was shown to interact

with the ectodomain of the RTK and altering its trafficking to a nonclathrin-dependent endocytosis, thereby promoting degradation via a polyubiquitination-associated proteosomal mechanism. This regulation by OPCML was expanded, but not limited to, EPHA2, FGFR1, FGFR3, and HER4. A mammalian-2-hybrid screen from the OPCML Lab (Figure I, courtesy Dr. Sushmitha Nawathe and Dr. Elisa Zanini) also showed interaction between AXL and OPCML.

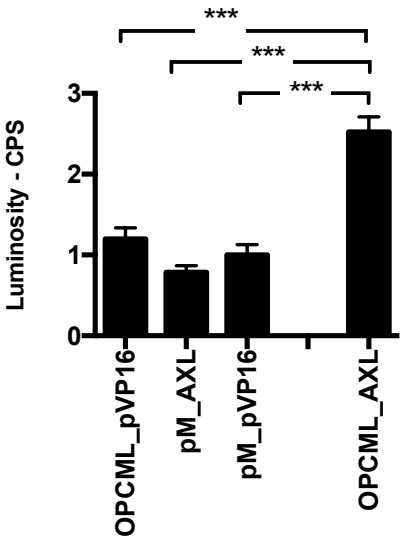


Figure I: Mammalian-2-Hybrid assay shows a clear signal for interaction between OPCML and AXL.
Proteins fused either to the Gal4 DNA-binding domain or to the activation domain derived from the VP16 protein of the herpes simplex virus were created by cloning the genes of interest (AXL, OPCML) into either pM or pVP16, respectively. Vectors were co-transfected into mammalian host cells together with a reporter gene, luciferase in this case. 24 hours after transfection, the interaction between the two proteins of interest is assayed by measuring the luciferase expression. The first three bars represent luciferase intensity in control experiments, while the fourth represents interaction between AXL and OPCML. (Courtesy Dr. Sushmitha Nawathe and Dr. Elisa Zanini)

1.4.3 OPCML and EMT

Apart from its classic tumor suppressor function, there is new evidence to suggest the role of OPCML in modulating EMT. In colon cancer, OPCML promoter hypermethylation correlates with minimal protein levels and poor survival[138]. Restoration of OPCML expression facilitated suppression of proliferation, migration, invasion and EMT, with downmodulation of N-cadherin and vimentin, and increased E-cadherin expression[138]. Mechanistically OPCML, at least in part, reversed the EMT state by regulating the TGF-β/Smad pathway and repressing phospho-SMADs[138].

1.5 AIMS AND HYPOTHESIS

Given the delineation of the molecular complexity of ovarian cancer into clinically relevant subtypes[39,41], there has been an imminent need to quest for subtype specific therapeutic targets that will improve patient outcomes. Among the EOC subtypes, the Mes subtype possesses a high EMT score and is linked to worse prognosis[41]. There is increasing evidence that converges on the EMT pathway in promoting migratory and invasive phenotypes alongside chemoresistance in EOC[139], and AXL has been implicated in conferring resistance to therapy and is strongly associated with the EMT state[105-109,113,140-144]. This study seeks to decipher the role of AXL in ovarian cancer.

Analysis of the kinome profile revealed AXL to have a significantly high rank in Mes subtype, but not in the other subtypes. EOC tumors and cell lines classified based on their gene expression profiles, also revealed high AXL expression in the Mes subtype; however the better prognosis epithelial subtypes were also moderately positive for AXL. The primary hypothesis of this project is that AXL signaling has divergent consequences in the various EOC subtypes with respect to signaling modulation, biological outcome, and response to therapy.

To test this hypothesis, the project sets out the following aims for Chapter III.

1. To analyze the effect of AXL signaling in EOC subtypes through phenotypic assays and response to therapy.
2. To validate the role of AXL in sustaining the EMT phenotype.

Also, given the prognostic relevance of OPCML in EOC, and its ability to modulate RTKs[145], the second hypothesis of this project is that OPCML regulates AXL in EOC.

To test this hypothesis, the projects sets out the following aims for Chapter IV.

3. To confirm the nature of interaction between AXL and OPCML.
4. To study the effects of OPCML-AXL interaction in EOC.

CHAPTER II: MATERIALS AND METHODS

2.1 EOC cell lines and culture

38 EOC cell lines from the SGOCL panel[41], PEA1 from Cancer Research UK, and Fallopian Tube Epithelium cell line FTE190 from Rony Drapkin's Lab at Dana Farber Cancer Institute USA, have been used in this study. The cell lines were cultured in their specified media with requisite amounts of Fetal Bovine Serum (FBS) (Table I), and 1% penicillin and streptomycin (Sigma-Aldrich), and grown at 37°C in a 95% air and 5% CO_2 regulated incubator. The SGOCL cell lines have been delineated based on the EMT molecular subtype[41] into Epi-A, Epi-B, Mes, Stem-A and Stem-B; as well as the EMT phenotype[146] into Epithelial (E), Intermediate Epithelial (IE), Intermediate Mesenchymal (IM) and Mesenchymal (M). These 38 EOC cell lines were used to analyze AXL protein expression.

For kinetic stimulation studies, 10 EOC cell lines were chosen to represent the EMT molecular subtypes and phenotypes: PEO1 (Epi-A, E), OVCA429 (Epi-A, IE), CAOV3 (Epi-B, E), JHOS3 (Epi-B, IE), OV56 (Mes, IE), SKOV3 (Mes, IM), HEYA8 (Mes, M), JHOS4 (Stem-A, IE), CH1 (Stem-A, IM), A2780 (Stem-A, M). These 10 EOC cell lines were seeded to attain 70% confluence and serum starved overnight and activated with 400ng.mL^{-1} Gas6 (#885-GS, R&D Systems) for 0, 10, 20, 30 minutes, 1, 3, 6, 12 and 24 hours and lysates were collected for analysis.

For AXL inhibitor studies, the 10 EOC cell lines were seeded so as to obtain 80% confluence at the end of study, incubated with R428 (Selleckchem, #BGB324) at varying doses between 0 and 80µM for 48 hours to calculate GI50 doses.

For kinetics of Gas6 signaling upon AXL inhibition, PEO1 (Epi-A, E), OVCA429 (Epi-A, IE), SKOV3 (Mes, IM), HEYA8 (Mes, M) cell lines were serum starved overnight, preincubated with 9.38 µM $GI50^{Non\text{-}Mes}$ or 2.91 µM $GI50^{Mes}$ concentrations of R428 for one hour, while control cells were incubated with 0.01% DMSO and then stimulated with 400ng.mL^{-1} Gas6 for requisite time points.

Name	EMT Subtype	EMT Phenotype	Media
OVCAR8	Epi-A	Epithelial	RPMI + 10% FBS + Insulin (10 mg/ml)
PEO1	Epi-A	Epithelial	RPMI 1640 + 10% FBS + Insulin (2.5 mg/ml) + 2mM NaPy
JHOS2	Epi-A	Intermediate Epithelial	DMEM/Ham's F-12 (1:1) + 10% FBS + 0.1 mM NEAA
OVCA429	Epi-A	Intermediate Epithelial	DMEM + 10% FBS
OVCA433	Epi-A	Intermediate Epithelial	DMEM + 10% FBS
PEO4	Epi-A	Intermediate Epithelial	DMEM (HG) + 15% FBS + Insulin (2.5 mg/ml) + 1x NEAA
UWB1.289	Epi-A	Intermediate Epithelial	RPMI 1640/ MEGM (1:1) + 3% FBS
CAOV3	Epi-B	Epithelial	DMEM + 10% FBS
JHOS3	Epi-B	Intermediate Epithelial	DMEM/Ham's F-12 (1:1) + 15% FBS + 0.1 mM NEAA
OVCA432	Epi-B	Intermediate Epithelial	DMEM + 10% FBS
EFO21	Mes	Intermediate Epithelial	RPMI 1640 + 20% FBS + 1 mM NaPy + 1x NEAA
OAW 28	Mes	Intermediate Epithelial	DMEM + 10% FBS + 20 IU/L Insulin + 1 mM NaPy
OV56	Mes	Intermediate Epithelial	DMEM/ Ham's F-12 (1:1) + 5% FBS + 0.5 mg/ml Hydrocortisone + 10 mg/ml Insulin
DOV13	Mes	Intermediate Mesenchymal	DMEM + 10% FBS
Hey	Mes	Intermediate Mesenchymal	RPMI 1640 + 10% FBS
HeyC2	Mes	Intermediate Mesenchymal	RPMI 1640 + 10% FBS
OV7	Mes	Intermediate Mesenchymal	DMEM/ Ham's F-12 (1:1) + 5% FBS + 0.5 mg/ml Hydrocortisone + 10 mg/ml Insulin
SKOV3	Mes	Intermediate Mesenchymal	DMEM (HG): DMEM (LG) (1:1) + 10% FBS
A1847	Mes	Mesenchymal	RPMI 1640 + 10% FBS + 10 mg/ml Insulin
HeyA8	Mes	Mesenchymal	RPMI 1640 + 10% FBS
TykNu	Mes	Mesenchymal	DMEM + 10% FCS
OVCAR3	Stem-A	Epithelial	RPMI 1640 + 20% FBS + 10 mg/ml Insulin
FUOV1	Stem-A	Intermediate Epithelial	DMEM/Ham's F-12 (1:1) + 10% FBS
IGROV1	Stem-A	Intermediate Epithelial	RPMI 1640 + 10% FBS
JHOS4	Stem-A	Intermediate Epithelial	DMEM/Ham's F-12 (1:1) + 10% FBS + 0.1 mM NEAA
OAW 42	Stem-A	Intermediate Epithelial	DMEM + 10% FBS + 20IU/L Insulin + 1 mM NaPy
OV17R	Stem-A	Intermediate Epithelial	DMEM/ Ham's F-12 (1:1) + 5% FBS + 0.4 mg/ml Hydrocortisone + 10 mg/ml Insulin
CH1	Stem-A	Intermediate Mesenchymal	DMEM + 10% FBS + Insulin (10 mg/ml) + Hydrocortisone (0.5 mg/ml)
A2780	Stem-A	Mesenchymal	RPMI 1640 + 10% FBS
OVCAR10	Stem-A	Mesenchymal	RPMI 1640 + 10% FBS + 10 mg/ml Insulin
OVK18	Stem-A	Mesenchymal	MEM + 10% FBS
TOV112D	Stem-A	Mesenchymal	MCDB105 (1.5 mg/ml Na2CO3)/ M199 + 15% FBS (1:1)
OV90	Stem-B	Epithelial	MCDB105 (1.5 mg/ml Na2CO3)/ M199 + 15% FBS (1:1)
OVCA420	Stem-B	Epithelial	DMEM + 10% FBS
CAOV2	Stem-B	Intermediate Epithelial	RPMI + 10% FBS
COLO 720E	Stem-B	Intermediate Epithelial	RPMI 1640 + 5-10% FBS
OVCAR2	Stem-B	Intermediate Epithelial	RPMI 1640 + 10% FBS + Insulin (10 mg/ml)
OVCAR5	Stem-B	Intermediate Epithelial	RPMI 1640 + 10% FBS + Insulin (10 mg/ml)
PEA1			RPMI 1640 + 10% FBS
FTE190			FTSEC Medium + 20% Ultroser G serum substitute

Table I: EOC Cell Lines with their respective EMT subtype and EMT Phenotype and culture media.

2.2 EOC patient tumor samples

16 frozen EOC patient tumor samples that have been previously subtyped were obtained from National University Hospital cohort (GSE69207) and used to evaluate phospho-ERK levels.

Tumor Sample	Molecular Subtype
1-0286	Epi-A
1-1021	Epi-A
1-1281	Epi-A
1-0668	Epi-B
1-0682	Epi-B
1-0683	Epi-B
1-0237	Mes
1-0372	Mes
1-0626	Mes
1-1140	Mes
1-0378	Stem-A
1-0585	Stem-A
1-1250	Stem-A
1-0156	Stem-B
1-0424	Stem-B
1-0444	Stem-B

Table II: EOC patient tumor samples with their respective EMT molecular subtype.

2.3 shRNA mediated AXL-knockdown

5 Validated AXL MISSION shRNA and control shRNA (sh-Luciferase targeting) bacterial glycerol stocks were purchased from Sigma-Aldrich. DNA was purified and extracted using PureYield^{TM} Plasmid Miniprep System (Promega) and used to transfect 293T cells according to manufacturer's protocol. The virus generated after 48 hours was subsequently filtered to remove 293T cell debris and used to infect OVCA429 and SKOV3 with 4µg.ml^{-1} polybrene. 48 hours post-infection, the transduced cell lines were selected with 10µg.ml^{-1} puromycin and stable cell lines were maintained at the same concentration. The sequences that gave maximum AXL protein downregulation post infection and selection with 5µg.mL^{-1} puromycin were TRCN0000001040 (Clone ID: NM_021913.x-2909s1c1 Sequence:

CCGGCGAAATCCTCTATGTCAACATCTCGAGATGTTGACATAGAGGATTTCGTTT TT) and TRCN0000001041 (Clone ID: NM_021913.x-2151s1c1 Sequence: *CCGGGCTGTGAAGACGATGAAGATTCTCGAGAATCTTCATCGTCTTCACAGCTT TTT*), and denoted shAXL#40 and shAXL#41 respectively. As a control, the non-specific sh-Luciferase shRNA comprising of the following sequence *CCGGCGCTGAGTACTTCGAAATGTCCTCGAGGACATTTCGAAGTACTCAGCGTT TTT* (#SHC007) was used. These clones were used for loss of function studies in experiments measuring proliferation, motility, anchorage independent growth, invasion, and tumor growth in SCID mice.

2.4 OPCML overexpression

The pLENTI-OPCML genomic plasmid was prepared by colleague Dr. Elena Sokolskaja. The complete wild-type coding sequence of *OPCML* along with the Kozak consensus sequence and the 3′ untranslated region overlap encompassing nucleotides 34–1,110 (NM_002545.4), were amplified by PCR from normal human OSE RNA. This was cloned into the entry vector pENTR4 (AdGene) to generate pENTR4-OPCML. Gateway cloning technology was used to swap the OPCML sequence from the pENTR4 to pLENTI using clonase enzyme (Thermo Fisher Scientific). 2µg of pLENTI-OPCML genomic plasmid along with 1.7µg pf packaging plasmid (8.9) and 0.3µg of VSV-G (pMDG) were diluted into 250µL OptiMEM. 10µL of Lipofectamine3000 (Thermo Fisher Scientific) was then diluted into another 250µL of OptiMEM. The two dilutions were combined and incubated at room temperature for 20 minutes prior to adding the mixture gently to 90% confluent 293T cells. The virus generated after 48 hours was subsequently filtered to remove 293T cell debris and used to infect SKOV3 and PEA1 cell lines with 4µg.ml^{-1} polybrene. As a control, the SKOV3 and PEA1 cell lines were also infected with pLENTI-EMPTY vector following

the same protocol. 48 hours post-infection, the transduced SKOV3 cell lines were selected with 10µg.ml^{-1} puromycin, and the transduced PEA1 cell lines were selected with 2.5µg.ml^{-1} puromycin and stable cell lines were maintained at their respective selection concentrations. These cell lines were used to assess the effect of tumor suppressor restoration on cancer cells, and functional studies included single and collective cell motility, invasion, and signaling kinetics.

For Gas6 signaling kinetics, the Control and OPCML-overexpressing cells were seeded to attain 70% confluence and serum starved overnight and activated with 400ng.mL^{-1} Gas6 for 0, 10, 20, 30 minutes, 1, 3, 6, 12 and 24 hours and lysates were collected for analysis.

In the AXL inhibitor studies, the SKOV3 Control and OPCML-overexpressing cells were seeded so as to obtain 80% confluence at the end of study, incubated with R428 at varying doses between 0 and 80µM for 48 hours to calculate GI50 doses.

For kinetics of Gas6 signaling upon AXL inhibition, the SKOV3 Control and OPCML-overexpressing cells were serum starved overnight, preincubated with 2.84 µM $GI50^{Control}$ or 1.09 µM $GI50^{OPCML}$ concentrations of R428 for one hour, while control cells were incubated with 0.01% DMSO and then stimulated with 400ng.mL^{-1} Gas6 for requisite time points.

2.5 siRNA mediated gene silencing

For siRNA mediated AXL silencing in SKOV3 parental, SKOV3-OPCML overexpressing and SKOV3-Control, and PEA1-OPCML overexpressing and PEA1-Control cells, 4 sequences from Dharmacon On-Target Plus were utilized along with a pooled non-targeting sequence. siAXL10 (#J-003104-10) with sequence ACAGCGAGAUUUAUGACUA, siAXL12 (#J-003104-12) with sequence GACGAAAUCCUCUAUGUCA and siAXL13 (#J-003104-13) with sequence

GAAGGAGACCCGUUAUGGA gave maximal knockdown of AXL protein and were chosen for further experiments. The pooled non-targeting (#D-001810-10-05) siRNA comprised of 4 oligonucleotide sequences, namely UGGUUUACAUGUCGACUAA, UGGUUUACAUGUUGUGUGA, UGGUUUACAUGUUUUCUGA and UGGUUUACAUGUUUUCCUA. The siRNA transfection was carried as per manufacturer's protocol, at final concentration of 25nM oligonucleotides per well of a six-well plate, along with 4µL oligofectamine diluted in 11µL OptiMEM. Six hours post transfection, the medium was replaced and knockdown was evaluated at 48 hours using immunoblotting. These siAXL transfected cells were used to validate the regulation of motility by AXL and also specificity of Gas6 on the AXL signaling axis.

For loss of tumor suppressor function studies, siRNA mediated OPCML silencing in FTE190 cell lines was performed using 4 sequences from Dharmacon On-Target Plus along with the pooled non-targeting sequence. siOPCML6 (#J-011743-06) with sequence GAUCAUGAAUAUCUCCUCAUU, and siOPCML7 (#J-011743-07) with sequence GACAGACAAUCAUCCCAAAUU, gave maximal protein knockdown as evident by immunoblotting and were used for Gas6 signaling kinetics analysis and motility studies.

2.6 Antibodies

AXL C89E7 rabbit mAb (#8661), phospho-AXL Tyr702 D12B2 rabbit mAb (#5724), phospho-AKT Ser473 D9E XP® rabbit mAb (#4060), phospho-AKT Thr308 D25E6 XP® rabbit mAb (#13038), AKT pan 11E7 rabbit mAb (#4685), GAPDH D16H11 XP® rabbit mAb (#5174), Slug C19G7 rabbit mAb (#9585), phospho-FRA1 Ser265 D22B1 rabbit mAb (#5841), phospho-HER2/Erb2 Tyr1248 rabbit mAb (#2247), HER2/Erb2 29D8 rabbit mAb (#2165), phospho-EGFR Tyr1068 D7A5 XP® rabbit mAb (#3777), phospho-Met Tyr1234/1235 3D7 rabbit mAb (#3129), cMET 25H2 mouse mAb

(#3127) were purchased from Cell Signaling Technology (CST). Phospho-ERK1 pT202/pY204 + phospho-ERK2 pT185/pY187 mouse mAb (ab50011), ERK1/2 rabbit pAb (ab17942), AXL mouse mAB (ab89224) were purchased from Abcam. EGFR /ErbB1 goat pAb (E1157) was bought from Sigma Aldrich. OPCML goat pAb (AF2777) was obtained from R&D Systems. The above listed primary antibodies were used in immunoblotting at 1:1000 dilution.

β–Catenin D10A8 XP® rabbit mAb (#8480) from CST, E-Cadherin Clone 36/E mouse mAb (#610182) from BD Biosciences, OPCML mouse mAb (MAB27771, Clone 341723) from R&D Systems were used 1:100 and 1:2000 for immunostaining respectively. The previously listed phospho-HER2, phospho-EGFR, phospho-Met and AXL antibodies were used at 1:100 for DUOLink and immunostaining. The phospho-AXL and phospho-ERK antibodies were used at 1:100 for immunostaining.

AXL mouse mAB (ab89224) from Abcam, and phospho-AXL Tyr691 (SAB4504605) from Sigma Aldrich were used in Co-immunoprecipitation experiment of AXL and OPCML.

2.7 Western Blotting

Whole cell lysates were generated by lysis with RIPA buffer (#R0278, Sigma–Aldrich), along with protease (#539134) and phosphatase (#524625) inhibitor cocktails, (Calbiochem, Boston, MA). Tumour samples were lysed in 200µL RIPA buffer with protease and phosphatase inhibitor cocktails using a tissue homogeniser. BCA assay was used to evaluate protein concentrations (#23225, Thermo Scientific, Rockford, IL). BioRad Mini Protean II apparatus was used to perform gel electrophoresis on the lysates and BioRad Mini Trans-Blot apparatus was used to transfer the gel onto PVDF membranes (#IPFL00010, Millipore, Billerica, MA). Membranes were blocked with Li-COR blocking buffer (#927-40000) and

subsequently probed with primary antibodies. Incubation with secondary antibodies containing fluorophores at 1:20,000 dilution (IRDye 800CW conjugated goat anti-mouse #926-32210 or anti-rabbit #926-32211, IRDye 680 conjugated goat anti-mouse #926-32220 or anti-rabbit #926-32221, and IRDye 800CW donkey anti-goat #926-32214 antibodies, LI-COR Biosciences, Lincoln, NE) enabled visualization on the Odyssey Infrared Imaging System from LI-COR Biosciences.

2.8 Immunofluorescence Staining

Cells were seeded on 13mm glass coverslips in full medium and left to adhere for 24 hours and to reach 50% confluence. After necessary treatments, cells were fixed with ice cold 100% Methanol for 5min at -20°C and then rehydrated thrice in PBS for 5 minutes each. Coverslips were blocked for 30 minutes with 3%BSA/PBS and then incubated with 1:100 dilution of primary antibodies in 1%BSA/PBS for 1 hour in a moist environment. After 3 washes with PBS, cells were incubated with fluorophore labeled secondary antibodies (Alexa Fluorophores Life technologies, Donkey-anti mouse Alexa Fluor® 488 R37114, Alexa Fluor® 546 A10036, Alexa Fluor® 680 A10038; Donkey-anti rabbit Alexa Fluor® 488 R37118, Alexa Fluor® 546 A10040, Alexa Fluor® 680 A10043; or Donkey-anti goat Alexa Fluor® 488 A11055, Alexa Fluor® 546 A11056, Alexa Fluor® 633 A21082) at 1:200 dilution in 1%BSA/PBS for 1 hour. After 3 washes with PBS, the coverslips were mounted using ProLong® Gold Antifade Reagent with DAPI (Thermo Fisher Scientific) as mounting media. Images were taken by the SP5 Leica Confocal system.

2.9 DUOLink Proximity Ligation Amplification (PLA) Assay

For this PLA assay (DUOLink, OLink Biosceinces, Sigma-Aldrich #DUO92102, #DUO92104), the various cell lines were seeded on 13mm glass coverslips. For AXL-RTK crosstalk experiments, PEO1, OVCA429, SKOV3 and HEYA8 were serum starved overnight and stimulated with 400ng.mL^{-1} Gas6 for 30 minutes, while control cells were left untreated. In AXL-OPCML interaction experiment, cells were either grown in complete medium for basal level of interaction, or serum starved and stimulated with 400ng.mL^{-1} Gas6 for 0, 30 minutes, 3, 12 hours to evaluate Gas6 mediated interaction. After the required treatments, the initial part of the immunofluoresence protocol was followed to label the fixed cells with primary antibodies, taking care to use two different species (e.g., Mouse anti-OPCML, and Rabbit anti-AXL). Meanwhile the two corresponding 5x PLA probes (e.g., Donkey anti-mouse, and Donkey anti-rabbit) were mixed and diluted 1:5 in 1%BSA/PBS for 20 minutes at room temperature. After the primary antibody, three 5-minute washes were carried out with PBS and the PLA dilutions were added. The slides were incubated in a pre-heated humidity chamber for 1 hour at 37°C. Subsequently the PLA solution was washed off and two 5-minute washes were carried out in 1x Wash Buffer A (0.01 M Tris, 0.15 M NaCl and 0.05% Tween 20) under gentle agitation. The 5x Ligation stock was diluted 1:5, and the Ligase enzyme was diluted 1:40 in high purity water and added to each sample. The slides were incubated in a pre-heated humidity chamber for 30 minutes at 37°C. The Ligation-Ligase solution was removed and the slides were washed twice with 1x Wash Buffer A for 2 minutes. The 5x Amplification stock was diluted 1:5, and the Polymerase enzyme 1:80 in high purity water. The Amplification-Polymerase solution was added to each sample and the slides were incubated in a pre-heated humidity chamber for 100 minutes at 37°C. Subsequently, the Amplification-Polymerase solution was washed from the slides

with 1x Wash Buffer B (0.2 M Tris and0.1 M NaCl). After two 10-minute washes, the slides were washed in 0.01x Wash Buffer B for 1 min. The slides were air dried at room temperature in the dark. The slides were mounted using DUOLink II mounting media with DAPI and visualized under the SP5 Leica Confocal system.

2.10 Colorimetric Assays

For assessing the proliferative effects of Gas6 on the 10 EOC cell lines, cell proliferation reagent WST-1 (#11644807001 Sigma Aldrich) was used. Each of the 10 EOC cell lines were seeded in quadruplicate, in a 96 well at a concentration of 5000 cells/well, for no treatment control and Gas6 stimulation. The next day complete medium was replaced with 0.1% medium, with or without 400ng.mL^{-1} Gas6. After 48 hours, WST-1 reagent was added to the wells, (10µL WST1 diluted in 100µL serum free DMEM, per well) and incubated for 2 hours. The stable tetrazolium salt WST-1 is cleaved to a soluble formazan by the succinate-tetrazolium reductase system (EC 1.3.99.1), which belongs to the respiratory chain of the mitochondria, and is only active in metabolically intact cells. This bioreduction is largely dependent on the glycolytic production of NAD(P)H in viable cells. Therefore, the amount of formazan dye formed directly correlates to the number of metabolically active cells in the culture. After the 2-hour incubation period, the formazan dye formed is quantitated with a scanning multi-well spectrophotometer. The absorbance is measured at 450nm and it directly correlates to the number of viable cells.

For assessing the growth inhibitory concentration (GI50) of R428 on the 10 EOC cell lines, Cell Titer 96 MTS colorimetric assay (#G3580 Promega) was utilized. Each of the 10 EOC cell lines were seeded in quadruplicate, in a 96 well at a concentration of 5000 cells/well for concentrations of R428 ranging from 0µM to 80µM. 48 hours after addition of R428, MTS reagent was added to the wells 10µL MST diluted in 100µL

serum free DMEM, per well) and incubated for 1 hour. Similar to the WST-1, the MTS tetrazolium compound is bioreduced by cells into a colored formazan product, and the absorbance is measured on a multi-well spectrophotometer at 490nM.

2.11 Single cell motility tracking

EOC cell lines were seeded at 50% confluence in ibidi 24 well µ-plate and necessary treatments were carried out.

For analysing effect of Gas6 on motility, cells were serum starved for 12 hours and stained for an hour with Hoechst nuclear dye (Life Technologies #62249, 1:500,000) and then stimulated with 400ng.mL^{-1} Gas6 (in 0.1% FBS DMEM), while control cells were left untreated (in 0.1% FBS DMEM).

For the R428 inhibitor studies in Epi-A versus Mes phenotypes, the cell lines were serum starved overnight, preincubated with 9.38 µM GI50$^{Non\text{-}Mes}$ or 2.91 µM GI50^{Mes} concentrations of R428 for one hour, while control cells were incubated with 0.01% DMSO; cells were concurrently stained with Hoechst nuclear dye.

For the MEK inhibitor studies, cells were serum starved overnight, preincubated with 2 µM PD0325901 (#S1036, Selleckchem) or 0.01% DMSO for 4 hours; concurrently cells were stained with Hoechst nuclear dye and then stimulated with 400ng.mL^{-1} Gas6 (in 0.1% FBS DMEM), while control cells were left untreated (in 0.1% FBS DMEM).

In the siAXL and siOPCML motility experiments, the transfected cells were seeded in the ibidi chambers 24 hours post siRNA transfection, and motility was evaluated between 48-50 hours post transfection upon staining with Hoechst nuclear dye; for Gas6 induced motility, the cells were serum starved for 12 hours prior to addition of 400ng.mL^{-1} Gas6 (in 0.1% FBS DMEM).

In shAXL motility experiments, the clones were evaluated in complete medium.

The cells were visualized under the SP5 Leica Confocal system overnight at intervals of 10 minutes. The results were analyzed in ImageJ software using Trackmate® to calculate individual cellular displacements, velocity of locomotion, speed, distance travelled and directional persistence.

2.12 Gap Closure assays

EOC cell lines were seeded at 100% confluence into culture inserts (ibidi #80209) in a 24 well µ-plate and necessary treatments were carried out.

For analysing effect of Gas6 on collective cell migration, cells were serum starved for 12 hours and stained for an hour with Cell Mask membrane dye (Life Technologies #C10049, 1:4000); this was followed by stimulation with 400ng.mL^{-1} Gas6 (in 0.1% FBS DMEM), while control cells were left untreated (in 0.1% FBS DMEM).

For the MEK inhibitor studies, cells were serum starved overnight, preincubated with 2 µM PD0325901 or 0.01% DMSO for 4 hours; concurrently cells were stained with Cell Mask membrane dye and then stimulated with 400ng.mL^{-1} Gas6 (in 0.1% FBS DMEM), while control cells were left untreated (in 0.1% FBS DMEM).

In the siOPCML gap closure experiments, the transfected cells were seeded in culture inserts inside the ibidi chambers 24 hours post siRNA transfection. The cells were serum starved for 12 hours, stained with Cell Mask membrane dye and stimulated with 400ng.mL^{-1} Gas6 (in 0.1% FBS DMEM). Gap closure was evaluated 48-50 hours post transfection.

In shAXL motility experiments, the stable clones were evaluated in complete medium upon staining with Cell Mask membrane dye.

The culture insert was removed to generate a 500µm gap and the cells were visualized under the SP5 Leica Confocal system overnight at intervals of 10 minutes. The results were analyzed in ImageJ to generate the gap closure at 12 hours.

2.13 Soft Agar assay

10^6 cells from shAXL clones and control, of SKOV3 and OVCA429 were seeded in a 6 well plate using a prior established protocol.

A stock of 1.8% noble agar in sterile deionized water was prepared by adding 1.8g noble agar to 100mL deionized water. Solution was autoclaved at 121°C for 15 minutes, and stored at 55°C prior to immediate use. Cancer cells were washed twice in 1X PBS, and dissociated using trypsin-EDTA. Cells were harvested by centrifugation, and 10^6 cells from shAXL clones and control, of SKOV3 and OVCA429 were counted per well of a six well plate. 2mL of bottom agar (final concentration 0.6% noble agar diluted in DMEM medium) was poured to cover the bottom of each well of a six well plate. This was performed in triplicates and allowed to solidify at room temperature for 10 minutes. 2mL of the top agar (final concentration 0.3% noble agar diluted in DMEM medium) containing the cells was plated onto the bottom agar and placed inside a cell culture incubator to facilitate colony formation. On Day 14, anoikis resistant cells that formed colonies on the soft agar were visualized using a microscope.

2.14 Spheroid Invasion Assay

5000 cells were seeded in a Cultrex® 96 Well kit (3D Spheroid BME Cell Invasion Assay, Trevigen, #3500-096-K) and the assay was performed as per manufacturer's protocol. Adherent cells grown under normal culture condition were trypsinized and harvested. 5000 cells were mixed with 5µL Spheroid Formation ECM and culture media (final volume to 50µL) and seeded into each well of a round-bottom ultra-low attachment 96-well plate (#7007, Corning). The plate was then centrifuged at 200 x g for 3 minutes and incubated at 37°C for 72 hours to induce spheroid growth. After the assembled cells formed spheroids, the plates was cooled to 4°C on ice for 15

minutes. Continuing to work on ice, 50µL BME matrix (Basement Membrane Extract) was added to each well, followed by centrifugation at 300 x g, 4°C for 5 minutes. The plate was then incubated at 37°C for 1 hour to allow gel formation, after which 100µl of cell culture media was added.

In the OVCA429 and SKOV3 shAXL clones spheroid invasion experiment, the culture medium added comprised of 10% FBS in DMEM. For the SKOV3 Control and OPCML-overexpressing clones, spheroid invasion experiment was carried out in the presence of Gas6. The culture medium consisted of 1% FBS in DMEM along with 400ng.mL^{-1} Gas6

The spheroids were grown under normal cell culture condition at 37°C and 5% CO_2 and invasion was monitored over a period of time. Optimal results were documents on Day 3.

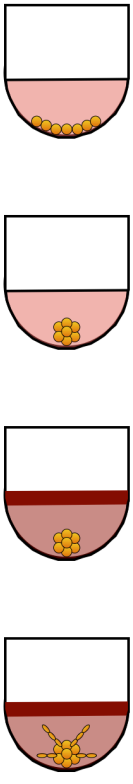


Figure J: Spheroid Invasion Assay.

2.15 SKOV3 Orthotopic xenograft mouse model

The SKOV3 Orthotopic Xenograft model was established by GenScript, New Jersey. The procedures involving the care and use of animals were reviewed and approved by the Institutional Animal Care and Use Committee (IACUC) to ensure compliance with the regulations of the Association for Assessment and Accreditation of Laboratory Animal Care (AAALAC). Five 6-week old female SCID-Beige mice were used per condition and inoculated by intraperitoneal injection with a single volume of 200 µl cell suspension with 5×10^6 cells to establish SKOV3 shLuciferase control, shAXL#40 and shAXL#41 ovarian cancer models. Study was concluded 4 weeks after injection of cells, and tumor number and tumor weight was measured in each mouse using calibrated calipers. Tumours volume was calculated using the formula: $\text{width}^2 \times \text{length} \times 0.5$.

2.16 Chick Chorion Aallantoic Memebrane (CAM) model

Fertilized chicken eggs were purchased from Henry Stewart & Co. Ltd (Fakenham, UK) washed and incubated at 37^{o}C with 60% relative humidity on embryonic day (ED) 1, for implantation on ED4. Under sterile conditions, a small hole was pierced through the pointed pole of the shell using a 19G needle and 3mL of albumin was removed to 'drop the CAM'. Semi-permeable sterile tape was placed over the top of the egg and sharp angled scissors were used to excise the shell and cut a 2 cm^2 window to expose the CAM. This window was sealed with Suprasorb® F sterile wound healing film (Lohmann & Rauscher, Germany). Between ED7 and ED10 of incubation the membranes are ready for the grafting of cancer cells.

In the sensitisation experiment of EOC molecular subtypes to AXL inhibition, PEO1, OVCA429, SKOV3, HEYA8 were preincubated with DMSO only (control cells), or $GI50^{Non\text{-}Mes}$ or $GI50^{Mes}$ concentrations of R428 for 48 hours. In the sensitisation

experiment of OPCML overexpressing cells to AXL inhibition SKOV3 Control and OPCML-overexpressing cells were preincubated with DMSO only (control cells), or $GI50^{Control}$ or $GI50^{OPCML}$ concentrations of R428 for 48 hours.

Grafts were prepared by suspending 10^6 cells in 100µL Matrigel (BD Biosciences). The 100µl of the prepared graft, containing 10^6 cells, were then inoculated onto this area. After inoculation, the window was then re-covered and sealed then placed back in the incubator. Tumour growth and viability of the embryo was checked daily. Tumour dimensions were measured using SteREO Discovery.V8 microscope (Zeiss, Germany) with Zen 2.0 blue edition software (Zeiss).

2.17 Reverse Phase Protein Array

Mes subtype SKOV3 cell line and Epi-A subtype PEO1 cell line were serum starved overnight and treated with 400ng.mL^{-1} Gas6 for for 0 minutes, 30 minutes or 12 hours. Also, the SKOV3 Control and OPCML-overexpressing cell lines were serum starved overnight and treated with 400ng.mL^{-1} Gas6 for 0 minutes, 30 minutes or 12 hours. Whole cell lysates were generated by lysis with RIPA buffer, along with protease and phosphatase inhibitor cocktails.

RPPA was carried out at MD Anderson Cancer Centre and the procedure involved serial dilution of samples and subsequent colorimetric detection by antibodies upon tyramid amplification. Spot intensity assessment was using R package developed in house at MD Anderson Cancer Center with protein levels being quantified by SuperCurve method (http://bioinformatics.mdanderson.org/OOMPA). Data were log-transformed (base 2) and median-control normalized across all proteins within a sample. The RPPA antibody list can be obtained here http://www.mdanderson.org/education-and-research/resources-for-professionals/scientific-resources/core-facilities-and-services/functional-proteomics-

rppa-core/antibody-lists-protocols/functional-proteomics-reverse-phase-protein-array-core-facility-antibody-lists-and-protocols.html

Also, for the phospho-MAPK (pT202) levels in ovarian tumors, level-3 RPPA data of ovarian cancer clinical samples were downloaded from TCGA data portal (https://tcga-data.nci.nih.gov/tcga/). The subtype information was extracted from our previous gene expression analysis of the corresponding samples[41].

2.18 Gene expression analysis and *AXL* signature

Gene expression data was extracted from previously processed meta-analysis of 1538 ovarian cancer[41]. To derive the AXL signature, genes that are most strongly and positively correlated with AXL gene expression (Rho > +0.45) were selected. These were performed by Dr. Tuan Zea Tan.

2.19 Statistical analysis

Statistical analyses were conducted using Matlab ® R2012a version 7.14.0.739, and statistics toolbox version 8.0 (MathWorks; Natick, MA). Statistical significance of differential expression was evaluated using either Student's t-test or Mann-Whitney U-test. A Spearman correlation coefficient test was applied to assess significance of correlation. Kaplan-Meier analyses were conducted using GraphPad Prism ® version 5.04 (GraphPad Software; La Jolla, CA). Statistical significance of the Kaplan-Meier analysis was calculated by log-rank test. To perform Kaplan-Meier analysis of overall and disease-free survival for AXL signature in various cancer, stratification of patients was based on AXL signature score which segregate patients into AXL-high and AXL-low groups referring to median score, or AXL-Q1 and AXL-Q4 referring to lowest 25% and highest 25% signature scores respectively. These were performed by Dr. Tuan Zea Tan.

2.20 GST-Pull Down Assay

To evaluate AXL and GST-OPCML interaction, SKOV3 Control cells were grown in complete medium in a 10cm dish to reach 80% confluence, and lysed with 1mL ice cold RIPA Buffer containing protease and phosphatase inhibitors.

To evaluate phospho-AXL and OPCML interaction, SKOV3 Control cells were grown in complete medium in a 10cm dish to reach 70% confluence and then serum starved overnight. Upon stimulation with 400ng.mL^{-1} Gas6 for 0 or 30 minutes, the plates were lysed with 1mL ice cold RIPA Buffer containing protease and phosphatase inhibitors.

Dr. Elisa Zanini generated recombinant GST-OPCML protein that was utilized to study the binding of OPCML to target proteins. OPCML was cloned into the pGEX-6P-2, a vector that encodes for Glutathione-S-Transferase (GST) followed by a PreScission Protease cleavage site and a multiple cloning site. An ampicillin-resistance box is present on the vector and ampicillin was used as selective agent during amplification of the constructs in bacteria. Refolded proteins obtained as described previously were capable of binding to a Gluthatione (GSH)- Sepharose 4B resin (GE Healthcare), confirming successful refolding of the GST-tag, and were analysed by both SDS-PAGE followed by Coomassie Blue staining and WB using a goat anti-OPCML antibody (R&D Systems).

The GST-OPCML protein was immobilized by Magne-GST^{TM} Pull-Down System (Promega) through the GSH-linked magnetic particles. This was incubated with cell lysate containing the target protein of interest, AXL. Beads were then washed 3 times and proteins were eluted by adding directly SDS sample buffer onto the particles and by boiling the sample for 5 minutes.

2.21 Co-Immunoprecipitation Assay

To confirm the protein-protein interaction between AXL and OPCML a Co-Immunoprecipitation experiment was carried out using the Pierce CO-IP Kit (#26149, Thermo Fisher Scientific) as per manufacturer's protocol. For AXL and OPCML interaction, SKOV3-OPCML overexpressing cells were grown in complete medium in a 10cm dish to reach 80% confluence, and lysed with 1mL ice cold IP Lysis Buffer containing protease and phosphatase inhibitors, for 1 hour at 4°C upon gentle agitation. For phospho-AXL and OPCML interaction, SKOV3-OPCML overexpressing cells were grown in complete medium in a 10cm dish to reach 70% confluence and then serum starved overnight. Upon stimulation with 400ng.mL^{-1} Gas6 for 0 or 30 minutes, the plates were lysed with 1mL ice cold IP Lysis Buffer containing protease and phosphatase inhibitors, for 1 hour at 4°C upon gentle agitation.

For the antibody immobilisation step, 50µg of AXL mAb (ab89224) or 100µg of pAXL pAb (SAB4504605) were diluted onto the AminoLInk Plus Coupling Resin (supplied in the kit). The cell lysates were precleared with control agarose resin, and Co-immunoprecipitation was carried out by adding the precleared cell lysate to the antibody immobilized resin, with end over end mixing at 4°C overnight. After elution, the sample was run on an SDS-Page gel and followed by immunoblotting to detect protein-protein interaction.

2.22 Membrane Fractionation Protocol for Lipid Raft generation

In order to investigate the effect of the AXL-OPCML interaction on membrane distribution of AXL, a membrane fractionation experiment was performed to partition the plasma membrane into 'disordered' detergent soluble membrane (DSM) fraction and the 'ordered' detergent-resistant insoluble membrane (DRM) fraction. In order to evaluate the effect of overexpression OPCML on membrane partitioning of AXL,

SKOV3 Control and OPCML-overexpressing cells were grown in complete medium in a 150cm dish to reach 80% confluence, and osmotically lysed in a low salt buffer (20 mM Tris-HCl, pH 7.0) containing protease and phosphatase inhibitors. In order to evaluate the effect overexpression of OPCML on membrane partitioning of AXL upon Gas6 stimulation and subsequent signaling kinetics, SKOV3 Control and OPCML-overexpressing cells were grown in complete medium in a 150cm dish to reach 70% confluence. After overnight serum starvation, the plates were stimulated with 400ng.mL^{-1} Gas6 for 0, 30 minutes, 3 hours or 12 hours and then subsequently osmotically lysed.

The cell suspension was passed through a 22-gauge needle and an aliquot was retained for whole-cell lysate analysis. The cell suspension was centrifuged at 63,000g (45,000 rpm) using Beckman Optimax Ultracentrifuge, for 1 hour at 4°C. The membrane pellet was resuspended in ice-cold PBS plus inhibitors and centrifuged a second time at 63,000g (45,000 rpm), for 30 minutes at 4°C. The membrane pellet was resuspended in ice-cold PBS, 1% Triton-X100, plus inhibitors, and allowed to incubate for 30 minutes at 4°C. The detergent treated membrane fraction was then centrifuged a third time at 63,000g (45,000 rpm) for 1 hour at 4°C. The supernatant or the 'disordered' detergent soluble membrane fraction was removed and retained for analysis. The remaining pellet or the 'ordered' detergent-resistant insoluble membrane fraction was solubilized in 1% SDS. The DRM was resuspended in a volume of 1% SDS equal to the volume of DSM.

2.23 Cholesterol Depletion Protocol

To validate the role of the lipid raft in modulation of Gas6/AXL signaling by OPCML, the lipid rafts or the 'ordered' detergent-resistant insoluble membrane fraction was perturbed using Methyl-β-cyclodextrin (MBCD, #C4555, Sigma Aldrich).

In order to deplete cholesterol, SKOV3 OPCML-overexpressing cells were grown on 13mm coverslips and treated with 5mM MBCD for 30 minutes at 37°C; control cells were maintained without cholesterol depletion. Following MBCD treatment, cells were allowed to recover for 0, 30 minutes, 3 and 12 hours in serum free medium and then fixed with ice-cold methanol for 5 minutes and rehydrated thrice with PBS. The cells were stained with 0.05mg.mL^{-1} Filipin (#C4767, Sigma Aldrich) diluted in PBS for 1 hour at room temperature and rinsed thrice with PBS. The coverslips were mounted in non-DAPI mounting medium and the filipin staining was observed under the 405nm wavelength of a fluorescent microscope.

After validating MBCD mediated cholesterol depletion, cells were plated to observe changes in Gas6/AXL mediated signaling upon cholesterol depletion in SKOV3 Control and OPCML-overexpressing cells via immunoblotting, to discern effects on membrane partitioning of AXL by OPCML via membrane fractionation, and also to determine the interaction of AXL-OPCML via proximity ligation assay.

CHAPTER III: GAS6/AXL SIGNALING NETWORK AS A MES MOLECULAR SUBTYPE SPECIFIC THERAPEUTIC TARGET FOR EPITHELIAL OVARIAN CANCER

3.1 INTRODUCTION

Epithelial ovarian cancer (EOC) is a lethal malignancy[147] with non-specific symptoms in early stages that enable silent progression of the disease[77]. Most cases are diagnosed in the advanced stages and despite treatment, prognosis is poor with 5 year survival lower than 30%[7]. Loco-regional dissemination of the tumor and metastases contribute to immense disease burden. Furthermore, EOC is hallmarked by a high degree of genetic and epigenetic aberrations resulting in a diverse repertoire of modified cellular networks[81] that can be delineated into distinct molecular subtypes based on gene expression profiling[39,40]. These gene expression molecular subtypes (GEMS) are robust and reproducible as reported in AOCS[39], TCGA[40], and our own group's large-scale meta-analysis study[41]. At least 5 distinct GEMS of EOC have been identified: Epithelial-A (Epi-A), Epithelial-B (Epi-B), Mesenchymal (Mes), Stem-A and Stem-B[41]. Elucidation of key signaling networks has further identified distinct players that promote tumorigenesis in each subtype.

The Mes subtype, which corresponds to the C1 subtype from the Tothill dataset and the Mesenchymal subtype from the TCGA dataset, shows high correlation with TGF-β pathway in gene set enrichment analysis (GSEA) with poor survival outcomes[39-41]. TGF-β pathway is a well-known driving mechanism for epithelial-mesenchymal transition (EMT)[58]. The C1/Mesenchymal/Mes (referred as Mes hereafter) subtype has indeed been found to demonstrate extensive desmoplastic stromal reactions[39] that are associated with a master miRNA regulatory network controlling the expression of E-cadherin, vimentin and *SNAI2,* genes that are related to EMT[148], the down-regulation of an epithelial transcriptional gatekeeper GRHL2[149], and to exhibit a high EMT score[150].

The concept of GEMS-specific therapeutics has been well-developed in breast cancer[151,152]. However, data supporting the GEMS-specific management in EOC is

newly emerging. The GEMS-specific pathways in EOC further point to the direction for developing novel therapeutic strategies. The Stem-A subtype is known to have a preferential sensitivity to microtubule destabilizers such as vinorelbine[41]. Inhibiting the TGF-β pathway might be a potential option for the Mes subtype[148]. The feasibility to stratify EOC patients based on GEMS by using a laboratory-based assay on formalin-fixed paraffin embedded (FFPE) diagnostic blocks has been demonstrated recently[153]. Therefore, there is an eminent need in the field to quest for GEMS-specific therapeutic targets for EOC patients to achieve personalized precision management.

In this study, we highlight how the differences in kinase signaling patterns among GEMS affect the sensitivity to kinase inhibition in EOC. Our data suggests that the Mes subtype is hallmarked by a receptor tyrosine kinase (RTK) crosstalk network sustained by the Gas6/AXL signaling node. The RTK AXL belongs to the Tyro3-Axl-Mer (TAM) family of RTKs[154] along with Mer and Tyro-3 and is activated by its ligand Growth Arrest Specific-6 (Gas6)[155]. Its expression has been shown to be of prognostic value in breast[105], lung[156], and pancreatic cancers[109]. AXL has also been suggested as a therapeutic target for breast[112] and pancreatic cancer[157], and cancers demonstrating resistance to EGFR and PI3K inhibition[107,108,158]. In EOC, AXL is highly expressed in advanced stage diseases, predominantly in peritoneal deposits and metastases[159]. Silencing of *AXL* and blocking the Gas6/AXL pathway prevents regional dissemination of ovarian cancer cells *in vivo*[160]. However, the role of AXL under the heterogeneous molecular backgrounds in EOC and the potential functional and therapeutic implication is yet to be defined. Here, we describe how the Gas6/AXL signaling transduction differs between the mesenchymal, worse prognosis Mes subtype and the epithelial, better prognosis Epi-A subtype. We also explore how the signaling patterns lead to differences in migration and therapeutic responses.

3.2 RESULTS

3.2.1 Kinome profiling identifies *AXL* as being highly expressed in Mes, and *AXL* over expression is associated with worse patient survival.

Our group has previously published a meta-analysis of expression microarray datasets from multiple repositories consisting of 1538 EOC tumors from which five EMT molecular subtypes – Epi-A, Epi-B, Mes, Stem-A and Stem-B were identified based on gene expression profiling. Upon interrogating the kinome expression[41] patterns by determining the top ranked kinases in each subtype, *AXL* was revealed to have a high ranking exclusively in the poor prognosis Mes subtype (Figure 1A and 1B).

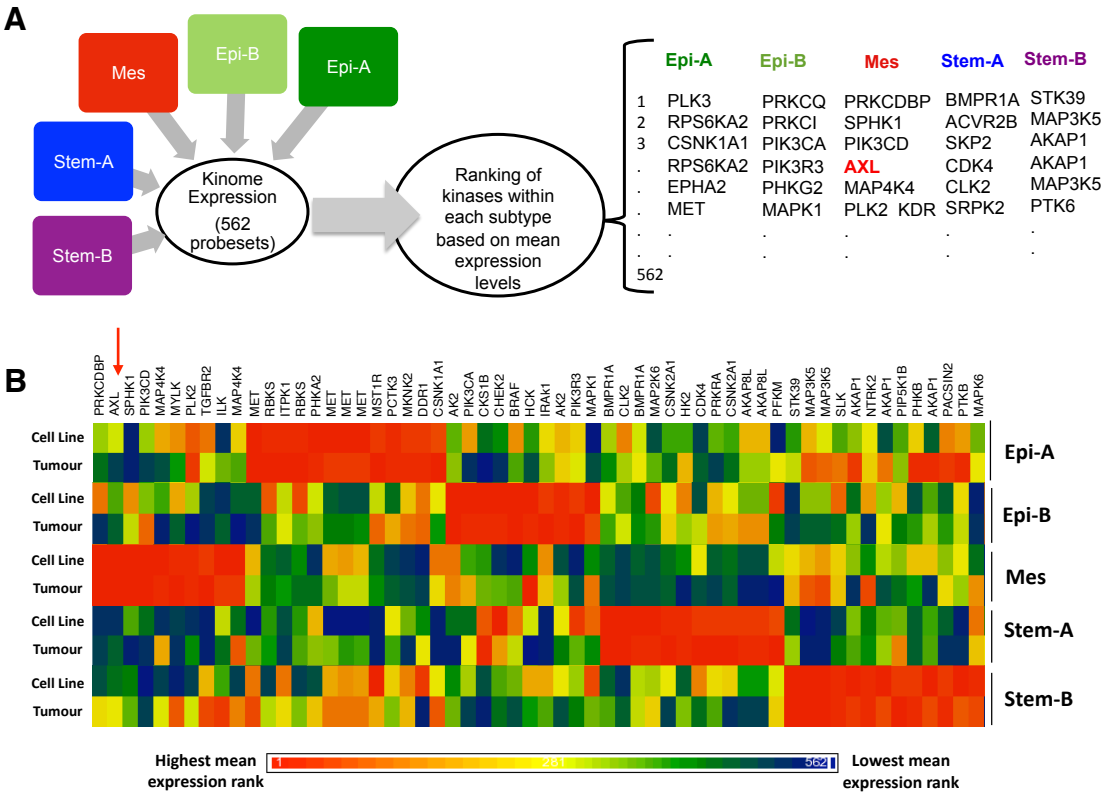


Figure 1: Kinome Profile of EMT subtyped EOC tumors and cell lines.
(A) The kinome profile of cell lines and tumors was evaluated from 562 probe sets and the kinases were ranked according to their mean expression levels within each EOC molecular subtype.
(B) Heat map showing AXL being one of the top 10 ranked kinases in the Mes subtype (arrow), but not in the other GEMS, and therefore chosen as a potential target for the Mes subtype.

Gene expression profiling of the ovarian cancer meta-analysis dataset revealed that Mes tumors showed significantly higher *AXL* gene expression (Figure 2A; p = 2.5e-47). Furthermore, Mes subtype EOC cell lines also showed significant enrichment for *AXL* gene expression. (Figure 2B; p = 1.26e-8) Survival analysis showed that *AXL* overexpression conferred poor prognosis in ovarian cancer (Figure 3) in both univariate (HR = 2.2, p = 6.46e-11) and multivariate analysis (HR = 1.513, p = 0.0012) (Table 1). Of note, *AXL* continued to validate as an independent prognostic factor, after adjusting for the effect resulting from five GEMS (Table 2).

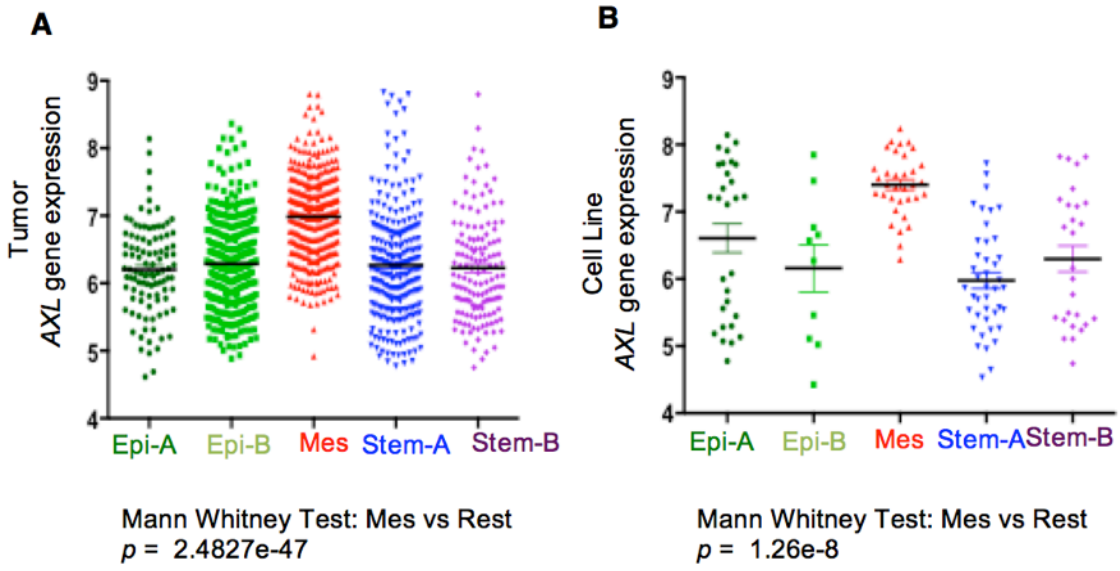


Figure 2: *AXL* expression is enriched in the Mes subtype of Ovarian Cancer.
(A) *AXL* gene expression in the 1538 ovarian tumor samples (y-axis) classified into five EMT molecular subtypes Epi-A, Epi-B, Mes, Stem-A and Stem-B (x-axis), shows enrichment in Mes subtype tumors (Mann Whitney Test: Mes vs Rest p = 2.4827e-47).
(B) *AXL* gene expression in 142 EOC cell lines (y-axis) delineated into the five EMT molecular subtypes (x-axis), shows enrichment in the Mes subtype cell lines (Mann Whitney Test: Mes vs Rest p = 1.28e-8).

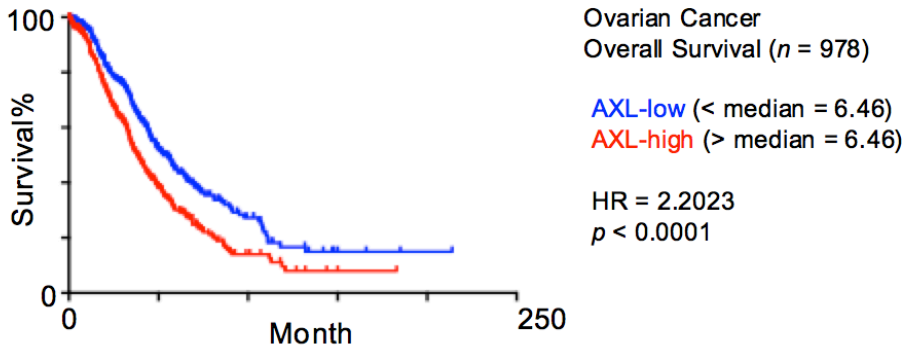


Figure 3: *AXL* over expression confers worse prognosis in Ovarian Cancer. Kaplan-Meier curves showing overall patient survival (y-axis) of AXL-high (red) and AXL-low (blue) patient groups. AXL-high, defined as an above median expression, conferred a worse prognosis with a hazard ratio of 2.2023 and log-rank test $p < 0.0001$.

N = 539 event = 258

Clinical Variable	Sample sizes	Univariate (HR, 95% CI)	Beta	p-value	Multivariate (HR, 95% CI)	Beta	p-value
Age (year)							
< 55	175 (32.47%)	1					
>= 55	364 (67.53%)	1.403 (1.071 - 1.839)	0.3387	0.0141	1.27 (0.9669 - 1.668)	0.239	0.0858
Stage							
I or II	47 (8.72%)	1					
III or IV	492 (91.28%)	3.907 (1.843 - 8.285)	1.3628	0.00038	3.44 (1.603 - 7.382)	1.235	0.00152
Grade							
1	17 (3.15%)	1					
>=2	522 (96.85%)	2.58 (0.9578 - 6.949)	0.9477	0.0608	1.528 (0.5597 - 4.171)	0.4239	0.408
Metastasis							
Primary	500 (92.76%)	1					
Metastatic	39 (7.24%)	1.349 (0.8323 - 2.185)	0.2991	0.224	1.083 (0.6606 - 1.774)	0.0794	0.7527
AXL							
<6.46	276 (51.21%)	1					
>6.46	263 (48.79%)	2.2023 (1.638 - 2.499)	0.7046	6.46E-11	1.513 (1.1771 - 1.946)	0.4144	0.0012

Table 1: Multivariate Analysis identifies AXL as an independent prognostic factor for worse prognosis in EOC.

Epi-A				
Clinical Variable	**Sample sizes**	**Multivariate**	**Beta**	**p-value**
Epi-A				
1	56 (10.39%)			
0	483 (89.615)	1.055 (0.6468 - 1.721)	0.05373	0.8296
Age (year)				
< 55	175 (32.47%)			
>= 55	364 (67.53%)	1.271 (0.9675 - 1.669)	0.2396	0.085
Stage				
I or II	47 (8.72%)			
III or IV	492 (91.28%)	3.469 (1.6106 - 7.473)	1.244	0.00149
Grade				
1	17 (3.15%)			
>=2	522 (96.85%)	1.58 (0.5531 - 4.514)	0.4575	0.3929
Metastasis				
Primary	500 (92.76%)			
Metastatic	39 (7.24%)	1.085 (0.6618 - 1.779)	0.0816	0.74627
AXL				
<6.46	276 (51.21%)			
>6.46	263 (48.79%)	1.52 (1.1785 - 1.959)	0.4184	0.00125

Epi-B				
Clinical Variable	**Sample sizes**	**Multivariate**	**Beta**	**p-value**
Epi-B				
1	155 (28.76%)			
0	384 (71.24%)	0.7923 (0.5936 - 1.0570)	-0.2328	0.1139
Age (year)				
< 55	175 (32.47%)			
>= 55	364 (67.53%)	1.2683 (0.9656 - 1.666)	0.23764	0.08754
Stage				
I or II	47 (8.72%)			
III or IV	492 (91.28%)	3.2698 (1.5213 - 7.0280)	1.1847	0.0024
Grade				
1	17 (3.15%)			
>=2	522 (96.85%)	1.6089 (0.5888 - 4.3960)	0.4756	0.3538
Metastasis				
Primary	500 (92.76%)			
Metastatic	39 (7.24%)	1.0674 (0.6512 - 1.7500)	0.0652	0.7959
AXL				
<6.46	276 (51.21%)			
>6.46	263 (48.79%)	1.4553 (1.1268 - 1.8790)	0.3752	0.004

Mes				
Clinical Variable	**Sample sizes**	**Multivariate**	**Beta**	**p-value**
Mes				
1	178 (33.02%)			
0	361 (66.98%)	0.8199 (0.6137 - 1.0950)	-0.1985	0.1791
Age (year)				
< 55	175 (32.47%)			
>= 55	364 (67.53%)	1.2687 (0.9660 - 1.6660)	0.238	0.087
Stage				
I or II	47 (8.72%)			
III or IV	492 (91.28%)	3.6734 (1.7033 - 7.9220)	1.3011	0.0009
Grade				
1	17 (3.15%)			
>=2	522 (96.85%)	1.5770 (0.5779 - 4.3030)	0.4555	0.3738
Metastasis				
Primary	500 (92.76%)			
Metastatic	39 (7.24%)	1.1426 (0.6927 - 1.8850)	0.1333	0.6016
AXL				
<6.46	276 (51.21%)			
>6.46	263 (48.79%)	1.6339 (1.2426 - 2.1480)	0.491	0.0004

Stem-A				
Clinical Variable	**Sample sizes**	**Multivariate**	**Beta**	**p-value**
Stem-A				
1	128 (23.75%)			
0	411 (76.25%)	1.5290 (1.1486 - 2.0350)	0.4245	0.0036
Age (year)				
< 55	175 (32.47%)			
>= 55	364 (67.53%)	1.2560 (0.9560 - 1.6500)	0.228	0.1016
Stage				
I or II	47 (8.72%)			
III or IV	492 (91.28%)	3.4130 (1.5905 - 7.3240)	1.2276	0.0016
Grade				
1	17 (3.15%)			
>=2	522 (96.85%)	1.3880 (0.5071 - 3.7990)	0.3278	0.5234
Metastasis				
Primary	500 (92.76%)			
Metastatic	39 (7.24%)	1.1600 (0.7059 - 1.9060)	0.1484	0.5582
AXL				
<6.46	276 (51.21%)			
>6.46	263 (48.79%)	1.6170 (1.2516 - 2.0890)	0.4805	0.0002

Stem-B				
Clinical Variable	**Sample sizes**	**Multivariate**	**Beta**	**p-value**
1	22 (4.08%)			
0	517 (95.92%)	1.1660 (0.6174 - 2.2020)	0.1535	0.6361
Age (year)				
< 55	175 (32.47%)			
>= 55	364 (67.53%)	1.2690 (0.9662 - 1.6670)	0.2382	0.0868
Stage				
I or II	47 (8.72%)			
III or IV	492 (91.28%)	3.4300 (1.5982 - 7.3620)	1.2326	0.0016
Grade				
1	17 (3.15%)			
>=2	522 (96.85%)	1.5210 (0.5570 - 4.1530)	0.4193	0.4133
Metastasis				
Primary	500 (92.76%)			
Metastatic	39 (7.24%)	1.0870 (0.6629 - 1.7810)	0.0832	0.7415
AXL				
<6.46	276 (51.21%)			
>6.46	263 (48.79%)	1.5150 (1.1785 - 1.9490)	0.4157	0.0012

Table 2: Multivariate Analysis accounting for the EMT molecular subtypes identifies AXL as an independent prognostic factor in EOC.

3.2.2 AXL expression is preferentially enriched in the EMT-ed Mes subtype, and moderately present in the epithelial Epi-A subtype.

Western blotting the SGOCL[161] panel of ovarian cancer cell lines that have been matched with the EMT molecular subtypes[41], revealed that Mes subtype EOC cell lines were largely positive for AXL protein expression (9/11, 81.8%), but not Stem-A (4/11, 36.4%) (Figure 4A and 4B). Interestingly, Epi-A and Epi-B collectively were moderately positive for AXL protein expression (7/10, 70%) (Figure 4A and 4B). The average AXL protein expression levels were high in both Epi-A and Mes, while Stem-A and Stem-B showed very low AXL protein expression levels. Since AXL has been associated with EMT[105,106], we further examined, within each GEMS, whether AXL expression would correlate with different phenotypes along the previously established EMT spectrum based on E-cadherin, pan-cytokeratin and vimentin

expression; Epithelial (E), Intermediate Epithelial (IE), Intermediate Mesenchymal (IM), Mesenchymal (M)[161]. From a phenotypic standpoint, the IM phenotype, which has previously been shown to be an aggressive, anoikis resistant state[161], is 100% positive for AXL expression (Figure 4C). Our data suggested that although AXL is highly expressed in Mes and the IM phenotype, it is also expressed abundantly in Epi-A and the IE phenotype.

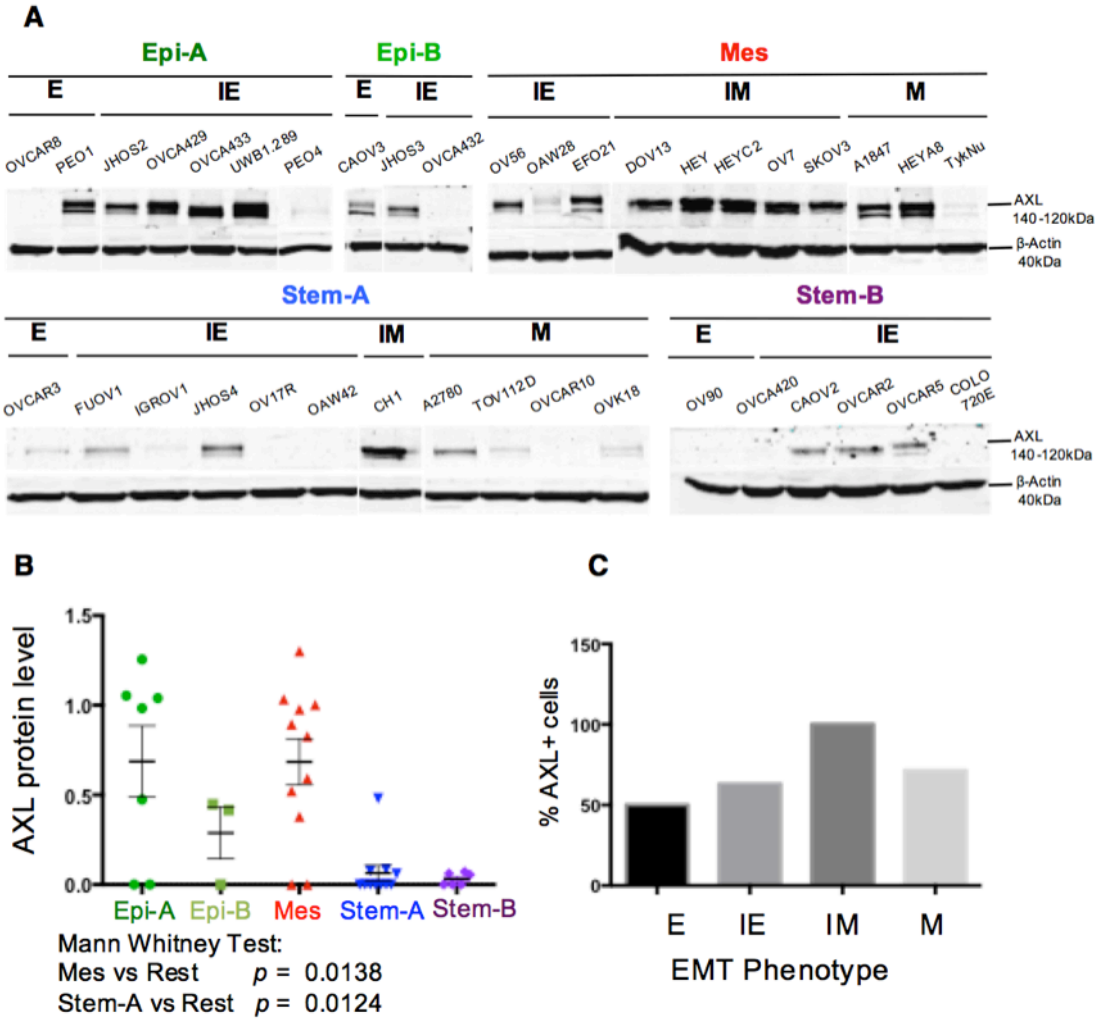


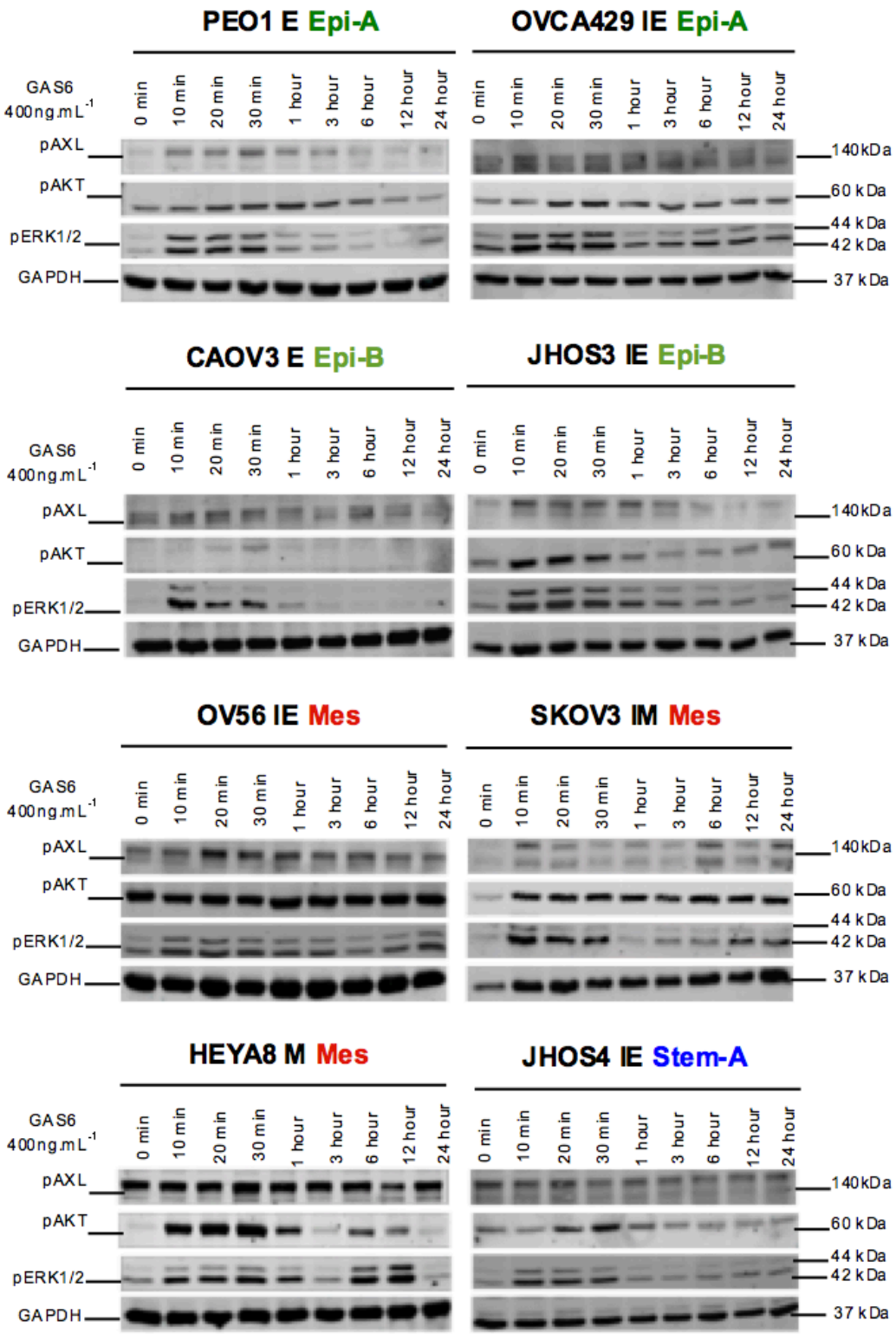
Figure 4: *AXL* expression is enriched in the Mes subtype of Ovarian Cancer.
(A) Western blots depicting AXL protein expression in 38 SGOCL EOC cell lines. Blots are representative of three experiments.
(B) Within the five molecular subtypes, scatter plots show the normalized protein AXL expression is highest in Mes and least in Stem-A. Mann Whitney Test was performed for statistical significance. Means ± SEM from three experiments.
(C) In the EMT phenotypes, the Intermediate Mesenchymal phenotype tested 100% positive with all IM cell lines expressing AXL.

3.2.3 Exclusive to Mes, AXL activation amplifies phospho-ERK signaling.

Given AXL was expressed abundantly in the worse prognosis EMT-ed Mes subtype, but also in the better prognosis epithelial Epi-A subtype, it was necessary to discern whether AXL played a different role in the context of GEMS. Cells representing the different ovarian cancer GEMS (Table 3) were stimulated with Gas6 over a time period to study the kinetics of downstream signaling by western blotting phosphorylated ERK (pERK) and phosphorylated AKT (pAKT) responses. Upon Gas6/AXL activation, Mes showed two peaks of pERK activations at early (10, 20, 30 min) and late time points (6, 12 hr) as visualized by western blotting and densitometric analysis (Figure 5 and 6A). The other subtypes such as Epi-A and Stem-A showed single pERK activation only at the early time points (10, 20, 30 min) (Figure 5 and 6A).

GEMS/ EMT Phenotype	**EPI-A**	**EPI-B**	**MES**	**STEM-A**
Epithelial	PEO1	CAOV3		
Intermediate Epithelial	OVCA429	JHOS3	OV56	JHOS4
Intermediate Mesenchymal			SKOV3	CH1
Mesenchymal			HEYA8	A2780

Table 3: Panel of 10 cell lines chosen to represent the EOC GEMS and the EMT Phenotypes to study AXL signaling kinetics.


PEO1 E Epi-A
OVCA429 IE Epi-A
CAOV3 E Epi-B
JHOS3 IE Epi-B
OV56 IE Mes
SKOV3 IM Mes
HEYA8 M Mes
JHOS4 IE Stem-A
GAS6 400ng.mL-1
0 min
10 min
20 min
30 min
1 hour
3 hour
6 hour
12 hour
24 hour
pAXL
pAKT
pERK1/2
GAPDH
140kDa
60 kDa
44 kDa
42 kDa
37 kDa

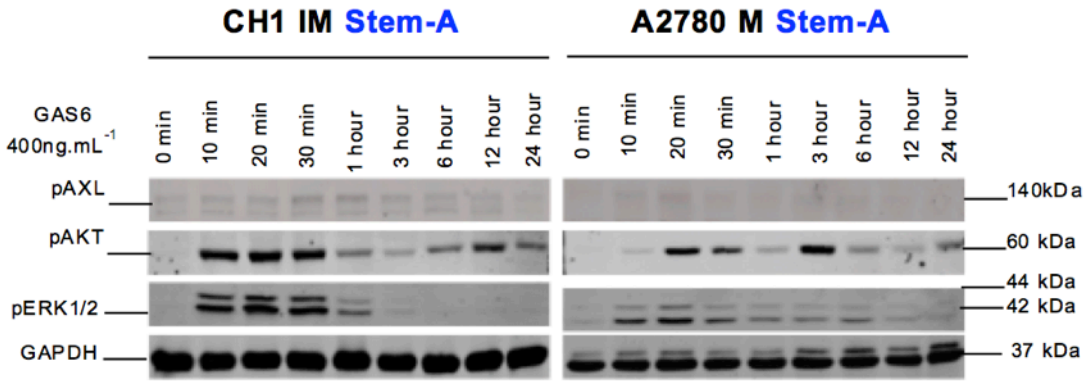


Figure 5: AXL activation has divergent consequences in downstream pERK and pAKT signaling in the context of GEMS and EMT phenotypes.
pAXL, pAKT and pERK activation pattern upon 400ng.mL^{-1} Gas6 stimulation in the 10 EOC cell lines chosen to represent the molecular heterogeneity and EMT phenotypes; PEO1 (E, Epi-A), OVCA429 (IE, Epi-A), CAOV3 (E, Epi-B), JHOS3 (IE, Epi-B), OV56 (IE, Mes), SKOV3 (IM, Mes), HEYA8 (M, Mes), JHOS4 (IE, Stem-A), CH1 (IM, Stem-A), A2780 (M, Stem-A). GAPDH was used as a loading control. Blots are representative of three experiments.

Within each GEMS, the EMT phenotypic classification further dictated the pattern of pAKT signaling (Figure 5 and 6B). In GEMS with single pERK peak such as Epi-A, Epi-B, and Stem-A, the pAKT activation was found to be a single peak in E or IE phenotypes. However, in IM or M phenotypes, the pAKT activation occurred in dual peaks (Figure 5 and 6B). For Mes, the pAKT activation persisted from the early to the late time points regardless of the EMT phenotype (Figure 5 and 6B). The modulation of the pAKT response by the EMT phenotype, as well as the recurrence of the pERK signal in Mes, suggests that the GEMS and EMT spectrum regulate duration and propagation of signal downstream of Gas6/AXL axis. Also, in order to ascertain the specificity of Gas6 in activating AXL, SKOV3 cells were transfected with siRNA to silence AXL and then stimulated with Gas6 (Figure 7). AXL silencing prevented activation of ERK even upon addition of Gas6, confirming that Gas6 activates intracellular signaling exclusively via AXL (Figure 7).

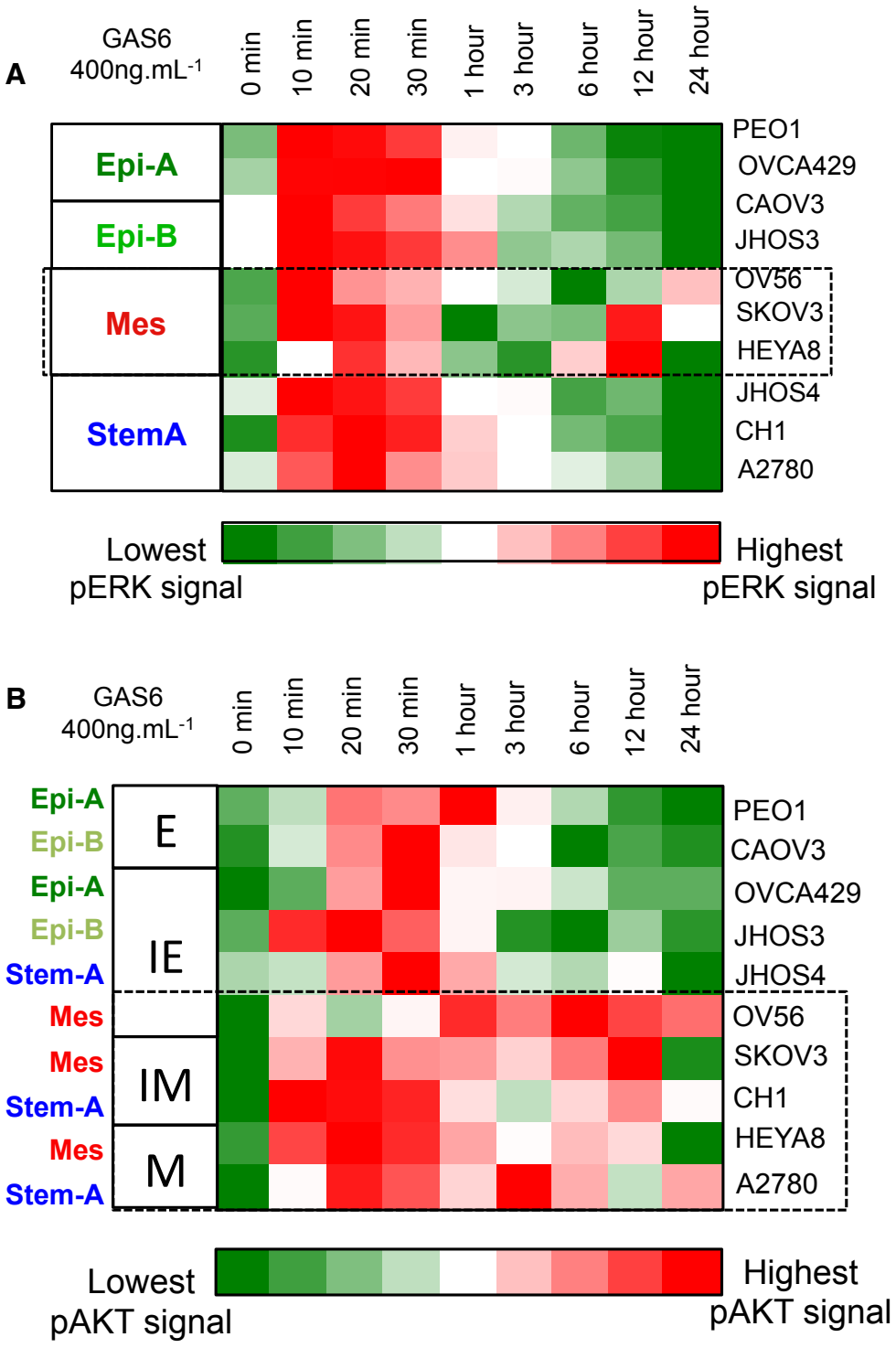


Figure 6: Mes GEMS delineates recurrent pERK response, while EMT phenotype modulates pAKT response.
Heat map based on normalized densitometry analysis of western blots representing (A) pERK and (B) pAKT response upon Gas6 stimulation of AXL in the 10 cell lines. Heatmaps are representative of densitometry from three experiments, wherein pAKT and pERK were normalised to total AKT and total ERK respectively, and then further normalised to loading control GAPDH.

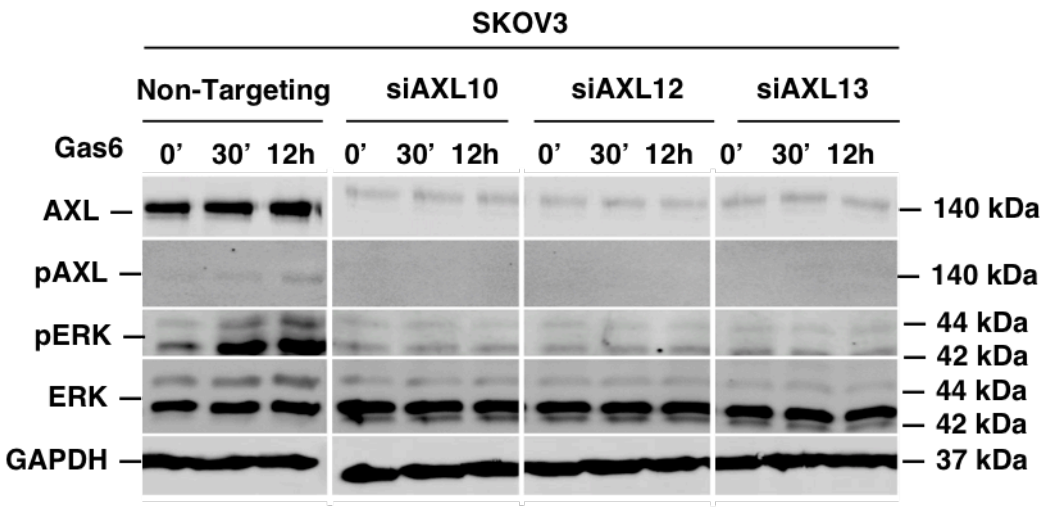


Figure 7: Silencing AXL prevents Gas6/AXL mediated phosphorylation ERK
Western blotting SKOV3 transfected with Non-Targeting siRNA, and three siAXL sequences (siAXL10, siAXL12, siAXL13) shows reduction in AXL protein levels. Stimulation with Gas6 reveals that in AXL silenced cells there is no phosphorylation of AXL or ERK at the early time point 30 minutes or late time point 12 hours, suggesting Gas6 activated intracellular signaling exclusively through AXL. Blots are representative of three experiments.

3.2.4 GEMS-specific AXL signaling schema has divergent consequences in cell proliferation and motility.

Since changes in the temporal duration of ERK signaling have been shown to elicit diverse biological outcomes[162-165], the recurrence of the pERK signal upon Gas6/AXL activation suggests that the temporal duration of the signal is sustained in Mes, and that this might affect relevant downstream biological functions. AXL signaling is known to sustain cancer cell survival[157,166]. A moderate increment in cell proliferation was observed upon Gas6 stimulation in all EOC cell lines without specific differences between GEMS or EMT phenotypes (Figure 8). Proliferation was assesed using the WST1 calorimetric assay.

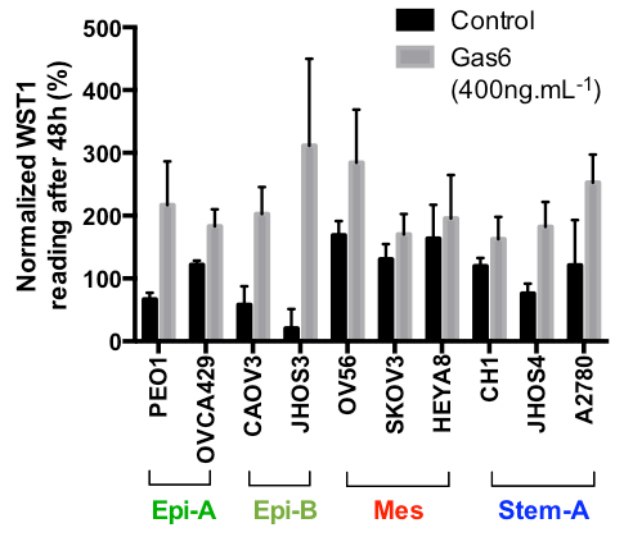


Figure 8: Gas6/AXL activation marginally increases cell proliferation in all EOC cell lines irrespective of GEMS status or EMT phenotype.
For all EOC cell lines, WST1 calorimetric proliferation assay showed marginal increase in proliferation when treated with Gas6, as compared to no treatment control, over a 48 hour period. Readings were normalized to 0 hour reading. Student's t tests was performed to analyse significance, with no Gas6 stimulated condition differening significantly from its paired untreated control. Means ± SEM from three experiments.

AXL signaling is also known to enhance cancer cell invasion and metastasis[157,167,168]. We utilized single cell tracking to monitor cell motility by measuring several kinetic parameters such as displacement, velocity, speed, and directional persistence. Upon Gas6/AXL stimulation, Mes cells showed significant increase in all the kinetic parameters, while the other GEMS cells showed minimal changes (Figure 9A-D). Mes cell lines showed a significant enhancement in displacement upon Gas6 stimulation, with a 10.51% increase in OV56 (p=0.031), 60.41% increase in SKOV3 (p=0.009), and 43.61% increase in HEYA8 (p=0.007). On the contrary, Epi-A cell lines showed minimal changes in displacement with a 2.56% increase in PEO1 (p=0.76), and an 8.32% decrease in OVCA429 (p=0.15), (Figure 9A).

In gap closure migration assays, Mes showed an increase in closure rates after Gas6 stimulation (Figure 10A and 10B). In SKOV3, the percentage of gap closure increased from 23.7% to 48.35% (p=0.046); in HEYA8, the percentage of gap closure increased from 61.81% to 83.33% (p=0.027). Similar to the single cell motility analysis, Epi-A cell lines such as PEO1 and OVCA429 showed minimal changes in closure rates after Gas6 stimulation (Figure 10A and 10B).

Taken together, Gas6/AXL activation has divergent control in downstream signaling and functions that are GEMS-specific in ovarian cancer. In Mes, it results in a recurrent sustained pERK response, which translates to the increase in both proliferation and cell motility. However, in Epi-A, Gas6/AXL activation leads to a single and transient pERK response that only results in the increase in proliferation.

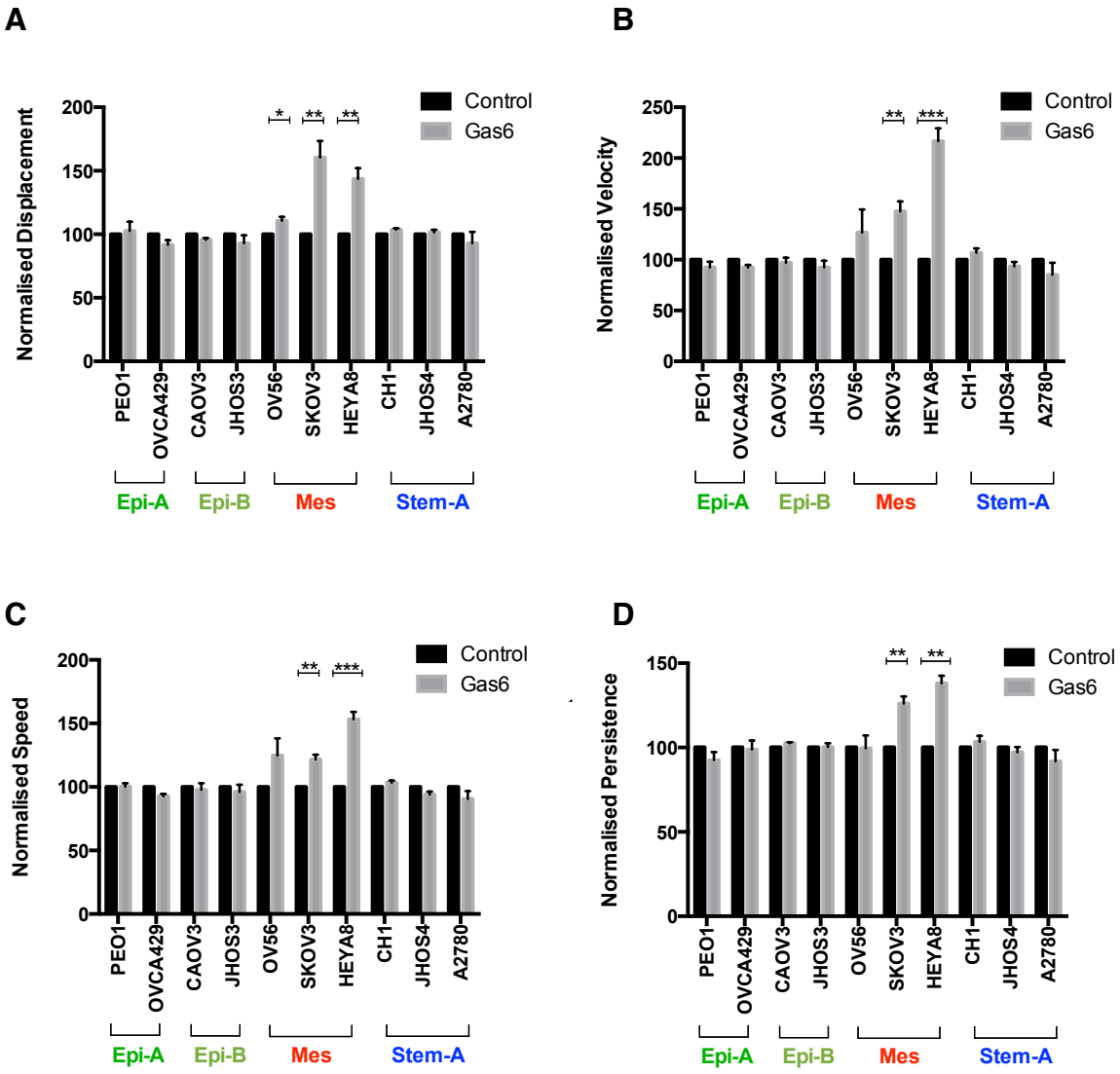


Figure 9: Gas6/AXL activation increases single cell motility exclusively in Mes. Specific to Mes, single cell motility parameters increase upon Gas6 activation of AXL compared to unstimulated control. Single cell tracking analysis was done on ImageJ using Trackmate, following overnight capture of cell tracks on Leica SP5 confocal at 10 minutes intervals and kinetic parameters are represented by (A) displacement, (B) velocity, (C) speed of locomotion, and (D) directional persistence. Means ± SEM from three experiments. Paired 2-tailed Student's t-tests were used to determine statistical significance * $p < 0.05$, ** $p < 0.01$, *** $p < 0.001$.

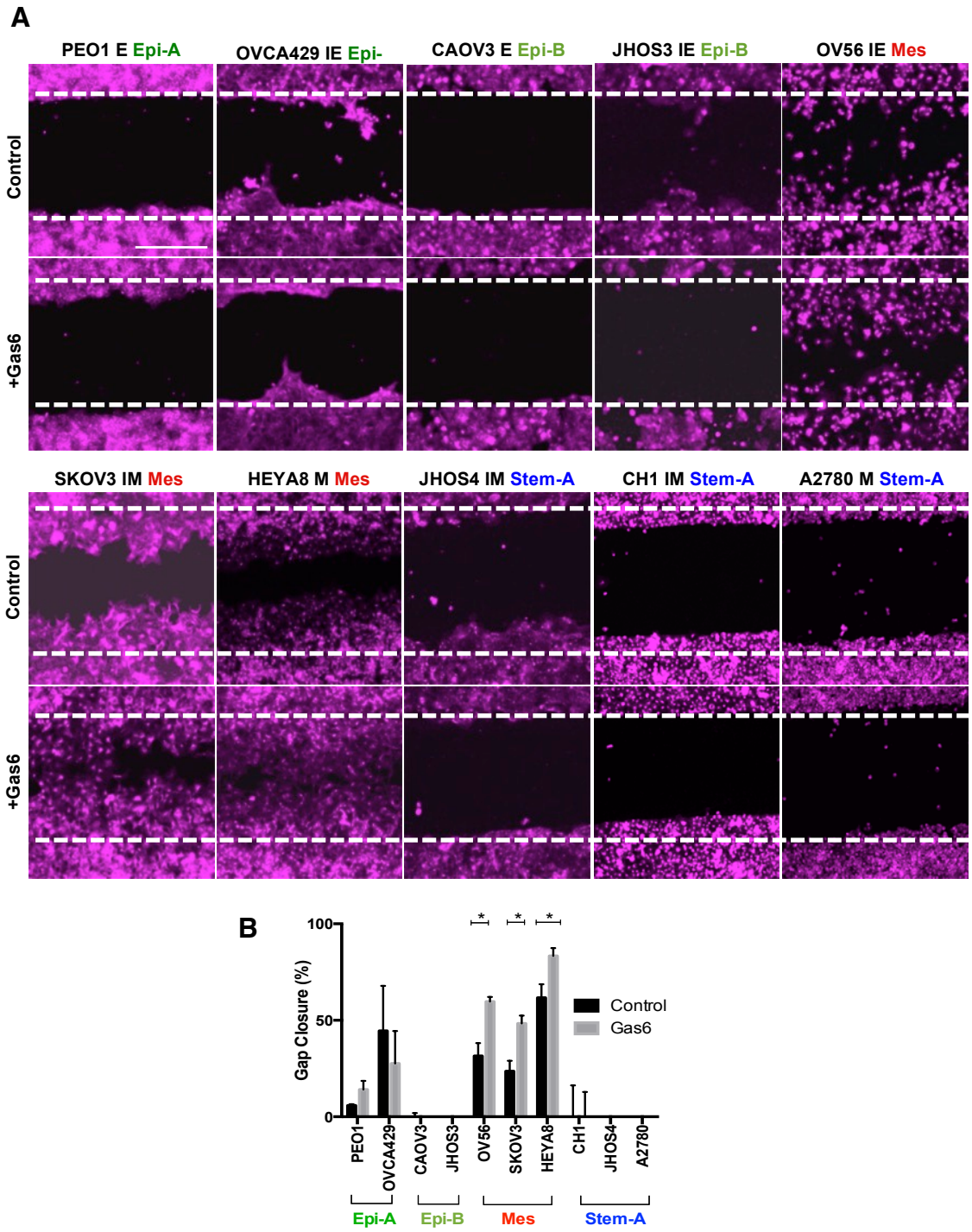


Figure 10: Gas6/AXL activation accelerates gap closure in Mes subtype.
(A) Exclusive to Mes subtype, collective cell migration improves upon AXL activation, compared to unstimulated control. Gap closure analysis was done on ImageJ, following overnight capture of gap closure on Leica SP5 confocal at 10 minutes intervals. Dashed white lines represent initial boundary and scale bars represent 200µm. Images representative of three experiments.
(B) Quantitation of Gap closure at 12 hours. Means ± SEM from three experiments. Paired 2-tailed Student's t-tests were used to determine statistical significance * $p < 0.05$, ** $p < 0.01$, *** $p < 0.001$.

3.2.5 GEMS-specific AXL activation reveals an extensive RTK crosstalk network in Mes.

In order to understand the signaling circuitry that is connected to the recurrent pERK response specific to Mes, a Reverse Phase Protein Array (RPPA) experiment was carried out using a Mes cell line (SKOV3) and an Epi-A cell line (PEO1) treated with Gas6 at 30 minutes and 12 hours to evaluate the early and late response, respectively. SKOV3 displayed elevated levels of phosphorylated EGFR (pEGFR), phosphorylated HER2 (pHER2), and phosphorylated cMET (pMET) at both 30 minutes and 12 hours post-Gas6 stimulation compared to the 0 min control (Figure 11A). This pattern was parallel to the higher and sustained pAXL signals observed previously by western blotting (Figure 5). This suggested that there were crosstalks between AXL and other RTKs in Mes. However, this RTK crosstalk phenomenon was completely deficient in the Epi-A PEO1 system, and no significant transactivation of EGFR, HER2, or cMET was detected post Gas6 treatment (Figure 11A).

The RPPA results were validated by western blotting and extended to other cell lines OVCA429 (Epi-A) and HEYA8 (Mes) (Figure 11B). An *in situ* proximity ligation assay, DUOLink, was carried out to confirm if the crosstalks between AXL and these RTKs were mediated via protein-protein interactions. Upon Gas6 stimulation in Mes cell lines SKOV3 and HEYA8, DUOLink showed signals for interactions between AXL and the phosphorylated RTKs pMET, pHER2 and pEGFR, respectively (Figure 12A and 12B). This transactivation was not seen at the resting state when Gas6 is absent (Figure 12A and 12B), and this indicated that ligand-activated AXL might trigger the phosphorylation of other RTKs via receptor clustering. This phenomenon of AXL-RTK clustering was not observed in Epi-A lines PEO1 and OVCA429 (Figure 12A and 12B). All chosen cell lines were positive for cMET, HER2, and EGFR expression (Figure 12C).

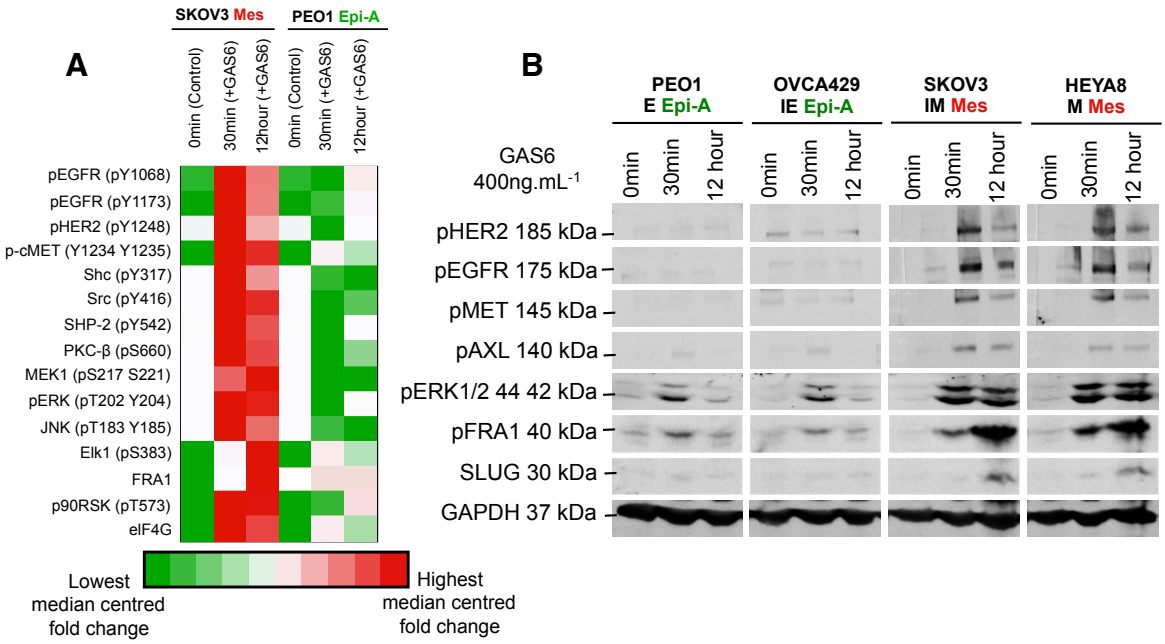


Figure 11: AXL in enmeshed in an RTK network in the Mes subtype.
(A) RPPA data showing phospho-RTK and downstream signaling moieties activated by Gas6/AXL stimulation in SKOV3 (Mes) and PEO-1 (Epi-A). Following serum starvation, cells were treated with Gas6 for 30 minutes or 12 hours, while control cells were unstimulated. Samples were run through the MD Anderson RPPA Core. Data is represented as Log2 normalized and median centred.
(B) Western Blotting of EOC cell lines PEO1, OVCA429 (Epi-A) and SKOV3, HEYA8 (Mes) upon AXL activation, for pAXL, pHER2, pEGFR, pMET, and downstream signaling moieties pERK1/2, FRA1 and the EMT transcription factor SLUG. Blots are representative of three experiments.

Downstream of the RTK network, adapter proteins such as Shc, Src and Shp2 and signaling proteins MEK1, ERK, and JNK along the Mitogen Activated Protein Kinase (MAPK) cascade displayed elevated phosphorylation levels upon Gas6 stimulation in SKOV3 but not in PEO1 (Figure 11A). This results into the phosphorylation of sustained response proteins such as ELK1, p90RSK, and FRA1 at 12 h in SKOV3, which was absent in PEO1 (Figure 11A). The FRA1 induction alongside with the sustained ERK activation were confirmed by western blot (Figure 11B). Sustained activation of ERK is known to stabilize FRA1[169] whose activity has been linked to the induction of EMT transcription factors ZEB1[169,170] and SLUG[171], and consequently, increased motility[172]. The SLUG induction in Mes was confirmed by western blotting (Figure 11B).

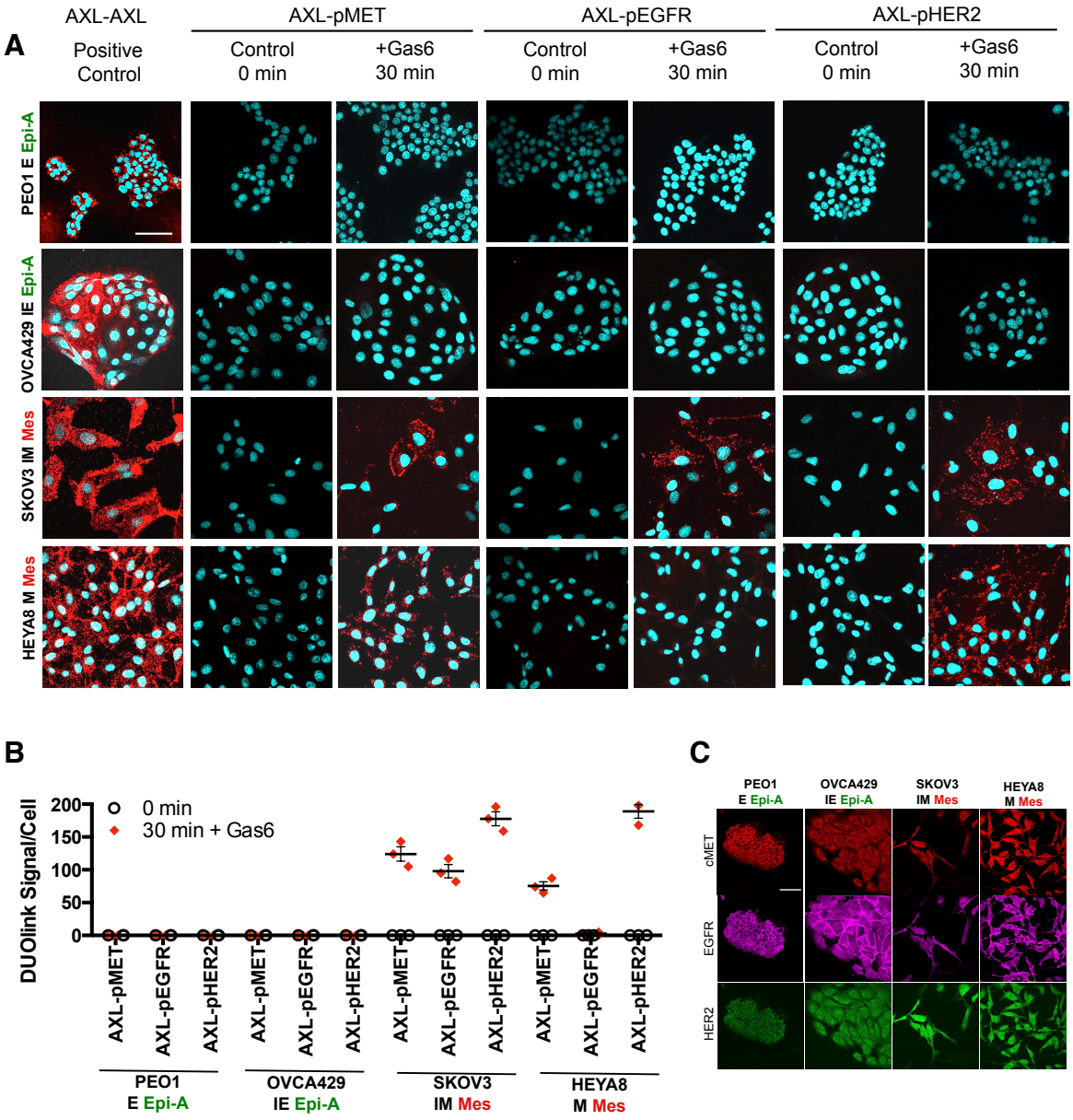


Figure 12: In the Mes subtype, AXL activated by Gas6, co-clusters with pMET, pEGFR and pHER2.

(A) In situ proximity ligation assay reveals cMET, HER2, EGFR, interactions with AXL activated by Gas6 in Mes subtype cell lines SKOV3 and HEYA8, but not in Epi-A subtype cell lines PEO1 and OVCA429. As a positive control, AXL-AXL interactions with visualized with two different antibodies targeting the c-terminus and n-terminus of AXL. Images are representative of three experiments.

(B) DUOLink signals were quantified using ImageJ Software and normalized to nuclei count. Means ± SEM from three experiments. Paired 2-tailed Student's t-tests were used to determine statistical significance * $p < 0.05$, ** $p < 0.01$, *** $p < 0.001$.

(C) Immunofluorescence staining depicting that all cell lines chosen were positive for cMET, HER2, and EGFR. Scale bars represent 50µm.

The MEK inhibitor PD0325901[173] prevented phosphorylation of the MEK/ERK axis in Epi-A and Mes, and consequently prevented induction of FRA1 and SLUG in Mes (Figure 13). Furthermore, MEK inhibition prevented Gas6/AXL mediated motility induction in Mes (Figure 14A-D), suggesting that pAXL signaling relies on the MEK/ERK cascade to induce motility.

Taken together, our data explains that the AXL-RTK network and the signaling cascade responsible for the increased cell motility in Mes, are deficient in other GEMS such as Epi-A. The Mes subtype is wired with a unique signaling crosstalk network that contributes to its biological functions.

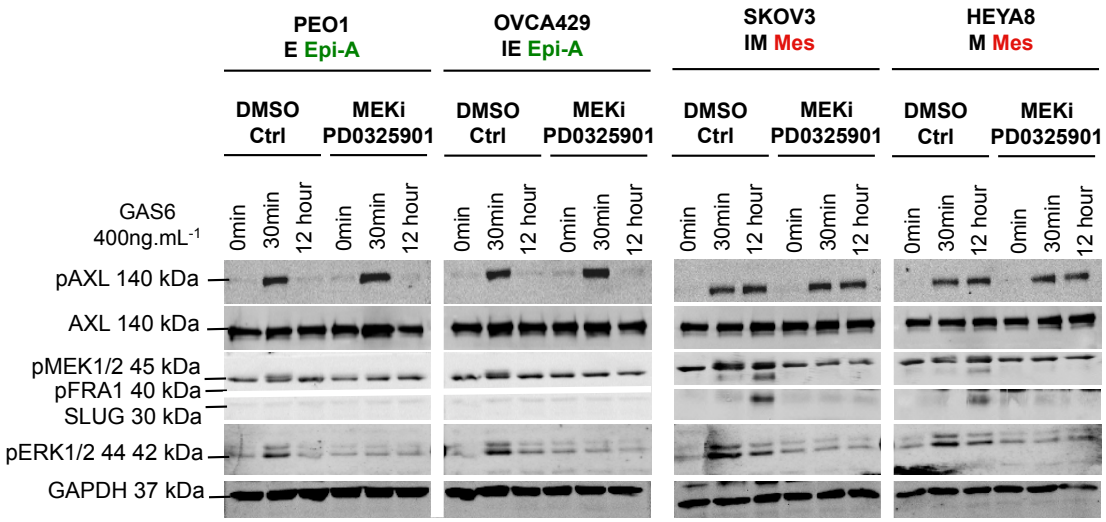


Figure 13: MEK inhibition prevents signaling downstream of the Gas6/AXL axis.
Western blots showing effect of MEK inhibitor PD0325901, on phosphorylation of both MEK and ERK, downstream of AXL/Gas6. In Mes, inhibition of MEK further prevented induction of pFRA1 and EMT transcription factor SLUG, confirming that the pAXL signal is transmitted via the MEK/ERK axis to induce motility related genes. The cells were pre incubated with with either no drug (DMSO only control) or 2µM PD0325901 for 4 hours and then stimulated with Gas6. Blots are representative of three experiments.

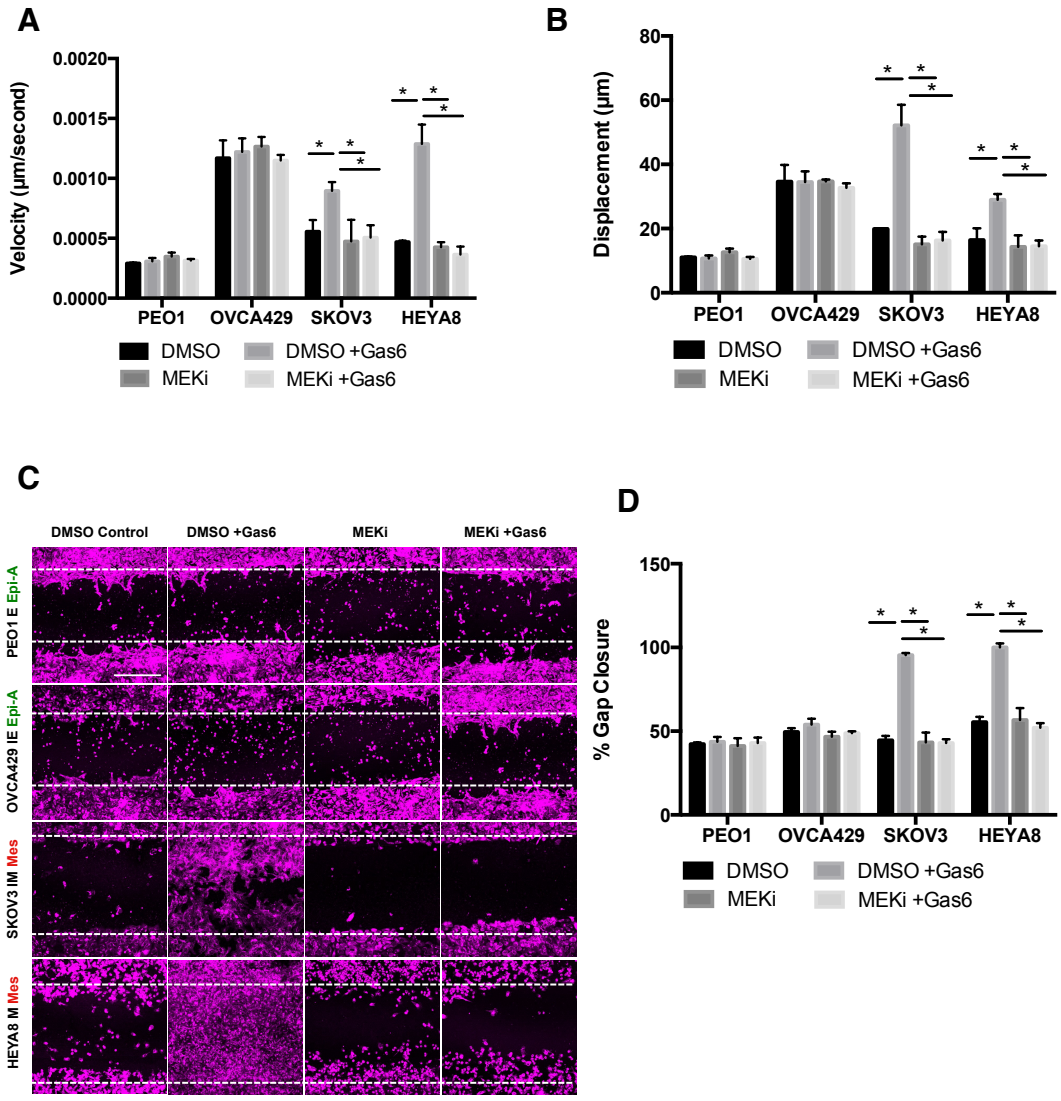


Figure 14: Inhibition of MEK prevents Gas6/AXL induced cell motility.
MEK inhibition by PD0325901 prevents Gas6/AXL induced motility in Mes as measured by kinetic parameters such as (A) velocity, (B) displacement and (C,D) Gap closure rates. In (C) Dashed white lines represent initial boundary and scale bars represent 200µm. For the motility assays, cells were pre incubated with with either no drug (DMSO only control) or 2µM PD0325901 for 4 hours and then stimulated with Gas6.
Means ± SEM from three experiments. Paired 2-tailed Student's t-tests were used to determine statistical significance * $p < 0.05$, ** $p < 0.01$, *** $p < 0.001$. Images are representative of three experiments.

3.2.6 The Mes subtype is more sensitive to the AXL inhibitor R428.

R428, an AXL-selective inhibitor, has been shown to block tumor dissemination and prolong survival in mouse models of metastatic breast cancer[112]. To test whether R428 causes different effects among ovarian cancer GEMS, the 10 previously selected EOC cell lines were treated with R428 for 48 h to determine the 50% growth inhibition (GI50) concentrations. Mes cell lines had a significantly lower mean GI50 of 2.91 µM compared to the other subtypes with a mean GI50 of 9.38 µM (p=0.016) (Figure 15). Since Mes has a unique Gas6/AXL signaling network, we explored the effect of R428 on this signaling network in comparison to Epi-A. Two Epi-A lines (PEO1, OVCA429) and two Mes lines (SKOV3, HEYA8) were chosen and pre-incubated with 0 µM (DMSO control), 2.91 µM ($GI50^{Mes}$), and 9.38 µM ($GI50^{Non\text{-}Mes}$) of R428. From western blots, the early phase pERK activation in Epi-A was only inhibited at the higher concentration of R428 at 9.38 µM ($GI50^{Non\text{-}Mes}$), while the early and late phase pERK peaks in Mes were effectively inhibited at the lower concentration of 2.91 µM ($GI50^{Mes}$) (Figure 16).

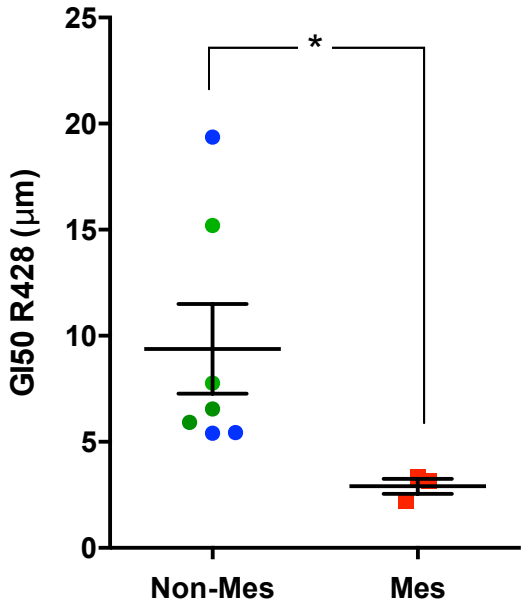


Figure 15: Mes subtype is more sensitive to AXL inhibitior R428.
The mean GI50 of Mes subtype cell lines were significantly lower at 2.91µM compared to the mean GI50 of 9.38µM in the non-Mes subtype cell lines, (p = 0.0167, Mann-Whitney U Test). GI50 values were calculated by assessing 50% growth inhibition using cell titer MTS calorimetric cell proliferation assay. Means ± SEM from three experiments.

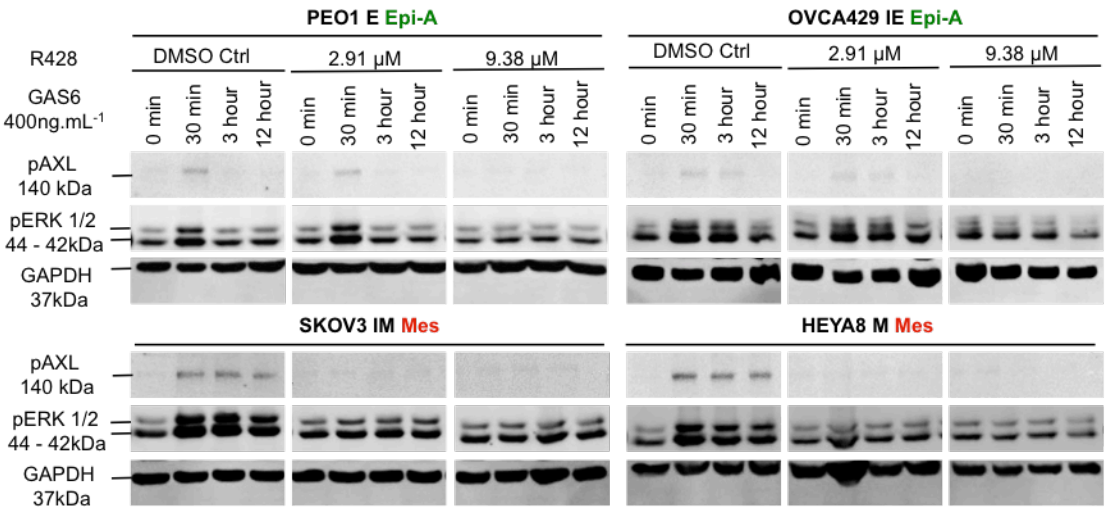


Figure 16: AXL inhibition curtails signaling at lower doses in Mes.
Western Blotting of EOC cell lines PEO1, OVCA429 (Epi-A) and SKOV3, HEYA8 (Mes) for pAXL and pERK, shows signaling inhibition at lower doses of R428 in Mes subtype preferentially. The cells were pre incubated with with either no drug (DMSO only control), 2.91 µM R428 ($GI50^{Mes}$) or 9.38 µM R428 ($GI50^{Non\text{-}Mes}$) for an hour and stimulated with 400ng.mL^{-1} Gas6 for 0 minutes, 30 minutes, 3 hours and 12 hours. Blots are representative of three experiments.

In addition, these four cell lines also represent different phenotypes along the EMT spectrum (PEO1: E; OVCA429: IE; SKOV3: IM; HEYA8: M). From the phenotypic perspective as evaluated by immunostaining, lower R428 concentration of 2.91 µM ($GI50^{Mes}$) had no effect on the pERK and pAXL activations in PEO1 (E), while OVCA429 (IE) showed a moderate reduction in pERK and pAXL signaling intensities by 57.83% and 33.62% respectively (Figure 17A and 17B). The SKOV3 (IM) line showed a drastic decrease of 79.96% in pERK signaling and 55.12% in pAXL signaling at 2.91 µM ($GI50^{Mes}$), while the HEYA8 (M) line showed complete inhibition at 2.91 µM ($GI50^{Mes}$) (Figure 17A and 17B). These results corroborated with the functional consequences of signal amplification in Mes upon AXL activation. Mes shows an addiction to the Gas6/AXL axis and is therefore very sensitive to AXL inhibition.

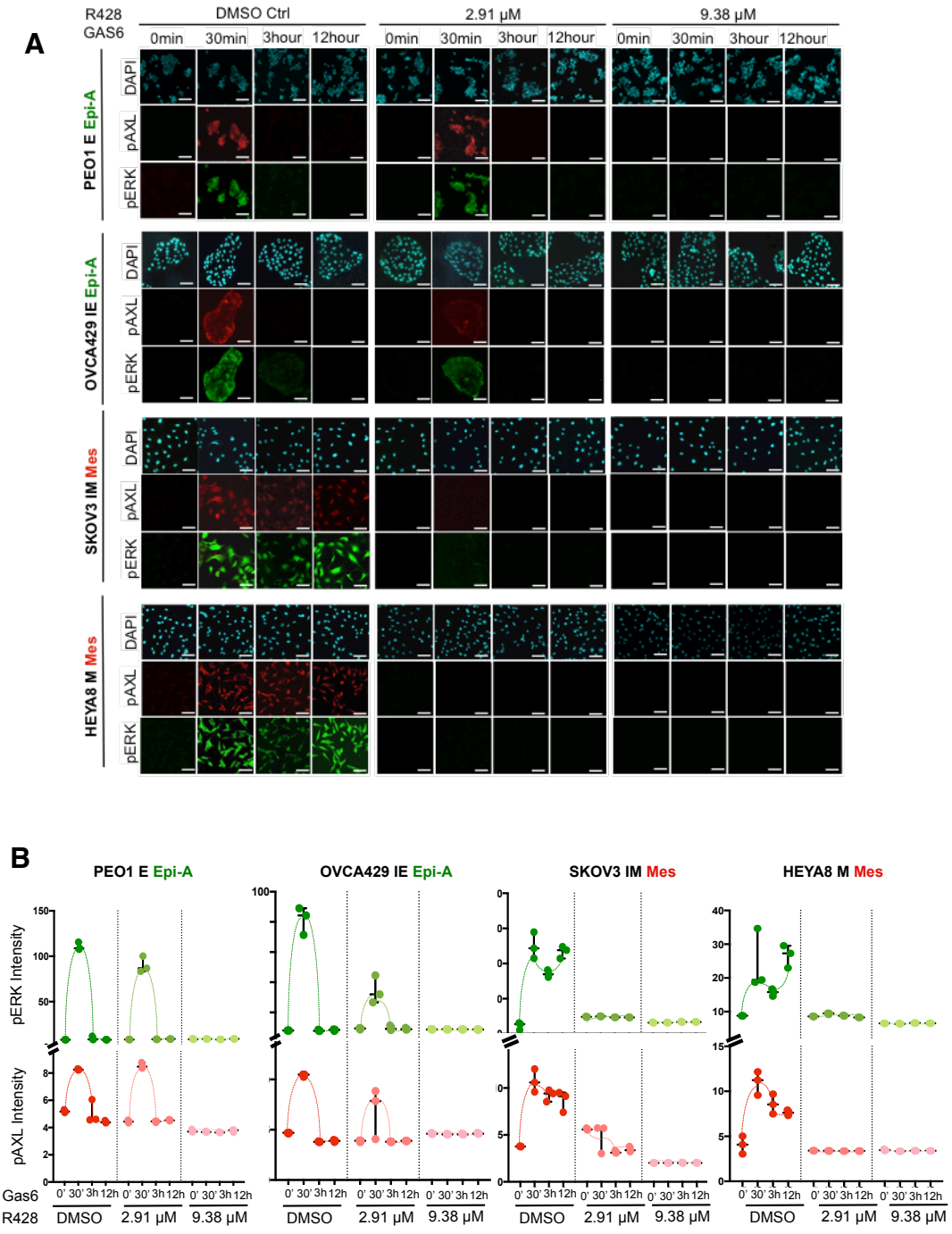


Figure 17: EOC cell lines are sensitized along an EMT gradient to AXL inhibition.

(A) Immunofluoresence staining of PEO1 (E), OVCA429 (IE), and SKOV3 (IM), HEYA8 (M), for pAXL and pERK, reveals preferential signaling inhibition at lower doses of R428 in EMTed systems. The cells were pre incubated with with either no drug (DMSO only control), 2.91µM R428 (GI50Mes) or 9.38µM R428 (GI50Non-Mes) for an hour and stimulated with 400ng.mL^{-1} Gas6 for 0 minutes, 30 minutes, 3 hours and 12 hours. Scale bars represent 50µm. Images are representative of three experiments.

(B) Immunostaining intensity was quantified using ImageJ software and normalized to nuclear area stained by DAPI. Means ± SEM from three experiments.

3.2.7 AXL inhibition attenuates motility and *in ovo* tumor growth in Mes.

To analyze the functional consequences following AXL signaling inhibition, PEO1, OVCA429, SKOV3, and HEYA8 were pre-incubated with R428 and tracked for motility. Similar to the pERK and pAXL signaling inhibition, Epi-A cell lines showed motility inhibition only at the higher concentration of R428, while Mes cell lines showed effective inhibition at the lower concentration (Figure 18A-D).

For example, the velocity of locomotion was unchanged between DMSO control (0.082 μm.sec^{-1}) and 2.91 μM (GI50^{Mes}) of R428 in PEO1 (0.081 μm.sec^{-1}, p = 0.86); but reduced at 9.38 μM (GI50$^{Non\text{-}Mes}$) (0.064 μm.sec^{-1}, p = 0.01). In OVCA429, the velocity of locomotion was similar between DMSO control (0.176 μm.sec^{-1}) and 2.91 μM (GI50^{Mes}) of R428 (0.167 μm.sec^{-1}, p = 0.46); however reduced at 9.38 μM (GI50$^{Non\text{-}Mes}$), (0.116 μm.sec^{-1}, p = 0.02).

Compared to DMSO control (0.128 μm.sec^{-1}), SKOV3 cells showed lowered velocity of locomotion at both 2.91 μM (GI50^{Mes}) and 9.38 μM (GI50$^{Non\text{-}Mes}$) of R428 (0.039 μm.sec^{-1}, p = 0.01; 0.041 μm.sec^{-1}, p = 0.01). The HEYA8 cells showed a similar trend with its velocity (0.227 μm.sec^{-1}) being inhibited at 2.91 μM (GI50^{Mes}) as well as at 9.38 μM (GI50$^{Non\text{-}Mes}$); (0.051 μm.sec^{-1}, p = 0.01; and 0.063 μm.sec^{-1}, p = 0.01, respectively).

Other kinetic parameters such as displacement, speed of locomotion, and directional persistence showed comparable trends upon R428 inhibition in the Epi-A and Mes GEMS (Figures 18A-D).

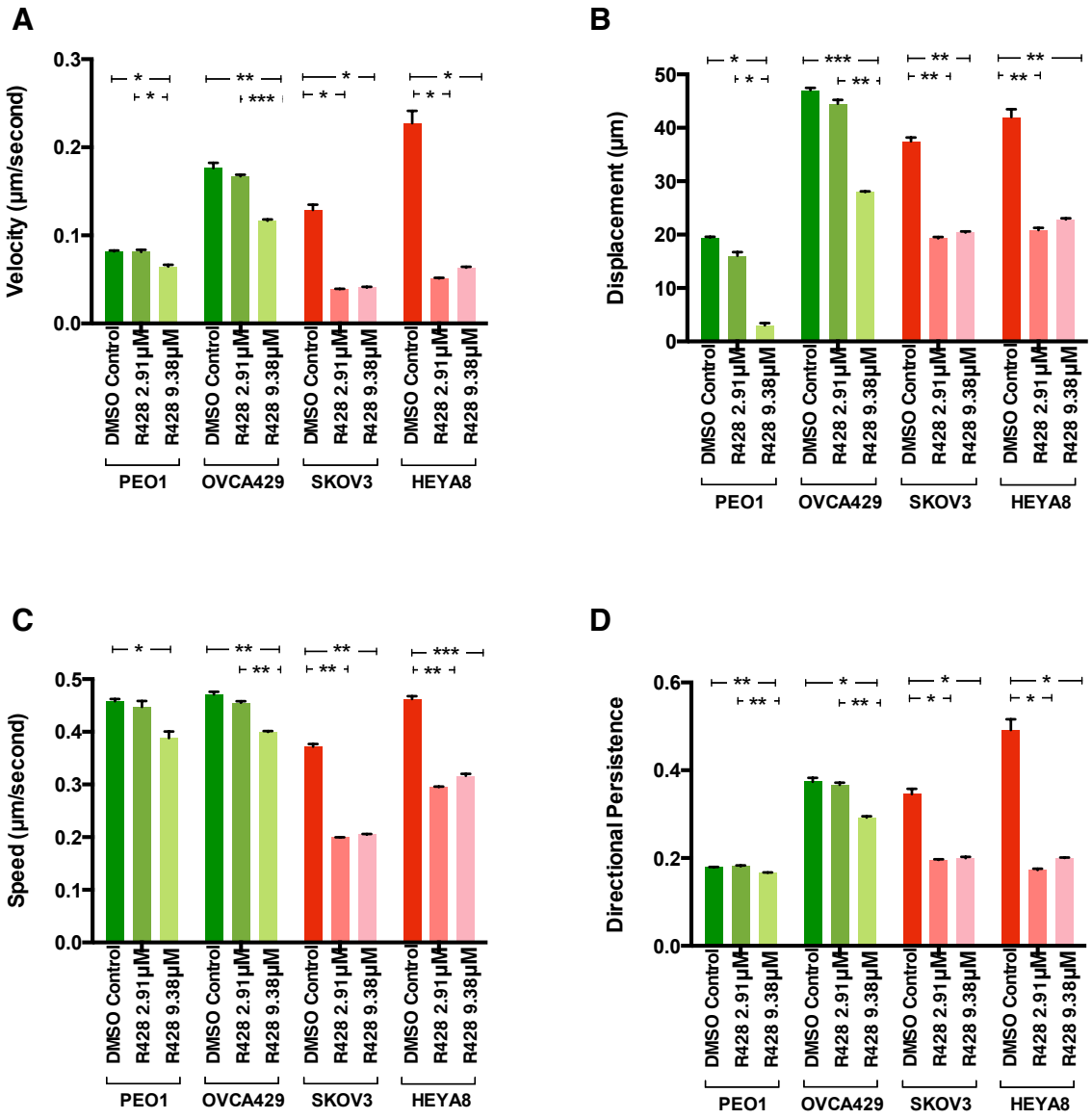


Figure 18: AXL inhibitior R428 reduces cell motility at lower doses in Mes.
Single cell motility reduced at lower doses of 2.91µM R428 ($GI50^{Mes}$) in Mes, and only at higher doses of 9.38µM R428 ($GI50^{Non\text{-}Mes}$) in Epi-A. Cells were pre incubated with with either no drug (DMSO only control), 2.91µM R428 ($GI50^{Mes}$) or 9.38µM R428 ($GI50^{Non\text{-}Mes}$) for an hour and stimulated with 400ng.mL^{-1} Gas6 and cell motility was tracked over 12 hours. Single cell motility analysis was done on ImageJ Trackmate to obtain kinetic parameters (A) Velocity, (B) Displacement, (C) Speed, (D) Directional Persistence.
Means ± SEM from three experiments. Paired 2-tailed Student's t-tests were used to determine statistical significance * $p < 0.05$, ** $p < 0.01$, *** $p < 0.001$. Images are representative of three experiments.

To translate the AXL signaling inhibition and functional repression to a biologically relevant system, the four cell lines were embedded in Matrigel and deposited on top of the chick chorion allantoic membrane (CAM). PEO1, OVCA429, SKOV3, HEYA8 were pre-incubated with R428 and allowed to form tumors in the CAM. The *in ovo* findings substantiated the *in vitro* results, with the HEYA8 and SKOV3 forming large tumors, which were significantly suppressed at 2.91 µM ($GI50^{Mes}$) as well as 9.38 µM ($GI50^{Non\text{-}Mes}$) of R428 (Figure 19A). Unlike its Mes counterparts, tumor formation in PEO1 was not inhibited at 2.91 µM ($GI50^{Mes}$), but only at 9.38 µM ($GI50^{Non\text{-}Mes}$) (Figure 19A and 19B). The OVCA429 line was proven to be non-tumorigenic in the CAM system. Consistent with the *in vitro* GI50 results, the Mes lines SKOV3 and HEYA8 show higher sensitivity to R428 in the attenuation of tumor formation and tumor growth. Taken together, these results indicated the preferential application of inhibiting AXL in the Mes subtype of EOC, in which significant sensitization to R428 can be achieved.

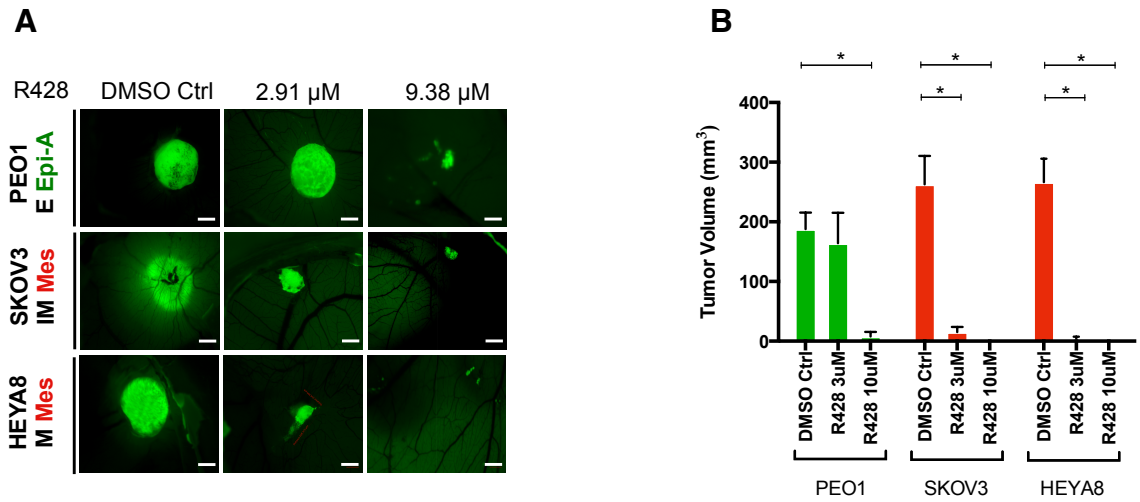


Figure 19: AXL inhibition preferentially sensitizes *in ovo* tumor growth in Mes.
(A) Chick Chorion Allantoic Membrane (CAM) model showed inhibition of *in ovo* tumor growth at lower doses of R428 in Mes, while Epi-A showed inhibition only at higher doses. Scale bars represent 2000µm. (B) For tumor volume, the mean radius (r) of the fluorescent tumor was calculated relative to background, and the tumor was assumed to be a spheroid with volume $4\pi r^3/3$.
Means ± SEM from two experiments. Unpaired 2-tailed Student's t-tests were used to determine statistical significance * $p < 0.05$, ** $p < 0.01$, *** $p < 0.001$. Images are representative of two experiments.

3.2.8 AXL governs the sequential phenotypic and functional transitions of EMT.

Apart from pharmacological inhibition of AXL, shRNA mediated silencing of AXL was also utilized to better understand its functional role in ovarian cancer. Two shRNAs (shAXL#40 and shAXL#41) were used to knockdown AXL, and a non-targeting shRNA (shLuciferase) was used as a control, in Epi-A OVCA429 and Mes SKOV3 cell lines. Over 90% reduction in total AXL protein expression was achieved by both shRNAs (Figure 20A). Phase contrast images revealed that in shAXL clones, OVCA429 formed more compact colonies and SKOV3 reverted from a fibroblastic to a loosely defined colony structure (Figure 20B). Immunofluorescence staining revealed that shAXL OVCA429 cells increased the intensity of E-cadherin staining at the cell-cell junctions together with a complete restoration of cytoplasmic β–catenin to the junctions (Figure 20C). The shAXL SKOV3 cells showed re-expression of E-cadherin, which was mostly cytoplasmic with partial restoration to the cell-cell junctions (Figure 20C). These data suggested that AXL knockdown causes a partial reversal along the EMT spectrum. The reversal in OVCA429 is from an IE state to a more epithelial state, while the SKOV3 reverts from an IM state to an IE state. This implies the extent of EMT reversal upon AXL knockdown is sequential and depends on the cell line's original EMT state (Figure 20D). It is of interest to note that while the Mes subtype is indeed more sensitive to pharmacological inhibition of AXL at lower doses of R428, shRNA mediated AXL silencing did not induce differential survival benefits, but induced EMT reversal in both Epi-A and Mes.

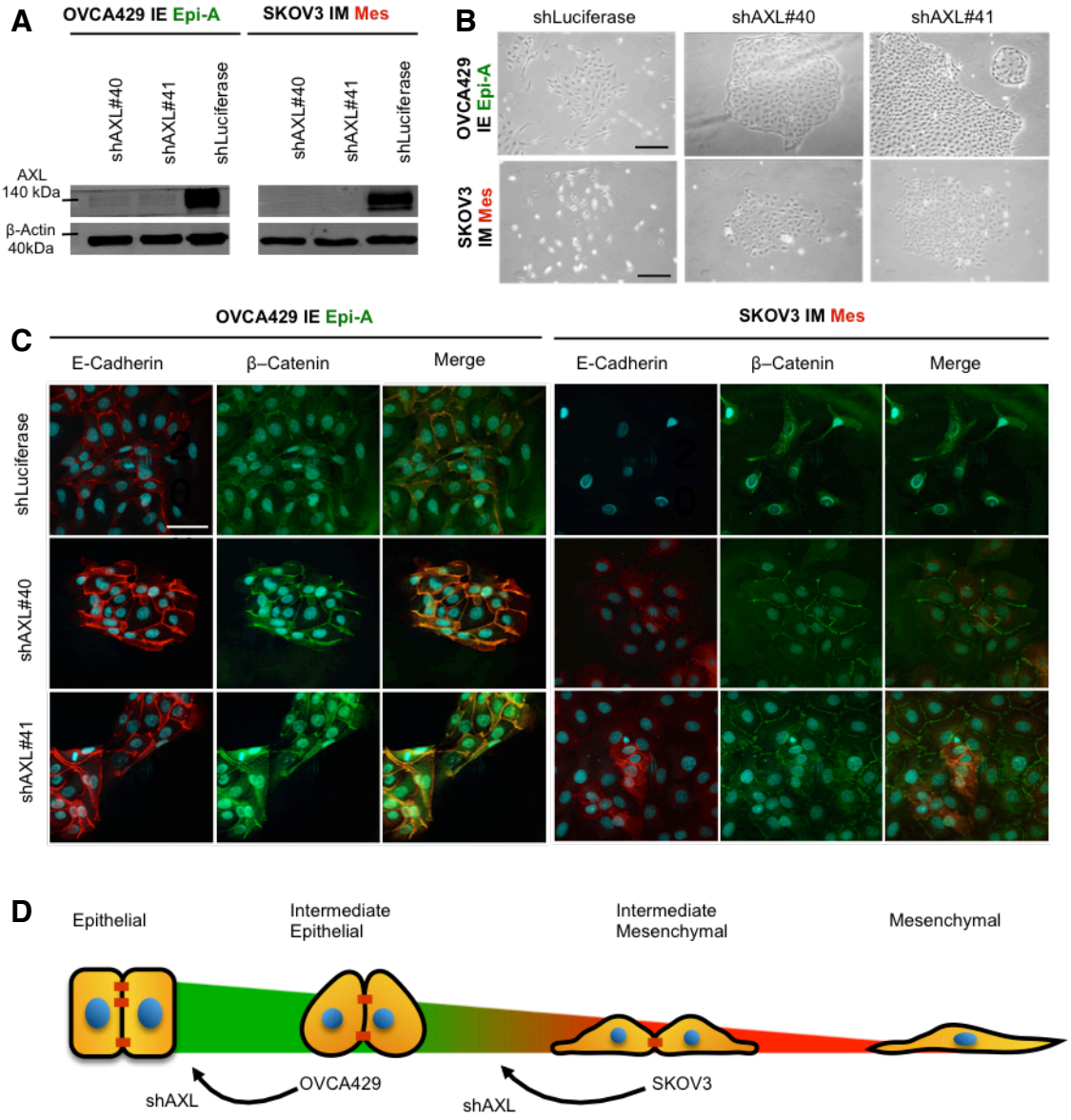


Figure 20: AXL governs the sequential phenotypic transitions of EMT.
(A) Western blot showing AXL knockdown using two different shRNAs in OVCA429 and SKOV3 cell lines along with a non-targeting shRNA control (shLuciferase control). Blots are representative of three experiments.
(B) Phase contrast images showing colony compaction upon AXL knockdown in OVCA429 and SKOV3. Scale bar represents 200µm. Images are representative of three experiments.
(C) Immunostaining depicting increased junctional E-cadherin and β-catenin in OVCA429 upon AXL knockdown; and re-expression of cytoplasmic E-cadherin and partial restoration of β-catenin to junctions in SKOV3 shAXL clones. Scale bar represents 50µm. Images are representative of three experiments.
(D) AXL knockdown facilitates partial EMT reversal with the SKOV3 reverting from an Intermediate mesenchymal state towards an intermediate epithelial state, and the OVCA429 reverting from an intermediate epithelial state to a more epithelial state.

To substantiate the functional effect of partial EMT reversal in shAXL cells, motility assays were carried out. Single cell motility analysis showed a significant retardation in all kinetic parameters such as displacement, velocity, speed of locomotion, and directional persistence. (Figure 21A and 21B). Gap closure assays were also performed to assess collective cell migration. In OVCA429, the shLuciferase control cells closed 31.1% of the gap, compared to the 10.6% closure by shAXL#40 (p = 0.003), and 7.9% closure by shAXL#41 cells (p = 0.025). SKOV3 showed a reduction from 99.9% gap closure in shLuciferase control, to 58.32% in shAXL#40 ($p < 0.001$), and to 28.41% in shAXL#41 (p = 0.002), (Figure 21C and 21D). These results were consistent with the functional changes in cell motility following R428 inhibition.

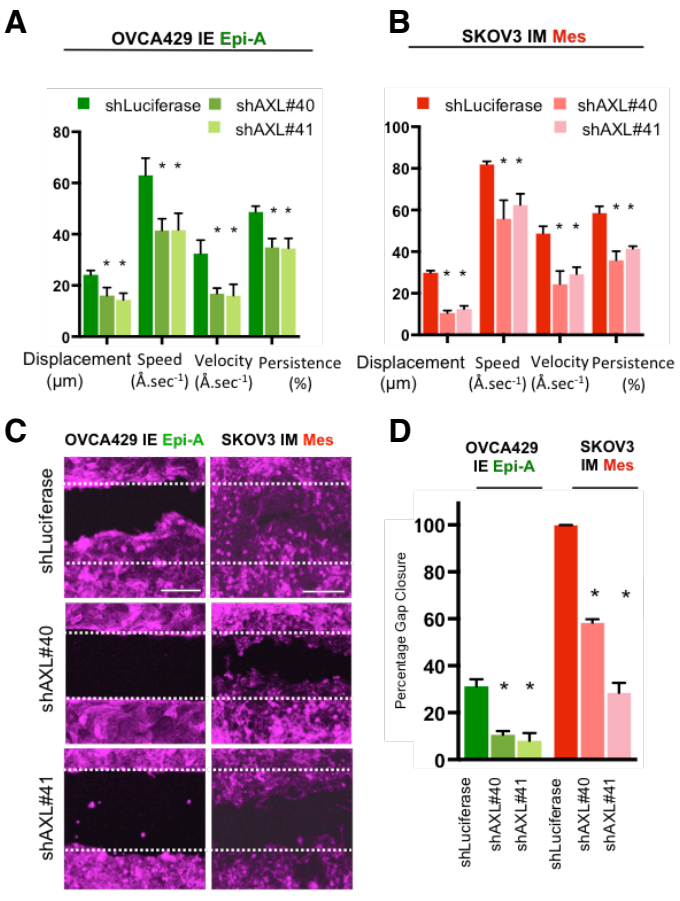


Figure 21: Silencing AXL reduces cell motility.
shAXL clones show reduced motility compared to the shLuciferase control in both (A) OVCA429 and (B) SKOV3. Single cell tracking analysis was performed on the ImageJ Trackmate platform. Kinetic parameters such as displacement, cell velocity, speed of locomotion, and directional persistence are represented.
(C) shAXL clones show reduced gap closure rates compared to shLuciferase control in both OVCA429 and SKOV3. Dashed white lines represent the initial boundary and scale bars represent 200µm. Images are representative of three experiments. (D) Gap closure was quantified on ImageJ Software.
Means ± SEM from three experiments. Paired 2-tailed Student's t-tests were used to determine statistical significance * $p < 0.05$, ** $p < 0.01$, *** $p < 0.001$.

3.2.9 AXL knockdown reduces anchorage independent growth, invasion, and tumor formation.

In addition to the effect on EMT reversal, proliferation, soft agar and invasion assays were carried out in the shAXL cells. Both Mes SKOV3 and Epi-A OVCA429 shAXL cell lines showed reduced proliferation (Figure 22). This is concordant with the proliferative effects observed after Gas6 stimulation that both Epi-A and Mes utilize AXL signaling for cell growth. For soft agar assays, OVCA429 cells showed minimal colony formation, which was completely abrogated in shAXL clones (Figure 23A and 23B). In SKOV3, the control cells showed significant colony formation in soft agar, and shAXL attenuated its clonogenic ability (Figure 23A and 23B). Spheroid invasion assays showed a similar trend with OVCA429 forming minimally invasive spheroids, an effect that was completely prevented in shAXL clones. SKOV3 showed numerous invasive protrusions from the spheroids, which was abolished by shAXL (Figure 23C and 23D). Our data suggested that AXL played an important role in both the anchorage-dependent and independent growth. It is particularly essential for the mesenchymal phenotype such as Mes that AXL is required for anchorage independency.

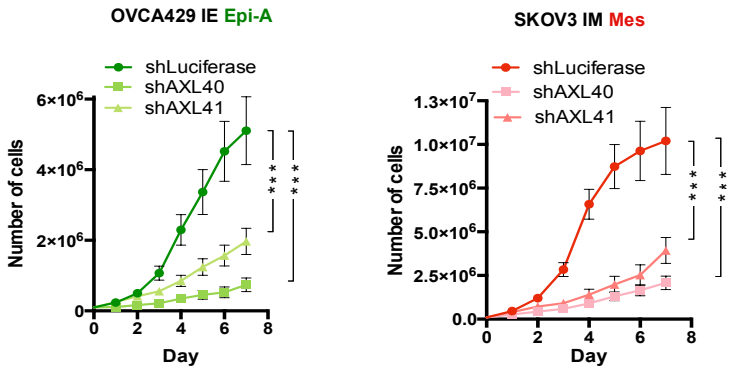


Figure 22: AXL knockdown slows cell proliferation.
shAXL clones had lower proliferation rates in both OVCA429 and SKOV3, compared to the shLuciferase control. Cell numbers were obtained using the automated cell counter Sceptre™ 2.0. Means ± SEM from three experiments. Paired 2-tailed Student's t-tests were used to determine statistical significance * $p < 0.05$, ** $p < 0.01$, *** $p < 0.001$.

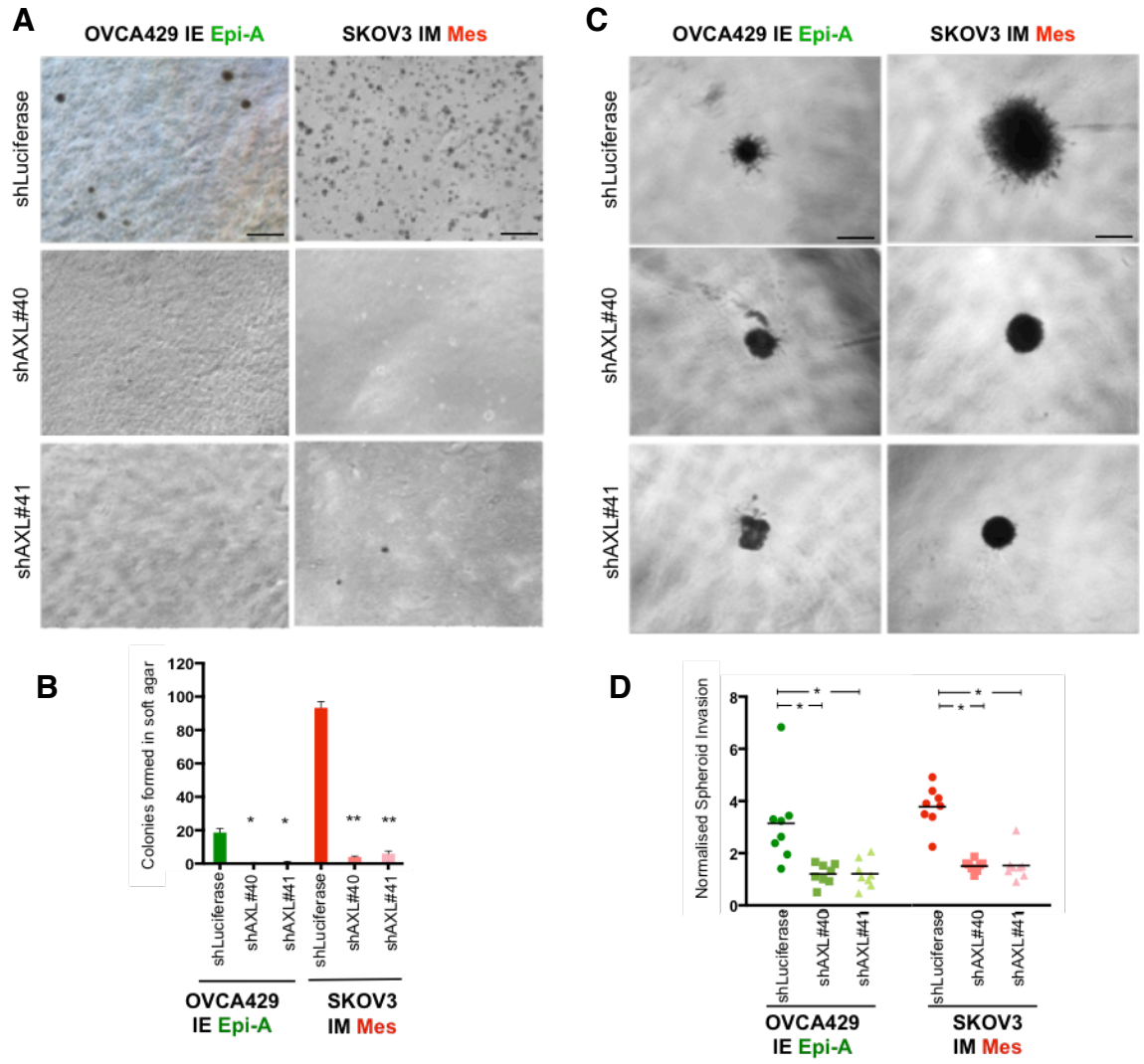


Figure 23: AXL knockdown reduces anchorage independent growth and invasion.

(A) AXL knockdown prevented colony formation in soft agar in OVCA429 and SKOV3. The anchorage independent state was achieved in 0.3% soft agar, containing 10^6 cells, atop solid 0.6% soft agar and colony formation was visualized on day 14. Scale bar represents 200µm. Images are representative of three experiments.

(B) Colony formation was quantified and averaged across 4 fields under the microscope at 20X magnification.

(C) AXL knockdown abolished spheroid invasion in complete medium in SKOV3 and OVCA429 cell lines. Cell that formed spheroids in low adherence round bottomed 96 well plate subsequently invaded into the invasion matrix upon introduction of chemotactic medium containing FBS. Scale bar represents 200µm. Images are representative of three experiments.

(D) Invasion was quantified using ImageJ software to calculate the average radius r of spheroid; and invasion volume was calculated using $4\pi r^3/3$, and normalized to spheroid volume prior to addition of chemotactic medium.

Means ± SEM from three experiments. Paired 2-tailed Student's t-tests were used to determine statistical significance * $p < 0.05$, ** $p < 0.01$, *** $p < 0.001$.

In an orthotopic xenograft tumor model, shAXL#40 and shAXL#41 SKOV3 cells showed complete inhibition of tumor formation and growth compared to shLuciferase control (Figure 24A-C). Tumor inhibition was 100%, with SKOV3 shLuciferase control forming tumors (average weight of 0.3658g, SEM ± 0.1563; average number of 5.8, SEM ± 0.74), while the SKOV3 shAXL#40 and shAXL#41 clones formed no tumors (p = 0.0474; p = 0.0001). This is consistent with the R428-mediated tumor reduction observed in *in ovo* suggesting that AXL is indeed a key signaling node for Mes.

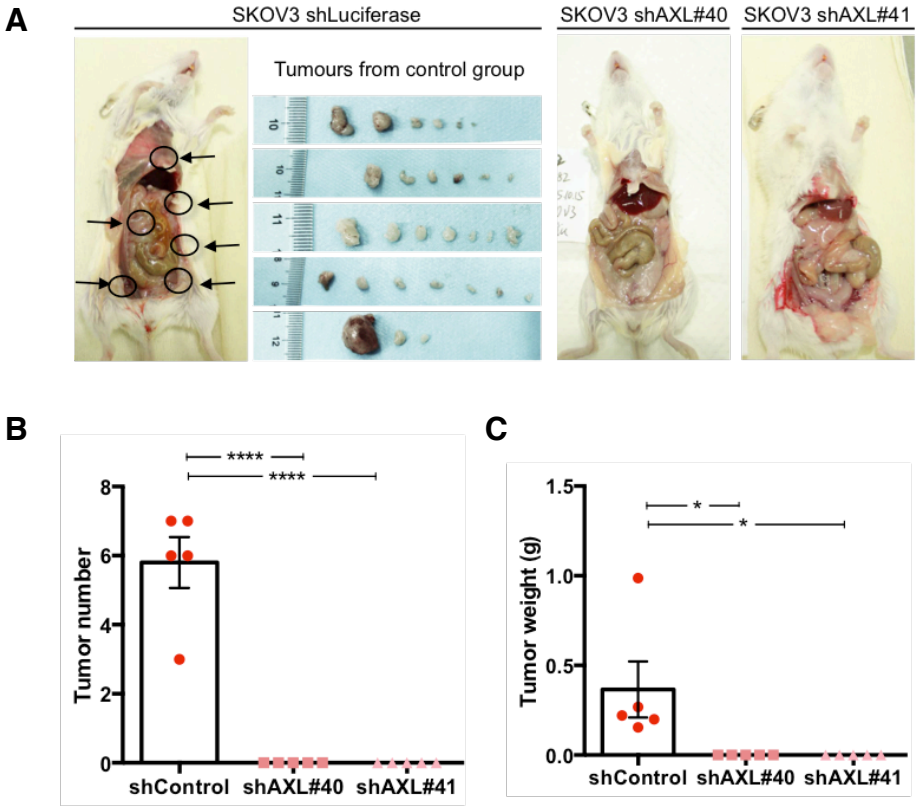


Figure 24: Silencing AXL abrogates tumor formation and growth.
(A) SCID-Beige mice were inoculated intraperitoneally to establish SKOV3 shLuciferase control, shAXL#40 and shAXL#41 ovarian cancer models. Study was concluded 4 weeks after injection of cells. Both shAXL#40 and shAXL#41 knockdown showed complete tumor inhibition effect on SKOV3 xenograft tumor model as compared to shLuciferase control, based on the measurement of (E) tumor number and (F) tumor weight. Means ± SD from five mice per condition. Paired 2-tailed Student's t-tests were used to determine statistical significance * $p < 0.05$, ** $p < 0.01$, *** $p < 0.001$.

3.2.10 *AXL* signature positively correlates with EMT and confers worse prognosis.

An *AXL* gene signature was derived from the gene expression microarray analysis (Figure 25A) and was found to be significantly overexpressed in Mes (Figure 25B). EMT scoring presents a quantitative measure of analysing effects of EMT on cancer progression[174]. In particular, ovarian cancer is known to have robust correlation between the GEMS, EMT status, and poor prognosis[174]. By analysing a gene expression profiling meta-analysis cohort[41], the *AXL* signature showed positive correlation with the ovarian-specific EMT score (Rho = +0.4148, *p* = 5.23e-65) (Figure 25C).

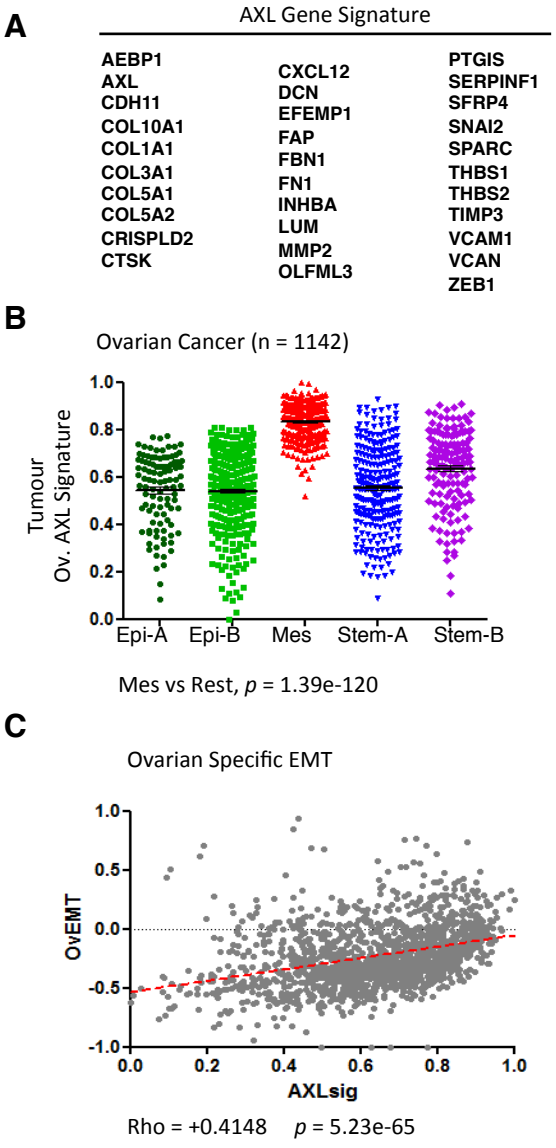


Figure 25: *AXL* signature in ovarian tumors.
(A) *AXL* signature given by cluster of genes correlating positively with *AXL* gene expression.
(B) *AXL* signature expression pattern in tumor samples (n = 1142) classified into EOC molecular subtypes, shows enrichment in Mes subtype (Man Whitney Test: Mes vs Rest *p* = 1.39e-120).
(C) *AXL* signature in tumor samples (n = 1142) shows significant positive correlation with ovarian specific EMT score (Rho = +0.4148, *p* = 5.23e-65)

This *AXL* signature correlated with overall survival (OS) with high *AXL* signature conferring a worse OS in ovarian cancer with a hazard ratio (HR) of 1.263 (p = 0.0096) and 1.58 (p = 0.003) when using the cutoff at median or lowest-highest quadrants, respectively (Figure 26A). A similar trend was observed in some cancers such as colorectal (Figure 26B) and gastric (Figure 26C), but not in others (Figure 26D-F), delineating the advantage of AXL inhibition in specific tumor types.

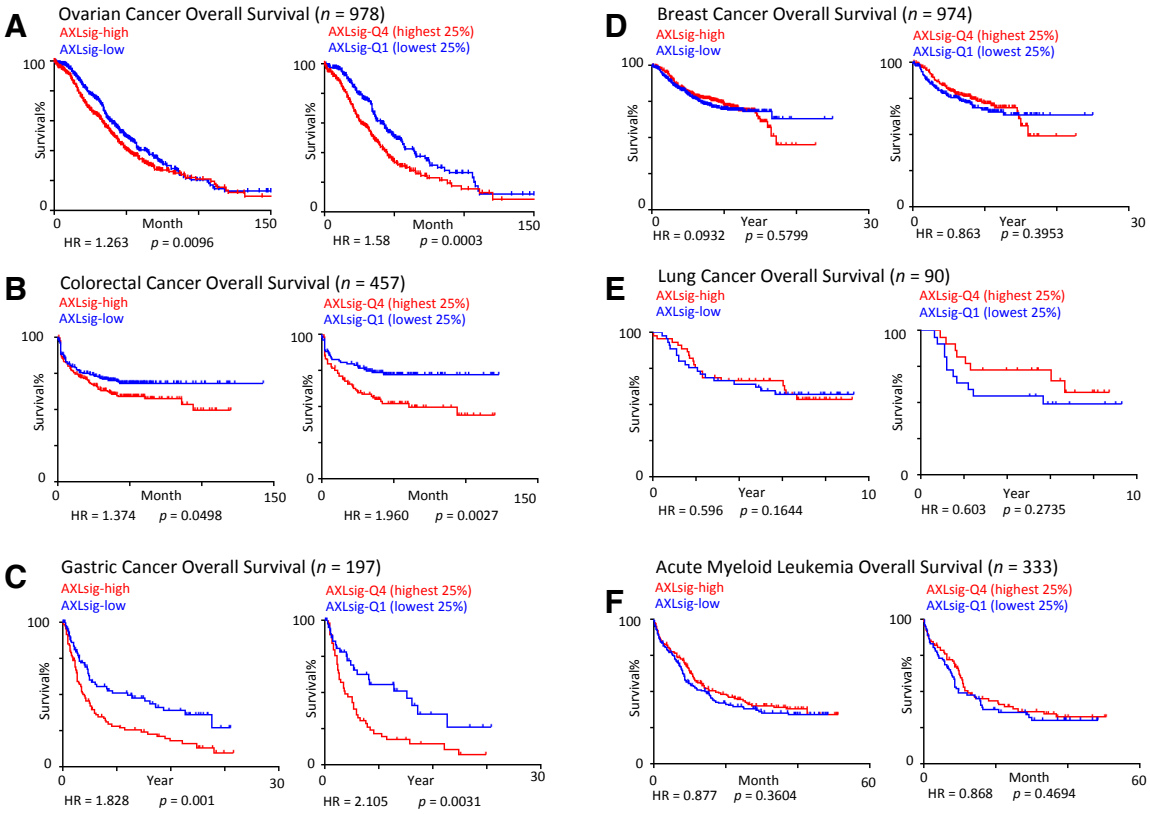


Figure 26: High *AXL* signature confers worse prognosis in specific cancers. Using the cutoff at median or lowest-highest quadrants, high *AXL* signature confers a worse overall survival in (A) ovarian cancer, with a hazard ratio of 1.263 (Log-Rank test p = 0.0096) and 1.58 (Log-Rank test p = 0.003); (B) colorectal cancer, with a hazard ratio of 1.374 (Log-Rank test p = 0.0498) and 1.960 (Log-Rank test p = 0.0027); and (C) in gastric cancer with a hazard ratio of 1.828 (Log-Rank test p = 0.001) and 2.105 (Log-Rank test p = 0.0031), respectively. High *AXL* signature, using the cutoff at median or lowest-highest quadrants, does not significantly impact overall survival in cancers such as (D) breast cancer, (E) lung cancer, and (F) Acute Myeloid Leukemia.

In addition, in ovarian cancer the *AXL* signature was also significantly overexpressed in the omental metastasis[175] (p = 0.0078) (Figure 27A) and in platinum-resistant relapsed tumors[71] (p = 0.0059) (Figure 27B) compared to their paired primary tumors. This is consistent with the notion that AXL overexpression is associated with poor prognosis[168]. The strong correlation between AXL and EMT further highlighted its relevance in EMT modulation and subsequent effects in promoting tumor dissemination and drug resistance which translates to patient survival.

Also, analysing the TCGA RPPA data shows higher phosphorylation of MAPK in Mes subtype (p = 0.0282) (Figure 28A), which could, at least partially, be due to increased Gas6/AXL activation and RTK crosstalk. The increased pERK in Mes is validated by western blotting GEMS-stratified tumor samples[176] (Figure 28B).

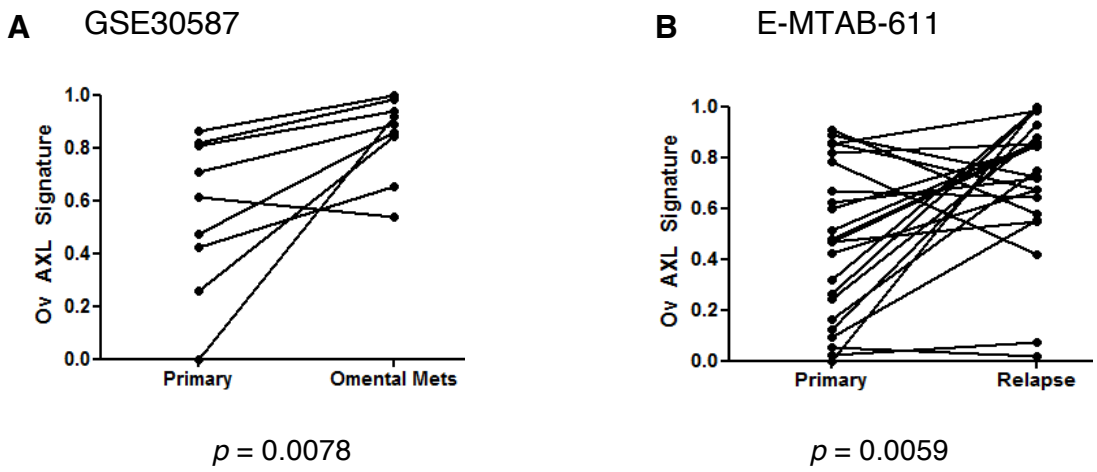


Figure 27: *AXL* signature expression levels in omental metastasis and relapsed tumors.
(A) *AXL* signature is significantly overexpressed in the omental metastasis (p = 0.0078) compared to the paired primary tumors from the GSE30587 microarray dataset. (B) *AXL* signature is also significantly overexpressed in platinum-resistant relapsed tumors (p = 0.0059) compared to their paired primary tumors from the E-MTAB-611 repository. Wilcoxon signed-rank tests were used to determine statistical significance * $p < 0.05$, ** $p < 0.01$, *** $p < 0.001$.

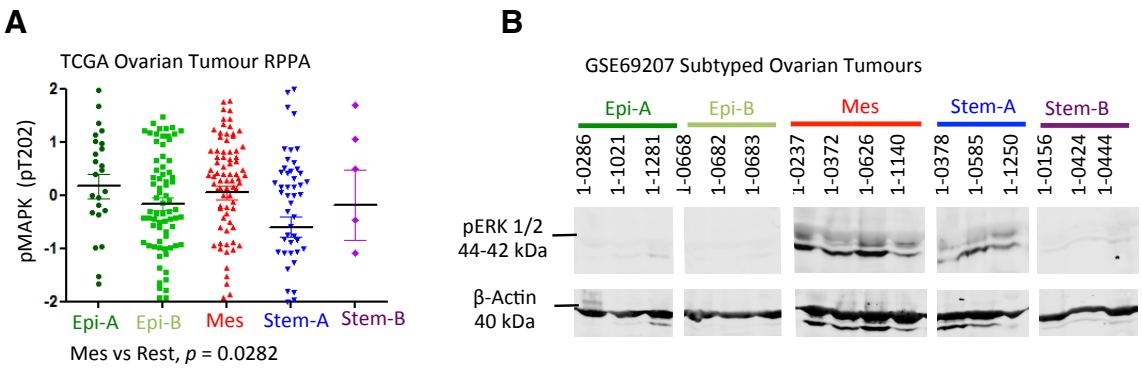


Figure 28: phospho-MAPK levels across EOC GEMS
(A) TCGA protein expression analysis revealed elevated phospho-MAPK (pT202) in the Mes subtype of ovarian cancer tumors (Mann Whitney Test: Mes vs Rest p = 0.0282)
(A) Western Blotting reveals elevated Phospho-ERK1 (pT202/pY204) + phospho-ERK2 (pT185/pY187) in Mes subtype tumor samples.

Taken together, we have demonstrated that different GEMS in ovarian cancer showed varied responses to the same kinase signaling axis that led to varied functional and therapeutic consequences. The Mes subtype is addicted to the Gas6/AXL-RTK crosstalk network. The recurrent temporal activation of ERK downstream to Gas6/AXL results functionally in a motile and invasive phenotype that is synonymous with EMT. Therapeutically, the amplified signaling sensitizes the Mes subtype to AXL inhibition, thus providing evidence to utilize AXL signature and pERK levels as a GEMS-specific target. Moreover, since AXL governs the transition of EMT, stratifying patients based on the EMT status for AXL inhibition, using a combination of the AXL signature and pERK levels, would also be a rational option.

3.3 DISCUSSION

AXL was originally identified as a transforming gene in human myeloid leukemia cells[84]. There is ectopic expression or overexpression in several cancers including glioblastoma, lung, breast, colorectal, gastric, pancreatic, bladder, renal, endometrial, and ovarian cancer[159]. In ovarian cancer, it is known that AXL is crucial to initiate and sustain metastasis and tumor dissemination in mouse models[160]. However, given the vast molecular heterogeneity of the disease, the biology of AXL requires further elucidation. In the current study, we illustrated the divergent roles of AXL among the GEMS in ovarian cancer. AXL is significantly enriched in Mes, and its activation potentiates crosstalk with EGFR and cMET, amplifying downstream oncogenic signaling such as recurrent pERK peaks. The differential pERK responses between Epi-A and Mes could potentially be linked to an increased complex network of RTK interactions along the EMT spectrum resulting in the amplification of RTK signaling. Our results do indicate a reliance of Mes on the Gas6/AXL module to propagate RTK signaling interactions. AXL has been previously shown to interact with cMET[177], EGFR[108] and HER2[178] in lung and breast cancers. In head and neck, and esophageal squamous cell carcinomas, it has been reported that AXL dimerises with EGFR to confer resistance to PI3K inhibition[158]. This AXL-RTK crosstalk might exist in reciprocal control since activation of EGFR was shown to transactivate AXL in triple negative breast cancer, thereby promoting additional signaling cascades to effect motility responses[143]. Of note, inhibiting AXL in MCF7 and T47D cell lines had no effect, while the MDA-MB-231 and MDA-MB-157 showed loss of EGFR-mediated functions when AXL was inhibited[143]. The former two cell lines possess a negative EMT score, and can be classified as epithelial, while the latter have a positive EMT score, classifying them as mesenchymal[174]. Therefore, this AXL-RTK reciprocal crosstalk might be tightly governed by the intrinsic EMT status that only exists in the

mesenchymal phenotype. This alludes to the conserved ability of one oncogenic RTK to recruit and activate other receptors through clustering, leading to the diversification of signaling pathways in EMTed cells, conferring the mesenchymal state with a more aggressive phenotype. Additional evidence comes from targeting AXL by using a high affinity RNA-based inhibitory aptamer GL21.T that abrogates AXL-mediated invasion and tumor growth in mice[179]. This aptamer selectively accumulates in the AXL overexpressing mesenchymal A549 xenograft [179] but not the AXL-low, epithelial MCF7. In mesenchymal systems such as A459 and MDA-MB-231, AXL inhibition improves responses to erlotinib and reduces metastasis *in vivo*[116]. Collectively, it is clear that anti-AXL therapy will principally benefit EMTed systems. However, it is worthwhile to note that in pancreatic cancer, anti-AXL mAbs have inhibited growth of pancreatic tumor xenografts *in vivo* with epithelial cell lines such as BxPC-3 as well as mesenchymal cell lines like MiaPaCa-2[180].

Downstream to the AXL-RTK network, several adapter proteins such as Shc, Src, Shp-2 are activated in Mes but not in Epi-A. This is paralleled to the recurrent pERK activation followed by FRA1 induction. Consequently, the sustained ERK and FRA1 activation contributes to an EMT-like phenotype in terms of enhanced motility. ERK activation has been previously linked to motility[181] via the EMT inducing transcription factor Slug[167]. The ERK/FRA1 axis is also known to be involved in modulating EMT transcription factors Slug and Zeb1, and motility[169,170]. Our data not only corroborates with these findings but also provides additional significance in the specific activation of this signaling cascade in a clinically relevant subset of ovarian cancer, the Mes subtype. This might lead to a targetable conduit for the AXL-RTK-ERK axis by precise patient stratification in ovarian cancer. The AXL addiction inherent in Mes results into an increase in the sensitivity to pharmacological inhibition of AXL compared to other ovarian cancer GEMS. In lung cancer, mesenchymal cells have

been noted to be more sensitive to AXL inhibition by small molecule inhibitor SGI-7079, and this is primarily due to the increased AXL expression[107]. However, our findings further show that in addition to AXL expression, the AXL-RTK-ERK crosstalk pattern is another important feature to determine the sensitivity to AXL inhibition.

AXL-associated EMT has been shown to mediate resistance to various targeted therapies[107,108,112,182,183]. Pharmacologic inhibition of AXL activity has been demonstrated to reverse the resistance. In non-small cell lung cancer (NSCLC), mesenchymal cells show greater resistance to EGFR-targeted therapy due to increased expression levels of AXL. This resistance can be reversed by inhibiting AXL[107], which suggests oncogenic addiction to AXL in EMTed systems. Increased activation of AXL in the absence of acquired EGFR T790M mutation, or c-MET activation, confers erlotinib resistance in multiple lung cancer models *in vitro* and *in vivo*, with genetic or pharmacologic inhibition of AXL restoring sensitivity[108]. These findings highlight the therapeutic potential of AXL inhibition in drug resistant tumors. Currently, there are several AXL-branded inhibitors such as, MGCD265, NPS-1034 [184], S49076 [185], CEP-40783 that cross inhibit other RTKs, in particular cMet. Most of these inhibitors are positioned to be used as the second line treatment after acquiring EGFR resistance[140,184]. However, another potential approach would be to target the mesenchymal system with AXL inhibition as the first-line treatment. The rational is based on our finding that the RTK activation network exhibit increasingly robust crosstalk along the EMT gradient, thereby drastically sensitizing EMTed carcinoma cells to inhibition of the RTK node such as AXL. Our data also implies that the epithelial systems will also show inhibition at higher doses. We speculate that the epithelial cells are likely to retain linear signaling axis, which shows a dose dependent inhibition. The linear signaling nature of the AXL axis in Epi-A shows lower dependency of AXL signaling in this subtype and also suggests that resistance

to selective AXL inhibitors would more likely emerge. It will be worth exploring whether those inhibitors targeting both AXL and other RTKs would be of better choice for the epithelial Epi-A subtype.

There are several strategies to target AXL. Several small molecular weight compounds that inhibit the kinase pocket of AXL are in the clinical pipelines[186]. A monoclonal antibody YW327.6S2 has proven effective in blocking the Gas6/AXL axis by binding and internalizing AXL[116]. Apart from targeting AXL directly, a 'decoy receptor' has been engineered to bind Gas6 and inhibit its function, and has shown to dramatically reduce metastatic spread in SKOV3 intraperitoneal mouse model[117]. Apart from pharmacological inhibition, genetic inhibition of AXL using shRNA showed partial reversal of EMT in ovarian cancer cell lines and reduction in motility and invasion, and tumorigenesis *in vivo*.

In conclusion, molecular stratification of ovarian cancer by GEMS enables the identification of key players in molecular networks that modulate the functions of a specific molecular subtype, with AXL being a crucial player in the Mes subtype. The Gas6/AXL pathway initiates a recurrent and sustained ERK response exclusively for the Mes subtype, which contributes to an increase in motility and signal amplification via extensive crosstalks with other RTKs. This inherent amplification of oncogenic signaling makes the Mes subtype more sensitive to AXL inhibition. Thus, stratifying Mes subtype patients based on AXL signature and pERK levels in tumors, followed by targeted AXL inhibition would be promising in a prospective clinical setting.

CHAPTER IV: THE TUMOR SUPPRESSOR OPCML BINDS TO, COMPARTMENTALIZES AND INHIBITS THE ONCOGENIC SIGNALING OF AXL

4.1 INTRODUCTION

OPCML is a glycosyl phosphatidylinositol (GPI)-anchored protein belonging to IgLON family of cell adhesion molecules, characterized by their conserved type-I immunoglobulin domains[187]. OPCML is silenced in over 80% of EOC cases by loss of heterozygosity (LOH) and epigenetic mechanisms[124]. Hypermethylation is common also in many other cancers such as lung, brain, breast, cervical, upper gastro-intestinal and lymphomas, suggesting a conserved tumor suppressor function across various tissues[131]. Epigenetic silencing and subsequent loss of OPCML expression correlate with poor patient progression-free and overall survival[145]. Our group has previously demonstrated that OPCML exerts its tumor suppressor effect by inhibiting proliferation *in vitro* and abrogating tumorigenesis *in vivo*[145], and that tumor suppressor phenotype is due to OPCML downregulating/inactivating a spectrum of RTKs, including but not limited to EPHA2, FGFR1, FGFR3, HER2 and HER4[145].

In this study, we describe how OPCML modulates oncogenic signaling downstream of AXL. Given AXL is an emerging novel therapeutic target for metastatic ovarian cancer[160], and has been implicated in several other cancers[159], it is crucial to quest for therapeutic strategies that can successfully repress AXL signaling. As OPCML has been previously shown to down modulate RTK oncogenic signaling[145], we focused on its mechanism of tumor suppressor action on AXL.

Here we show that OPCML preferentially binds to the activated form of AXL and alters the localisation of the receptor from the soluble phase of the plasma membrane to the more ordered 'lipid rafts', where GPI-anchored moieties preferentially cluster[188]. This OPCML-mediated change in compartmentalization of AXL culminates in the accumulation of the non-phosphorylated form of the receptor in the rafts and subsequent deactivation of downstream signaling. Thereupon, Gas6/AXL-mediated increase in single cell motility, and invasion are abrogated.

4.2 RESULTS

4.2.1 OPCML expression moderates AXL survival detriment.

We initially analyzed the expression levels of AXL and OPCML in the CSIOVDB[176] dataset. While AXL overexpression conferred a significantly worse overall survival (HR = 1.335, p = 0.0013) (Figure 29A), the subset of patients that had concomitantly an elevated expression of OPCML showed a survival benefit. With below median expression of OPCML, AXL overexpression continued to confer a significantly worse overall survival (HR = 1.431, p = 0.0015) (Figure 29B), while above median expression of OPCML reduced this effect (HR = 1.322, p = 0.0651) (Figure 29C).

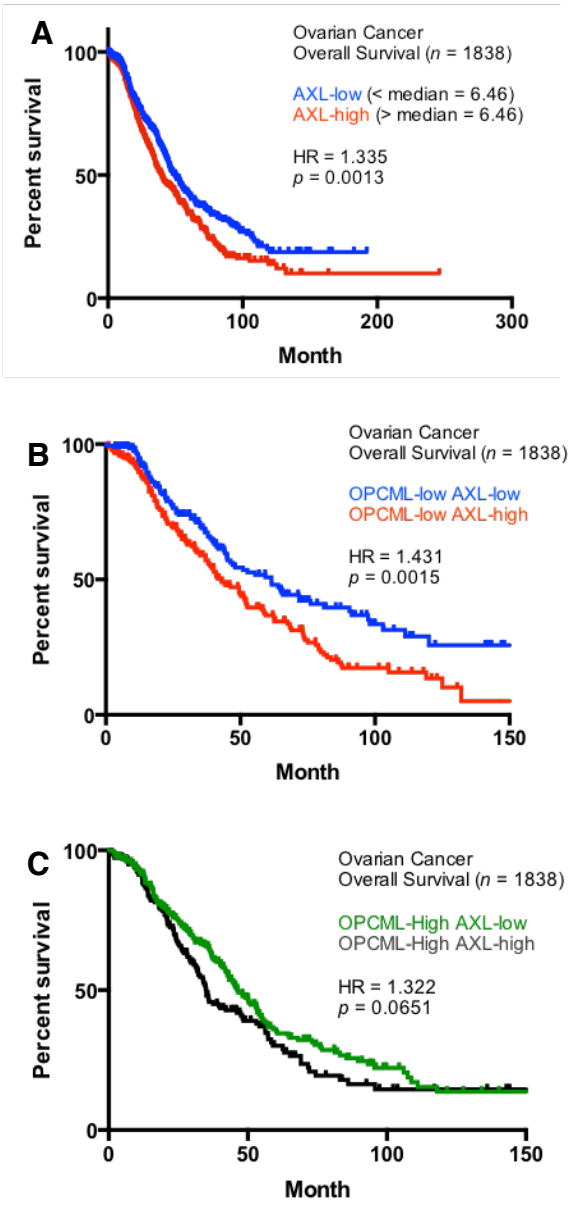


Figure 29: OPCML expression alters the association between AXL and patient survival.
(A) Kaplan-Meier curves showing overall patient survival of AXL-high (red) and AXL-low (blue) patient groups. AXL-high, defined as an above median expression, conferred a worse prognosis with a hazard ratio of 1.335 and log-rank test p = 0.0013.
(B) Kaplan-Meier curves in a OPCML-low expression state, showing overall patient survival of AXL-high (red) and AXL-low (blue) patient groups. OPCML-low, defined as a below median expression, conferred a hazard ratio of 1.431 and log-rank test p = 0.0015.
(C) Kaplan-Meier curves in a OPCML-high expression state, showing overall patient survival of AXL-high (black) and AXL-low (green) patient groups. OPCML-high, defined as an above median expression, conferred a hazard ratio of 1.322 and log-rank test p = 0.0651.
In OPCML-high state, there was reduced impact of AXL in conferring a survival disadvantage.

Furthermore, while analyzing the effects of OPCML promoter methylation from the ICGC dataset[189], a similar trend was observed. AXL overexpression conferred a significantly worse overall survival (HR = 1.997, p = 0.017) (Figure 30A). In the subset where there was methylation of the OPCML promoter region, AXL overexpression continued to confer a significantly worse overall survival (HR = 1.929, p = 0.0411) (Figure 30B), while in the unmethylated cohort, the difference was no longer significant (HR = 1.939, p = 0.1505) (Figure 30C). These findings, while underscoring the clinical relevance of OPCML as tumor suppressor, led to the hypothesis that AXL oncogenic function could be downmodulated by OPCML.

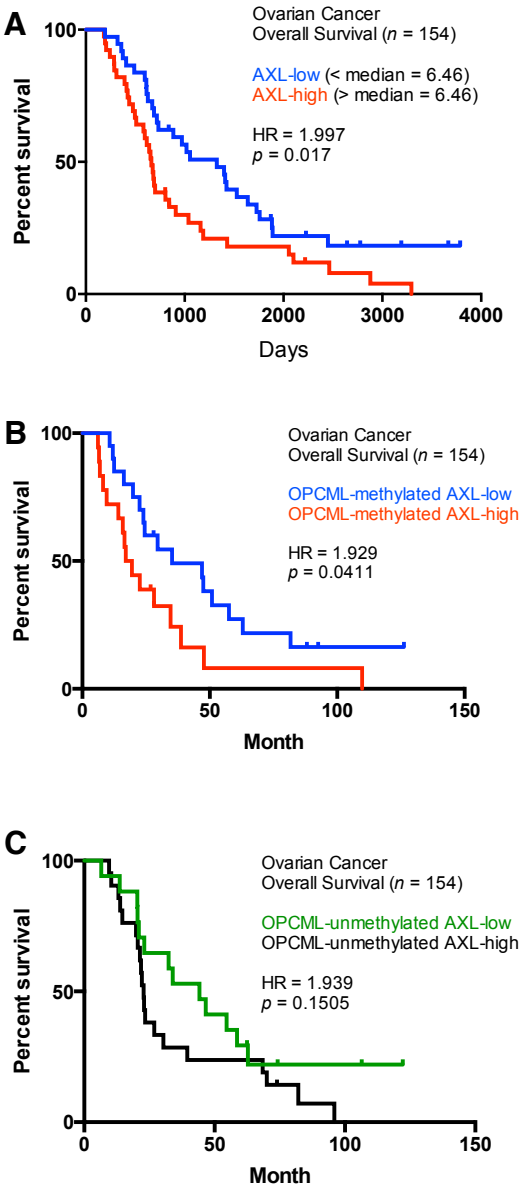


Figure 30: OPCML methylation alters the association between AXL and patient survival.
(A) Kaplan-Meier curves showing overall patient survival of AXL-high (red) and AXL-low (blue) patient groups. AXL-high, defined as an above median expression, conferred a worse prognosis with a hazard ratio of 1.997 and log-rank test p = 0.017.
(B) Kaplan-Meier curves in OPCML promoter-methylated cases, showing overall patient survival of AXL-high (red) and AXL-low (blue) patient groups. OPCML promoter-methylation was defined using the cg15885337 and cg18710784 probe sets, conferred a hazard ratio of 1.929 and log-rank test p = 0.0411.
(C) Kaplan-Meier curves in OPCML promoter-unmethylated cases, showing overall patient survival of AXL-high (black) and AXL-low (green) patient groups. OPCML promoter-unmethylated cases, conferred a hazard ratio of 1.939 and log-rank test p = 0.1505.
In promoter-unmethylated cases, OPCML expression potentially reduced the survival disadvantage of AXL overexpression.

4.2.2 AXL and OPCML function in the same pathway.

In order to investigate whether OPCML could indeed countermand the oncogenic properties of AXL, we first evaluated the effect of OPCML overexpression on modulating AXL mediated cell motility in ovarian cancer cells.

AXL-expressing, OPCML-null SKOV3 and PEA1 cell lines were stably transduced with OPCML and the control EMPTY vectors to generate SKOV3-OPCML, SKOV3-EMPTY, PEA1-OPCML and PEA1-EMPTY which were used in subsequent experiments (Figure 31).

In SKOV3-EMPTY cells, silencing AXL (Figure 32A) induced a strong reduction in all parameters compared to cells transfected with non-targeting siRNA (Figure 32B), pointing to an important role for AXL in stimulating cell motility. Interestingly, the motility of SKOV3-OPCML cells was comparable to AXL-silenced SKOV3-EMPTY cells (Figure 32B), suggesting that OPCML expression had the same effect on reducing motility as depleting AXL. Importantly, silencing AXL in SKOV3-OPCML cells did not reduce motility further (Figure 32B), suggesting that OPCML and AXL function in the same pathway with respect to motility and that the effect of the tumor suppressor is mainly mediated through AXL inhibition with respect to this phenotype. In the PEA1 system, the effects of silencing AXL in PEA1-EMPTY or PEA1-OPCML cells was identical to that observed in the SKOV3 system (Figure 32C), alluding to the conserved nature of AXL modulation by OPCML.

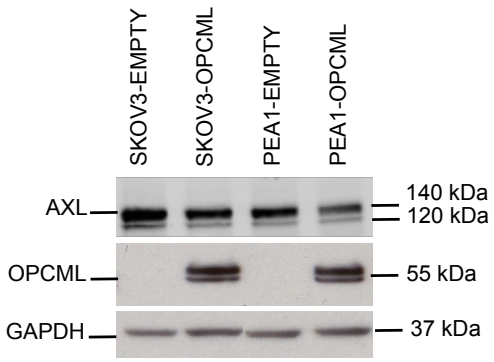


Figure 31: Generation of OPCML expressing SKOV3 and PEA1 clones.
AXL positive cell lines SKOV3 and PEA1 were stably transduced with OPCML.

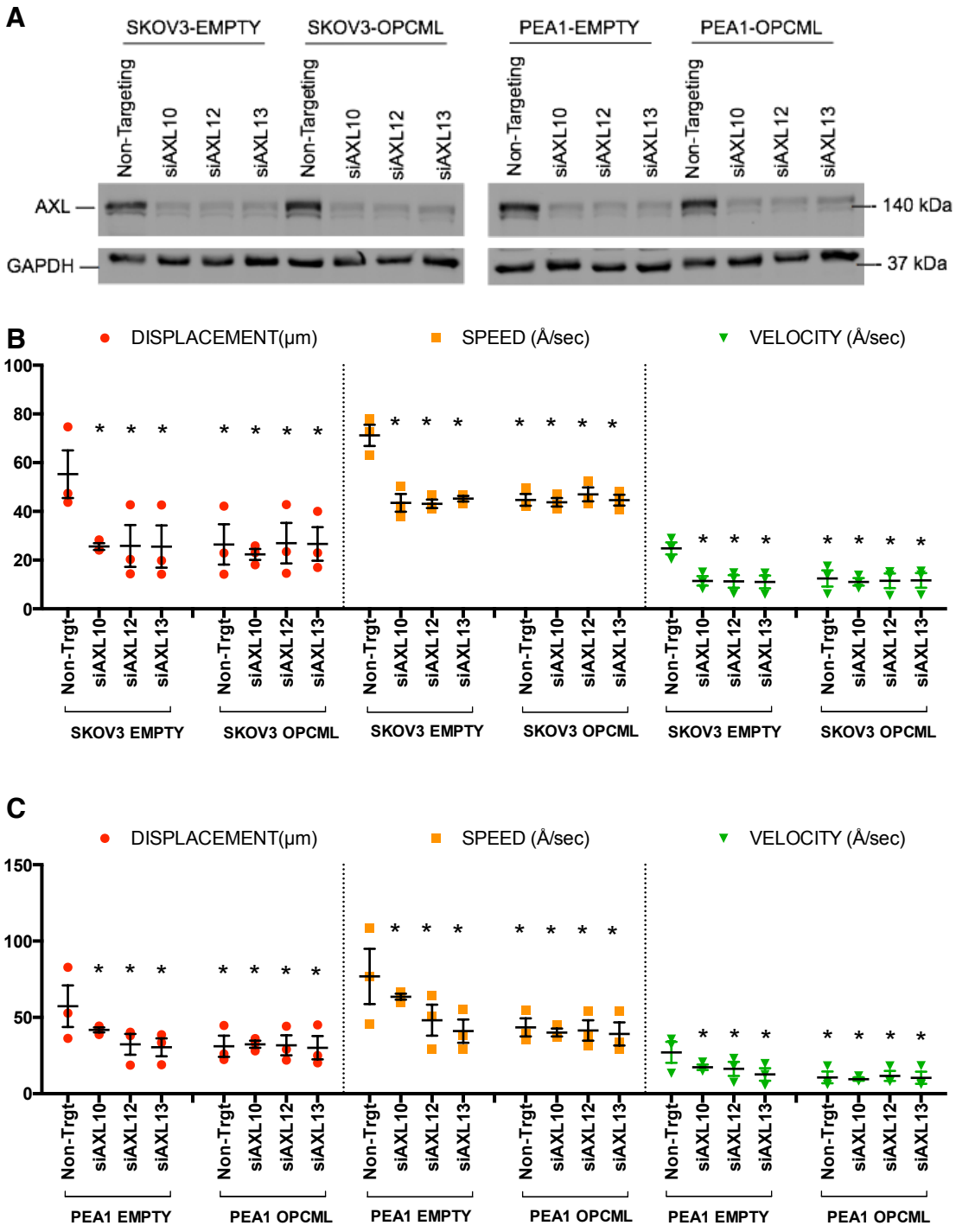


Figure 32: Modulation of cell motility by AXL and OPCML.
(A) SKOV3-EMPTY, SKOV3-OPCML, PEA1-EMPTY and PEA1-OPCML cell lines were transfected with non-targeting siRNA and three siAXL sequences. Blots are representative of three experiments.
(B, C) AXL depletion reduced motility in EMPTY vector cells as given by displacement, speed and velocity. OPCML expressing cells had reduced motility comparable to an AXL depleted state in the EMPTY vector cells. Silencing AXL in OPCML overexpressing cells did not further reduce motility.
Means ± SEM from three experiments. Paired 2-tailed Student's t-tests were used to determine statistical significance * $p < 0.05$, ** $p < 0.01$, *** $p < 0.001$.

4.2.3 OPCML interacts with AXL.

In order to investigate whether OPCML modulation of AXL was through direct protein-protein interaction, a GST pull-down assay was carried out in SKOV3-EMPTY, where AXL was detected in the eluate together with GST-OPCML (Figure 33A). The interaction between AXL and OPCML was also observed by co-immunoprecipitation in SKOV3-OPCML cells, where OPCML co-precipitated together with AXL (Figure 33B).

The localisation of the proteins at the plasma membrane was analyzed by microscopy and immunofluorescence staining revealed extensive co-localisation between AXL and OPCML on the cell surface in both SKOV3-OPCML and PEA1-OPCML under standard cell culture conditions (Figure 34A). This association was further substantiated using in situ proximity ligation assay (PLA) DUOLink, which showed a clear proximity between AXL and OPCML, strengthening our observations that the tumor suppressor associates with the RTK (Figure 34B).

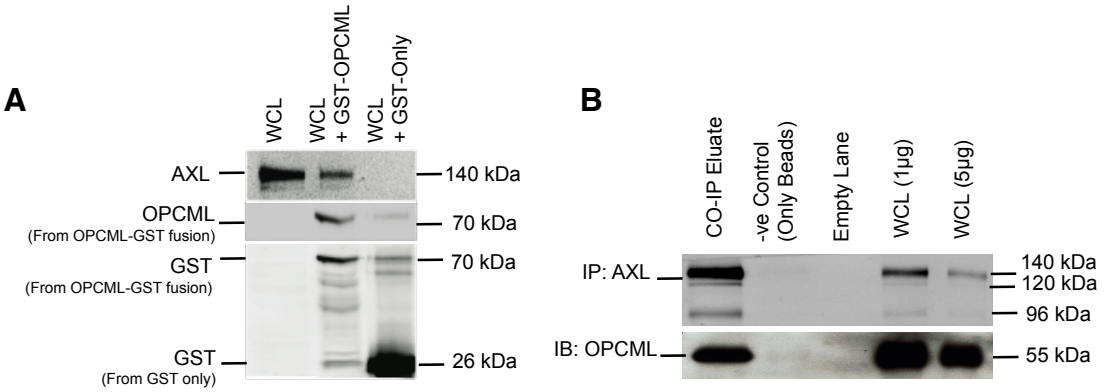


Figure 33: Pull down and Co-immunoprecipitation assays to detect AXL-OPCML interaction.
(A) Western blotting the OPCML-GST pull down eluate for AXL showed a positive signal. As a negative control, GST only was used and there was no visible interaction with AXL. WCL: Whole cell lysate from SKOV3-EMPTY cells that are positive for AXL
(B) Western blotting the co-immunoprecipitation eluate for OPCML showed a positive signal. As a negative control, the co-immunoprecipitation beads were used to check for interaction with OPCML. Anti-AXL antibody was cross-linked to the co-immunoprecipitation beads and incubated with the WCL to detect AXL-OPCML complex. WCL: Whole cell lysate from SKOV3-OPCML cells that are positive for AXL and OPCML. IP: Immuoprecipitated protein, IB: Immunoblotted (detected) protein.
Blots are representative of three experiments.

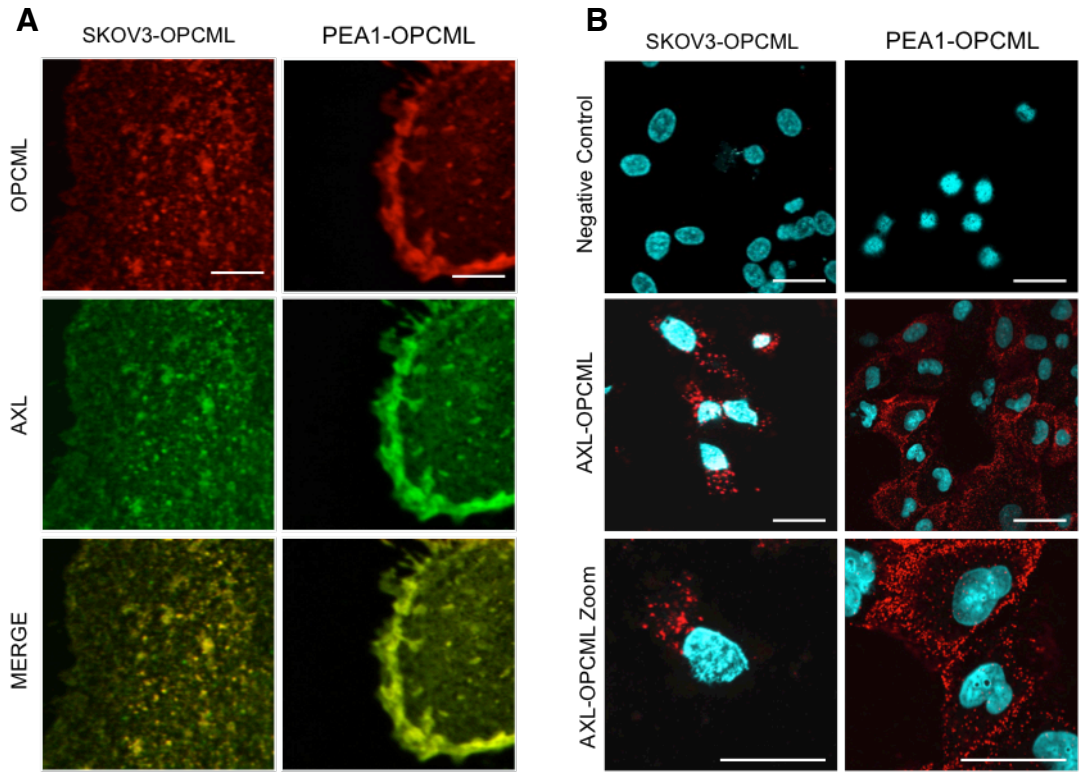


Figure 34: Immunostaining and Proximity Ligation assay to visualize AXL-OPCML association.
(A) Immunostaining SKOV3-OPCML and PEA1-OPCML cells with mouse Anti-OPCML antibody and rabbit Anti-AXL antibody showed extensive co-localisation. Scale bar represents 10µm.
(B) PLA in SKOV3-OPCML and PEA1-OPCML cells with mouse Anti-OPCML antibody and rabbit Anti-AXL antibody, showed positive signal for AXL-OPCML interaction. As a negative control, SKOV3-EMPTY and PEA-EMPTY cells were used with the same protocol. Scale bar represents 50µm.
Images are representative of three experiments.

We also investigated the effect of this interaction on the membrane distribution of AXL by fractionating the plasma membrane into the 'disordered' detergent soluble membrane (DSM) fraction and the 'ordered' detergent-resistant insoluble membrane (DRM) fraction. This showed that, upon OPCML expression, there is a shift in AXL localisation from the DSM to the DRM, where GPI-anchored proteins like OPCML are located (Figure 35A and 35B).

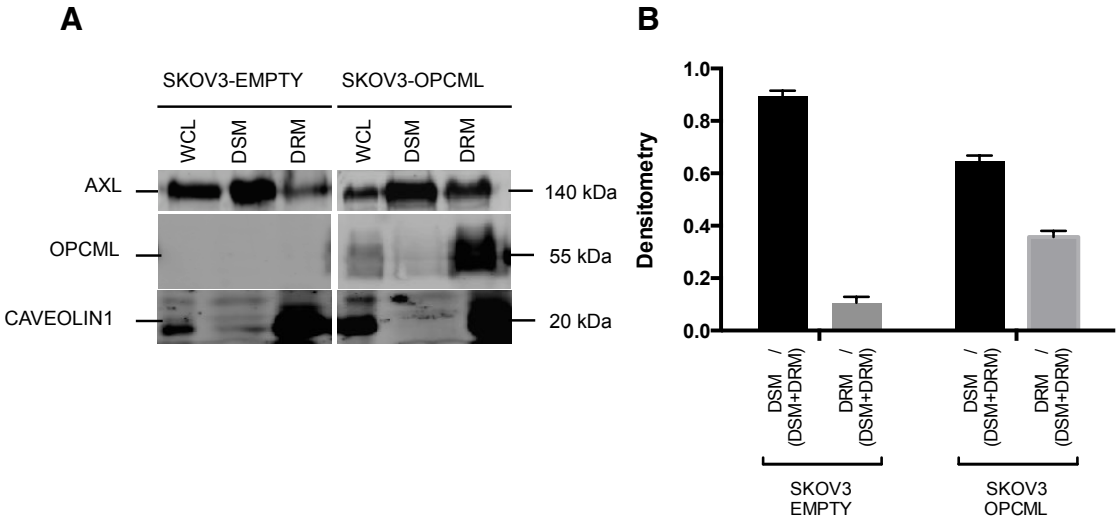


Figure 35: OPCML expression alters membrane distribution of AXL.
(A) Western blotting the membrane fractions of SKOV3-EMPTY cell line showed AXL predominantly in the DSM, while OPCML expression caused a shift into the DRM. OPCML resides predominantly in the DRM and Caveolin1 was used as a marker of the lipid rafts. WCL: Whole cell lysate, DSM: Detergent Soluble Membrane fraction, DRM: Detergent Resistant Membrane fraction. Blots are representative of three experiments
(B) Quantification of AXL band intensities in DSM and DRM by densitometry, normalized to AXL intensity in input WCL from three experiments.

4.2.4 OPCML has increased affinity for activated AXL.

To further understand the nature of the OPCML/AXL interaction, we decided to investigate how the binding of AXL to its ligand Gas6 would affect the functional interaction between AXL and OPCML. Surprisingly, in serum-free non-stimulated conditions there was minimal co-localisation between AXL and OPCML in SKOV3-OPCML as observed by immunofluorescence staining (Figure 36). However, addition of Gas6 strongly and progressively induced co-localisation at 30 minutes, 3 and 12 hours, suggesting an increased interaction between activated AXL and OPCML (Figure 36). This finding was further confirmed using PLA, which showed negligible association between the two proteins in non-stimulating conditions, but very strong interaction upon addition of Gas6 (Figure 37A). Again, this interaction increased over time (Figure 37B).

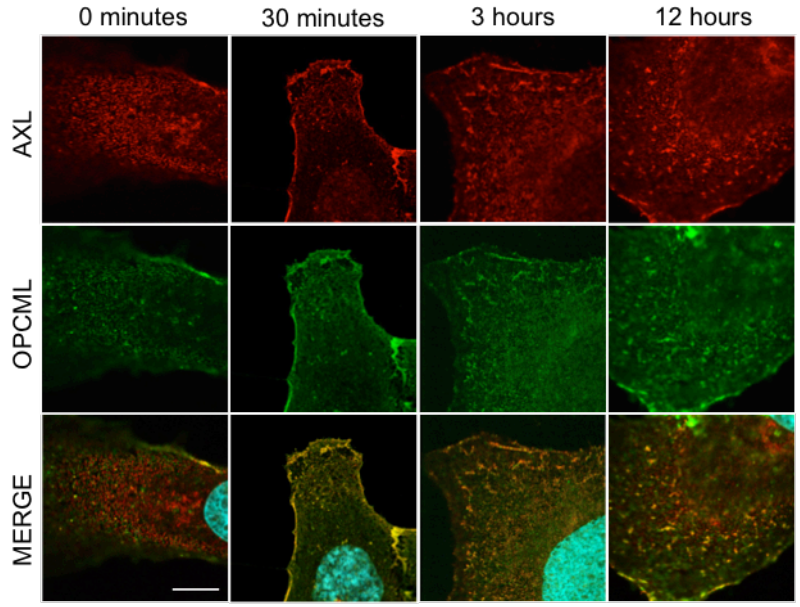


Figure 36: Immunostaining reveals increase in AXL-OPCML interaction upon Gas6 stimulation.
SKOV3-OPCML cells were serum starved and stimulated with Gas6 over a 12 hour time course and stained with mouse Anti-OPCML antibody and rabbit Anti-AXL antibody. There was no co-localisation in an un-stimulated state, but addition of Gas6 increased co-localisation between AXL and OPCML. Scale bar represents 10µm. Images are representative of three experiments.

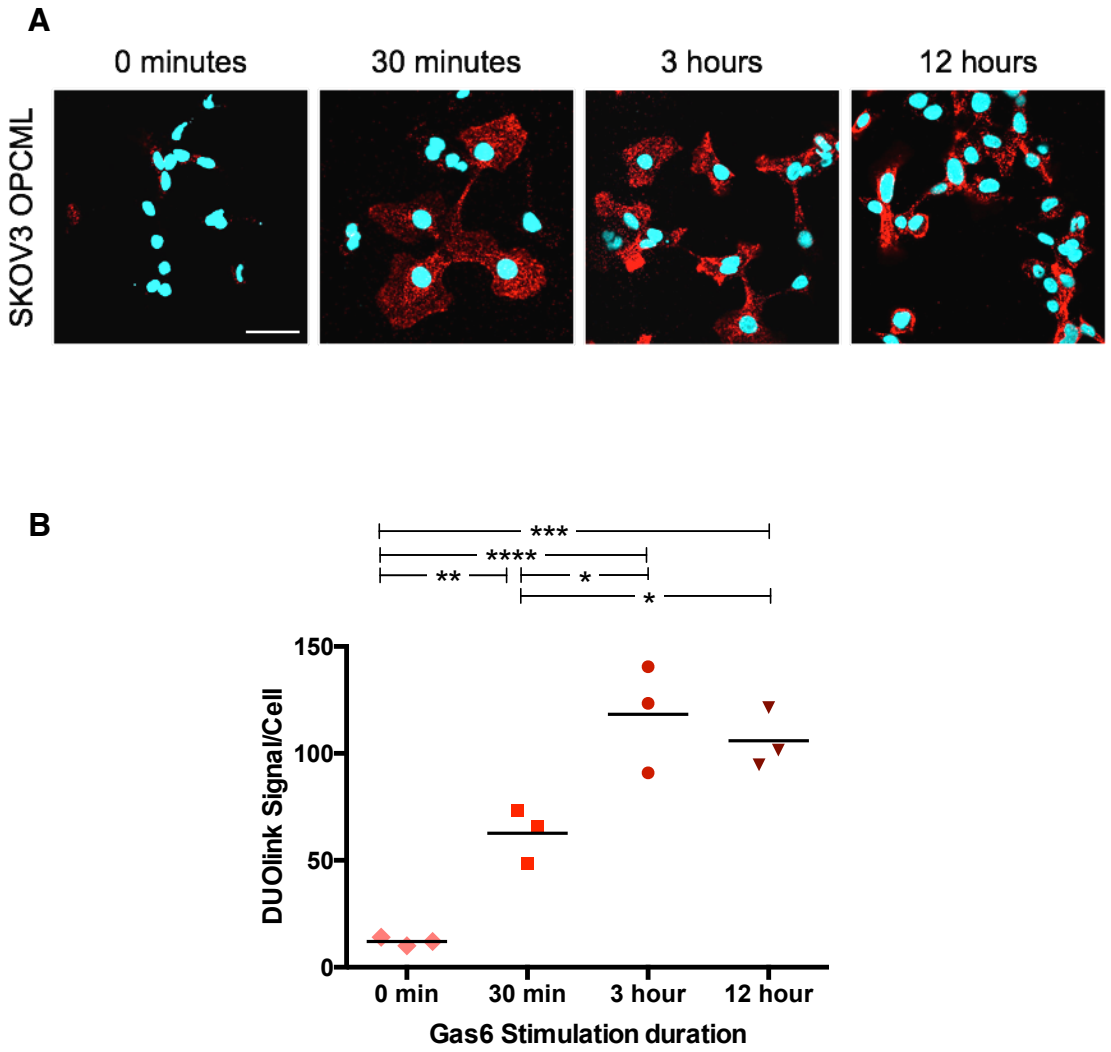


Figure 37: PLA reveals increase in AXL-OPCML interaction upon Gas6 stimulation.

(A) SKOV3-OPCML cells were serum starved and stimulated with Gas6 over a 12 hour time course and stained with mouse Anti-OPCML antibody and rabbit Anti-AXL antibody. Upon completion of PLA protocol, no signal was observed an un-stimulated state, but addition of Gas6 increased interaction between AXL and OPCML, giving a positive signal. Scale bar represents 50µm. Images are representative of three experiments.

(B) Quantification of three independent experiments shows AXL-OPCML interaction increasing with time. Means from three experiments. Paired 2-tailed Student's t-tests were used to determine statistical significance * $p < 0.05$, ** $p < 0.01$, *** $p < 0.001$.

Similarly, we could observe over a 3-fold increase in the amount of OPCML immunoprecipitated by AXL upon Gas6 treatment, suggesting again that the addition of Gas6 increases the affinity between AXL and OPCML (Figure 38A and 38B). As it was crucial to decipher whether OPCML bound the active phosphorylated form of AXL, further experiments were carried out. The interaction between pAXL and OPCML was observed by co-immunoprecipitation, where OPCML co-precipitated together with pAXL (Figure 38C). A GST pull-down assay was also carried out, where pAXL was detected in the eluate together with GST-OPCML (Figure 38D). This advocates the possibility that the tumor suppressor preferentially binds to and modulates active forms of oncogenic RTKs such as AXL to exert its anti-tumor effect.

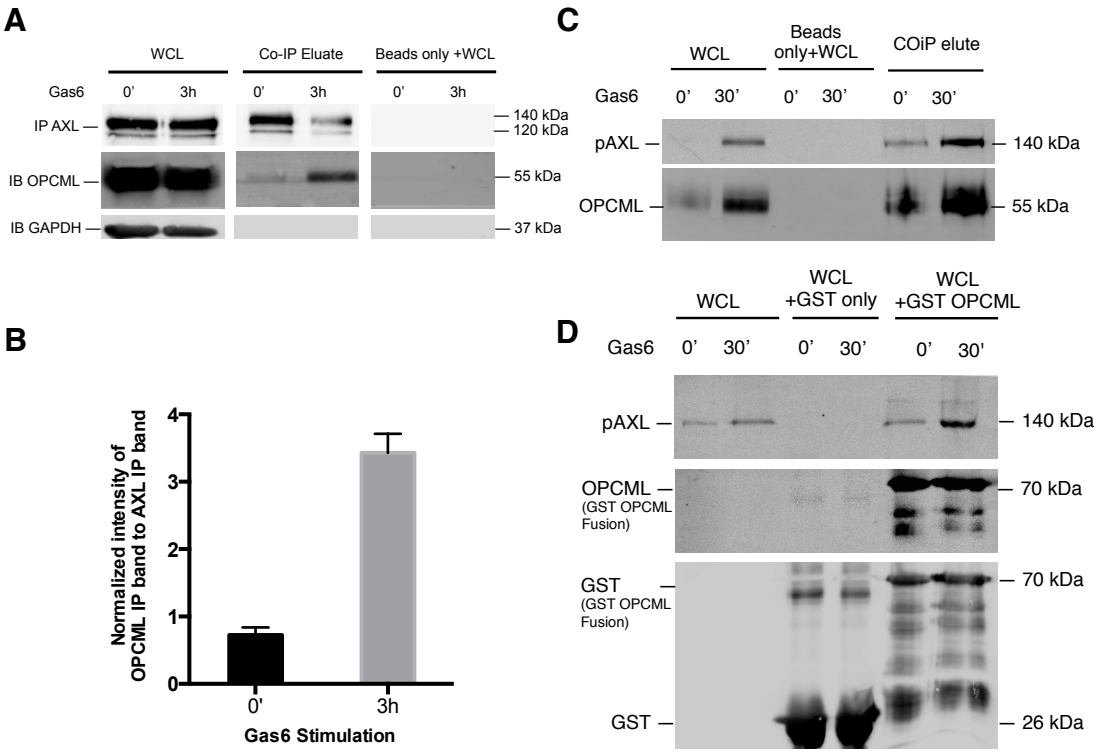


Figure 38: OPCML binds to, and has a higher affinity for activated AXL.
(A, B) Co-immunoprecipitation using anti-AXL antibody, showed more OPCML bound to AXL activated by Gas6 than un-stimulated condition. WCL: Whole cell lysate from SKOV3-OPCML cells that are positive for AXL and OPCML. IP: Immuoprecipitated protein, IB: Immunoblotted (detected) protein.
(C) Co-immunoprecipitation with anti-pAXL antibody showed that OPCML co-immunoprecipitated along with pAXL.
(D) OPCML-GST pull down assay also revealed interaction between OPCML and phosphorylated AXL. Blots and densitometry are representative of three experiments.

When we analyzed pAXL distribution by membrane fractionation in SKOV3-EMPTY, pAXL was detected mostly in the disordered DSM, with a negligible amount in the DRM, and upon addition of Gas6, increased pAXL was observed in the DSM (Figure 39A). The total AXL protein was distributed between the DSM and DRM and this distribution remained constant over time upon addition of Gas6. However, in SKOV3-OPCML the addition of Gas6 caused a shift over time of AXL from the DSM into the DRM, where the GPI-anchored protein resides (Figure 39A and 39B). Low levels of phosphorylated AXL were still detected in the DSM but to a much lesser extent (Figure 39A), as there was a significant shift of total protein into the DRM. Importantly, there was no phosphorylated AXL in the DRM (Figure 39A), suggesting that the RTK is not in its active form following its interaction with OPCML and subsequent movement into the DRM.

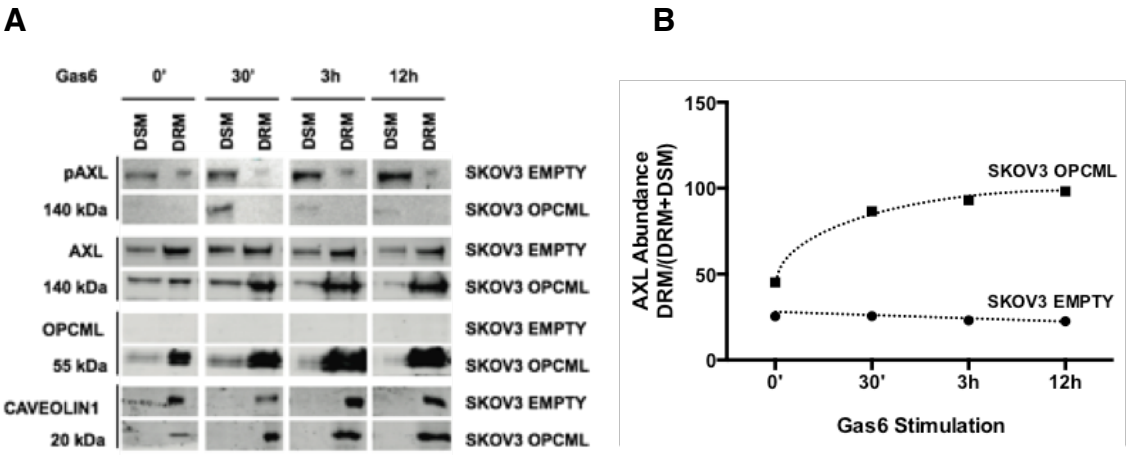


Figure 39: OPCML changes compartmentalization of activated AXL to modulate signaling.
(A) Membrane fractionation experiment shows elevated sequestration of AXL by OPCML into the DRM when stimulated by Gas6, compared to SKOV3-EMPTY cells. It also shows the localisation of pAXL to the DSM, thereby accounting for reduced AXL signaling upon OPCML expression. SKOV3-EMPTY and SKOV3-OPCML cells were serum starved and then stimulated with Gas6 over a 12 hour time course, and lysates were membrane fractionated.
(B) Ratio of AXL band intensity in DRM, to total AXL in DRM and DSM.
Blots and densitometry are representative of three experiments.

4.2.5 OPCML curtails the sustained Gas6/AXL signaling in Mes.

Observing the changes in membrane distribution and activation status of AXL upon binding to OPCML, we sought to understand how OPCML would therefore affect the AXL signaling cascade. SKOV3-EMPTY and PEA1-EMPTY cell lines were stimulated with Gas6 over a 24 hour time-course. Gas6 induced phosphorylation of AXL leading to sustained activation of downstream effector molecules such as ERK for up to 24 hours (Figure 40). In OPCML deficient controls, the sustained ERK activation was followed by the induction of EMT transcription factor Slug, a key player in cell motility and invasiveness (Figure 40). However, OPCML transfection reduced both the magnitude and the temporal duration of AXL phosphorylation and, interestingly, the temporal duration of the pERK response in both cell lines, where pERK was completely abolished after 1-3 hours (depending on cell line). This had a profound effect on Slug induction, which was completely abrogated due to lack of a sustained pERK signal (Figure 40).

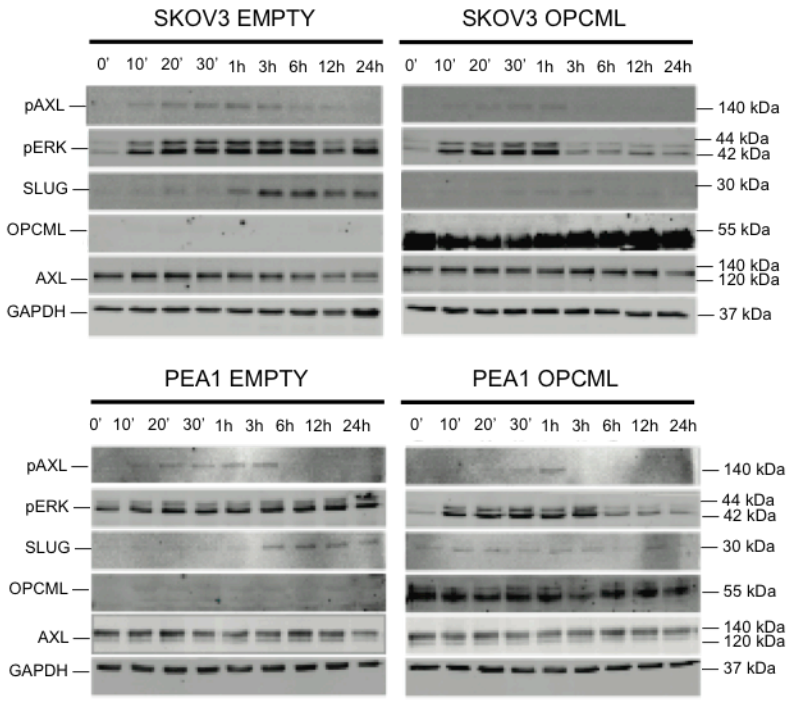


Figure 40: OPCML expression reduced temporal duration of pAXL and pERK signaling. SKOV3 and PEA1, EMPTY and OPCML transduced cell lines, were serum starved and stimulated with Gas6 over a 24 hour time course. In both cell lines OPCML expression reduced the pAXL and pERK response and abrogated SLUG induction. GAPDH was used as a loading control. Blots are representative of three experiments.

This observation was confirmed using immunofluorescence staining to visualize the pERK response upon Gas6 treatment and again, in the presence of OPCML, we could observe only a transient phosphorylation of ERK (Figure 41).

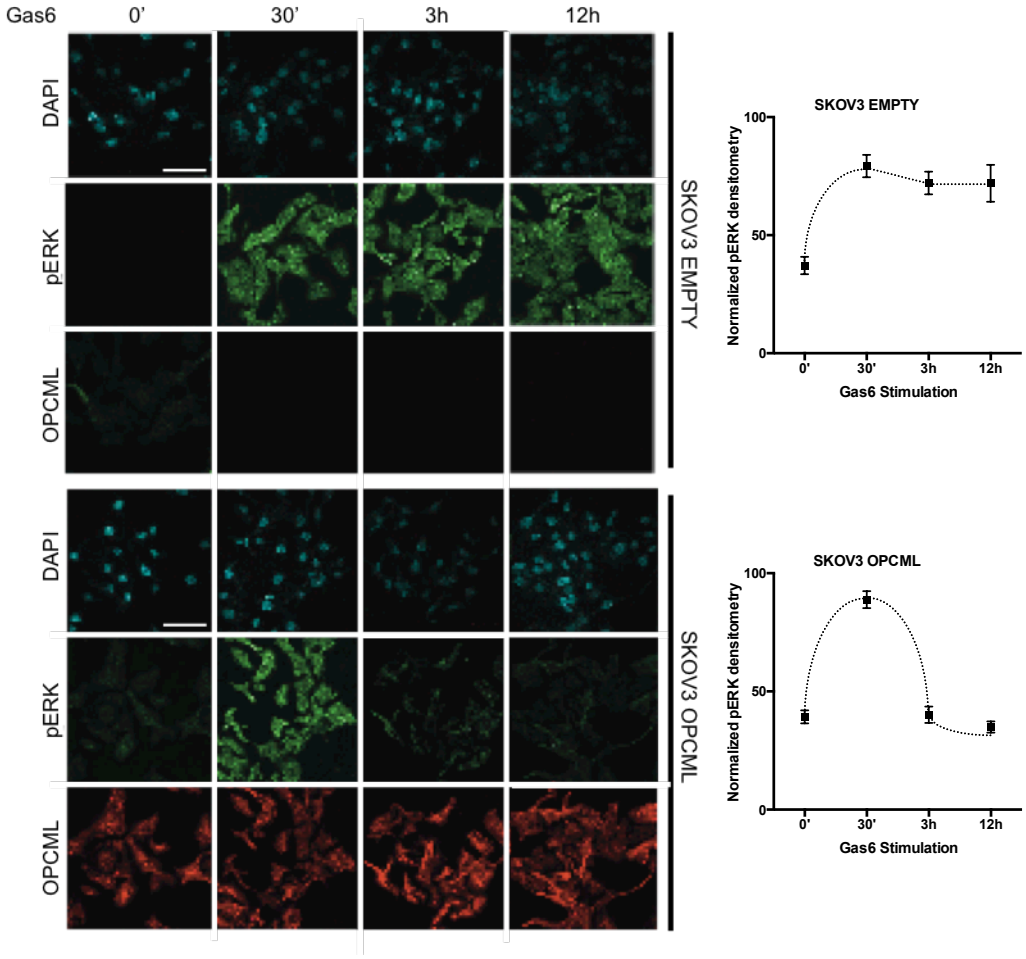


Figure 41: OPCML expression reduced pERK response to Gas6 stimulation.
Immunostaining reveals shortened pERK temporal response to Gas6 stimulation in SKOV3-OPCML cells compared to SKOV3-EMPTY. pERK staining at 0, 30 minutes and 3, 12 hours was normalized to DAPI stained nuclear area to quantify pERK response. Scale bar represents 50µm.
Images and quantification are representative of three experiments. Means from three experiments.

To expand our understanding of the tumor suppressor effect of OPCML on the Gas6/AXL pathway at a network-based system level, Reverse Phase Protein Array (RPPA) was carried out on SKOV3-EMPTY and SKOV3-OPCML. Upon Gas6 stimulation, we found elevated pEGFR and pMET levels in SKOV3-EMPTY, both at 30 minutes and 12 hours (Figure 42A), analogous to the higher and sustained pAXL status observed previously by western blotting, confirming cross talk between AXL and other RTKs[177]. However, this effect was completely abolished in the presence of OPCML (Figure 42A), underscoring its potent inhibition of activation of multiple RTKs. These results were confirmed also by western blot (Figure 42B). A similar pattern was observed immediately downstream of the RTK network, with adapter proteins such as Shc, Src and Shp-2 displaying induction of phosphorylation levels in SKOV3-EMPTY treated with Gas6, but not in SKOV3-OPCML cells (Figure 42A and 42B). Further downstream in the signal cascade, MEK1, ERK and JNK echoed similar strongly induced phosphorylation status in SKOV3-EMPTY cells, which was abrogated by OPCML (Figure 42A and 42B), confirming the pERK dynamics observed above. The sustained induction of phosphorylation of response proteins such as ELK1[190], p90RSK[191] and FRA1[169] at 12h in control cells was abrogated by OPCML expression (Figure 42A and 42B). As stated in the previous chapter, FRA1 activity has been linked to the induction of the EMT transcription factor ZEB1, SLUG and motility[45,46,64,170], and this could explain the Slug induction observed in control cells upon Gas6 stimulation of AXL[172,192] and its abrogation upon OPCML expression. Apart from the MAPK cascade, the RPPA analysis also revealed suppression of the AKT pathway by OPCML (Figure 42C). Therefore, functional proteomics clearly revealed the extent of suppression of oncogenic signaling by OPCML at a systems level.

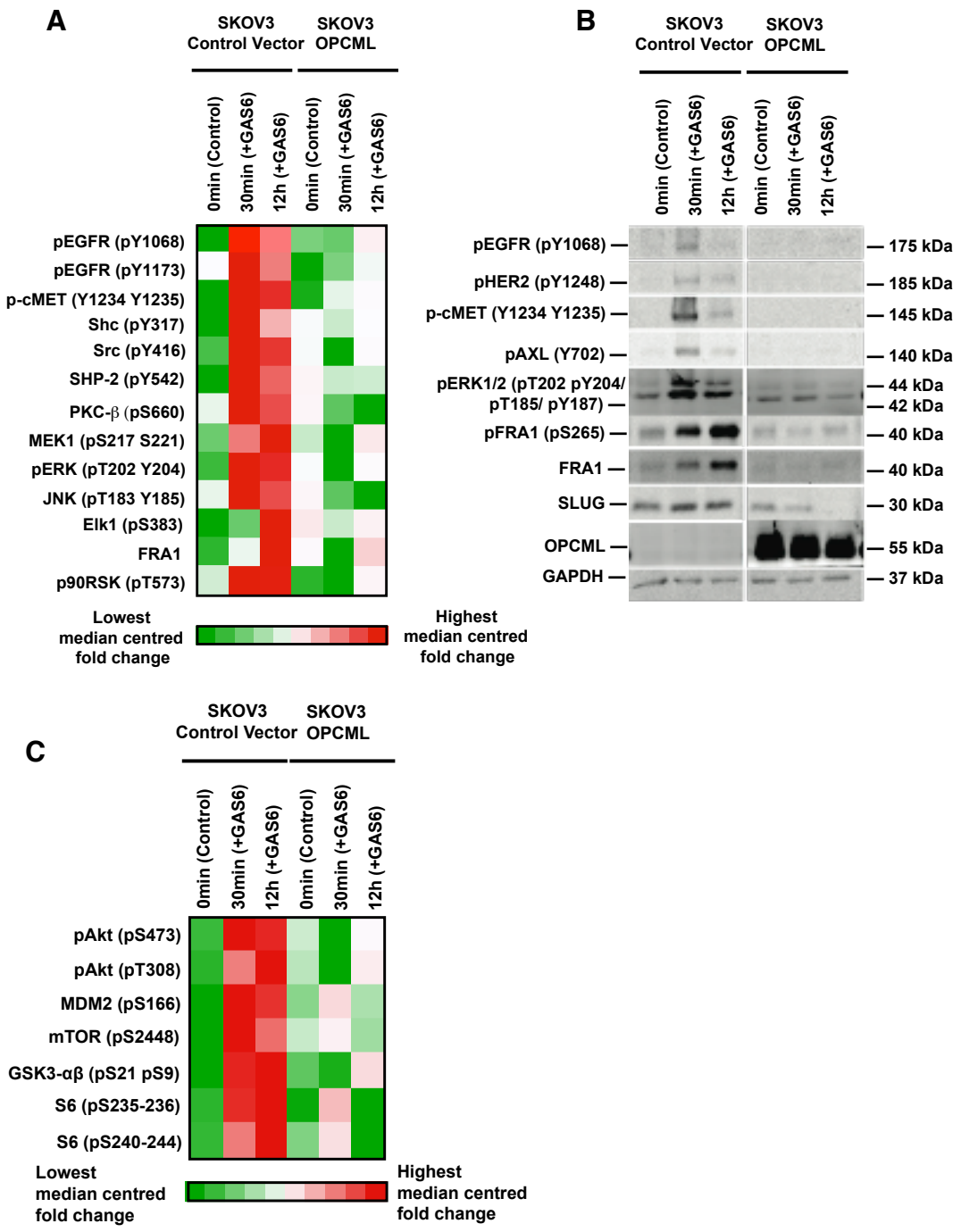


Figure 42: Functional Proteomics reveals suppression of oncogenic signaling by OPCML at a systems level.

(A, C) RPPA data showing phospho-RTK and downstream signaling moieties activated by Gas6/AXL stimulation in SKOV3-EMPTY and SKOV3-OPCML. Following serum starvation, cells were treated with Gas6 for 30 minutes or 12 hours, while control cells were unstimulated. Samples were run through the MD Anderson RPPA Core. Data is represented as Log2 normalized and median centred.

(B) Western Blotting of SKOV3-EMPTY and SKOV3-OPCML upon AXL activation, for pEGFR, pHER2, pMET, pAXL and downstream signaling moieties pERK1/2, pFRA1, FRA1 and the EMT transcription factor SLUG. GAPDH was used as loading control. Blots are representative of three experiments.

Drawing a parallel to the epithelial Epi-A versus EMT-ed Mes systems, it is intriguing that OPCML expression in the Mes subtype SKOV3 reverts AXL signaling to one that mimics an epithelial phenotype. The next step was to evaluate if OPCML expression in an epithelial system altered the transient Gas6/AXL/ERK signaling. Epi-A subtype PEO1 cell line was stably transduced with OPCML to check for changes in signaling kinetics. In PEO1-OPCML, there was no alteration of temporal duration of pAXL or pERK upon Gas6 stimulation compared to PEO1-EMPTY (Figure 43), suggesting that OPCML modulation of AXL would principally benefit EMT-ed systems that amplified AXL signaling.

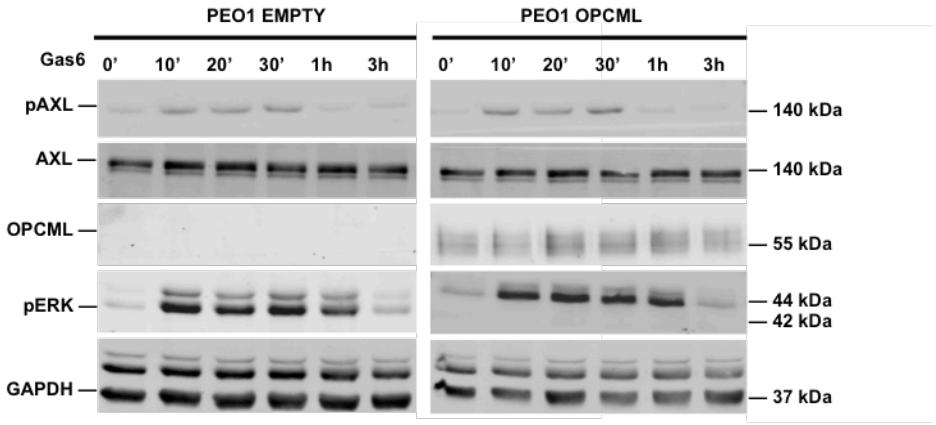


Figure 43: OPCML overexpression does not alter signaling dynamics in epithelial PEO1 cells.
PEO1 cells stimulated with Gas6 over a 3-hour time course, revealed no change in temporal duration of pAXL and pERK response upon OPCML overexpression. Given the transient nature of signaling in epithelial systems, OPCML overexpression does not further curtail signaling dynamics. GAPDH was used as loading control. Blots are representative of three experiments.

4.2.6 OPCML abrogates Gas6/AXL mediated cell motility and invasion.

As AXL has been described widely for its role in stimulating cell migration and motility[181], similar to the MAPK pathway[181], we investigated how the suppression of AXL signaling by OPCML would affect Gas6/AXL-mediated motility in SKOV3 and PEA1 cells.

In both cell lines, control cells responded to Gas6 stimulation and showed a significant increase in kinetic parameters of motility, such as displacement and speed, compared to non-stimulated cells (Figure 44A-D). In contrast, OPCML expressing cells showed no change in these parameters upon stimulation with Gas6, with displacement and speed values at the same levels as non-stimulated cells (Figure 44A-D).

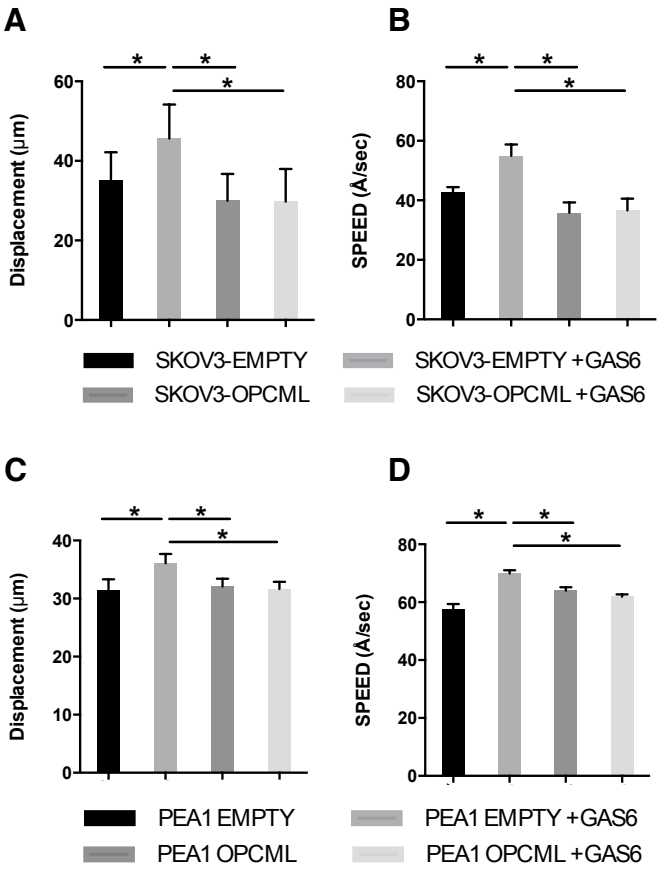


Figure 44: OPCML expression abrogates Gas6/AXL induced cell motility.
(A, B) In SKOV3 cells stimulated with Gas6, there was an induction of motility over a 12 hour period as recorded by displacement and speed, which was prevented upon OPCML expression
(C, D) Similarly in PEA1, Gas6/AXL induced increase in displacement and speed was abrogated upon OPCML expression.
Single cell tracking analysis was done on ImageJ using Trackmate, following overnight capture of cell tracks on Leica SP5 confocal at 10 minutes intervals. Means ± SEM from three experiments. Paired 2-tailed Student's t-tests were used to determine statistical significance * $p < 0.05$.

We also measured collective cell migration in wound healing assays using both cell lines. Gap closure measurements showed that SKOV3-EMPTY responded very efficiently to Gas6 stimulation and rapidly closed the gap (74% closure at 10 hours), while the untreated did not (23% closure) (Figure 45A and 45B) Nonetheless, SKOV3-OPCML cells did not respond to Gas6 stimulation (8% closure) and showed no difference in collective cell migration compared to their untreated counterparts (9% closure) (Figure 45A and 45B). Similarly, though more migratory, PEA1-EMPTY cells were also responsive to Gas6 stimulation and closed the gap faster, while PEA1-OPCML cells showed no response to Gas6 and no change in their collective cell migration compared to untreated cells (Figure 45C and 45D).

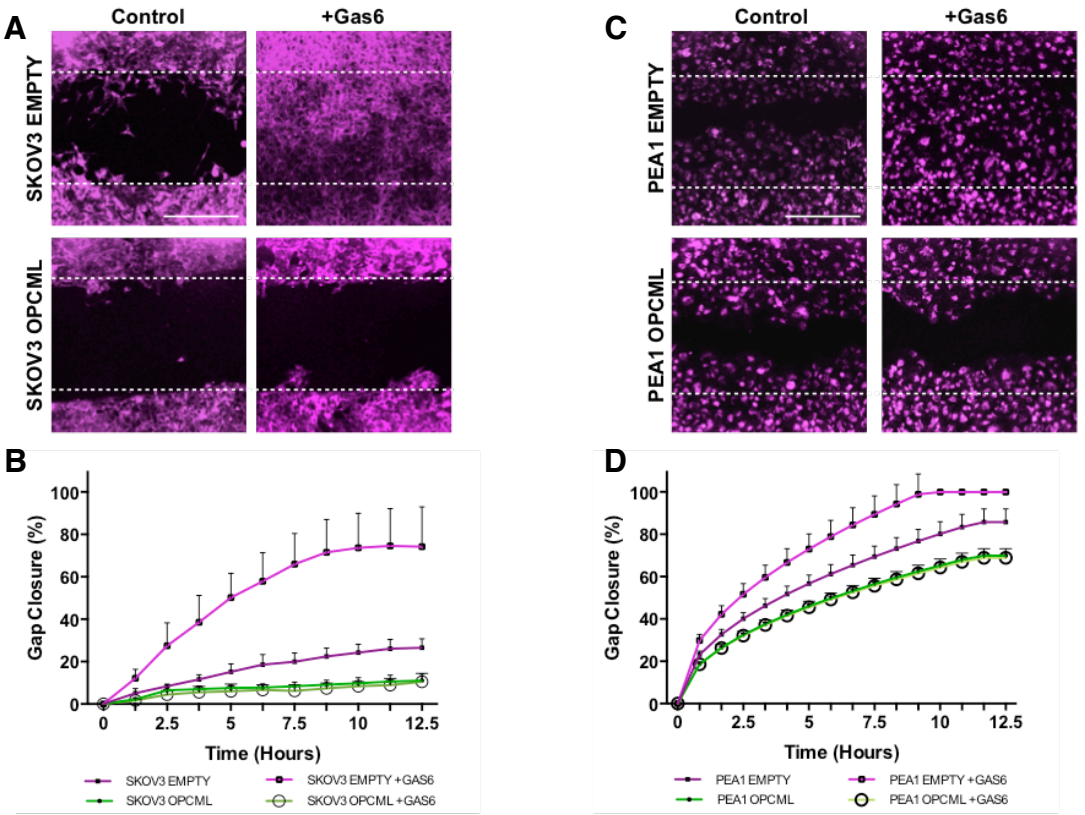


Figure 45: OPCML expression reduces gap closure rates.
(A, C) Gas6/AXL activation inducd acceleration in cell migration was countermanded by OPCML expression, in both SKOV3 and PEA1. (B, D) Gap closure analysis was done on ImageJ, following overnight capture of Gap closure on Leica SP5 confocal at 10 minutes intervals. Dashed white lines represent initial boundary and scale bars represent 200µm. Images and quantitation are representative of three experiments.

SKOV3-EMPTY cells had elevated phospho-ERK staining at 12 hours upon Gas6 stimulation, while this was negated in SKOV3-OPCML cells (Figure 46), thus confirming our previous observations that OPCML blunts the response to Gas6, and this prevents Gas6/AXL mediated motility.

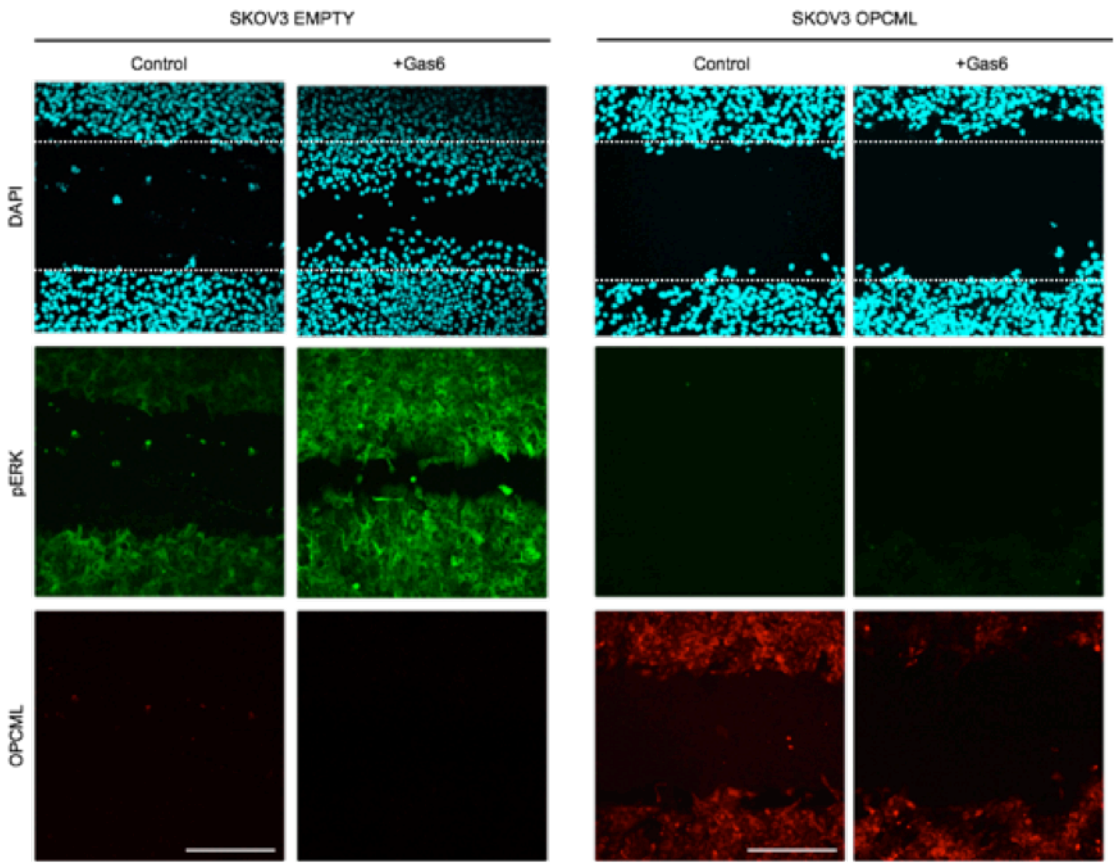


Figure 46: Immunostaining of gap closure reveals abrogation of pERK upon OPCML expression.
In SKOV3-EMPTY and SKOV3-OPCML, gap closure after 12 hours Gas6 stimulation was fixed with ice-cold methanol and stained for DAPI, pERK and OPCML. Immunostaining revealed pERK response to Gas6 stimulation in SKOV3-EMPTY and accelerated gap closure, but not in SKOV3-OPCML. Dashed white lines represent initial boundary and scale bars represent 200µm. Images are representative of three experiments.

To evaluate the effect of OPCML on cell invasion in a three-dimensional environment, SKOV3-EMPTY and SKOV3-OPCML cells were seeded as spheroids into a collagen matrix and stimulated with Gas6. While stimulated SKOV3-EMPTY spheroids showed hairy-like invasive cells/protrusions compared to their untreated counterparts after 3 days, OPCML expressing cells remained unresponsive to Gas6 stimulation (Figure 47A and 47B). This points to OPCML exerting a powerful tumor suppressor effect upon activation of the Gas6/AXL oncogenic pathways in a 3D setting. Interestingly, the fold change of the untreated SKOV3-EMPTY cells was also significantly higher compared to the SKOV3-OPCML cells suggesting OPCML exerts a basal tumor suppressor effect in a 3 dimensional environment, even in the absence of a ligand.

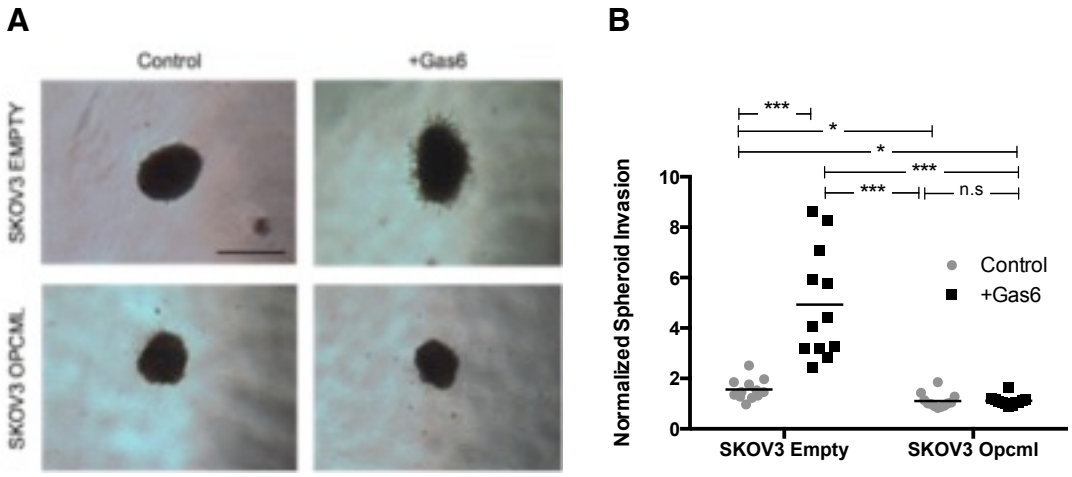


Figure 47: OPCML negates Gas6/AXL mediated spheroid invasion.
(A) Spheroid invasion assay showed invasion of SKOV3-EMPTY spheroid 72 hours post stimulation with Gas6. Upon OPCML expression, Gas6 mediated invasion is averted. Scale bars represent 1000µm. Images are representative of three experiments.
(B) ImageJ software to calculate the average radius r of spheroids; invasion volume was calculated using $4\pi r^3/3$, and normalized to spheroid volume prior to addition of chemotactic medium. Means from three experiments. Paired 2-tailed Student's t-tests were used to determine statistical significance * $p < 0.05$, ** $p < 0.01$, *** $p < 0.001$.

4.2.7 Integrity of Lipid Rafts is crucial for OPCML modulation of AXL signaling.

Upon activation of AXL by Gas6, and subsequent interaction with OPCML, the RTK-tumor suppressor complex is recruited into the lipid rafts where the GPI-anchored OPCML resides. There is subsequent dephosphorylation of AXL and deterrence of downstream signaling and function. In order to determine whether this change in compartmentalization of AXL into the lipid rafts is one of the main mechanisms of action of OPCML, experiments were carried out to disrupt the integrity of the DRM.

Methyl-β-cyclodextrin (MBCD) was used to extract cholesterol from the sphingolipid micro-domains that comprise of the DRM, so as to solubilize GPI-anchored and trans-membrane proteins from the DRM into the DSM[193]. 30 minutes treatment with MBCD was sufficient to deplete cholesterol as evident by lack of cholesterol-bound Filipin staining[194] compared to untreated control (Figure 48). This cholesterol depletion lasted up to 12 hours post MBCD treatment (Figure 48), enabling analysis of the effects of lipid raft perturbation on Gas6 kinetics over this time course.

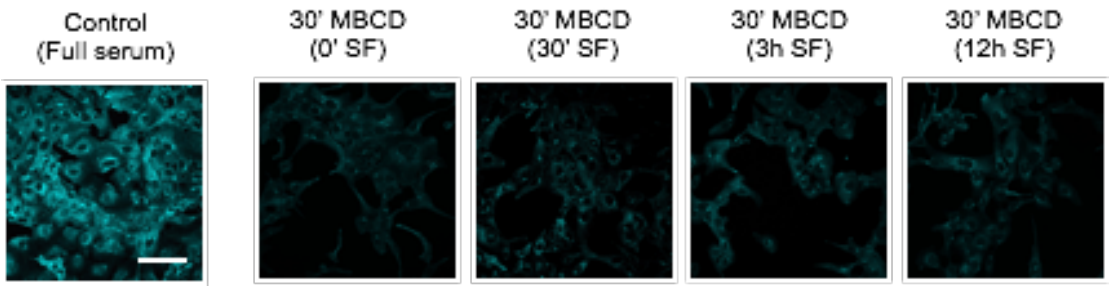


Figure 48: MBCD treatment depletes cells of cholesterol.
SKOV3-OPCML cells were treated for 30 minutes with 5mM MBCD and allowed to recover for 0, 30 minutes, 3 and 12 hours in serum free medium, and subsequently fixed with ice-cold methanol. The cells were stained with 0.05mg.mL^{-1} Filipin to visualize cholesterol, and observed under the Leica SP5 confocal. As a control, SKOV3-OPCML cells that were not treated with MBCD were also fixed and stained with Filipin. Images are representative of three experiments.

Post MBCD treatment, we analyzed AXL distribution by membrane fractionation in SKOV3-OPCML. In MBCD treated SKOV3-OPCML, there is no shift of total AXL protein from the DSM into the DRM, unlike the control cells, where OPCML modulation of activated AXL causes accumulation of the RTK in the DRM (Figure 49A and 49B). Interestingly, Caveolin-1, which is used as a marker for the DRM, was observed in both fractions upon MBCD perturbation of the rafts (Figure 49A). The GPI-anchored OPCML, which also preferentially resides in the rafts, showed a similar trend (Figure 49A). Given MBCD solubilizes cholesterol and modifies the integrity of the ordered lipid rafts, this could explain why there is shift of OPCML and Caveolin-1 into the remodeled DSM. Following the lack of discrete membrane micro domains, and free movement of OPCML, there can be only minimal membrane partitioning of AXL.

Given the lack of AXL accumulation in the remnants of the original raft fraction or DRM, we analyzed the pAXL kinetics. Upon Gas6 stimulation in MBCD treated SKOV3-OPCML, there was a significant increase in pAXL accumulation in the both membrane fractions (Figure 49A and 49C). Given the mechanism of modulation of OPCML wherein it modulates AXL by changing its membrane localisation, it is not surprising that loss of membrane architecture prevents AXL compartmentalization, and enables the RTK to signal in its activated form in the remodeled membrane fractions. Also, upon MBCD treatment, there is pAXL present in the remnants of the DRM (Figure 49A). This could be due to changes in the raft architecture that prevent the previously observed dephosphorylation of pAXL.

To further analyse the effect of raft perturbation, SKOV3 cells were stimulated with Gas6 post MBCD treatment. In SKOV3-EMPTY, the sustained pAXL and pERK responses increased in magnitude upon loss of raft architecture (Figures 50A-C). This could be due to reorganization of signaling platforms and loss of the integral

DRM domains where AXL is usually inactive. In SKOV3-OPCML, MBCD reversed the transient pAXL and pERK response (Figures 50A-C). The pAXL and pERK activation persisted from early time point of 30 minutes up till 12 hours in MBCD treated SKOV3-OPCML cells, accounting for complete loss of function of OPCML in the disruption of raft domains. Given the previous observations, where raft integrity was crucial for the GPI-anchored OPCML to sequester and shut down AXL in the DRM, it follows that loss of spatial reorganization of AXL upon OPCML binding in MBCD treated cells enables sustained signaling of AXL, and consequently pERK.

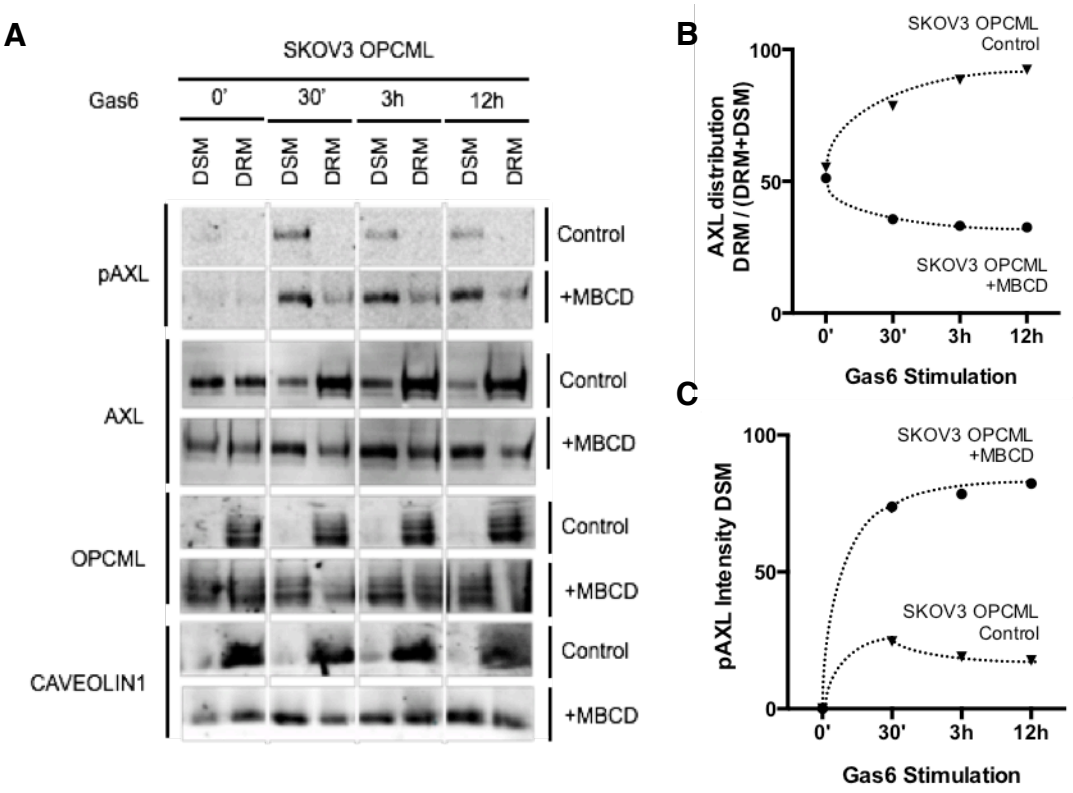


Figure 49: Disruption of lipid rafts prevents OPCML mediated sequestering of AXL in the rafts, and consequently fails to curtail signaling.
(A) MBCD treatment mediated lipid raft disruption showed a shift of the raft marker Caveolin-1, as well as the GPI-anchored OPCML, from the DRM into the DSM. Subsequently, OPCML failed to sequester AXL in the drafts, allowing a larger portion of the RTK to remain in the DSM and signal through its phosphorylated form.
(B) Ratio of AXL band intensity in DRM, to total AXL in DRM and DSM, in SKOV3-OPCML cells, treated with MBCD, as well as no treatment control.
(C) Ratio of pAXL band intensity in DSM in SKOV3-OPCML cells, treated with MBCD, as well as no treatment control.
Blots and quantification are representative of three experiments.

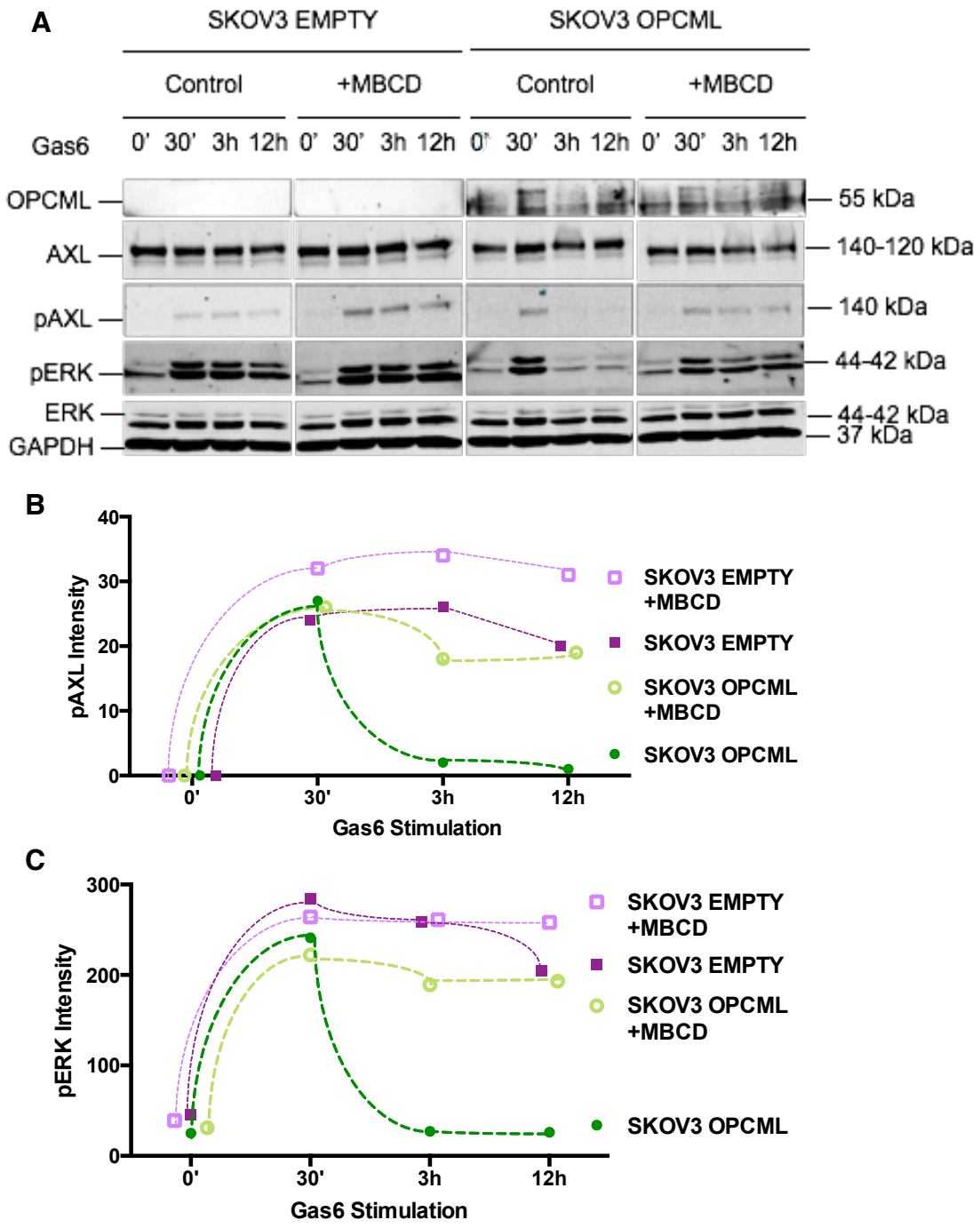


Figure 50: Lipid Raft perturbation prevents OPCML from restraining Gas6/AXL signaling.

(A) MBCD treatment in SKOV3-EMPTY and SKOV3-OPCML cell lines, followed by Gas6 signaling kinetics. As evident by the persistent pAXL and pERK response, disruption of lipid rafts in SKOV3-OPCML returns the system to a sustained signaling phenotype such as the SKOV3-EMPTY. GAPDH was used as loading control.

(B, C) Signaling kinetics as represented by pAXL and pERK in SKOV3-EMPTY and SKOV3-OCPML, treated with MBCD and control, normalized to GAPDH.

Blots and quantification are representative of three experiments.

Also, it was crucial to decode whether the loss of signaling suppression was exclusively due to disruption of the rafts, or possibly due to other mechanisms such as loss of interaction between AXL and OPCML. Following MBCD treatment, SKOV3-OPCML cells were stimulated with Gas6 over a 12 hour time course. Even upon loss of raft architecture, AXL-OPCML interaction could be visualized post Gas6 stimulation but not in serum starved condition (Figure 51A). However, this interaction reached maximal values at 30 minutes and was retained till 12 hours, unlike the control SKOV3-OPCML, where the AXL-OPCML interaction accumulated over time (Figure 51A and 51B). Following raft disruption, this could be due to increased mobility of OPCML through the membrane architecture, enabling it to bind activated AXL.

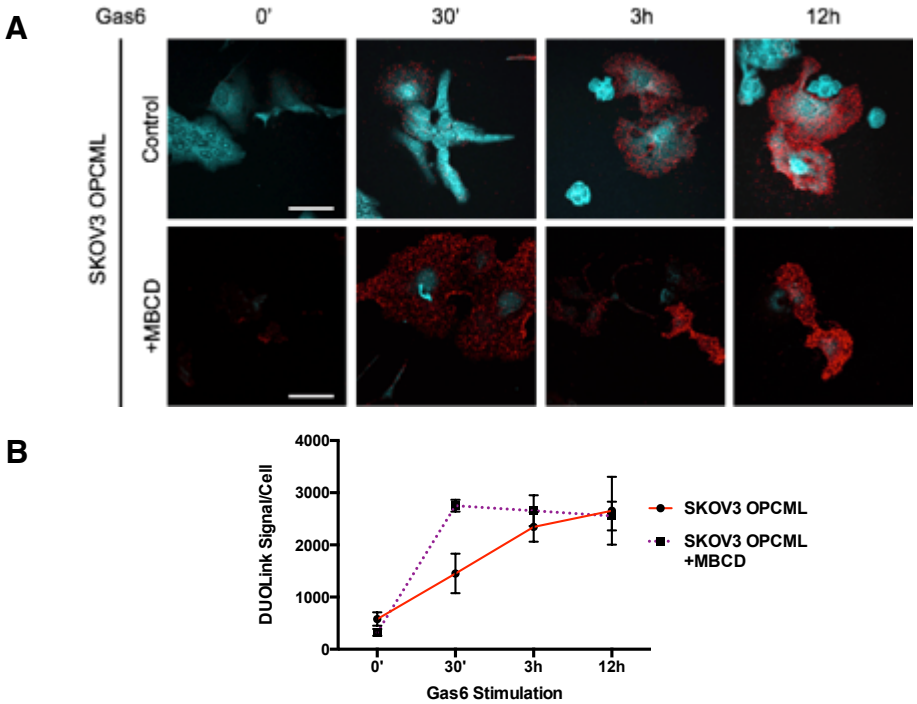


Figure 51: PLA assay reveals AXL-OPCML interaction irrespective of lipid raft integrity.
(A) DUOLink PLA assay revealed increasing AXL-OPCML interaction upon Gas6 stimulation in both MBCD treated and control SKOV3-OPCML cells. Scale bar represents 50µm. Images are representative of three experiments.
(B) Quantification of PLA signals showed AXL-OPCML interaction increasing with time. Means ± SEM from three experiments.

4.2.8 OPCML modulation of other RTK signaling nodes.

To further understand the nature of the OPCML modulation of RTK signaling, SKOV3-EMPTY and SKOV3-OPCML cells were serum starved and then stimulated with either Gas6, Hepatocyte Growth Factor (HGF), and Epidermal Growth Factor (EGF), for 3 hours. Gas6 stimulation phosphorylated AXL and subsequently activated EGFR, HER2 and cMET in SKOV3-EMPTY cells (Figure 52). The Gas6 mediated activation was countermanded in SKOV3-OPCML cells, possibly due to change in localisation of AXL from the DSM to DRM that prevented AXL-RTK clustering and cross phosphorylation (Figure 52).

Due to the degree of RTK cross talk prevalent in the Mes subtype, HGF stimulation phosphorylated cMET and also AXL, EGFR, and HER2 in SKOV3-EMPTY. Similarly, EGF stimulation phosphorylated EGFR, HER2, and eventually AXL and cMET (Figure 52). Interestingly, OPCML overexpression annulled this signal propagation through cMET as it did to signal propagated through AXL, but to a much lesser degree for signal propagated through EGFR (Figure 52).

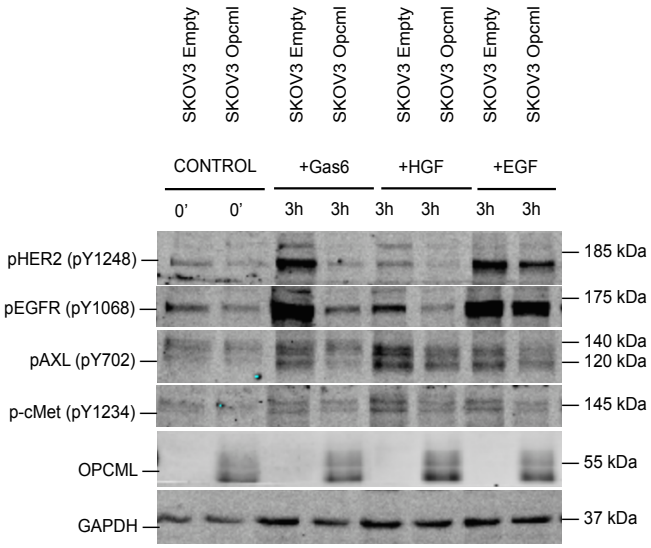


Figure 52: In addition to Gas6, OPCML suppresses HGF mediated signaling, but not EGF.
Western blotting of and SKOV3-OPCML treated with Gas6, HGF and EGF showed reduced RTK cross talk and phosphorylation in a Gas6/AXL, and HGF/cMET system, but to a lesser extent through EGF/EGFR, when compared to SKOV3-EMPTY cells. GAPDH was used a loading control. Ligand induced stimulation was compared to unstimulated controls (0 minutes). Blots are representative of three experiments.

Our group has previously shown that OPCML does not interact with EGFR, and to reconfirm this, GST-OPCML pull down assays were utilized. The results showed that OPCML did indeed interact with HER2 and cMET, but not EGFR (Figure 53). This could potentially mean that following cMET activation by HGF, OPCML might bind the activated form of the RTK and change its localisation to the lipid raft and subsequently prevent activation of AXL, EGFR and HER2. However, given OPCML does not bind to EGFR, activated EGFR potentially continues to signal in the DSM and can cluster and activate other RTKS. However, the partial modulation of the EGF/EGFR pathway could be due to OPCML interaction with HER2.

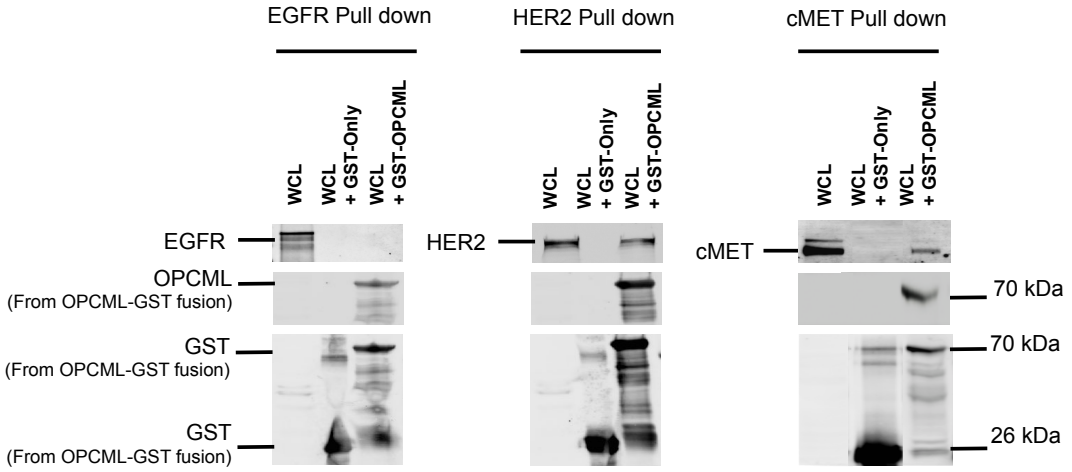


Figure 53: GST-OPCML pull down assay reveals OPCML interaction with HER2 and cMET, but not EGFR.
Western blotting the OPCML-GST pull down eluate for HER2 and cMET shows a positive signal, but not EGFR As a negative control, GST only was used and there was no visible interaction with AXL. WCL: Whole cell lysate from SKOV3-EMPTY (in cMET pull down) or breast cancer cell line SKBR3 (for EGFR and HER2 pull down) that are positive for AXL Blots are representative of three experiments.

Given the interaction between cMET and OPCML, SKOV3 cells were stimulated with HGF over a 24 hour time-course. SKOV3-EMPTY cells showed strong pMET activation from 10 minutes onwards, till 1 hour and a weaker activation that persisted till 12 hours. This was succeeded by a strong pERK response at the early time points that extended till the 6 hour time point (Figure 54). In SKOV3-OPCML, only a faint pMET response was seen upon HGF stimulation and this did not persist past 1 hour (Figure 54). This was similar of the effect of OPCML expression on reducing temporal duration of pAXL response to Gas6 in SKOV3 and PEA1. Consequently, the pERK response to HGF was also shorter in SKOV3-OPCML (Figure 54).

These experiments served to highlight the conserved yet specific nature of RTK modulation by OPCML. The studies on AXL can be extended to other RTKs, such as cMET, to show a proof of concept of tumor suppressor function in either the same tumor driven by multiple aberrations or different tumors driven by a specific network. However, the nature of modulation is restricted to a certain combination of RTK nodes and hence an EGFR driven tumor system might be less responsive to OPCML based therapy.

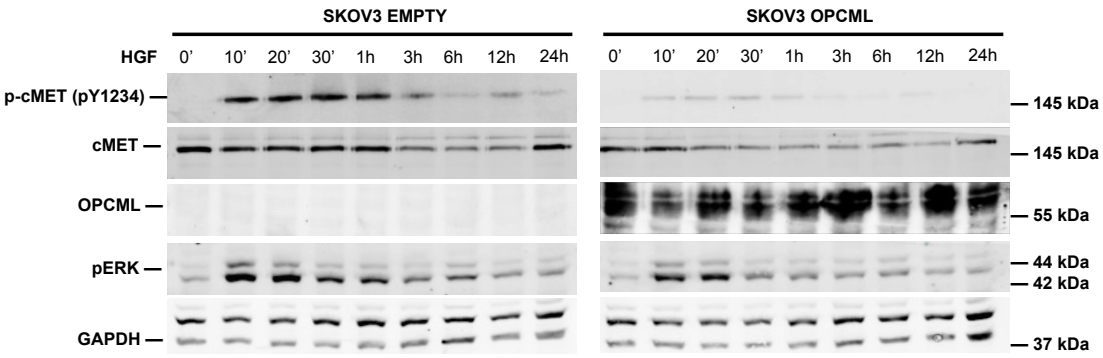


Figure 54: OPCML expression curtails HGF mediated signaling.
SKOV3-EMPTY and SKOV3 OPCML cell lines were serum starved and stimulated with HGF over a 24 hour time course. OPCML expression reduced both the magnitude, as well as temporal duration of pMET and pERK response. GAPDH was used as a loading control. Blots are representative of three experiments.

4.2.9 Silencing OPCML increases temporal duration of Gas6/AXL signaling.

Given OPCML overexpression in ovarian cancer cell lines decreases oncogenic signaling, experiments were performed to analyze if silencing OPCML would amplify the same. Due to lack of expression of OPCML in most cancerous systems, immortalized Fallopian Tube Epithelium 190[195] (FTE190) cells were utilized. In this non-cancerous system, OPCML was silenced using siRNA (Figure 55).

Following siOPCML transfection, the FTE190 cells were treated with Gas6 over a time course period. In the Non-targeting siRNA control, the FTE190 showed minimal response to Gas6 stimulation with only a slight pERK response at 20 minutes (Figure 56). In OPCML silenced cells, the Gas6 stimulation strongly induced a pERK response that persisted from 10 minutes till an hour (Figure 56). This suggests that in non-cancerous systems, AXL is under tight regulation by several tumor suppressors. Hence silencing OPCML, while amplifying the minimal signal to a stronger response, fails to sustain it over a 24 hour time course, unlike the cancerous SKOV3 or PEA1 system.

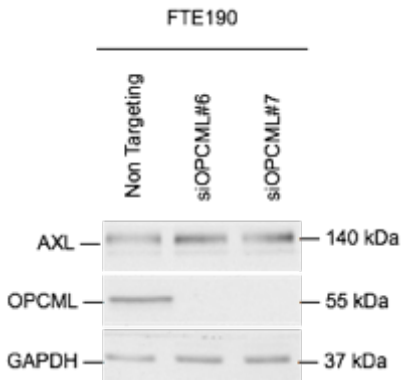


Figure 55: siRNA mediated OPCML silencing in FTE190.
Non-cancerous fallopian tube epithelium cells FTE190, which express OPCML were transfected with siRNA to study the effect of OPCML inhibition. Two sequences siOCPML#6 and siOPCML#7 gave more than 90% protein knockdown as visualized by western blotting. A non-specific non-targeting siRNA was used as a negative control. GAPDH was used as loading control. Blots are representative of three experiments.

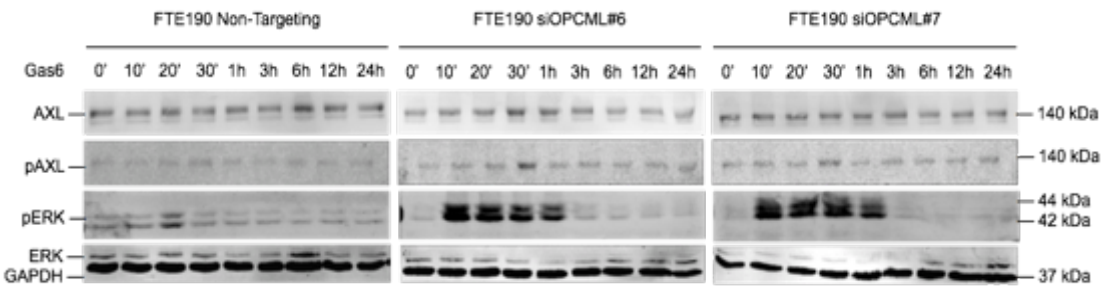


Figure 56: siOPCML FTE190 show increased response to Gas6 stimulation. FTE190 cells were transfected with a non-specific non-targeting siRNA or OCPML silencing sequences, siOPCML#6 and siOPCML#7. After serum starvation and stimulation with Gas6 over a 24 hour time course, lysates were collected and immunoblotted for pAXL and pERK. While silencing OPCML in non-cancerous FTE190 increased the magnitude of pAXL and pERK response, the temporal response did not return to the sustained state observed in cancerous systems such as SKOV3 or PEA1. GAPDH was used as loading control. Blots are representative of three experiments.

To translate the effect of signaling amplification phenotypic assays with OPCML silenced FTE190 cells were carried out. Colorimetric proliferation assays revealed that silencing OPCML increased proliferation in FTE190 (figure 57A). In the non-targeting siRNA control, Gas6 stimulation had minimal effects on proliferation. However in siOPCML cells, Gas6 stimulation increased proliferation (Figure 57A). From the previous chapter, we have seen that a transient ERK activation is sufficient to increase proliferation, and given siOPCML increases the ERK activation to an hour, it could explain the Gas6 induced proliferation in FTE190.

In single cell motility assays siOPCML increased kinetic parameters such as displacement and speed compared to non-targeting siRNA transfected FTE190 (Figure 57B and 57C), potentially due to loss of tumor suppressor function. However, there was no further increase in motility in response to Gas6 stimulation (Figure 57B and 57C). This could be due to the requirement of a sustained ERK response for motility response. As siOPCML only partially restores the temporal duration Gas6/AXL signaling in FTE190, it causes the system to show a proliferative response to Gas6 rather than the motility phenotype. The gap closure rates showed no difference between siOPCML and non-targeting siRNA (Figure 57D and 57E).

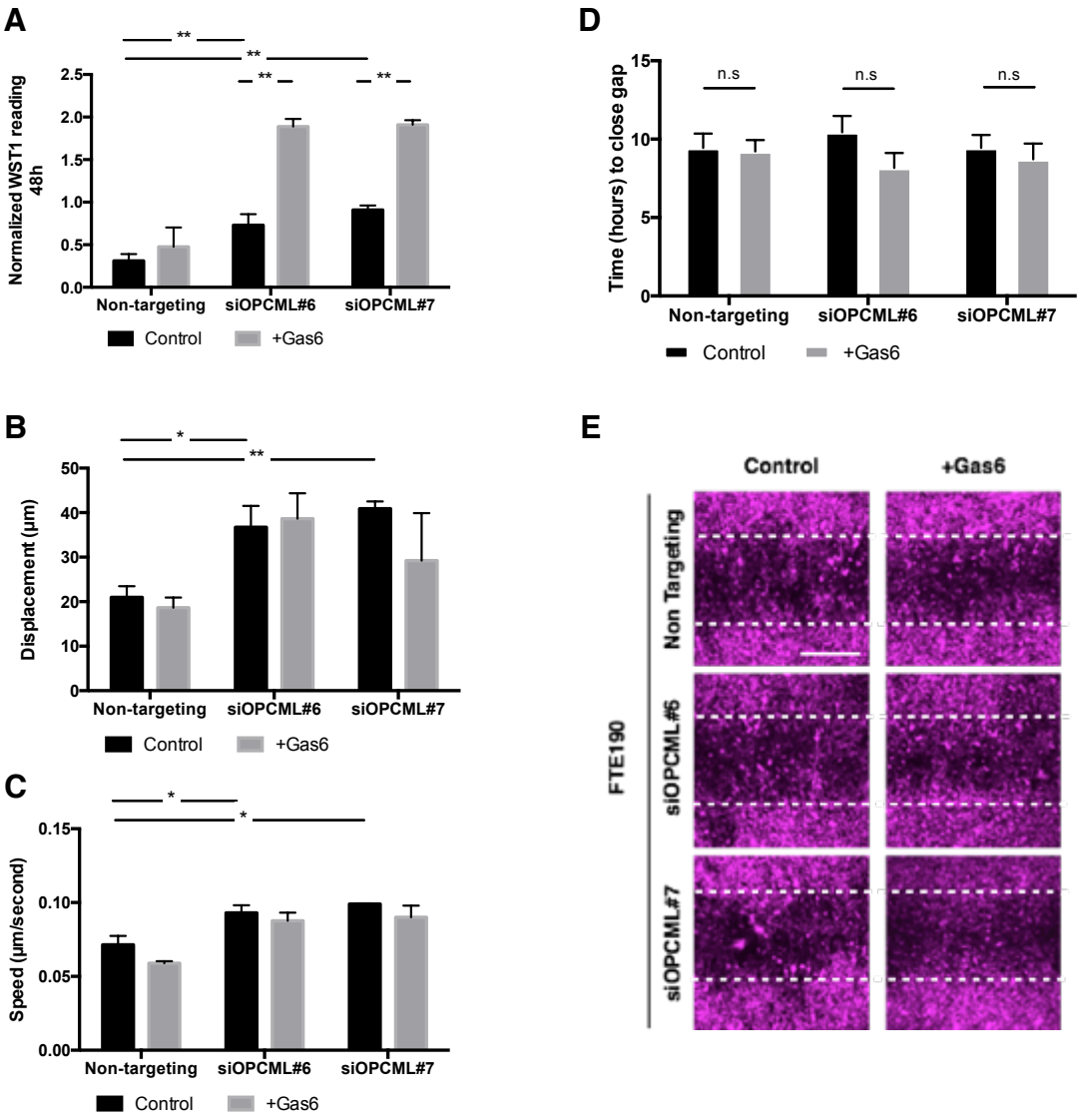


Figure 57: Silencing OPCML in FTE190 increases proliferation but not motility upon Gas6 stimulation.

(A) For OPCML silenced FTE190 cell lines, WST1 calorimetric proliferation assay showed significant increase in proliferation compared to non-targeting siRNA control. Also, siOPCML transfected FTE190 showed dramatic increase in proliferation when treated with Gas6, as compared to no treatment control, but not the non-targeting siRNA transfected control. WST1 readings at 48 hours were normalized to day 0 readings to measure proliferation.

(B, C) Single cell motility analysis of FTE190 cells transfected with siOPCML showed no Gas6 induced motility, compared to si-Non Targeting control. The basal motility of siOPCML transfected FTE190 was however higher than the si-Non Targeting control.

(D, E) Gap closure assays showed no difference in cell migration rates between FTE190 transfected with si-Non targeting control or siOPCML, with or without Gas6. Dashed white lines represent initial boundary and scale bars represent 200µm. Images are representative of three experiments.

Means ± SEM from three experiments. Paired 2-tailed Student's t-tests were used to determine statistical significance * $p < 0.05$, ** $p < 0.01$, *** $p < 0.001$.

4.2.10 OPCML potentiates the effects of the AXL inhibitor R428.

In order to investigate whether the OPCML-induced abrogation of signaling could translate into a potential clinical benefit, SKOV3 control and OPCML expressing cells were treated with the AXL inhibitor R428. As shown in Figure 58, when we measured cell viability in R428 treated cells, we could observe that OPCML reduced the mean GI-50 of R428 from 2.84 µM to 1.09 µM, resulting in a 2.6 fold decrease of the dose of the inhibitor required for an GI-50 effect. Furthermore, in the presence of OPCML cells showed attenuation of Gas6/AXL signaling at lower doses of R428 compared to control cells in both western blot and immunofluorescence (Figure 59A and 59B). AXL, AKT and ERK phosphorylation were attenuated when SKOV3-EMPTY cells were incubated with R428 at 2.84 µM, but not at lower doses, whilst upon OPCML expression, Gas6/AXL signaling was curtailed at 1.09 µM of the drug. This sensitization to the AXL inhibitor is thus a consequence of the synergistic effect between OPCML downmodulation of Gas6/AXL signaling and R428 inhibition of the catalytic kinase domain of AXL. To translate the AXL signaling inhibition to a biologically relevant system, the SKOV3-EMPTY and SKOV3-OPCML cell lines were embedded in Matrigel and deposited on top of the chick chorion allantoic membrane (CAM). The cell lines were pre-incubated with R428 and allowed to form tumors in the CAM.

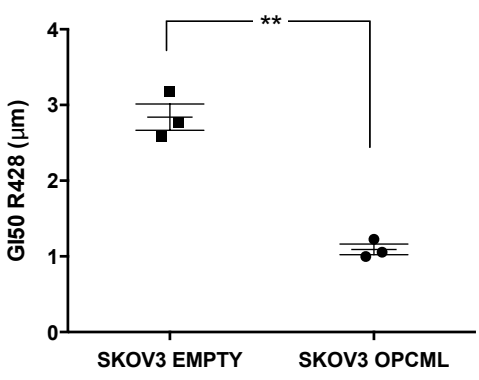


Figure 58: OPCML expression sensitizes SKOV3 cell lines to AXL inhibitor R428.
The mean GI50 of SKOV3-OPCML was significantly lower at 1.09 µM compared to the mean GI50 of SKOV3-EMPTY at 2.84 µM (p = 0.0045, Student's t-tests). GI50 values were calculated by assessing 50% growth inhibition using cell titer MTS calorimetric cell proliferation assay.
Means ± SEM from three experiments. Paired 2-tailed Student's t-tests were used to determine statistical significance * $p < 0.05$, ** $p < 0.01$, *** $p < 0.001$.

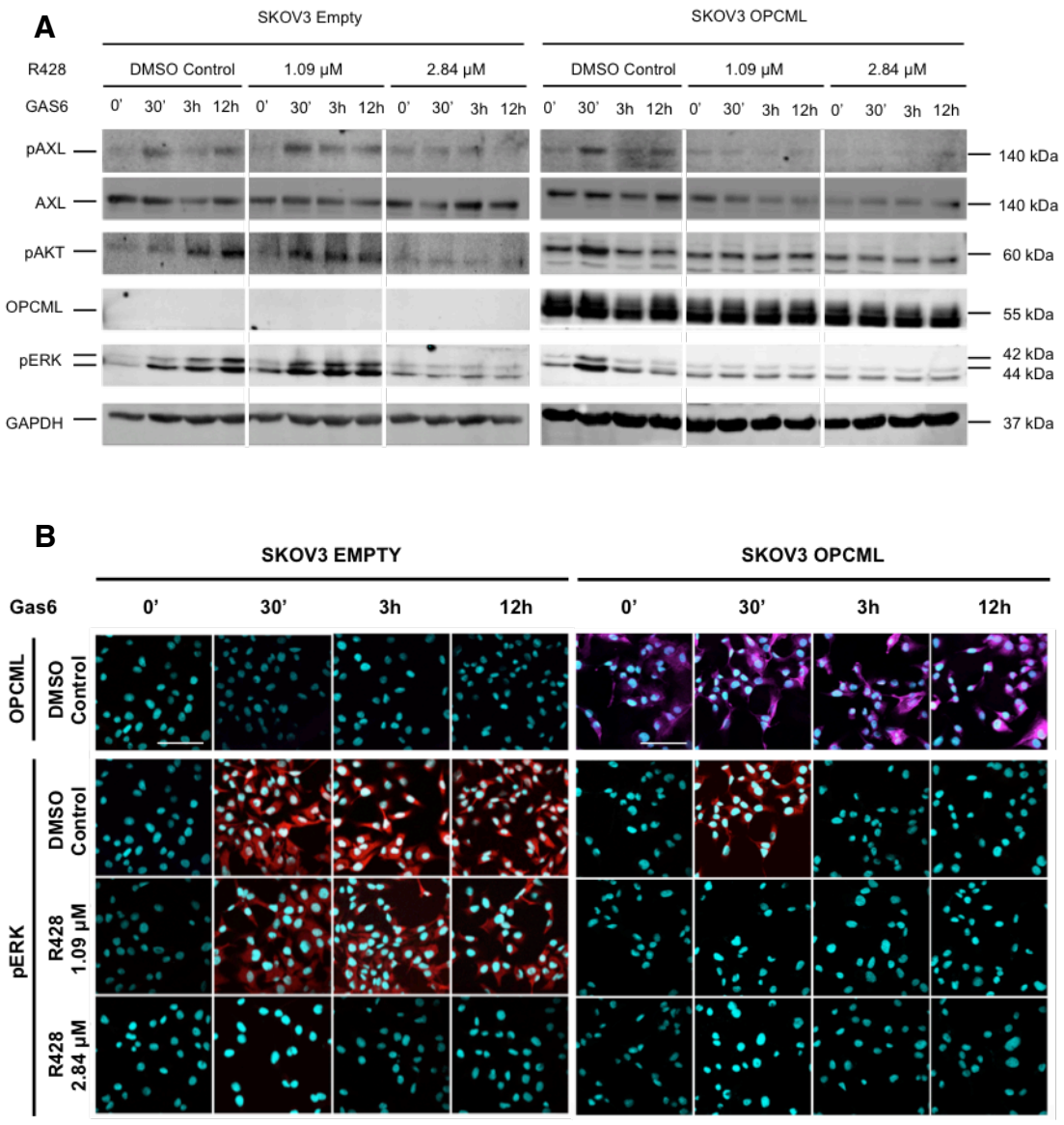


Figure 59: OPCML expression synergizes signaling inhibition by AXL inhibitor R428.

(A) Western Blotting of SKOV3-EMPTY and SKOV3-OPCML cell lines for pAXL, pAKT and pERK, showed signaling inhibition at lower doses of R428 in OPCML expressing cells preferentially. The cells were pre incubated with with either no drug (DMSO only control), 1.09 µM R428, or 2.84 µM R428 for an hour and stimulated with Gas6 for 0 minutes, 30 minutes, 3 hours and 12 hours. GAPDH was used as loading control. Images are representative of three experiments.

(B) Immunofluoresence staining for pAXL, pAKT and pERK, revealed preferential signaling inhibition at lower doses of R428 in SKOV3-OPCML. The transient pERK observed in SKOV3-OPCML was abrogated even at 1.09 µM R428, while the sustained pERK activation in SKOV3-EMPTY was reduced only at 2.84 µM R428. Scale bars represent 50µm. Images are representative of three experiments.

The *in ovo* findings substantiated the *in vitro* signaling inhibition results, with the SKOV3-EMPTY forming large tumors, which were significantly suppressed at 2.84 µM, but less so at 1.09 µM of R428 (Figure 60A and 60B). However, SKOV3-OPCML showed significant sensitization at both concentrations of R428 (Figure 60A and 60B). Of note, at 1.09 µM of R428, SKOV3-OPCML shows a much higher sensitisation to AXL inhibition, compared to SKOV3-EMPTY (Figure 60A and 60B). Potentially, this could have thrapeutic benefits in terms of reduced systems doses of RTK inhibitiors in conjuction with OPCML based biotherapies, and therefore drastically reduce toxicity associated with small molecule inhibitors.

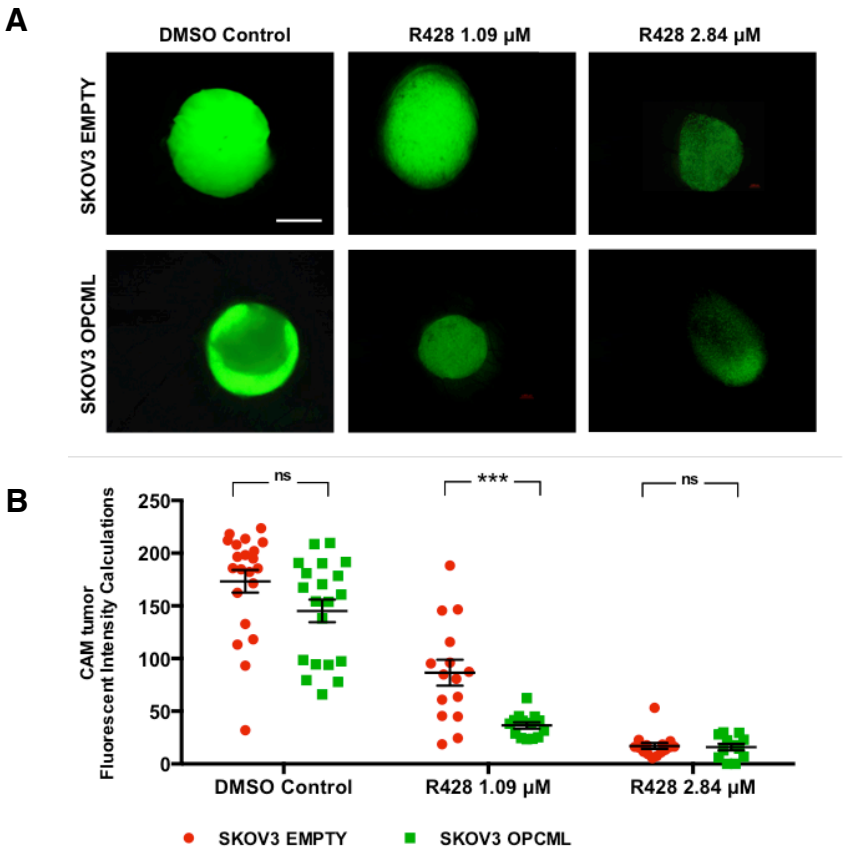


Figure 60: OPCML expression sensitizes SKOV3 to AXL inhibitor mediated in ovo tumor reduction.
(A) CAM assay showed inhibition of *in ovo* tumor growth at lower doses of R428 in SKOV3-OPCML, while SKOV3-EMPTY showed only partial inhibition At higher doses, both SKOV3-OPCML and SKOV3-EMPTY were inhibited. Scale bars represent 2000µm. Images representative of two experiments. (B) For tumor measurement, the mean fluorescent intentsity was calculated. Means ± SEM from two experiments. Unpaired 2-tailed Student's t-tests were used to determine statistical significance * $p < 0.05$, ** $p < 0.01$, *** $p < 0.001$.

4.3 DISCUSSION

The tumor suppressor OPCML is frequently silenced epigenetically by somatic methylation or through LOH mechanisms across a broad spectrum of cancers, implying selection for a powerful oncogenic effect through loss of a tumor suppressor protein. Given the previously observed prognostic relevance[145], delineating its mechanism of action is pivotal to understanding the cancer biology of this GPI-anchored protein. OPCML modulates the RTK AXL, which has been implicated in metastatic ovarian as well as breast[105], lung[107], thyroid, colorectal, pancreatic, renal, prostate and liver cancers[154]. In ovarian cancer, AXL is ectopically over-expressed and is prognostically adverse. It is implicated in metastasis and chemoresistance[159], and its role in cancer cell biology warrants further elucidation.

OPCML exhibits a higher affinity for AXL activated by Gas6, demonstrating remarkable specificity for tempering the effects of signaling in the oncogenic cancer state. Upon interaction with activated AXL, OPCML modifies the RTK's membrane distribution from the disordered plasma membrane to the more ordered 'lipid rafts' where GPI-anchored proteins like OPCML cluster. The partitioning of AXL away from the freely mobile DSM is followed by dephosphorylation of AXL in the DRM. Given the active phosphorylated form of AXL signals from the DSM, this change in RTK localization by OPCML could explain why AXL is prevented from trans-activating other RTKs such as EGFR and cMET. This drastically reduces the RTK cross talk and strongly abrogates downstream oncogenic responses from the Ras/MEK1/ERK pathway and also the PI3K-Akt pathway. The abrogation of the sustained oncogenic signaling downstream of the Gas6/AXL pathway by OPCML prevents induction and activation of response proteins such as ELK-1, p90RSK and FRA-1. FRA-1 induced cell motility[181] via the EMT transcription factor network involving ZEB-1, SLUG[170] etc. is also profoundly inhibited as a consequence of OPCML mediated abrogation of the

signaling cascade. The tumor suppressor effect of OPCML extended from abolishing Gas6/AXL induced single and collective cell motility in 2D, to inhibiting spheroid invasion in 3D systems. From a therapeutic perspective, OPCML modulation of AXL signaling further sensitizes the system to the AXL inhibitor R428, as evident by drastic decrease in signaling kinetics and *in ovo* tumor growth.

The ability of OPCML to exert its anti-tumor effect depends on it capacity to sequester and compartmentalize AXL to the lipid rafts. Depletion of cholesterol and perturbation of the membrane architecture prevented OPCML and consequently AXL from localizing to the rafts, and reversed the signaling kinetics in OPCML expressing cells to a sustained pAXL and pERK response state. This further leads to the speculation that by altering the membrane distribution of AXL, OPCML facilitates changes in signaling platforms by varying the availability of kinases and phosphatases; the role of the lipid rafts in modulating signaling kinetics has been well documented[188,196,197].

Interestingly, the modulation of RTK networks by OPCML is not restricted to the Gas6/AXL node. Its interaction with cMET prevents HGF mediated signaling, possibly via similar mechanisms. However, the specificity of RTK modulation depends on the ability of OPCML to interact with the RTK itself, and therefore it does not curtail signaling through the EGF/EGFR axis.

Given the nature of reversal of signaling kinetics by OPCML from a more sustained to a transient response, OPCML biotherapy would principally benefit EMT-ed mesenchymal systems in conjunction with relevant RTK inhibitors.

CHAPTER V: CONCLUSIONS AND FUTURE DIRECTIONS

5.1 SUMMARY OF RESULTS

The key findings from Chapters III and IV are summarized as follows:

1. In ovarian cancer AXL overexpression confers worse prognosis, and is enriched in the worse prognosis Mes subtype.
2. AXL signaling is amplified in Mes, due to RTK cross talk with EGFR, HER2, cMET to induce enhanced temporal duration of pERK response, and consequently motility.
3. Epi-A subtype, though positive for AXL, shows reduced signaling upon AXL activation by Gas6, suggesting an underlying mechanism for modulation in epithelial systems.
4. The amplification of AXL signaling sensitizes the Mes subtype to the AXL inhibitor R428. This opens up the potential to stratify patients based on the AXL gene signature, which is significantly enriched in Mes.
5. In Mes subtype, overexpression of the GPI-anchored tumor suppressor OPCML reverts the signaling from a persistent mesenchymal like phenotype to a transient epithelial like signaling modality.
    a. OPCML interacts with AXL and has a high affinity for the activated form of the RTK.
    b. OPCML alters AXL signaling by altering the membrane compartmentalization of AXL in Mes systems, from the liquid-disordered phase to the detergent-insoluble, liquid-ordered ‘lipid rafts’.
    c. Proteomics revealed that OPCML overexpression in Mes subtype reversed the global gene signature changes upon AXL activation to an epithelial like phenotype.

5.2 CONSIDERATIONS

One of the key questions that arose from the findings of Chapter III was to elucidate the mechanisms that dictated the linear AXL signaling module in Epi-A, versus the AXL-RTK crosstalk driven network in Mes. To validate if it is the EMT state of the system modulating the signaling schema, we utilized isogenic lines to study Gas6/AXL signaling kinetics. We proceeded to knock down epithelial status maintaining transcription factor GRHL2[149], or overexpress EMT inducing TWIST1[198] in epithelial OVCA429. This promoted a mesenchymal phenotype, and induced AXL-RTK crosstalk and recurrent pERK response (Appendix I), confirming our hypothesis that the EMT state dictates the signaling schema in EOC.

Another aspect that required further work was the mechanisms that regulated epithelial systems. In order to further decipher the differential modulation of AXL signaling in Epi and Mes systems, we investigated the role of membrane organized lipid rafts, which are known to regulate signal transduction[132,188]. Particularly, given the modulation of AXL signaling by OPCML occurs due to membrane partitioning of the RTK, we perturbed the membrane architecture in Epi-A systems to visualize the effect of functional rafts on AXL signaling. We proceeded to deplete cholesterol, an integral component of the lipid rafts, using Methyl-β-cyclodextrin (MBCD) in Epi-A cell lines PEO1, OVCA429 and Mes cell lines SKOV3 and HEYA8. Cholesterol depletion as measured by intensity of cholesterol bound Filipin staining, showed reduced membrane bound cholesterol up to 12 hours post MBCD treatment (Appendix II, Figure IIA). Following loss of integrity of membrane architecture, Gas6 stimulation resulted in AXL-RTK cross talk in Epi-A subtype PEO1 and OVCA429 at early (30 minutes) and late (12 hours) time points, but only induced pERK response at the early time point (Appendix II, Figure IIB). This suggested that epithelial systems are under modulation of more than just the membrane rafts. In order to investigate the

cause for the reduced pERK response, even upon increased AXL-RTK cross talk, the expression pattern of Dual Specificity Phosphatases (DUSPs) across Epi-A and Mes subtypes was analyzed. Interestingly, DUSP4, which was significantly lower in Mes subtype (Appendix II, Figure IIC and IID), is also known to dephosphorylate ERK and modulate the MEK-ERK cascade in ovarian cancer[199]. Silencing DUSP4 in Epi-A PEO1 and OVCA429 (Appendix II, Figure IIE), increased the temporal pERK response (Appendix II, Figure IIF), but not to the extent observed in mesenchymal systems. This could be explained by lack of AXL-RTK cross talk in Epi-A systems. Epi-A systems treated with both MBCD and siDUSP4 resulted in extensive AXL-RTK cross talk as well as pERK response at a later time point (Appendix II, Figure IIG). This confirms that the epithelial systems are under membrane modulation of RTK networks and DUSP4 regulation of pERK response, and loss of both these regulatory mechanisms will allow a signaling phenotype that is mesenchymal like (Figure J).

These findings serve to integrate the mechanism of action of OPCML in mesenchymal systems with the membrane modulation inherent in epithelial systems (Figure J). When OPCML is expressed in mesenchymal systems, it interacts with AXL and alters the RTK's membrane compartmentalization into the lipid rafts, thereby restoring the membrane modulatory effects. Given the lack of DUSP4 in mesenchymal systems, OPCML mediated restoration of raft-membrane modulation on AXL serves to curtail the AXL signaling schema (Figure J). This opens up avenues for potential OPCML based biotherapy as an alternative to small molecule inhibitors such as R428, to negate the oncogenic effects of AXL in ovarian cancer.

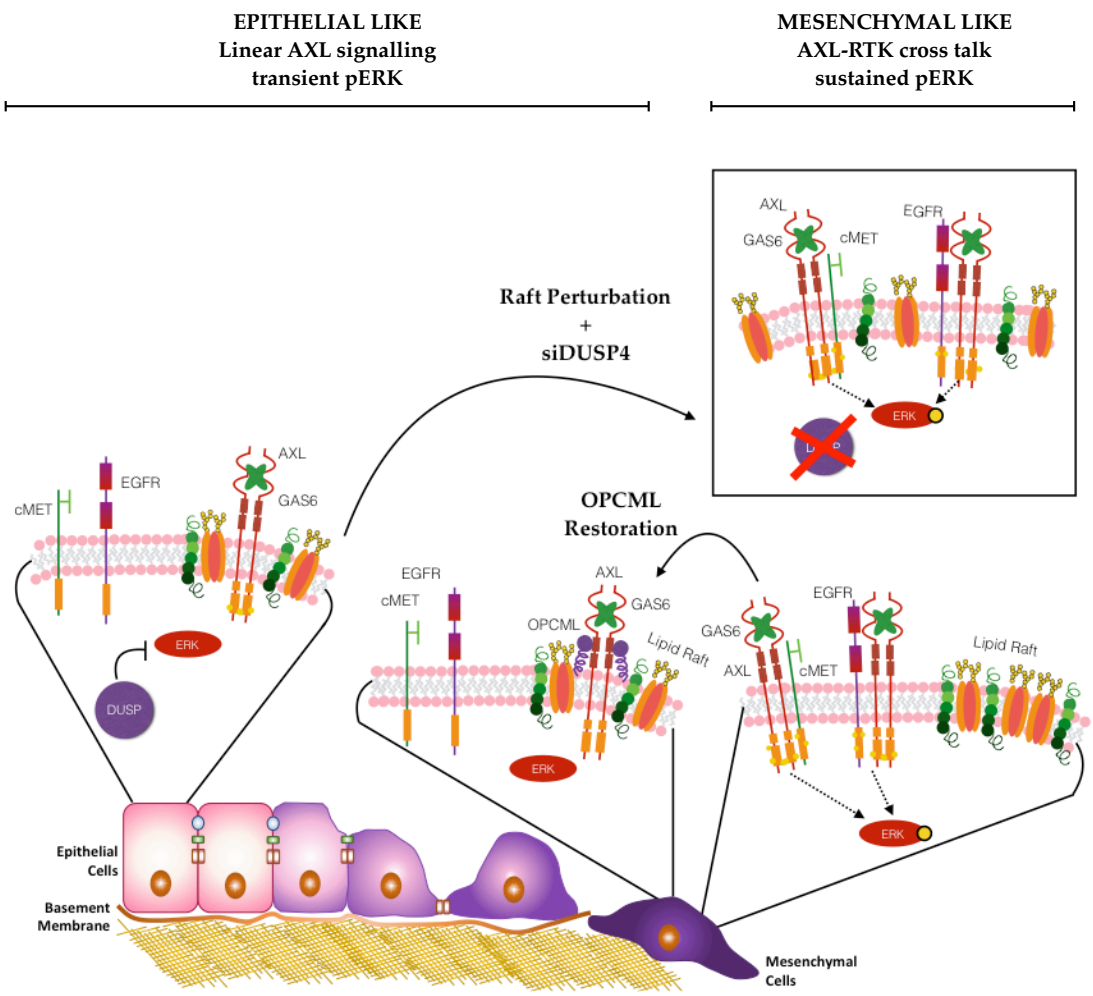


Figure K: Overview of AXL signaling in Epithelial and Mesenchymal states, and modulatory mechanisms.

Another area that required further work was the relevance of the AXL kinase domain in the AXL-RTK signaling complex in Mes. In the activation of EGFR, HER2 and cMET by the Gas6/AXL nodule, it was uncertain whether the kinase activity of AXL was responsible for phosphorylation of the other RTKs, or whether the clustering itself was sufficient to trigger RTK activation.

In order to study the functional relevance of the AXL kinase domain, AXL null cell lines PEO4 (Epi-A) and TYKnu (Mes) were transfected with either a functional AXL plasmid, or a kinase dead AXL plasmid encoding a K567R mutation[200] (Appendix III, Figure IIIA). Stimulation with Gas6 for 30 minutes in Epi-A subtype PEO4 transfected with AXL, showed phosphorylation of AXL, but not EGFR, as expected of epithelial

systems (Appendix III, Figure IIIB). In the Mes subtype TYKnu, Gas6 activation of AXL, resulted in phosphorylation of AXL, as well as EGFR. However, in AXL kinase dead transfected TYKnu, there was no activation of AXL, and consequently no pEGFR (Appendix III, Figure IIIB). To corroborate the western blot results, DUOLink was carried out to validate the interaction between AXL and EGFR. AXL-EGFR clustering occurred in both AXL and AXL kinase dead transfected Mes subtype TYKnu, however, there was no pEGFR immunofluorescence detected in AXL kinase dead transfected TYKnu (Appendix III, Figure IIIC). This suggests that Gas6/AXL induced RTK crosstalk relies on the AXL kinase domain to phosphorylate the other RTKs (Figure K).

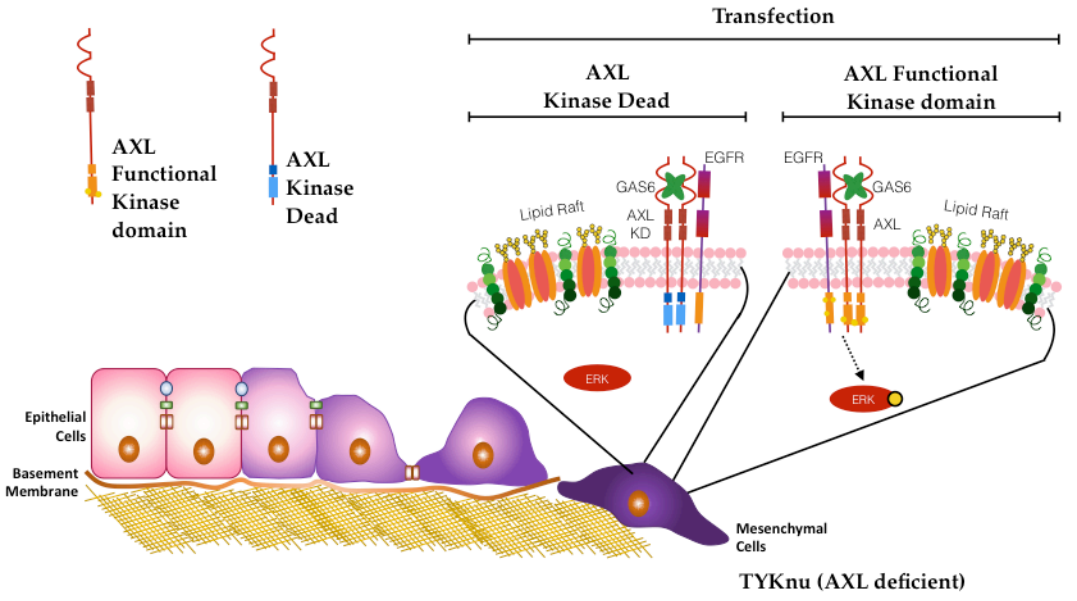


Figure L: AXL kinase domain is crucial to initiate phosphorylation of RTKs in Gas6/AXL-RTK crosstalk networks in Mes.

5.3 LIMITATIONS

5.3.1 Phenotypic assays with small molecule inhibitor R428.

The documented IC50 for the Axl inhibitor R428 in a fluorescence polarization–based in vitro kinase assay using recombinant Axl protein is 14nM[112] and the dose that showed phenotypic responses in vitro was 3μM, which is within the range of GI50 reported in the thesis. However, given the large difference between the reported IC50 for phospho-tyrosine assay, and GI50 observed in phenotypic assays, potential off target effects must be considered. Given R428 is a Type I small molecule tyrosine kinase inhibitor, at concentrations in the micro molar range it has the potential to inhibit other kinase domains and the phenotypic effects observed might be due to the inhibition of a combination of kinases. However, these concerns are partially reduced as we have shown the specificity of the inhibitor by checking for inhibition of pEGFR upon EGF stimulation[201]; indeed even at concentrations of 9.38μM there was no inhibition of pEGFR. Furthermore, we have evaluated the GI50 of R428 in AXL-null cell lines PEO4 and TYKnu, and these are correspondingly high; upon expression of AXL in these systems, they are sensitized to the inhibitor and present lowered GI50 values. Expression of AXL kinase domain deficient constructs does not sensitize the cells to R428, underscoring the specificity of inhibitor for AXL.

In addition it might be necessary to evaluate the off target effects on other kinases such as cMET that have a high sequence similarity with AXL. In addition, R428 studies in shAXL cells could be performed to show an increase in GI50 values. To strengthen the observations, AXL inhibition could be carried out by complementary approaches such as anti-AXL therapy using monoclonal antibodies, or aptamers; as well as AXL knockout using CRISPR-Cas9 systems.

5.3.2 Gene manipulation using RNAi and overexpression systems.

The major cause for concern from RNA interference are off target effects where there is silencing other similar sequence mRNAs, overloading the cell and altering the native RNAi equilibrium, as well as incomplete knockdown of target protein. Given the drawback that shRNA-mediated silencing may show such off-target effects, this study is short of rescue experiments that have yet to be successfully demonstrated. However, the use of shRNA control and two different shAXL constructs in two EOC cell lines helps ensure consistency in the associated phenotype and lowers the concern for off-target effects. Also in the siRNA approach we have used three different siAXL sequences and a pooled non-targeting control siRNA; these lend confidence to our findings as they show the same phenotype as shRNA mediated AXL silencing. Furthermore, CRISPR mediated gene knockout could be employed to show phenotypic effects that mimic those observed upon RNAi.

The phenotype associated with OPCML overexpression similarly involves changes in the intrinsic protein synthesis machinery and trafficking which could confound the observations, as well as random insertions into the genome that might alter transcription of other genes. These concerns could be addressed in the future by using recombinant OPCML protein, GPI-anchored mimetics, or CRISPR mediated activation of OPCML.

5.3.3 Comparison between R428 inhibition assays and shAXL studies.

The partially overlapping results upon R428 mediated AXL inhibition and shAXL mediated AXL silencing warrants further analysis. Given R428 functions principally as an ATP competitive inhibitor, it prevents Gas6/AXL mediated signaling, but does not prevent co-clustering of AXL with other RTKs. However in shAXL silenced cells, AXL can no longer act as a scaffold to trigger RTK clustering, and this might result in

a slightly altered phenotype compared to AXL inhibition by R428. Furthermore, R428 can be administered in a dose-dependent manner to observe a dose dependent phenotype, whereas shAXL represents a 'on' or 'off' system wherein the protein is present or absent, with little gradient to observe dose dependency. Growth inhibition is observed upon R428 treatment, and this is mimicked by a slower proliferation upon AXL knockdown. Reduced motility is also observed upon R428 treatment as well as shAXL. Importantly the Mes show inhibition of motility in lower doses of R428, but the Epi-A show inhibition only at higher doses; however given shAXL represents a on-off state, with high AXL knockdown comparable to high R428 doses, there is motility inhibition in Mes as well as Epi-A. Given drug inhibition and knockdown by RNAi are not equivalent, care must be taken while interpreting the results. While the directionality of the phenotype upon AXL knockdown or inhibition are comparable, the differences between the two systems must be appreciated. Furthermore given the R428 experiments are conducted in a shorter window of time, the cancer cells are not given sufficient time to adapt to their selection pressure mediated by AXL inhibition, while the shAXL experiments possibly allow for compensatory mechanisms to come into play.

5.3.4 Histology of cell lines used in the study.

While cell lines were chosen keeping in mind the gene expression subtype, it is important to consider what effects the histology might have. From our classification system (Appendix V) the majority of cell lines are of serous histology, however there is a discrepancy when comparing to reports published by other groups[202]. However it has previously been shown by unsupervised hierarchical clustering analysis that pathway driven clusters are dispersed through histological subtypes[203], and therefore it might be beneficial to stratify based on gene expression profiles, than histology.

5.4 ON-GOING AND FUTURE WORK

5.4.1 Pull Down SILAC Mass-Spectrometry of AXL to discern binding partners in Epithelial and Mesenchymal systems.

Given the membrane modulation in epithelial systems that curtail signaling, it is of interest to screen for EMT-related AXL binding partners that could potentially regulate the RTK at a membrane level. For instance, in breast cancer, FGFR receptors are known to be stabilized by N-cadherin through interaction of Ig-like domains, which prevents their ligand-induced internalization[204]. This in turn leads to sustained ERK activation and metastasis[204,205]. In a similar manner, there is the possibility of AXL being stabilized by N-cadherin or similar molecules in Mes systems, that enable sustained activation. In epithelial systems, it could be the lack of such stabilizing molecules that enable modulation of AXL signaling at a membrane level. Also, it is known that epithelial markers such as E-cadherin, localize to the membrane rafts[206], and could potentially regulate AXL through interaction, and subsequent movement into the rafts. The membrane rafts are also known to regulate EGFR signaling, wherein Caveolin-1 alters the membrane compartmentalization of EGFR from the soluble liquid-disordered phase to the rafts, and thereby curtails EGFR signaling[207]. In order to screen for EMT-related membrane molecules that regulate AXL signaling, a pull down SILAC (Stable Isotope Labeling by Amino acids in Cell culture) Mass-Spec of AXL is being performed in Epithelial and Mesenchymal systems. In this scenario, potential regulation of AXL by E-cadherin in Epithelial systems could account for loss of RTK regulatory mechanisms along the EMT gradient.

5.4.2 FCCS of AXL-OPCML to establish membrane dynamics

Another area that requires further elucidation is the dynamics of AXL-OPCML interaction. FCS (Fluorescent Correlation Spectroscopy)[208,209] experiments are currently being undertaken in collaboration with Christian Eggeling's Lab in Oxford, to establish diffusion co-efficients of AXL upon modulation by OPCML. In this venture, we have some preliminary data that shows the diffusion co-efficient of AXL in SKOV3 OPCML expressing cells is significantly lower upon Gas6 stimulation (Appendix IV). This could potentially be explained by increased AXL-OPCML interaction upon Gas6 stimulation that causes an alteration of membrane compartmentalization of AXL from the soluble liquid-disordered phase to the lipid rafts, where the GPI-anchored OPCML resides.

5.4.3 Phosphatase Screen

The mechanism of deactivation of AXL requires further insight. Further work will be carried out to screen the phosphatases and identify potential candidates that dephosphorylate AXL. Of note, there is no AXL-specific phosphatase that has been discovered till date, although C1-TEN has been suggested as a putative AXL phosphatase[100]. The governing hypothesis in this experiment would be the identification of a raft-specific phosphatase that can dephosphorylate AXL, and thereby explain the membrane-raft modulation of AXL by OPCML in mesenchymal systems.

5.5 CONCLUDING REMARKS

Taken together, this body of work provides insights regarding the influence of EMT states on signaling networks through the Gas6/AXL nodule. In epithelial systems, this modulation exists through interplay of membrane-raft dynamics that alter the localisation of the RTK and Dual Specificity Phosphatases that regulate temporal responses of ERK signaling, while in mesenchymal systems, the restoration of GPI-anchored tumor suppressors such as OPCML serves to curtail AXL signaling and restore an epithelial-like signaling nodule. We further identify the Mes subtype as being over reliant on the amplified, cross talk driven AXL signaling state, and believe this will be useful in stratifying ovarian cancer patients in Phase II clinical trials involving R428.

REFERENCES

1 Jayson, G. C., Kohn, E. C., Kitchener, H. C. & Ledermann, J. A. Ovarian cancer. *Lancet* **384**, 1376-1388, doi:10.1016/S0140-6736(13)62146-7 (2014).

2 Gubbels, J. A., Claussen, N., Kapur, A. K., Connor, J. P. & Patankar, M. S. The detection, treatment, and biology of epithelial ovarian cancer. *J Ovarian Res* **3**, 8, doi:10.1186/1757-2215-3-8 (2010).

3 Prat, J., Ribe, A. & Gallardo, A. Hereditary ovarian cancer. *Hum Pathol* **36**, 861-870, doi:10.1016/j.humpath.2005.06.006 (2005).

4 King, M. C., Marks, J. H., Mandell, J. B. & New York Breast Cancer Study, G. Breast and ovarian cancer risks due to inherited mutations in BRCA1 and BRCA2. *Science* **302**, 643-646, doi:10.1126/science.1088759 (2003).

5 Vergote, I. *et al.* Current perspectives on recommendations for BRCA genetic testing in ovarian cancer patients. *European Journal of Cancer* **69**, 127-134, doi:http://dx.doi.org/10.1016/j.ejca.2016.10.006 (2016).

6 Thibodeau, S. N., Bren, G. & Schaid, D. Microsatellite instability in cancer of the proximal colon. *Science* **260**, 816-819 (1993).

7 Auersperg, N., Wong, A. S., Choi, K. C., Kang, S. K. & Leung, P. C. Ovarian surface epithelium: biology, endocrinology, and pathology. *Endocr Rev* **22**, 255-288 (2001).

8 McCluggage, W. G. Morphological subtypes of ovarian carcinoma: a review with emphasis on new developments and pathogenesis. *Pathology* **43**, 420-432, doi:10.1097/PAT.0b013e328348a6e7 (2011).

9 Singer, G. *et al.* Patterns of p53 mutations separate ovarian serous borderline tumors and low- and high-grade carcinomas and provide support for a new model of ovarian carcinogenesis: a mutational analysis with immunohistochemical correlation. *Am J Surg Pathol* **29**, 218-224 (2005).

10 Wiegand, K. C. *et al.* ARID1A mutations in endometriosis-associated ovarian carcinomas. *N Engl J Med* **363**, 1532-1543, doi:10.1056/NEJMoa1008433 (2010).

11 Lalwani, N. *et al.* Histologic, molecular, and cytogenetic features of ovarian cancers: implications for diagnosis and treatment. *Radiographics* **31**, 625-646, doi:10.1148/rg.313105066 (2011).

12 McAlpine, J. N. *et al.* HER2 overexpression and amplification is present in a subset of ovarian mucinous carcinomas and can be targeted with

trastuzumab therapy. *BMC Cancer* **9**, 433, doi:10.1186/1471-2407-9-433 (2009).

13 Lin, W. L. *et al.* Identification of the coexisting HER2 gene amplification and novel mutations in the HER2 protein-overexpressed mucinous epithelial ovarian cancer. *Ann Surg Oncol* **18**, 2388-2394, doi:10.1245/s10434-011-1572-z (2011).

14 Schwartz, D. R. *et al.* Gene expression in ovarian cancer reflects both morphology and biological behavior, distinguishing clear cell from other poor-prognosis ovarian carcinomas. *Cancer Res* **62**, 4722-4729 (2002).

15 Fathalla, M. F. Non-hormonal interruption of incessant ovulation as a potential approach for ovarian cancer prevention. *Int J Gynaecol Obstet* **132**, 356-358, doi:10.1016/j.ijgo.2015.11.006 (2016).

16 Fathalla, M. F. Incessant ovulation and ovarian cancer - a hypothesis re-visited. *Facts Views Vis Obgyn* **5**, 292-297 (2013).

17 Fathalla, M. F. Incessant ovulation--a factor in ovarian neoplasia? *Lancet* **2**, 163 (1971).

18 Konishi, I., Kuroda, H. & Mandai, M. Review: gonadotropins and development of ovarian cancer. *Oncology* **57 Suppl 2**, 45-48, doi:55274 (1999).

19 Cramer, D. W., Hutchison, G. B., Welch, W. R., Scully, R. E. & Knapp, R. C. Factors affecting the association of oral contraceptives and ovarian cancer. *N Engl J Med* **307**, 1047-1051, doi:10.1056/NEJM198210213071703 (1982).

20 Risch, H. A., Marrett, L. D. & Howe, G. R. Parity, contraception, infertility, and the risk of epithelial ovarian cancer. *Am J Epidemiol* **140**, 585-597 (1994).

21 Dubeau, L. The cell of origin of ovarian epithelial tumours. *Lancet Oncol* **9**, 1191-1197, doi:10.1016/S1470-2045(08)70308-5 (2008).

22 Perets, R. *et al.* Transformation of the fallopian tube secretory epithelium leads to high-grade serous ovarian cancer in Brca;Tp53;Pten models. *Cancer Cell* **24**, 751-765, doi:10.1016/j.ccr.2013.10.013 (2013).

23 Kurman, R. J. & Shih Ie, M. The origin and pathogenesis of epithelial ovarian cancer: a proposed unifying theory. *Am J Surg Pathol* **34**, 433-443, doi:10.1097/PAS.0b013e3181cf3d79 (2010).

24 Bast, R. C., Jr., Hennessy, B. & Mills, G. B. The biology of ovarian cancer: new opportunities for translation. *Nat Rev Cancer* **9**, 415-428, doi:10.1038/nrc2644 (2009).

25 Vaughan, S. *et al.* Rethinking ovarian cancer: recommendations for improving outcomes. *Nat Rev Cancer* **11**, 719-725, doi:10.1038/nrc3144 (2011).

26 Jones, P. M. & Drapkin, R. Modeling High-Grade Serous Carcinoma: How Converging Insights into Pathogenesis and Genetics are Driving Better Experimental Platforms. *Front Oncol* **3**, 217, doi:10.3389/fonc.2013.00217 (2013).

27 Hennessy, B. T., Coleman, R. L. & Markman, M. Ovarian cancer. *Lancet* **374**, 1371-1382, doi:10.1016/S0140-6736(09)61338-6 (2009).

28 Prat, J. New insights into ovarian cancer pathology. *Ann Oncol* **23 Suppl 10**, x111-117, doi:10.1093/annonc/mds300 (2012).

29 Shih Ie, M. & Kurman, R. J. Ovarian tumorigenesis: a proposed model based on morphological and molecular genetic analysis. *Am J Pathol* **164**, 1511-1518 (2004).

30 Cannistra, S. A. Cancer of the ovary. *N Engl J Med* **351**, 2519-2529, doi:10.1056/NEJMra041842 (2004).

31 Gubbels, J. A. *et al.* MUC16 provides immune protection by inhibiting synapse formation between NK and ovarian tumor cells. *Mol Cancer* **9**, 11, doi:10.1186/1476-4598-9-11 (2010).

32 Moore, R. G., MacLaughlan, S. & Bast, R. C., Jr. Current state of biomarker development for clinical application in epithelial ovarian cancer. *Gynecol Oncol* **116**, 240-245, doi:10.1016/j.ygyno.2009.09.041 (2010).

33 Kerbrat, P. *et al.* Ovarian cancer. *Br J Cancer* **84 Suppl 2**, 18-23, doi:10.1054/bjoc.2000.1758 (2001).

34 Perren, T. J. *et al.* A phase 3 trial of bevacizumab in ovarian cancer. *N Engl J Med* **365**, 2484-2496, doi:10.1056/NEJMoa1103799 (2011).

35 du Bois, A. *et al.* Incorporation of pazopanib in maintenance therapy of ovarian cancer. *J Clin Oncol* **32**, 3374-3382, doi:10.1200/JCO.2014.55.7348 (2014).

36 Aghajanian, C. *et al.* OCEANS: a randomized, double-blind, placebo-controlled phase III trial of chemotherapy with or without bevacizumab in patients with platinum-sensitive recurrent epithelial ovarian, primary peritoneal, or fallopian tube cancer. *J Clin Oncol* **30**, 2039-2045, doi:10.1200/JCO.2012.42.0505 (2012).

37 Burger, R. A. *et al.* Incorporation of bevacizumab in the primary treatment of ovarian cancer. *N Engl J Med* **365**, 2473-2483, doi:10.1056/NEJMoa1104390 (2011).

38 Ledermann, J. *et al.* Olaparib maintenance therapy in patients with platinum-sensitive relapsed serous ovarian cancer: a preplanned retrospective analysis of outcomes by BRCA status in a randomised phase 2 trial. *Lancet Oncol* **15**, 852-861, doi:10.1016/S1470-2045(14)70228-1 (2014).

39 Tothill, R. W. *et al.* Novel molecular subtypes of serous and endometrioid ovarian cancer linked to clinical outcome. *Clin Cancer Res* **14**, 5198-5208, doi:10.1158/1078-0432.CCR-08-0196 (2008).

40 Cancer Genome Atlas Research, N. Integrated genomic analyses of ovarian carcinoma. *Nature* **474**, 609-615, doi:10.1038/nature10166 (2011).

41 Tan, T. Z. *et al.* Functional genomics identifies five distinct molecular subtypes with clinical relevance and pathways for growth control in epithelial ovarian cancer. *EMBO Mol Med* **5**, 983-998, doi:10.1002/emmm.201201823 (2013).

42 Reese, D. E., Mikawa, T. & Bader, D. M. Development of the coronary vessel system. *Circ Res* **91**, 761-768 (2002).

43 Lee, J. M., Dedhar, S., Kalluri, R. & Thompson, E. W. The epithelial-mesenchymal transition: new insights in signaling, development, and disease. *J Cell Biol* **172**, 973-981, doi:10.1083/jcb.200601018 (2006).

44 Lim, J. & Thiery, J. P. Epithelial-mesenchymal transitions: insights from development. *Development* **139**, 3471-3486, doi:10.1242/dev.071209 (2012).

45 Thiery, J. P. Epithelial-mesenchymal transitions in tumour progression. *Nat Rev Cancer* **2**, 442-454, doi:10.1038/nrc822 (2002).

46 Thiery, J. P. & Sleeman, J. P. Complex networks orchestrate epithelial-mesenchymal transitions. *Nat Rev Mol Cell Biol* **7**, 131-142, doi:10.1038/nrm1835 (2006).

47 Heldin, C. H., Vanlandewijck, M. & Moustakas, A. Regulation of EMT by TGFbeta in cancer. *FEBS Lett* **586**, 1959-1970, doi:10.1016/j.febslet.2012.02.037 (2012).

48 Reya, T. & Clevers, H. Wnt signalling in stem cells and cancer. *Nature* **434**, 843-850, doi:10.1038/nature03319 (2005).

49 Wang, Z., Li, Y., Kong, D. & Sarkar, F. H. The role of Notch signaling pathway in epithelial-mesenchymal transition (EMT) during development and tumor aggressiveness. *Curr Drug Targets* **11**, 745-751 (2010).

50 Lu, Z., Ghosh, S., Wang, Z. & Hunter, T. Downregulation of caveolin-1 function by EGF leads to the loss of E-cadherin, increased transcriptional activity of beta-catenin, and enhanced tumor cell invasion. *Cancer Cell* **4**, 499-515 (2003).

51 Chavez, M. G. *et al.* Differential downregulation of e-cadherin and desmoglein by epidermal growth factor. *Dermatol Res Pract* **2012**, 309587, doi:10.1155/2012/309587 (2012).

52 Fixman, E. D., Fournier, T. M., Kamikura, D. M., Naujokas, M. A. & Park, M. Pathways downstream of Shc and Grb2 are required for cell transformation by the tpr-Met oncoprotein. *J Biol Chem* **271**, 13116-13122 (1996).

53 Lai, A. Z., Abella, J. V. & Park, M. Crosstalk in Met receptor oncogenesis. *Trends Cell Biol* **19**, 542-551, doi:10.1016/j.tcb.2009.07.002 (2009).

54 Susuki, D. *et al.* Regulation of microRNA expression by hepatocyte growth factor in human head and neck squamous cell carcinoma. *Cancer Sci* **102**, 2164-2171, doi:10.1111/j.1349-7006.2011.02096.x (2011).

55 Morali, O. G. *et al.* IGF-II induces rapid beta-catenin relocation to the nucleus during epithelium to mesenchyme transition. *Oncogene* **20**, 4942-4950, doi:10.1038/sj.onc.1204660 (2001).

56 Kim, H. J. *et al.* Constitutively active type I insulin-like growth factor receptor causes transformation and xenograft growth of immortalized mammary epithelial cells and is accompanied by an epithelial-to-mesenchymal transition mediated by NF-kappaB and snail. *Mol Cell Biol* **27**, 3165-3175, doi:10.1128/MCB.01315-06 (2007).

57 Graham, T. R. *et al.* Insulin-like growth factor-I-dependent up-regulation of ZEB1 drives epithelial-to-mesenchymal transition in human prostate cancer cells. *Cancer Res* **68**, 2479-2488, doi:10.1158/0008-5472.CAN-07-2559 (2008).

58 Thiery, J. P., Acloque, H., Huang, R. Y. & Nieto, M. A. Epithelial-mesenchymal transitions in development and disease. *Cell* **139**, 871-890, doi:10.1016/j.cell.2009.11.007 (2009).

59 Andrae, J., Gallini, R. & Betsholtz, C. Role of platelet-derived growth factors in physiology and medicine. *Genes Dev* **22**, 1276-1312, doi:10.1101/gad.1653708 (2008).

60 Yang, L., Lin, C. & Liu, Z. R. P68 RNA helicase mediates PDGF-induced epithelial mesenchymal transition by displacing Axin from beta-catenin. *Cell* **127**, 139-155, doi:10.1016/j.cell.2006.08.036 (2006).

61 Olsson, A. K., Dimberg, A., Kreuger, J. & Claesson-Welsh, L. VEGF receptor signalling - in control of vascular function. *Nat Rev Mol Cell Biol* **7**, 359-371, doi:10.1038/nrm1911 (2006).

62 Gonzalez-Moreno, O. *et al.* VEGF elicits epithelial-mesenchymal transition (EMT) in prostate intraepithelial neoplasia (PIN)-like cells via an autocrine loop. *Exp Cell Res* **316**, 554-567, doi:10.1016/j.yexcr.2009.11.020 (2010).

63 Wanami, L. S., Chen, H. Y., Peiro, S., Garcia de Herreros, A. & Bachelder, R. E. Vascular endothelial growth factor-A stimulates Snail expression in breast tumor cells: implications for tumor progression. *Exp Cell Res* **314**, 2448-2453, doi:10.1016/j.yexcr.2008.05.004 (2008).

64 Yang, J. & Weinberg, R. A. Epithelial-mesenchymal transition: at the crossroads of development and tumor metastasis. *Dev Cell* **14**, 818-829, doi:10.1016/j.devcel.2008.05.009 (2008).

65 Kalluri, R. & Weinberg, R. A. The basics of epithelial-mesenchymal transition. *J Clin Invest* **119**, 1420-1428, doi:10.1172/JCI39104 (2009).

66 Tsai, J. H. & Yang, J. Epithelial-mesenchymal plasticity in carcinoma metastasis. *Genes Dev* **27**, 2192-2206, doi:10.1101/gad.225334.113 (2013).

67 Lamouille, S., Xu, J. & Derynck, R. Molecular mechanisms of epithelial-mesenchymal transition. *Nat Rev Mol Cell Biol* **15**, 178-196, doi:10.1038/nrm3758 (2014).

68 Friedl, P., Locker, J., Sahai, E. & Segall, J. E. Classifying collective cancer cell invasion. *Nat Cell Biol* **14**, 777-783, doi:10.1038/ncb2548 (2012).

69 Thiery, J. P. & Lim, C. T. Tumor dissemination: an EMT affair. *Cancer Cell* **23**, 272-273, doi:10.1016/j.ccr.2013.03.004 (2013).

70 Yu, M. *et al.* Circulating breast tumor cells exhibit dynamic changes in epithelial and mesenchymal composition. *Science* **339**, 580-584, doi:10.1126/science.1228522 (2013).

71 Marchini, S. *et al.* Resistance to platinum-based chemotherapy is associated with epithelial to mesenchymal transition in epithelial ovarian cancer. *Eur J Cancer* **49**, 520-530, doi:10.1016/j.ejca.2012.06.026 (2013).

72 Hu, X. *et al.* A miR-200 microRNA cluster as prognostic marker in advanced ovarian cancer. *Gynecol Oncol* **114**, 457-464, doi:10.1016/j.ygyno.2009.05.022 (2009).

73 Cochrane, D. R. *et al.* MicroRNAs link estrogen receptor alpha status and Dicer levels in breast cancer. *Horm Cancer* **1**, 306-319, doi:10.1007/s12672-010-0043-5 (2010).

74 Feng, B., Wang, R. & Chen, L. B. Review of miR-200b and cancer chemosensitivity. *Biomed Pharmacother* **66**, 397-402, doi:10.1016/j.biopha.2012.06.002 (2012).

75 Cittelly, D. M. *et al.* Restoration of miR-200c to ovarian cancer reduces tumor burden and increases sensitivity to paclitaxel. *Mol Cancer Ther* **11**, 2556-2565, doi:10.1158/1535-7163.MCT-12-0463 (2012).

76 Bacac, M. & Stamenkovic, I. Metastatic cancer cell. *Annu Rev Pathol* **3**, 221-247, doi:10.1146/annurev.pathmechdis.3.121806.151523 (2008).

77 Naora, H. & Montell, D. J. Ovarian cancer metastasis: integrating insights from disparate model organisms. *Nat Rev Cancer* **5**, 355-366, doi:10.1038/nrc1611 (2005).

78 Sundfeldt, K. Cell-cell adhesion in the normal ovary and ovarian tumors of epithelial origin; an exception to the rule. *Mol Cell Endocrinol* **202**, 89-96 (2003).

79 Christiansen, J. J. & Rajasekaran, A. K. Reassessing epithelial to mesenchymal transition as a prerequisite for carcinoma invasion and metastasis. *Cancer Res* **66**, 8319-8326, doi:10.1158/0008-5472.CAN-06-0410 (2006).

80 Elloul, S. *et al.* Expression of E-cadherin transcriptional regulators in ovarian carcinoma. *Virchows Arch* **449**, 520-528, doi:10.1007/s00428-006-0274-6 (2006).

81 Ahmed, N., Thompson, E. W. & Quinn, M. A. Epithelial-mesenchymal interconversions in normal ovarian surface epithelium and ovarian carcinomas: an exception to the norm. *J Cell Physiol* **213**, 581-588, doi:10.1002/jcp.21240 (2007).

82 Linger, R. M., Keating, A. K., Earp, H. S. & Graham, D. K. TAM receptor tyrosine kinases: biologic functions, signaling, and potential therapeutic targeting in human cancer. *Adv Cancer Res* **100**, 35-83, doi:10.1016/S0065-230X(08)00002-X (2008).

83 Robinson, D. R., Wu, Y. M. & Lin, S. F. The protein tyrosine kinase family of the human genome. *Oncogene* **19**, 5548-5557, doi:10.1038/sj.onc.1203957 (2000).

84 O'Bryan, J. P. *et al.* axl, a transforming gene isolated from primary human myeloid leukemia cells, encodes a novel receptor tyrosine kinase. *Mol Cell Biol* **11**, 5016-5031 (1991).

85 Varnum, B. C. *et al.* Axl receptor tyrosine kinase stimulated by the vitamin K-dependent protein encoded by growth-arrest-specific gene 6. *Nature* **373**, 623-626, doi:10.1038/373623a0 (1995).

86 Manfioletti, G., Brancolini, C., Avanzi, G. & Schneider, C. The protein encoded by a growth arrest-specific gene (gas6) is a new member of the vitamin K-dependent proteins related to protein S, a negative coregulator in the blood coagulation cascade. *Mol Cell Biol* **13**, 4976-4985 (1993).

87 Verma, A., Warner, S. L., Vankayalapati, H., Bearss, D. J. & Sharma, S. Targeting Axl and Mer kinases in cancer. *Mol Cancer Ther* **10**, 1763-1773, doi:10.1158/1535-7163.MCT-11-0116 (2011).

88 Blume-Jensen, P. & Hunter, T. Oncogenic kinase signalling. *Nature* **411**, 355-365, doi:10.1038/35077225 (2001).

89 Sasaki, T. *et al.* Structural basis for Gas6-Axl signalling. *EMBO J* **25**, 80-87, doi:10.1038/sj.emboj.7600912 (2006).

90 Fridell, Y. W. *et al.* Differential activation of the Ras/extracellular-signal-regulated protein kinase pathway is responsible for the biological consequences induced by the Axl receptor tyrosine kinase. *Mol Cell Biol* **16**, 135-145 (1996).

91 Braunger, J. *et al.* Intracellular signaling of the Ufo/Axl receptor tyrosine kinase is mediated mainly by a multi-substrate docking-site. *Oncogene* **14**, 2619-2631, doi:10.1038/sj.onc.1201123 (1997).

92 Bellosta, P., Costa, M., Lin, D. A. & Basilico, C. The receptor tyrosine kinase ARK mediates cell aggregation by homophilic binding. *Mol Cell Biol* **15**, 614-625 (1995).

93 Konishi, A., Aizawa, T., Mohan, A., Korshunov, V. A. & Berk, B. C. Hydrogen peroxide activates the Gas6-Axl pathway in vascular smooth muscle cells. *J Biol Chem* **279**, 28766-28770, doi:10.1074/jbc.M401977200 (2004).

94 Goruppi, S., Ruaro, E., Varnum, B. & Schneider, C. Requirement of phosphatidylinositol 3-kinase-dependent pathway and Src for Gas6-Axl mitogenic and survival activities in NIH 3T3 fibroblasts. *Mol Cell Biol* **17**, 4442-4453 (1997).

95 Demarchi, F., Verardo, R., Varnum, B., Brancolini, C. & Schneider, C. Gas6 anti-apoptotic signaling requires NF-kappa B activation. *J Biol Chem* **276**, 31738-31744, doi:10.1074/jbc.M104457200 (2001).

96 Hasanbasic, I., Cuerquis, J., Varnum, B. & Blostein, M. D. Intracellular signaling pathways involved in Gas6-Axl-mediated survival of endothelial cells. *Am J Physiol Heart Circ Physiol* **287**, H1207-1213, doi:10.1152/ajpheart.00020.2004 (2004).

97 Allen, M. P. *et al.* Adhesion-related kinase repression of gonadotropin-releasing hormone gene expression requires Rac activation of the extracellular signal-regulated kinase pathway. *J Biol Chem* **277**, 38133-38140, doi:10.1074/jbc.M200826200 (2002).

98 Nielsen-Preiss, S. M. *et al.* Adhesion-related kinase induction of migration requires phosphatidylinositol-3-kinase and ras stimulation of rac activity in immortalized gonadotropin-releasing hormone neuronal cells. *Endocrinology* **148**, 2806-2814, doi:10.1210/en.2007-0039 (2007).

99 Hafizi, S., Ibraimi, F. & Dahlback, B. C1-TEN is a negative regulator of the Akt/PKB signal transduction pathway and inhibits cell survival, proliferation, and migration. *FASEB J* **19**, 971-973, doi:10.1096/fj.04-2532fje (2005).

100 Hafizi, S., Alindri, F., Karlsson, R. & Dahlback, B. Interaction of Axl receptor tyrosine kinase with C1-TEN, a novel C1 domain-containing protein with homology to tensin. *Biochem Biophys Res Commun* **299**, 793-800 (2002).

101 Kinjyo, I. *et al.* SOCS1/JAB is a negative regulator of LPS-induced macrophage activation. *Immunity* **17**, 583-591 (2002).

102 Nakagawa, R. *et al.* SOCS-1 participates in negative regulation of LPS responses. *Immunity* **17**, 677-687 (2002).

103 Gioia, R. *et al.* CBL controls a tyrosine kinase network involving AXL, SYK and LYN in nilotinib-resistant chronic myeloid leukaemia. *J Pathol* **237**, 14-24, doi:10.1002/path.4561 (2015).

104 Paolino, M. *et al.* The E3 ligase Cbl-b and TAM receptors regulate cancer metastasis via natural killer cells. *Nature* **507**, 508-512, doi:10.1038/nature12998 (2014).

105 Gjerdrum, C. *et al.* Axl is an essential epithelial-to-mesenchymal transition-induced regulator of breast cancer metastasis and patient survival. *Proc Natl Acad Sci U S A* **107**, 1124-1129, doi:10.1073/pnas.0909333107 (2010).

106 Asiedu, M. K. *et al.* AXL induces epithelial-to-mesenchymal transition and regulates the function of breast cancer stem cells. *Oncogene* **33**, 1316-1324, doi:10.1038/onc.2013.57 (2014).

107 Byers, L. A. *et al.* An epithelial-mesenchymal transition gene signature predicts resistance to EGFR and PI3K inhibitors and identifies Axl as a therapeutic target for overcoming EGFR inhibitor resistance. *Clin Cancer Res* **19**, 279-290, doi:10.1158/1078-0432.CCR-12-1558 (2013).

108 Zhang, Z. *et al.* Activation of the AXL kinase causes resistance to EGFR-targeted therapy in lung cancer. *Nature genetics* **44**, 852-860, doi:10.1038/ng.2330 (2012).

109 Koorstra, J. B. *et al.* The Axl receptor tyrosine kinase confers an adverse prognostic influence in pancreatic cancer and represents a new therapeutic target. *Cancer Biol Ther* **8**, 618-626 (2009).

110 Rankin, E. B. *et al.* AXL is an essential factor and therapeutic target for metastatic ovarian cancer. *Cancer Res* **70**, 7570-7579, doi:10.1158/0008-5472.CAN-10-1267 (2010).

111 Vajkoczy, P. *et al.* Dominant-negative inhibition of the Axl receptor tyrosine kinase suppresses brain tumor cell growth and invasion and prolongs survival. *Proc Natl Acad Sci U S A* **103**, 5799-5804, doi:10.1073/pnas.0510923103 (2006).

112 Holland, S. J. *et al.* R428, a selective small molecule inhibitor of Axl kinase, blocks tumor spread and prolongs survival in models of metastatic breast cancer. *Cancer Res* **70**, 1544-1554, doi:10.1158/0008-5472.CAN-09-2997 (2010).

113 Debruyne, D. N. *et al.* ALK inhibitor resistance in ALK(F1174L)-driven neuroblastoma is associated with AXL activation and induction of EMT. *Oncogene* **35**, 3681-3691, doi:10.1038/onc.2015.434 (2016).

114 Myers, S. H., Brunton, V. G. & Unciti-Broceta, A. AXL Inhibitors in Cancer: A Medicinal Chemistry Perspective. *J Med Chem* **59**, 3593-3608, doi:10.1021/acs.jmedchem.5b01273 (2016).

115 Yen, S. Y. *et al.* Biodegradable interstitial release polymer loading a novel small molecule targeting Axl receptor tyrosine kinase and reducing brain tumour migration and invasion. *Oncogene* **35**, 2156-2165, doi:10.1038/onc.2015.277 (2016).

116 Ye, X. *et al.* An anti-Axl monoclonal antibody attenuates xenograft tumor growth and enhances the effect of multiple anticancer therapies. *Oncogene* **29**, 5254-5264, doi:10.1038/onc.2010.268 (2010).

117 Kariolis, M. S. *et al.* An engineered Axl 'decoy receptor' effectively silences the Gas6-Axl signaling axis. *Nat Chem Biol* **10**, 977-983, doi:10.1038/nchembio.1636 (2014).

118 Shark, K. B. & Lee, N. M. Cloning, sequencing and localization to chromosome 11 of a cDNA encoding a human opioid-binding cell adhesion molecule (OBCAM). *Gene* **155**, 213-217 (1995).

119 Itoh, S. *et al.* Glycosylation analysis of IgLON family proteins in rat brain by liquid chromatography and multiple-stage mass spectrometry. *Biochemistry* **47**, 10132-10154, doi:10.1021/bi8009778 (2008).

120 Cavallaro, U. & Christofori, G. Cell adhesion in tumor invasion and metastasis: loss of the glue is not enough. *Biochim Biophys Acta* **1552**, 39-45 (2001).

121 Cavallaro, U. & Christofori, G. Cell adhesion and signalling by cadherins and Ig-CAMs in cancer. *Nat Rev Cancer* **4**, 118-132, doi:10.1038/nrc1276 (2004).

122 Cavallaro, U. & Christofori, G. Multitasking in tumor progression: signaling functions of cell adhesion molecules. *Ann N Y Acad Sci* **1014**, 58-66 (2004).

123 Gabra, H. *et al.* Definition and refinement of a region of loss of heterozygosity at 11q23.3-q24.3 in epithelial ovarian cancer associated with poor prognosis. *Cancer Res* **56**, 950-954 (1996).

124 Sellar, G. C. *et al.* OPCML at 11q25 is epigenetically inactivated and has tumor-suppressor function in epithelial ovarian cancer. *Nature genetics* **34**, 337-343, doi:10.1038/ng1183 (2003).

125 Zhou, F. *et al.* Methylation of OPCML promoter in ovarian cancer tissues predicts poor patient survival. *Clin Chem Lab Med* **52**, 735-742, doi:10.1515/cclm-2013-0736 (2014).

126 Zhou, F. *et al.* Detection of circulating methylated opioid binding protein/cell adhesion molecule-like gene as a biomarker for ovarian carcinoma. *Clin Lab* **60**, 759-765 (2014).

127 Ye, F., Zhang, S. F., Xie, X. & Lu, W. G. OPCML gene promoter methylation and gene expression in tumor and stroma cells of invasive cervical carcinoma. *Cancer Invest* **26**, 569-574, doi:10.1080/07357900701837044 (2008).

128 Anglim, P. P., Alonzo, T. A. & Laird-Offringa, I. A. DNA methylation-based biomarkers for early detection of non-small cell lung cancer: an update. *Mol Cancer* **7**, 81, doi:10.1186/1476-4598-7-81 (2008).

129 Reed, J. E. *et al.* Expression of cellular adhesion molecule 'OPCML' is down-regulated in gliomas and other brain tumours. *Neuropathol Appl Neurobiol* **33**, 77-85, doi:10.1111/j.1365-2990.2006.00786.x (2007).

130 Liu, W. J. *et al.* [Correlations of CpG island methylator phenotype and OPCML gene methylation to carcinogenesis of hepatocellular carcinoma]. *Ai Zheng* **25**, 696-700 (2006).

131 Cui, Y. *et al.* OPCML is a broad tumor suppressor for multiple carcinomas and lymphomas with frequently epigenetic inactivation. *PloS one* **3**, e2990, doi:10.1371/journal.pone.0002990 (2008).

132 Simons, K. & Toomre, D. Lipid rafts and signal transduction. *Nat Rev Mol Cell Biol* **1**, 31-39, doi:10.1038/35036052 (2000).

133 Shah, A. D. *et al.* Integrative analysis of subcellular quantitative proteomics studies reveals functional cytoskeleton membrane-lipid raft interactions in cancer. *J Proteome Res*, doi:10.1021/acs.jproteome.5b01035 (2016).

134 Pike, L. J. Growth factor receptors, lipid rafts and caveolae: an evolving story. *Biochim Biophys Acta* **1746**, 260-273, doi:10.1016/j.bbamcr.2005.05.005 (2005).

135 Mishra, S. & Joshi, P. G. Lipid raft heterogeneity: an enigma. *J Neurochem* **103 Suppl 1**, 135-142, doi:10.1111/j.1471-4159.2007.04720.x (2007).

136 Lajoie, P. & Nabi, I. R. Regulation of raft-dependent endocytosis. *J Cell Mol Med* **11**, 644-653, doi:10.1111/j.1582-4934.2007.00083.x (2007).

137 McKie, A. B. *et al.* The OPCML tumor suppressor functions as a cell surface repressor-adaptor, negatively regulating receptor tyrosine kinases in epithelial ovarian cancer. *Cancer Discov* **2**, 156-171, doi:10.1158/2159-8290.CD-11-0256 (2012).

138 Li, C. *et al.* OPCML is frequently methylated in human colorectal cancer and its restored expression reverses EMT via downregulation of smad signaling. *Am J Cancer Res* **5**, 1635-1648 (2015).

139 Huang, R. Y., Chung, V. Y. & Thiery, J. P. Targeting pathways contributing to epithelial-mesenchymal transition (EMT) in epithelial ovarian cancer. *Curr Drug Targets* **13**, 1649-1653 (2012).

140 Wu, X. *et al.* AXL kinase as a novel target for cancer therapy. *Oncotarget* **5**, 9546-9563, doi:10.18632/oncotarget.2542 (2014).

141 Giles, K. M. *et al.* Axl mediates acquired resistance of head and neck cancer cells to the epidermal growth factor receptor inhibitor erlotinib. *Mol Cancer Ther* **12**, 2541-2558, doi:10.1158/1535-7163.MCT-13-0170 (2013).

142 Bansal, N., Mishra, P. J., Stein, M., DiPaola, R. S. & Bertino, J. R. Axl receptor tyrosine kinase is up-regulated in metformin resistant prostate cancer cells. *Oncotarget* **6**, 15321-15331, doi:10.18632/oncotarget.4148 (2015).

143 Meyer, A. S., Miller, M. A., Gertler, F. B. & Lauffenburger, D. A. The receptor AXL diversifies EGFR signaling and limits the response to EGFR-targeted inhibitors in triple-negative breast cancer cells. *Sci Signal* **6**, ra66, doi:10.1126/scisignal.2004155 (2013).

144 Zhou, L. *et al.* Targeting MET and AXL overcomes resistance to sunitinib therapy in renal cell carcinoma. *Oncogene*, doi:10.1038/onc.2015.343 (2015).

145 McKie, A. B. *et al.* The OPCML tumor suppressor functions as a cell surface repressor-adaptor, negatively regulating receptor tyrosine kinases in epithelial ovarian cancer. *Cancer Discovery* **2**, 156-171, doi:10.1158/2159-8290.CD-11-0256 (2012).

146 Asad, M. *et al.* FZD7 drives in vitro aggressiveness in Stem-A subtype of ovarian cancer via regulation of non-canonical Wnt/PCP pathway. *Cell Death Dis* **5**, e1346, doi:10.1038/cddis.2014.302 (2014).

147 Jemal, A. *et al.* Global cancer statistics. *CA: a cancer journal for clinicians* **61**, 69-90, doi:10.3322/caac.20107 (2011).

148 Yang, D. *et al.* Integrated analyses identify a master microRNA regulatory network for the mesenchymal subtype in serous ovarian cancer. *Cancer Cell* **23**, 186-199, doi:10.1016/j.ccr.2012.12.020 (2013).

149 Chung, V. Y. *et al.* GRHL2-miR-200-ZEB1 maintains the epithelial status of ovarian cancer through transcriptional regulation and histone modification. *Sci Rep* **6**, 19943, doi:10.1038/srep19943 (2016).

150 Ruby Yun-Ju Huang, T. Z. T., Meng Kang Wong, Noriomi Matsumura, Hung Cheng Lai, Vin Yee Chung, Jieru Ye, Seiichi Mori, Jean Paul Thiery. in *AACR 103rd Annual Meeting* (Cancer Research).

151 Sorlie, T. *et al.* Gene expression patterns of breast carcinomas distinguish tumor subclasses with clinical implications. *Proc Natl Acad Sci U S A* **98**, 10869-10874, doi:10.1073/pnas.191367098 (2001).

152 Sotiriou, C. & Pusztai, L. Gene-expression signatures in breast cancer. *N Engl J Med* **360**, 790-800, doi:10.1056/NEJMra0801289 (2009).

153 Leong, H. S. *et al.* Efficient molecular subtype classification of high-grade serous ovarian cancer. *J Pathol* **236**, 272-277, doi:10.1002/path.4536 (2015).

154 Linger, R. M. A., Keating, A. K., Earp, H. S. & Graham, D. K. TAM Receptor Tyrosine Kinases: Biologic Functions, Signaling, and Potential Therapeutic Targeting in Human Cancer. **100**, 35-83, doi:10.1016/s0065-230x(08)00002-x (2008).

155 Goruppi, S., Ruaro, E. & Schneider, C. Gas6, the ligand of Axl tyrosine kinase receptor, has mitogenic and survival activities for serum starved NIH3T3 fibroblasts. *Oncogene* **12**, 471-480 (1996).

156 Ishikawa, M. *et al.* Higher expression of receptor tyrosine kinase Axl, and differential expression of its ligand, Gas6, predict poor survival in lung adenocarcinoma patients. *Ann Surg Oncol* **20 Suppl 3**, S467-476, doi:10.1245/s10434-012-2795-3 (2013).

157 Song, X. *et al.* Overexpression of receptor tyrosine kinase Axl promotes tumor cell invasion and survival in pancreatic ductal adenocarcinoma. *Cancer* **117**, 734-743, doi:10.1002/cncr.25483 (2011).

158 Elkabets, M. *et al.* AXL mediates resistance to PI3Kalpha inhibition by activating the EGFR/PKC/mTOR axis in head and neck and esophageal squamous cell carcinomas. *Cancer Cell* **27**, 533-546, doi:10.1016/j.ccell.2015.03.010 (2015).

159 Graham, D. K., DeRyckere, D., Davies, K. D. & Earp, H. S. The TAM family: phosphatidylserine sensing receptor tyrosine kinases gone awry in cancer. *Nat Rev Cancer* **14**, 769-785 (2014).

160 Rankin, E. B. *et al.* AXL Is an Essential Factor and Therapeutic Target for Metastatic Ovarian Cancer. *Cancer Research* **70**, 7570-7579, doi:10.1158/0008-5472.can-10-1267 (2010).

161 Huang, R. Y. *et al.* An EMT spectrum defines an anoikis-resistant and spheroidogenic intermediate mesenchymal state that is sensitive to e-cadherin restoration by a src-kinase inhibitor, saracatinib (AZD0530). *Cell Death Dis* **4**, e915, doi:10.1038/cddis.2013.442 (2013).

162 Marshall, C. J. Specificity of receptor tyrosine kinase signaling: transient versus sustained extracellular signal-regulated kinase activation. *Cell* **80**, 179-185 (1995).

163 Kholodenko, B. N., Hancock, J. F. & Kolch, W. Signalling ballet in space and time. *Nat Rev Mol Cell Biol* **11**, 414-426, doi:10.1038/nrm2901 (2010).

164 Murphy, L. O. & Blenis, J. MAPK signal specificity: the right place at the right time. *Trends Biochem Sci* **31**, 268-275, doi:10.1016/j.tibs.2006.03.009 (2006).

165 Breitkreutz, A. & Tyers, M. MAPK signaling specificity: it takes two to tango. *Trends Cell Biol* **12**, 254-257 (2002).

166 Sawabu, T. *et al.* Growth arrest-specific gene 6 and Axl signaling enhances gastric cancer cell survival via Akt pathway. *Mol Carcinog* **46**, 155-164, doi:10.1002/mc.20211 (2007).

167 Lee, H. J., Jeng, Y. M., Chen, Y. L., Chung, L. & Yuan, R. H. Gas6/Axl pathway promotes tumor invasion through the transcriptional activation of Slug in hepatocellular carcinoma. *Carcinogenesis* **35**, 769-775, doi:10.1093/carcin/bgt372 (2014).

168 Rea, K. *et al.* Novel Axl-driven signaling pathway and molecular signature characterize high-grade ovarian cancer patients with poor clinical outcome. *Oncotarget* **6**, 30859-30875, doi:10.18632/oncotarget.5087 (2015).

169 Vial, E. & Marshall, C. J. Elevated ERK-MAP kinase activity protects the FOS family member FRA-1 against proteasomal degradation in colon carcinoma cells. *Journal of cell science* **116**, 4957-4963, doi:10.1242/jcs.00812 (2003).

170 Shin, S. & Blenis, J. ERK2/Fra1/ZEB pathway induces epithelial-to-mesenchymal transition. *Cell cycle (Georgetown, Tex.)* **9**, 2483-2484 (2010).

171 Chen, H. *et al.* Extracellular signal-regulated kinase signaling pathway regulates breast cancer cell migration by maintaining slug expression. *Cancer Res* **69**, 9228-9235, doi:10.1158/0008-5472.CAN-09-1950 (2009).

172 Bakiri, L. *et al.* Fra-1/AP-1 induces EMT in mammary epithelial cells by modulating Zeb1/2 and TGFbeta expression. *Cell death and differentiation* **22**, 336-350, doi:10.1038/cdd.2014.157 (2015).

173 Chua, K. N. *et al.* A cell-based small molecule screening method for identifying inhibitors of epithelial-mesenchymal transition in carcinoma. *PLoS One* **7**, e33183, doi:10.1371/journal.pone.0033183 (2012).

174 Tan, T. Z. *et al.* Epithelial-mesenchymal transition spectrum quantification and its efficacy in deciphering survival and drug responses of cancer patients. *EMBO Mol Med* **6**, 1279-1293, doi:10.15252/emmm.201404208 (2014).

175 Brodsky, A. S. *et al.* Expression profiling of primary and metastatic ovarian tumors reveals differences indicative of aggressive disease. *PloS one* **9**, e94476, doi:10.1371/journal.pone.0094476 (2014).

176 Tan, T. Z. *et al.* CSIOVDB: a microarray gene expression database of epithelial ovarian cancer subtype. *Oncotarget* **6**, 43843-43852, doi:10.18632/oncotarget.5983 (2015).

177 Gujral, T. S. *et al.* Profiling phospho-signaling networks in breast cancer using reverse-phase protein arrays. *Oncogene* **32**, 3470-3476, doi:10.1038/onc.2012.378 (2013).

178 Liu, L. *et al.* Novel mechanism of lapatinib resistance in HER2-positive breast tumor cells: activation of AXL. *Cancer Res* **69**, 6871-6878, doi:10.1158/0008-5472.CAN-08-4490 (2009).

179 Cerchia, L. *et al.* Targeting Axl with an high-affinity inhibitory aptamer. *Mol Ther* **20**, 2291-2303, doi:10.1038/mt.2012.163 (2012).

180 Leconet, W. *et al.* Preclinical validation of AXL receptor as a target for antibody-based pancreatic cancer immunotherapy. *Oncogene* **33**, 5405-5414, doi:10.1038/onc.2013.487 (2014).

181 Vial, E., Sahai, E. & Marshall, C. J. ERK-MAPK signaling coordinately regulates activity of Rac1 and RhoA for tumor cell motility. *Cancer Cell* **4**, 67-79, doi:http://dx.doi.org/10.1016/S1535-6108(03)00162-4 (2003).

182 Wilson, C. *et al.* AXL inhibition sensitizes mesenchymal cancer cells to antimitotic drugs. *Cancer Res* **74**, 5878-5890, doi:10.1158/0008-5472.CAN-14-1009 (2014).

183 Wu, F., Li, J., Jang, C., Wang, J. & Xiong, J. The role of Axl in drug resistance and epithelial-to-mesenchymal transition of non-small cell lung carcinoma. *Int J Clin Exp Pathol* **7**, 6653-6661 (2014).

184 Rho, J. K. *et al.* MET and AXL inhibitor NPS-1034 exerts efficacy against lung cancer cells resistant to EGFR kinase inhibitors because of MET or AXL activation. *Cancer Res* **74**, 253-262, doi:10.1158/0008-5472.CAN-13-1103 (2014).

185 Burbridge, M. F. *et al.* S49076 is a novel kinase inhibitor of MET, AXL, and FGFR with strong preclinical activity alone and in association with bevacizumab. *Mol Cancer Ther* **12**, 1749-1762, doi:10.1158/1535-7163.MCT-13-0075 (2013).

186 Okimoto, R. A. & Bivona, T. G. AXL receptor tyrosine kinase as a therapeutic target in NSCLC. *Lung Cancer: Targets and Therapy*, 27-34 (2015).

187 Lodge, A. P., Howard, M. R., McNamee, C. J. & Moss, D. J. Co-localisation, heterophilic interactions and regulated expression of IgLON family proteins in the chick nervous system. *Brain research. Molecular brain research* **82**, 84-94 (2000).

188 Simons, K. & Ikonen, E. Functional rafts in cell membranes. *Nature* **387**, 569-572, doi:10.1038/42408 (1997).

189 International Cancer Genome, C. *et al.* International network of cancer genome projects. *Nature* **464**, 993-998, doi:10.1038/nature08987 (2010).

190 Ebisuya, M., Kondoh, K. & Nishida, E. The duration, magnitude and compartmentalization of ERK MAP kinase activity: mechanisms for providing signaling specificity. *Journal of cell science* **118**, 2997-3002, doi:10.1242/jcs.02505 (2005).

191 Hauge, C. & Frodin, M. RSK and MSK in MAP kinase signalling. *Journal of cell science* **119**, 3021-3023, doi:10.1242/jcs.02950 (2006).

192 Lee, Y., Lee, M. & Kim, S. Gas6 induces cancer cell migration and epithelial–mesenchymal transition through upregulation of MAPK and Slug. *Biochemical and Biophysical Research Communications* **434**, 8-14, doi:http://dx.doi.org/10.1016/j.bbrc.2013.03.082 (2013).

193 Ilangumaran, S. & Hoessli, D. C. Effects of cholesterol depletion by cyclodextrin on the sphingolipid microdomains of the plasma membrane. *Biochem J* **335 (Pt 2)**, 433-440 (1998).

194 Robinson, J. M. & Karnovsky, M. J. Evaluation of the polyene antibiotic filipin as a cytochemical probe for membrane cholesterol. *J Histochem Cytochem* **28**, 161-168 (1980).

195 Karst, A. M. & Drapkin, R. Primary culture and immortalization of human fallopian tube secretory epithelial cells. *Nat Protoc* **7**, 1755-1764, doi:10.1038/nprot.2012.097 (2012).

196 Ozhan, G. *et al.* Lypd6 enhances Wnt/beta-catenin signaling by promoting Lrp6 phosphorylation in raft plasma membrane domains. *Dev Cell* **26**, 331-345, doi:10.1016/j.devcel.2013.07.020 (2013).

197 Chen, C. L. *et al.* Betulinic acid enhances TGF-beta signaling by altering TGF-beta receptors partitioning between lipid-raft/caveolae and non-caveolae membrane microdomains in mink lung epithelial cells. *J Biomed Sci* **23**, 30, doi:10.1186/s12929-016-0229-4 (2016).

198 Yang, J. *et al.* Twist, a master regulator of morphogenesis, plays an essential role in tumor metastasis. *Cell* **117**, 927-939, doi:10.1016/j.cell.2004.06.006 (2004).

199 Sieben, N. L. *et al.* Differential gene expression in ovarian tumors reveals Dusp 4 and Serpina 5 as key regulators for benign behavior of serous borderline tumors. *J Clin Oncol* **23**, 7257-7264, doi:10.1200/JCO.2005.02.2541 (2005).

200 Meyer, A. S., Zweemer, A. J. & Lauffenburger, D. A. The AXL Receptor is a Sensor of Ligand Spatial Heterogeneity. *Cell Syst* **1**, 25-36, doi:10.1016/j.cels.2015.06.002 (2015).

201 Antony, J. *et al.* The GAS6-AXL signaling network is a mesenchymal (Mes) molecular subtype-specific therapeutic target for ovarian cancer. *Sci Signal* **9**, ra97, doi:10.1126/scisignal.aaf8175 (2016).

202 Domcke, S., Sinha, R., Levine, D. A., Sander, C. & Schultz, N. Evaluating cell lines as tumour models by comparison of genomic profiles. *Nat Commun* **4**, 2126, doi:10.1038/ncomms3126 (2013).

203 Sereni, M. I. *et al.* Functional characterization of epithelial ovarian cancer histotypes by drug target based protein signaling activation mapping: implications for personalized cancer therapy. *Proteomics* **15**, 365-373, doi:10.1002/pmic.201400214 (2015).

204 Suyama, K., Shapiro, I., Guttman, M. & Hazan, R. B. A signaling pathway leading to metastasis is controlled by N-cadherin and the FGF receptor. *Cancer Cell* **2**, 301-314 (2002).

205 Hulit, J. *et al.* N-cadherin signaling potentiates mammary tumor metastasis via enhanced extracellular signal-regulated kinase activation. *Cancer Res* **67**, 3106-3116, doi:10.1158/0008-5472.CAN-06-3401 (2007).

206 Marquez, M. G., Favale, N. O., Leocata Nieto, F., Pescio, L. G. & Sterin-Speziale, N. Changes in membrane lipid composition cause alterations in epithelial cell-cell adhesion structures in renal papillary collecting duct cells. *Biochim Biophys Acta* **1818**, 491-501, doi:10.1016/j.bbamem.2011.11.018 (2012).

207 Lajoie, P. *et al.* Plasma membrane domain organization regulates EGFR signaling in tumor cells. *J Cell Biol* **179**, 341-356, doi:10.1083/jcb.200611106 (2007).

208 Leutenegger, M. *et al.* Dual-color total internal reflection fluorescence cross-correlation spectroscopy. *J Biomed Opt* **11**, 040502, doi:10.1117/1.2221714 (2006).

209 Eggeling, C. *et al.* Direct observation of the nanoscale dynamics of membrane lipids in a living cell. *Nature* **457**, 1159-1162, doi:10.1038/nature07596 (2009).

APPENDICES

APPENDIX I

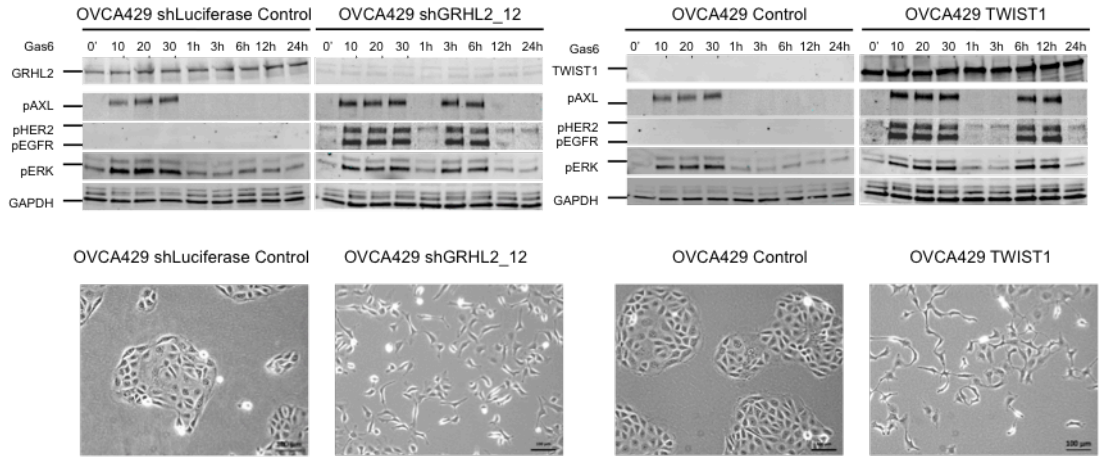


Figure I: EMT status influences Gas6/AXL signaling.
OVCA429 isogenic cell lines were generated by either knockdown of epithelial status maintaining GRHL2, or overexpression of EMT promoting TWIST1. Western blotting of Gas6 stimulated OVCA429, with either GRHL2 knockdown or TWIST1 overexpression, showed AXL-RTK crosstalk and recurrent pERK activation, unlike the isogenic controls. Knockdown of GRHL2, or overexpression of TWIST1 showed OVCA429 undergoing EMT as visualized by phase contrast images. Blots and images are representative of three experiments.

APPENDIX II

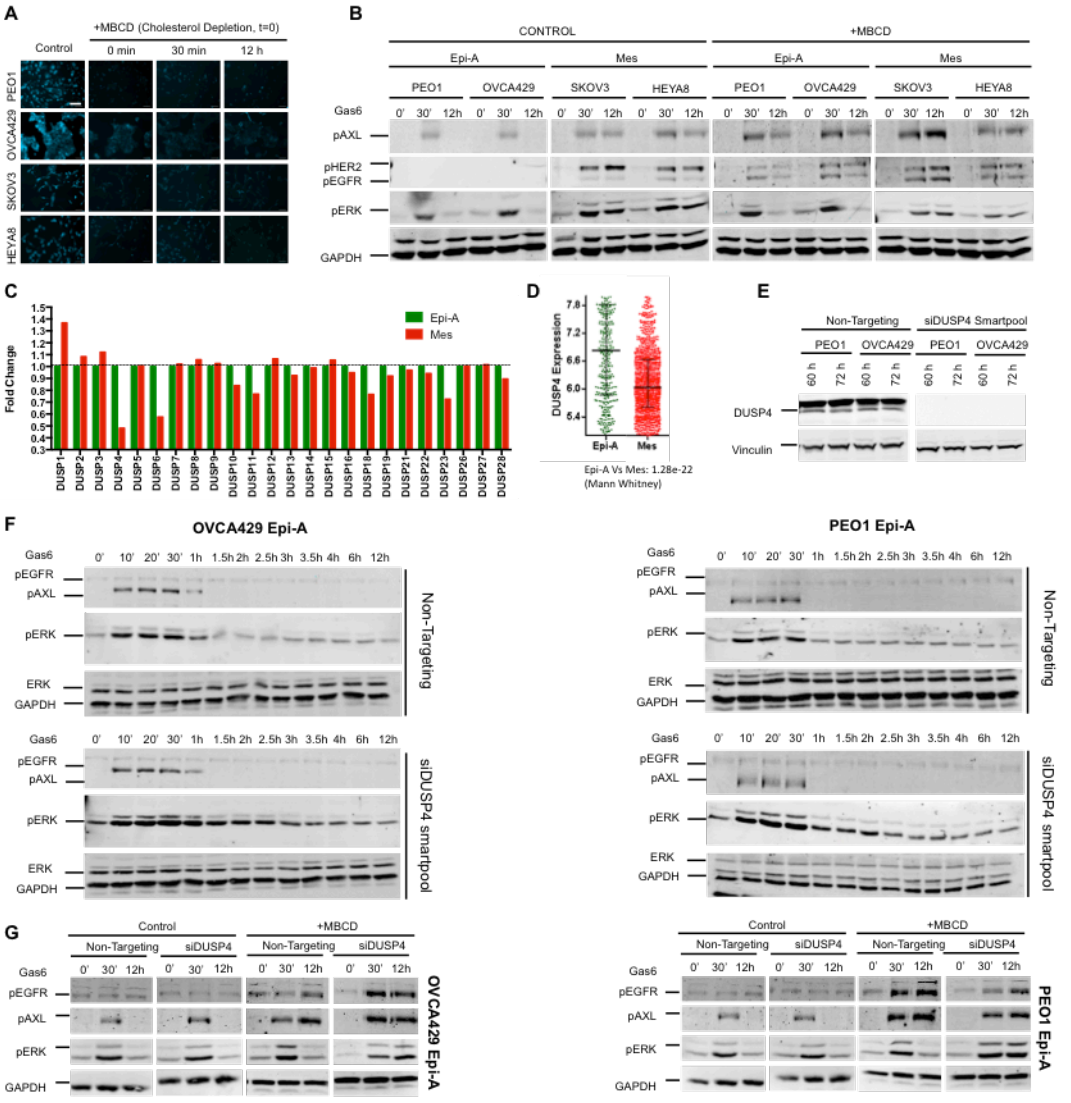


Figure II: Membrane rafts and cellular phosphatases regulate AXL signaling in epithelial systems.

(A) Cholesterol visualized by Filipin staining, was depleted using Methyl-β-cyclodextrin (MBCD), and depletion persisted up-to 12 hours post treatment.

(B) Gas6 stimulation post MBCD treatment, showed AXL-RTK cross talk in Epi-A subtype PEO1 and OVCA429 at early and late time points, but pERK response was limited to early time point.

(C) Screening the levels of Dual Specificity Phosphatases (DUSPs) in CSIOVDB, revealed (D) low DUSP4 levels in Mes subtype compared to Epi-A.

(E) siDUSP4 smartpool reduced DUSP4 protein levels from 60 hours till 72 hours, and experiments were carried out in this time period.

(F) Gas6 stimulation of DUSP4 depleted OVCA429 and PEO1 showed increase in duration of pERK signaling utp 3 hours, compared to 1 hour in Non targeting control.

(G) Gas6 stimulation upon depletion of DUSP4 as well as cholesterol depletion, induced AXL-RTK cross talk at early and late time points, and increased temporal duration of pERK response till the later time point.

Blots and images are representative of three experiments.

APPENDIX III

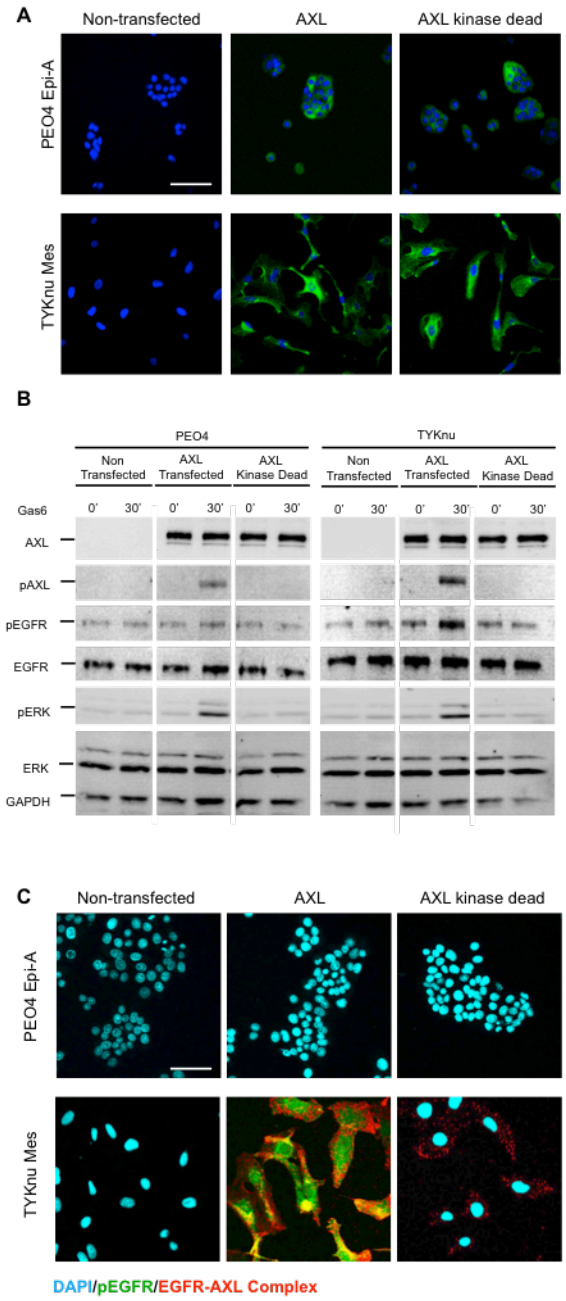


Figure III: AXL kinase domain is crucial for phosphorylation of other RTKs

(A) Immunostaining of AXL deficient Epi-A subtype PEO4, and Mes subtype TYKnu, transfected with *AXL* or *AXL* kinase dead plasmid.
(B) Western blotting of Mes subtype TYKnu transfected with *AXL* reveals EGFR phosphorylation upon Gas6 stimulation, but this is deficient in Epi-A PEO4. Upon *AXL* kinase dead transfection, there is no pAXL response upon Gas6 stimulation, and consequently no pEGFR response in TYKnu.
(C) DUOLink shows AXL-EGFR crosstalk (red dots) upon stimulation with Gas6 in Mes TYKnu transfected with AXL, as well as AXL kinase dead. However immunostaining for pEGFR (green) is not present in AXL kinase dead transfected TYKnu, suggesting that the AXL kinase domain is necessary to trans-phosphorylate RTKs in complex with AXL. AXL transfected Epi-A subtype PEO4 shows no AXL-EGFR complex formation upon Gas6 stimulation, or pEGFR signal.
Blots and images are representative of three experiments.

APPENDIX IV

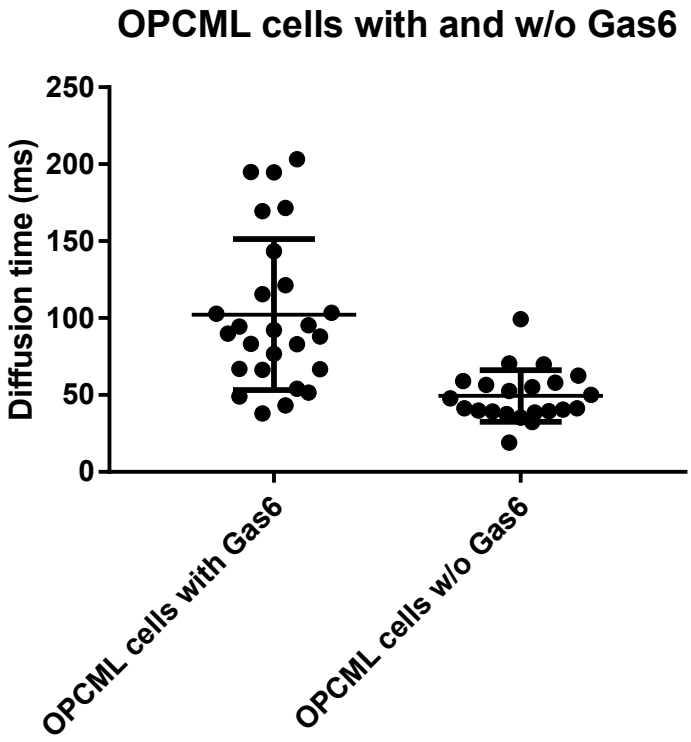


Figure IV: OPCML-AXL interaction upon Gas6 stimulation affects diffusion of AXL.

APPENDIX V

Name	Histology	Original Repository	Catalogue Number	Source
A2780	Undifferentiated	ECACC	93112519	ECACC
CAOV2	Adenocarcinoma			Kyoto U.
CAOV3	Serous	ATCC	HTB-75	ATCC
CH1	Papillary cystadenocarcinoma			Kyoto U.
COLO 720E	Adenocarcinoma	ECACC	93072111	ECACC
DOV13	Adenocarcinoma	M.D. Anderson Cancer Center		Kyoto U.
EFO21	Dedifferentiated serous cystadenocarcinoma	DSMZ	ACC-235	DSMZ
FUOV1	Serous papillary adenocarcinoma	DSMZ	ACC-444	DSMZ
Hey	Serous			Kyoto U.
HeyA8	Serous			Kyoto U.
HeyC2	Serous			Kyoto U.
IGROV1	Endometrioid	NCI-Frederick		Kyoto U.
JHOS2	Serous cystadenocarcinoma	RIKEN	RCB1521	Kyoto U.
JHOS3	Serous cystadenocarcinoma	RIKEN	RCB1546	Kyoto U.
JHOS4	Serous cystadenocarcinoma	RIKEN	RCB1678	Kyoto U.
OVCAR3	Serous	ATCC	HTB-161	ATCC
OAW 28	Cystadenocarcinoma	ECACC	85101601	ECACC
OAW 42	Papillary serous cystadenocarcinoma	ECACC	85073102	ECACC
OV17R	Adenocarcinoma	ECACC	96020763	ECACC
OV56	Poorly differentiated	ECACC	96020759	ECACC
OV7	Poorly differentiated	ECACC	96020764	ECACC
OV90	Serous	ATCC	CRL-11732	ATCC
ovary1847 (A1847)	Serous			Kyoto U.
OVCA420	Serous			Kyoto U.
OVCA429	Serous			Kyoto U.
OVCA432	Serous			Kyoto U.
OVCA433	Papillary serous cystadenocarcinoma			Kyoto U.
OVCAR10	Poorly differentiated			Kyoto U.
OVCAR2				Kyoto U.
OVCAR5	Adenocarcinoma	NCI-Frederick		Kyoto U.
OVCAR8	Undifferentiated	NCI-Frederick		Kyoto U.
OVK18	Endometrioid	RIKEN	RCB1903	Kyoto U.
PEO1	Poorly differentiated serous adenocarcinoma	CRT	PE Ovarian Adenocarcinoma Cell Line	CRT
PEO4	Poorly differentiated serous adenocarcinoma	CRT	PE Ovarian Adenocarcinoma Cell Line	CRT
SKOV3	Serous	ATCC	HTB-77	ATCC
TOV112D	Endometrioid	ATCC	CRL-11731	ATCC
TykNu	Undifferentiated	JCRB	JCRB0234.0	Kyoto U.
UWB1.289	Papillary serous	ATCC	CRL-2945	ATCC

ATCC: American Type Culture Collection
CRT: Cancer Research Technology (Cancer Research UK)
DSMZ: Deutsche Sammlung von Mikroorganismen und Zellkulturen

Table 4: Histopathology of 38 ovarian cancer cell lines.